RESONANT NANOPHOTONIC STRUCTURES FOR PHOTOVOLTAICS

Cover image: artistic view of an engineered silver nanowire network on glass with reflections from the sun and sky. Network is drawn to scale, with typical dimensions labeled. Resonant photonic interactions are indicated in red.
Designed by Jair de Haan.

Ph.D. Thesis University of Amsterdam, December 2015
Resonant nanophotonic structures for photovoltaics
Jorik van de Groep

ISBN 978-90-77209-96-7

A digital version of this thesis can be downloaded from http://www.amolf.nl.

RESONANT NANOPHOTONIC STRUCTURES FOR PHOTOVOLTAICS

Resonante nanofotonische structuren
met toepassingen in fotovoltaïca

Academisch Proefschrift

ter verkrijging van de graad van doctor
aan de Universiteit van Amsterdam
op gezag van de Rector Magnificus
prof. dr. D.C. van den Boom
ten overstaan van een door het college voor promoties
ingestelde commissie,
in het openbaar te verdedigen in de Agnietenkapel
op dinsdag 15 december 2015 te 10:00 uur

door

Jorik van de Groep

geboren te Putten

Promotiecommissie

Promotor:	Prof. dr. A. Polman	Universiteit van Amsterdam
Overige Leden:	Prof. dr. A. Alù	The University of Texas at Austin
	Prof. dr. A. Fiore	Technische Universiteit Eindhoven
	Prof. dr. T. Gregorkiewicz	Universiteit van Amsterdam
	Prof. dr. A. F. Koenderink	Universiteit van Amsterdam
	Prof. dr. W. C. Sinke	Universiteit van Amsterdam

Faculteit der Natuurwetenschappen, Wiskunde en Informatica

This work is part of the research program of the 'Stichting voor Fundamenteel Onderzoek der Materie' (FOM), which is financially supported by the 'Nederlandse organisatie voor Wetenschappelijk Onderzoek' (NWO). It is also funded by NanoNextNL, a nanotechnology program funded by the Dutch ministry of economic affairs, and the European Research Council (ERC).

Contents

1

Introduction

1.1 Light scattering by nanostructures

The ability to control the flow of light has given rise to a wide range of applications that strongly influence our daily life. For example, the development of optical microscopy has revolutionized our understanding of nature, the introduction of optical fibers facilitates high-speed worldwide telecommunication, and advances in optical lithography have enabled the large-scale fabrication of computer chips.

Light can be manipulated using lenses and mirrors, as well as by small objects. The interaction between light and matter is governed by the refractive index of the material. Similar to a rock in a stream of water, the flow of light is perturbed when it runs into a (local) region of space with a refractive index different from that of the surrounding medium. The redirection of light upon such a perturbation is called scattering. The most well known examples of light scattering in nature are the scattering off small particles in the atmosphere which causes the blue color of the sky [1], and the scattering by small water droplets in rainy weather which allows for the observation of the rainbow.

The scattering behavior of a structure is strongly dependent on its size. If the geometrical size of the structure is comparable to the wavelength of visible light (hundreds of nm), resonant effects can occur. Optical resonances in such a nanostructure strongly enhance the interaction with light, and thereby determine the optical properties of the structure. The physical mechanism underlying the optical resonance, on the other hand, is determined by the material of which the nanostructure is composed.

Metal nanostructures exhibit resonant oscillations of the free conduction electrons during optical illumination, termed localized surface plasmon resonances (LSPR) [2]. Figure 1.1a (red) shows the scattering efficiency, defined as the ratio

of the scattering cross section and the geometrical cross section, of a 120 nm silver sphere in vacuum calculated using Mie theory. A clear peak can be observed around 439 nm, as a result of the lowest-order dipolar plasmon resonance. At resonance, the free electrons in the nanoparticle exhibit a collective motion, driven by the oscillating electric field of the incident radiation. Due to interactions with the positively charged atomic lattice and geometrical confinement, the oscillating electrons experience a restoring force. The resonance frequency is therefore strongly sensitive to the geometry [3–6], dielectric surrounding [3, 5], and material of the nanostructure [5, 7, 8]. As a result of the resonant interaction, the incident light is strongly concentrated at the interface of the nanoparticle. Figure 1.1b shows the numerically calculated electric field distribution as a result of the plasmon resonance; large field enhancements are observed at the interface, whereas there is no field inside the metal nanoparticle. The asymmetry in the field distribution is caused by the direction of propagation of the incident plane wave. LSPRs are typically characterized by a large scattering cross section, equal to several times their geometrical cross section (see Fig. 1.1a).

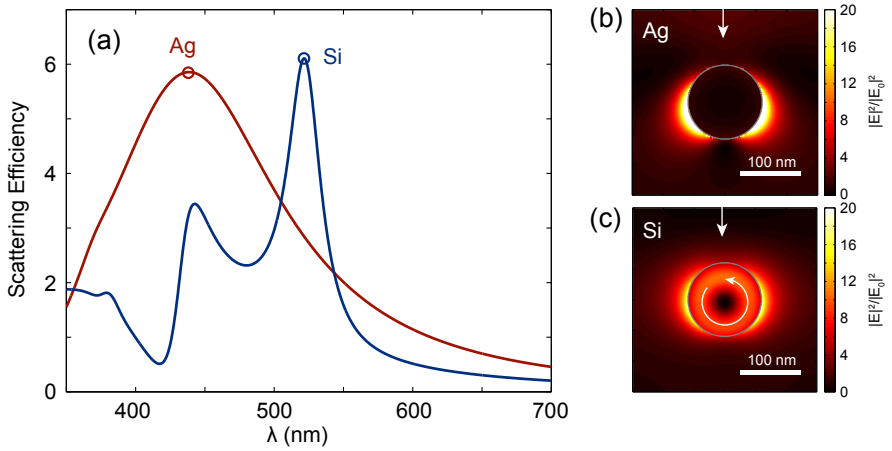

Figure 1.1: (a) Scattering efficiency ($\sigma_{scat}/\sigma_{geo}$) for a 120 nm silver sphere (red) and silicon sphere (blue) illuminated by a plane wave in vacuum, calculated using Mie theory. The circles indicate the wavelength for the field plots in (b,c). (b) Numerically calculated field enhancement (color) for the lowest order dipolar plasmon resonance on the silver sphere (λ = 439 nm). The field is strongly confined at the interface of the nanoparticle. (c) Field enhancement (color) for the lowest order magnetic dipolar Mie resonance in a silicon sphere (λ = 520 nm). The field is delocalized throughout the particle in a well-defined geometrical profile. The displacement current loop is schematically indicated by the arrow. The plane wave is incident from the top.

Due to the high sensitivity of the LSPR to the local geometry, and its ability to strongly concentrate and scatter light, LSPRs have found numerous applications

in nanophotonic studies and devices [9]. For example, resonant metal particles are commonly employed as a nanoscale antennas [10] for local emitters [11, 12] or detectors [13–15]. Similarly, two-dimensional arrays of plasmonic antennas have been demonstrated to enhance the outcoupling of light in light-emitting diodes (LEDs) [16, 17]. The high sensitivity of the LSPR to its dielectric surrounding is used to realize highly-efficient (bio)sensors [18] and nanoscale rulers [19, 20]. Furthermore, by changing the shape of the nanostructures into ring-like geometries, the nanoscale flow of charges associated with the LSPR gives rise to a magnetic response [21]. Three-dimensional arrays of such resonators can be used to construct materials with optical properties unlike anything found in nature. Such metamaterials can be engineered to have refractive indices that are close to zero or even negative [22]. Likewise, two-dimensional surfaces of engineered scatterers (metasurfaces) allow for controlled beam-steering as a result of engineered phase profiles across the surface [23, 24].

Due to the physical flow of electrons associated with plasmon resonances, LSPRs are strongly damped by parasitic absorption in the metal [7]. This is clearly visible from the scattering spectrum in Fig. 1.1a, which shows a spectrally wide (low-Q) resonance. Although such resonant absorption is exploited in a wide range of applications, such as non-invasive thermal cancer treatment [25, 26], and thermographic sensing of DNA [27], parasitic losses are often undesired when LSPRs are used as scattering elements.

Dielectric nanostructures, on the other hand, support geometrical resonances by which incident light is confined in a well-defined spatial mode profile inside the nanostructure [28]. These geometrical resonances were first described by the German physicist Gustav Mie, who solved Maxwell's equations for a sphere in a homogeneous medium illuminated by plane waves [29]. Note that the Mie solutions are valid for both metallic and dielectric particles, and thereby also predict the plasmonic resonances. However, due to the difference in dielectric permittivity, the two physical mechanisms are distinctively different. Unlike for metal nanoparticles, the current loops inside geometrical structures are displacement current loops rather than actual current loops [30]. As a result, geometrical resonances in dielectric nanoparticles are most often characterized by very low absorption losses.

Figure 1.1a (blue) shows the scattering efficiency of a 120 nm silicon sphere in vacuum. Two clear resonances can be observed, corresponding to the lowest-order magnetic (λ = 520 nm) and electric (λ = 442 nm) dipolar modes, respectively (as will be discussed in Chapter 9). The peaks in the scattering spectrum are significantly sharper (higher Q) than those for the silver nanoparticle as a result of the reduced absorption losses. The displacement current loop is clearly visible in Fig. 1.1c, which shows the electric field distribution inside a 120 nm silicon sphere at λ = 520 nm as a result of the Mie resonance. Unlike for the plasmon resonance (Fig. 1.1b), the field is distributed inside the particle with a characteristic modal field distribution.

For dielectric particles the resonance wavelength scales linearly with size and refractive index [31], which allows accurate tuning of the resonance spectra for

specific applications. Furthermore, since the fields are primarily concentrated inside the nanostructures, geometrical resonances are less sensitive to changes in the surrounding medium [32]. Compared to their plasmonic counterparts, dielectric nanostructures allow for similar or higher scattering efficiencies with strongly reduced absorption losses [32–34]. Plasmonic nanostructures, on the other hand, allow for deep sub-wavelength concentration of optical fields [35], which is unachievable with dielectric resonators due to the delocalization of optical fields within the nanostructure.

Note that silicon is a high-index material (n = 3.5–6.5), but strictly a semiconductor rather than a pure dielectric. However, due to its indirect band gap the absorption coefficient in the visible spectral range is low [36], and silicon nanostructures have been demonstrated to be effective scatterers in the visible spectral range [37–41]. Furthermore, for energies lower than the band gap (1.11 eV) [42] silicon is effectively a high-index dielectric, with excellent scattering properties in the near-infrared and infrared spectral range [43–45].

The accurate tunability and low absorption losses of dielectric resonators have resulted in widespread application in optical studies and nanoscale devices. For example, by spectral alignment of the magnetic and electric modes, the backscattering of light can by fully suppressed [30, 45, 46]. Coupled resonators (dimers and trimers) allow for even more control over the bandwidth and directionality of the scattered light [47, 48], as well as electric and magnetic field enhancements in the gap between the particles [49–52]. Such directional scattering can be used to construct low-loss optical antennas or angle-sensitive photodetectors. Furthermore, the magnetic dipolar mode supported by simple geometries such as spheres and cylinders [39, 40, 46] allows for the realization of all-dielectric low-loss analogies of the plasmonic metamaterials [53, 54] and metasurfaces [55, 56]. These materials and surfaces open new pathways for the controlled manipulation of light with low absorption losses. Additionally, by engineering geometrical resonances in absorbing semiconductor materials, active nanoscale resonators can be constructed. The ability to extract and insert electrical charges in single optical resonators gives rise to a wide range of nanoscale devices, including photodetectors [57–60], sensors [61], lasers [62], and solar cells [63–65].

1.2 Resonant nanostructures for photovoltaics

Photovoltaics - the conversion of optical energy to electrical energy through the photovoltaic effect - is based on the cross-band gap excitation of electrons in a semiconductor material upon absorption of a photon. After excitation of an electron from the valence band to the conduction band of the semiconductor, the electron-hole pair carries chemical potential, which can be extracted as an electrical potential. The most commonly used semiconductor material is silicon; close to 90% of the installed solar modules worldwide are based on silicon [66]. Roughly, three optical processes must be controlled for optimized photovoltaic

power conversion (see Fig. 1.2).

(1) The incident solar radiation must enter the slab of absorber material. Depending on the specific geometry, reflection losses from the top interface can be significant (e.g. 30–40% for an air-silicon interface). It is therefore essential to minimize these losses using *anti-reflection* (AR) coatings.

(2) Light must be absorbed by the active material such that charge carriers are excited across the electronic band gap. For materials with an indirect band gap (including silicon), the absorption coefficient is relatively low. As a result, very long optical path lengths are required in order to achieve full absorption for wavelengths near the band gap. The optical path length - and thereby the absorption - can be enhanced by trapping light inside the absorber material using *light trapping* schemes.

(3) The generated charge carriers need to be extracted to avoid recombination. This step requires high-quality materials with low defect densities, well passivated surfaces, and low-resistivity electrodes to transport the charge carriers out of the cell. The latter requires large metal fingers on the surface of the solar cell, which compromises the transmission of light into the cell. Hence, *transparent electrodes* - materials with high optical transmission and low electrical resistivity - are desirable. As we will show in this thesis, optically resonant nanostructures can be used to address all these challenges simultaneously.

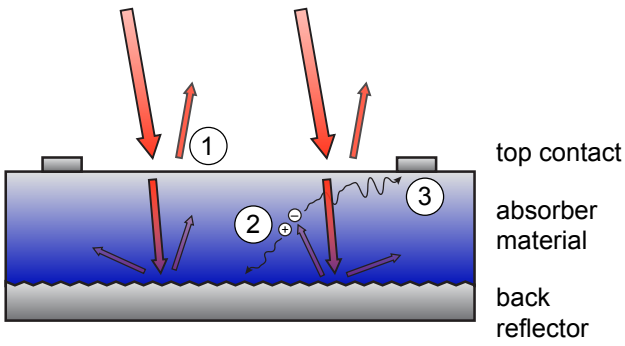

Figure 1.2: Schematic of the three main optical processes in a photovoltaic cell: **(1)** light needs to enter the absorber material; **(2)** light must be absorbed by the active material; and **(3)** the optically generated charge carriers must be extracted.

1.2.1 Anti-reflection and light trapping

Optically resonant nanostructures scatter light in well-defined radiation patterns, e.g. dipolar or higher-order radiation profiles [67–69]. These radiation patterns can be strongly modified through accurate tuning of the resonator geometry and

dielectric surrounding. For example, a point dipole at the Si-air interface radiates up to 96% of the scattered light into the Si substrate, as a result of the high local density of optical states (LDOS) [70]. This directional scattering of resonant nanostructures can be used to construct efficient anti-reflection coatings [47]. Such AR-coatings have been demonstrated experimentally using both plasmonic [71, 72] and dielectric nanostructures [33, 73].

Patterns of resonant nanostructures at the front or back of the solar cell can also function as efficient light trapping schemes. Using the large scattering cross section at resonance (Fig. 1.1a), incident light is efficiently scattered into the absorber layer. Both plasmonic scattering arrays [74, 75] and dielectric resonant structures [76] have been applied as back scattering patterns in thin-films solar cells.

For optically thin layers, application of scattering nanostructures on top of the absorber layer often results into a combined anti-reflection and light trapping effect. Besides directional scattering into the substrate [33, 47, 71–73], scattering under large angles results into optical path length enhancements, as well as coupling to guided modes in the substrate [77–81]. A widespread variety of geometries, both plasmonic [78] and dielectric [82], have been demonstrated to significantly enhance the optical absorption in thin-film devices. These include 1D-gratings [83], arrays of particles or voids [84, 85], nanopyramids [86, 87], randomly structured surfaces [88], and silica whispering gallery resonators [89, 90]. Alternatively, the absorber layer itself may be shaped as a geometrical resonator, such as nanoshells [91], micro-wires [92, 93], nanowires [94, 95], or nanocylinders [96], thereby effectively enhancing the absorption in extremely small volumes of semiconductor. More exotic geometries include simultaneous texturing of the front and back surfaces [97], or metal-semiconductor core-shell nanowires in which both plasmonic and dielectric resonances are supported [98].

The examples discussed above demonstrate that scattering by resonant nanostructures has large potential in the optimization of “light management” in photovoltaic devices, and is well-established in the field. However, many very fundamental questions remain. To fully benefit from the possibilities provided by controlled scattering of light, a fundamental understanding of the scattering processes by individual nanostructures is essential. What is the nature of the optical resonances in individual nanostructures on substrates? How does the geometry, material, and dielectric surrounding affect these resonances? How does the near-field interaction between two resonators influence its optical response? Can we use the effective response of an array of particles to enhance the performance of photovoltaic devices? In this thesis, we systematically study both individual nanoparticles and arrays of nanostructures in order to gain such fundamental insights and answer these questions.

1.2.2 Transparent electrodes

Besides enhanced light incoupling and trapping (discussed in Section 1.2.1), resonant nanostructures can also contribute to the efficient extraction of charge car-

riers from absorber material. Photovoltaic devices based on materials with short charge carrier diffusion lengths such as, for example, Si heterojunction, perovskite, or organic cells, require the inclusion of a transparent electrode for the short-scale transport of charge carriers. High-quality transparent electrodes optimize the balance between optical transparency and electrical conductivity for specific applications [99]. The industry-standard material is indium-tin-oxide (ITO). However, relatively high sheet resistances and optical absorption in the UV and NIR spectral range limit the performance of this material as a transparent conductor [80, 100]. This, as well as high costs [101, 102], brittleness [103, 104], and incompatibility with organic materials [105] motivate the search for a replacement of ITO.

In contrast with dielectric nanostructures, the metallic nature of plasmonic nanostructures allows for charge conduction. This enables the simultaneous use of plasmonic resonators as a scattering and electrode geometry. Due to the high conductivity of metals, random nanowire meshes [106–108], one-dimensional gratings [103, 104, 109], and percolated films [110, 111] have been studied as transparent electrodes. Concurrent low sheet resistances and high optical transmittance have been demonstrated, with performances better than ITO [112]. However, due to the random nature of many of these geometries, it remains difficult to systematically study resonant plasmonic effects in the nanowire networks. Are engineered periodic networks of metal nanowires better transparent conductors than random networks? What resonant effects play a role in the transmittance through such networks? How can we use these resonances to optimize the transmittance and light trapping effects simultaneously? Can we optimize the quality of the metal comprising the nanowire networks to further enhance the performance as a transparent conductor? In this thesis we experimentally investigate the fundamental properties of engineered metal nanowire networks, and explore the answers to the above questions in detail.

1.3 Resonantly induced potentials

Sections 1.2.1 and 1.2.2 both describe how resonant nanostructures can enhance light management and charge conduction in photovoltaic devices. Interestingly, plasmonically resonant nanostructures can also directly induce electrostatic potentials. Within ~100 fs after excitation, LSPRs decay into hot electrons [113, 114]. When in contact with a rectifying contact, the excess energy of hot electrons can be transferred into chemical potential by crossing the Schottky barrier into the neighboring semiconductor [14, 115]. Such hot electron devices allow for tunable sub-band gap photodetectors, albeit with very low quantum efficiencies [14, 116, 117]. Alternatively, hot electrons from plasmonic nanoparticles can be used to drive photochemical reactions [118, 119]. Stimulated by these examples, further questions arise: can plasmonic resonators be used in new ways to induce electrostatic potentials? Can this be done without a semiconductor material and rectifying contact? Is this also be possible with non-plasmonic (e.g. dielectric)

resonators? To answer these questions, we explore in this thesis the fundamental thermodynamics of electrical potential generation by resonant nanostructures.

1.4 Outline of this thesis

Each chapter in this thesis reports on advances in the fundamental understanding of the interaction of light with nanostructures, within three main topics: nanowire networks as transparent conductors (Chapters 2–4), the plasmoelectric effect (Chapters 5–7), and the resonant properties of dielectric resonators (Chapters 8–11).

In **Chapter 2** we present a two-dimensional network of silver nanowires that can act as a transparent conductor for optoelectonic devices. We fabricate such networks with electron beam lithography and study the optical resonances supported by the structure. We find that the transmittance is governed by an interplay of localized plasmon resonances, grating diffraction, and surface plasmon polaritons. Moreover, we demonstrate that such networks of silver nanowires can outperform the industry-standard material indium-tin-oxide as a transparent conductor.

In **Chapter 3** we use soft-imprint lithography to demonstrate large-area fabrication of the silver nanowire networks. Using this, we apply these nanowire networks as the transparent conductor in polymer solar cells. We find that the nanowire networks effectively combine the functions of charge conduction and light scattering.

Chapter 4 describes how the time- and energy-intensive step of metal evaporation in the fabrication process of the nanowire networks described in Chapters 2 and 3 can be replaced by a solution-based process. We show that the resulting nanowire networks have significantly enhanced electrical performance as a result of a strong reduction of grain boundary scattering, due to a large increase in the metal crystallite size.

In **Chapter 5** we demonstrate a new optoelectronic phenomenon: *the plasmoelectric effect*, which is an optically induced electrostatic potential in metal nanostructures. We present a thermodynamic model, which explains the surface potentials as the tendency of a plasmonic structure to spectrally align its resonant absorption frequency with that of the incident illumination by varying the charge density. Using Kelvin-probe force-microscopy, we experimentally demonstrate surface potentials as high as 100 mV on gold colloidal particles and circuits composed of sub-wavelength hole arrays in a thin gold film.

Chapter 6 describes the thermodynamic theory of the plasmoelectric effect in detail. We use a model system comprised of a 20 nm silver sphere in vacuum to derive the fundamental theory, which is based on the generation of entropy and minimization of the thermodynamic free energy of the system. Next, we discuss the applicability of this analysis for realistic experimental geometries, and find that systems with a large entropy can generate significant potentials as a result of minute increases in the steady-state temperature. Finally, we show that the plasmoelectric

effect is generic for optical structures in which an optical resonance is linked to the charge density.

In **Chapter 7** we describe the first steps towards the experimental demonstration of circuit-based plasmoelectric power conversion. We use simulations to design and study a plasmonic hole array in a 20 nm thick Au film that shows near-unity absorption as a result of resonant coupling to a damped SPP mode. We fabricate Au–Al_2O_3–Ag parallel-plate micro-scale capacitors that have the hole array integrated in the top plate, and experimentally study their absorption spectra. We design an AC optoelectronic experiment which exploits the transient currents generated by the plasmoelectric effect to charge and discharge the micro-scale capacitors.

In **Chapter 8** we study the resonant behavior of silicon nanodiscs using angle-resolved cathodoluminescence (CL) spectroscopy. We use the high resolution of an electron beam in SEM to locally excite geometrical resonances in individual nanodisks. Using this technique, we measure the resonance spectra and determine the corresponding field profiles for different disc diameters. Using the angular emission profiles we resolve the electric and magnetic nature of the disc resonances, and explore their directional properties.

In **Chapter 9** we numerically study the influence of geometry, excitation mechanism and dielectric surrounding on the resonant properties of the nanodisks discussed in Chapter 8. We show how retardation of the incoming field is essential for the excitation of magnetic (dipolar) resonances inside the nanoparticle. Furthermore, we find that stratified media can be used to engineer the scattering amplitude of the electric and magnetic modes, and that the interference of these modes can be used for directional scattering into the substrate.

In **Chapter 10** we investigate how coupling between silicon particles that are placed in close proximity gives rise to hybridized resonant modes. Using dark-field scattering spectroscopy we study the influence of spacing between the particles on the scattering spectra. For closely spaced particles, we use CL spectroscopy to directly measure the hybridized field profiles, and compare to modeled eingenmodes to identify the hybridized modes.

Chapter 11 demonstrates how an array of non-resonant silica particles behaves as an effective medium to function as an efficient anti-reflection coating for glass substrates. Using substrate-conformal imprint-lithography, the anti-reflection coating is fabricated over large areas in a simple manner. We show that the coating effectively eliminates the reflection off glass surfaces, and apply the coating to solar modules and smartphone screens.

Finally, **Chapter 12** describes two applications inspired by the work in Chapters 2–11. (1) Silver nanowire networks as transparent electrodes on high-efficiency Si heterojunction solar cells; we find that the high conductivity of the nanowire networks gives rise to a good fill factor, even after a 2.5-fold increase in the macroscopic finger spacing, increasing the efficiency from 14.8% to 16.0%. (2) Soft-imprinted dielectric nanopattern for flat plasmonic back scattering in nc-Si solar cells; we demonstrate that a flat plasmonic scattering electrode gives rise to a strong en-

hancement in photocurrent without the loss in voltage that is commonly found for cells grown on textured front contacts.

Overall, this thesis provides fundamental insights in light scattering and absorption by resonant metallic and dielectric nanostructures, that can be used in the design and development of improved photovoltaic devices and other optoelectronic applications.

2

Transparent conducting silver nanowire networks

We present a transparent conducting electrode composed of a periodic two-dimensional network of silver nanowires. Networks of Ag nanowires are made with wire diameters of 45–110 nm and pitch of 500, 700 and 1000 nm. Anomalous optical transmission is observed, with an averaged transmission up to 91% for the best transmitting network and sheet resistances as low as 6.5 Ω/sq for the best conducting network. Our most dilute networks show lower sheet resistance and higher optical transmittance than an 80 nm thick layer of ITO sputtered on glass. By comparing measurements and simulations we identify four distinct physical phenomena that govern the transmission of light through the networks: all related to the excitation of localized surface plasmons and surface plasmon polaritons on the wires. The insights given in this paper provide the key guidelines for designing high-transmittance and low-resistance nanowire electrodes for optoelectronic devices, including thin-film solar cells. For the latter, we discuss the general design principles to use the nanowire electrodes also as a light trapping scheme.

2.1 Introduction

Transparent conducting electrodes (TCEs) are essential components in many optoelectronic devices, including LEDs, electronic displays and solar cells.

Their unique combination of optical transparency and electrical conductivity provides the possibility to extract electrical carriers while transmitting light through the layer. Indium-tin-oxides (ITOs) are commonly used in many applications, but suffer from several important drawbacks, such as high materials costs [101, 102], scarcity of indium, damaging of organic substrates during sputtering [102], and brittleness [101–104]. An important further drawback for applications in solar cells is the strong absorption of ITO in the UV/blue spectral range [80, 120]. These problems motivate the search for new TCE materials. Presently, many new materials and geometries are being investigated, including macroscopic metallic grids (down to sizes of tens of microns) [103, 121], one-dimensional (nano-)imprinted metal electrodes [101, 104, 109], solution-processed random metal nanowire (NW) meshes [106, 107, 122–124], graphene [125, 126], and aluminum nanomeshes fabricated through self-assembly of silica spheres [110]. Each of these material geometries represents a trade-off between optical transmittance and electrical conduction. Thicker and denser layers provide better electrical conduction but reduce the optical transmission and vice versa. Furthermore, the compatibility with optoelectronic device fabrication techniques limits the applicability of several of these materials.

Recently, a detailed numerical analysis of the physics of the transmission of light through 1D and 2D metal NW networks has shown how a combination of guided optical modes in metal-insulator-metal (MIM) waveguides (formed by the NWs) and surface plasmon polaritons (SPPs) on the NWs determine the optimal design of such networks [102]. Thin, high aspect ratio wires were evaluated in simulations to have optimum transmission without losing electrical conductance. The 1D design has been realized experimentally [101], yielding performances comparable to ITO. This structure, however is only effective for one polarization. Two dimensional periodic networks of sub-wavelength nanowires and wavelength-sized pitch have been realized before [127], however these were optimized for absorption in the metal nanowires. So far, there is no experimental study on 2D subwavelength NW networks with wavelength-sized pitch optimized for high optical transmission and low electrical resistivity.

In this Chapter, we simulate and fabricate a 2D network of silver NWs, and study the performance of such NW networks as transparent conducting electrodes. By simulating different wire widths, we recognize four different scattering mechanisms that govern the transmittance of the network, and also observe these experimentally. We show that several additional physical effects to the ones described in ref. [102] come into play when considering 2D NW networks with wire spacing on the scale of the wavelength of light. Measurements show that our best geometries show higher optical transmittance and lower electrical resistance than an 80 nm thick layer of ITO.

2.2 Optical experiments

Figure 2.1a shows a sketch of a typical NW network design used in this work. The total size of the network was 50 × 50 μm, and electrical contact pads with a size of 80 × 50 μm were designed on two opposing sides of the network to allow electrical characterization. The Ag NW networks were fabricated using electron beam lithography. A SiO_2 substrate was used to allow both high optical transmission and electrical insulation. Networks of NWs with 500, 700 and 1000 nm wire spacing (Λ) were written with a 30 kV electron beam (7.5 μm aperture, ~0.018 nA current, ~2.7 μs dwell time, ~4.8 nm step size) in positive resist (ZEP) using single pixel line exposure. The dose was varied between 400 and 1000 pC/cm to obtain wires with different widths. After development, ~3 nm of germanium (at a rate of 0.2 Å/s) and 60 ± 5 nm of silver (0.5 Å/s) were deposited using thermal evaporation. The layer thickness defines the height of the wires in the network. The thin layer of germanium underneath the silver reduces the grain size of the silver and thereby gives rise to high quality silver NWs [128–130]. Lift-off is performed by soaking in anisole (methoxybenzene) for 24 hours, followed by 1:30 minutes of ultra-sonification in anisol.

Figure 2.1b,c shows Scanning Electron Microscopy (SEM) images of the Λ = 500 nm sample with 55 nm wire width. The image shows the excellent uniformity of the network over a large area. The inset in Fig. 2.1b shows the high quality of the individual NWs. The NW width for different networks made using different e-beam exposures ranged from 45–110 nm. Figure 2.1c shows the wire network is well connected to the electrical contact pads. Figure 2.1d shows an Atomic Force Microscopy (AFM) image of the network in Fig. 2.1b,c. The inset shows a line scan from which the NW height is determined to be 60 ± 5 nm.

Optical transmission measurements were performed using an integrating sphere setup. A supercontinuum white light source (Fianium) was used to illuminate the networks close to normal incidence. A microscope setup with a 20× objective (NA = 0.4) was used to focus the unpolarized light into a 10 μm spot in the center of the NW networks. A large core diameter detection fiber connected the integrating sphere with a spectrometer consisting of a spectrograph and a Si CCD array. Measurements were performed in the spectral range from 420 nm < λ < 970 nm.

Figure 2.2 shows the results of the optical transmission measurements. In Fig. 2.2a the normalized transmission (defined as the transmission through the network normalized to the transmission through a bare glass reference sample) is shown as a function of wavelength for a Λ = 500 nm network with different wire width in the range w = 45–110 nm (colors). Several clear features can be observed. First, an overall reduction in transmittance is observed for larger w, which is attributed to the increase in surface area that is covered by silver as w increases. Second, a deep and spectrally broad dip in transmittance is observed around λ = 450–550 nm which shifts to larger wavelengths for larger w. This feature is attributed to the excitation of the localized surface plasmon resonance

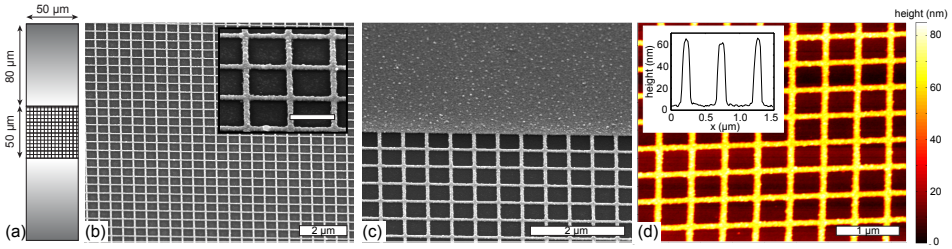

Figure 2.1: (a) Sketch of the sample geometry. Silver nanowire networks, 50 × 50 μm in size, with wire diameters between 45–110 nm and a pitch of 500, 700 or 1000 nm were fabricated using electron beam lithography. Silver electrical contact pads with a size of 80 × 50 μm were fabricated on two opposing sides. The lines in the network are not to scale. (b) SEM image of the Λ = 500 nm, w = 55 nm network showing the uniformity of the network over a large area. A large-magnification SEM image (inset) shows the high quality of the individual Ag wires. Scale bar in the inset is 500 nm. (c) SEM image showing the contact area of the wire network and the electrical contact pads. (d) Height profile (colorbar) of the Λ = 500 nm, w = 55 nm network obtained from AFM measurements. The inset shows a line scan from which the height of the wires is determined to be 60 ± 5 nm. Note the different horizontal and vertical scales in the inset.

(LSPR) of individual Ag NWs. Third, a sharp dip in transmittance is observed for 750 < λ < 850 nm that shifts to shorter wavelength as w increases. This spectrally sharp feature is attributed to the excitation of propagating surface plasmon polaritons (SPPs) along the individual wires. Finally, a downward slope is observed in the transmittance for λ > 850 nm that decreases for larger wire diameters. This decrease in transmission is attributed to the cut-off of the fundamental TE_0 waveguide mode that is supported by the metal-insulator-metal (MIM) waveguides formed by the air gaps in between the wires [102]. Each of these features will be discussed in more detail in the simulations section.

SEM images were used to determine the fraction of the surface area that is covered by the silver network for all wire diameters and each pitch. We define the clear aperture of a network as the fraction of surface area that is not covered by silver. Based on simple geometrical optics, one would expect the transmittance of the network to be equal to the clear aperture. The inset of Fig. 2.2a shows the same transmission curves as in Fig. 2.2a, normalized to the clear aperture of each network. Anomalous transmission (i.e. transmission larger than the clear aperture) is observed for all wire diameters at wavelengths above the LSPR wavelength. The average transmission, weighted for the AM1.5 solar spectrum and normalized to the clear aperture, is found to be ~1.1 for all wire diameters. The anomalous transmission is a result of the fact that the individual wires of the network are sub-wavelength structures that strongly scatter light [131–133]. Unlike bulk metal structures, sub-wavelength structures can have large scattering cross sections compared to their geometrical cross section, due to their plasmonic behavior. The fraction of

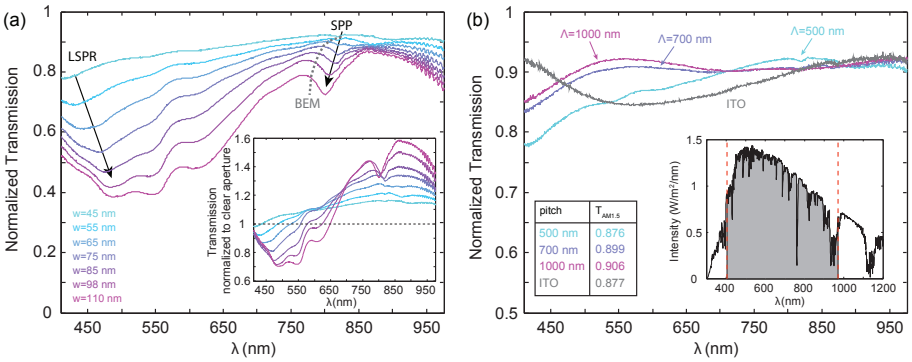

Figure 2.2: (a) Normalized optical transmittance through nanowire networks with a pitch of 500 nm as a function of wavelength for different wire diameter w (colors). Arrows indicate the dips in transmission due to the excitation of LSPRs and SPPs. The inset shows the same transmission data normalized to the clear aperture. Anomalous transmission is observed for wavelengths above the LSPR wavelength. (b) Normalized transmission as a function of wavelength for networks with the smallest wire diameter (w = 45 nm) and pitch of 500 nm (blue), 700 nm (purple) and 1000 nm (pink). Also shown is the transmittance through an 80 nm thick layer of ITO sputtered on glass (gray). The inset shows the spectral intensity distribution of the AM1.5 solar spectrum, with the measured spectral region shaded in gray. The average transmission weighted for the AM1.5 spectrum is listed in the table as an inset.

forward-scattered light depends on the local density of states (LDOS) of the top and bottom medium, as stated by Fermi's Golden Rule. As the substrate has a higher refractive index than air, and thus a higher LDOS, the nanowires will preferentially scatter into the substrate [70]. The asymmetric shape of the transmittance in the inset of Fig. 2.2a can be understood from the Fano interference between light scattered by the LSPR of the individual wires and the directly transmitted light [71, 72, 134, 135]. Fano interference occurs when light scattered from a spectrally narrow resonance (here the LSPR) interferes with a broad continuum of states (the broadband directly transmitted light), as a result of the different phase pick-up at scattering. Light scattered at wavelengths below the LSPR wavelength interferes destructively with the directly transmitted light, giving rise to a dip in transmission, whereas at wavelengths above the LSPR resonance the scattered light interferes constructively with the directly transmitted light, thus resulting into an increase in transmission.

To compare the optical transmittance through the Ag NW networks to that of ITO we used an 80 nm thick layer of ITO that was sputtered on glass. This is a standard thickness used on amorphous Si and organic solar cells [80, 136]. In Fig 2.2b we compare the transmittance of the highest transmitting network (w = 45 nm) with three different pitches (Λ = 500 (blue), 700 (purple) and 1000 nm (pink)) with

the normalized transmission of ITO (gray). The NW networks show better transmittance than ITO over a broad spectral range, except near the LSPR located around λ = 400 nm. To compare the transmittance of the Ag NW networks and ITO for photovoltaic applications we calculate the average transmission weighted for the AM1.5 solar spectrum. The part of the spectrum considered in this measurement is highlighted in the plotted spectrum that is shown as an inset in Fig. 2.2b. As can be seen, this spectral region accounts for a large fraction of the AM1.5 spectral intensity. The average transmission values are listed in the inset in Fig. 2.2b. The 500 nm pitched network has a transmittance that is equal to that of ITO (88%). The networks with 700 and 1000 nm pitch show slightly higher transmittance: 90% and 91% respectively. This shows that the NW networks have an optical transmittance equal or better than ITO, depending on the NW spacing.

2.3 Optical simulations

Finite-difference time-domain (FDTD) simulations [137] were used to further investigate the physical phenomena responsible for the transmission of the NW networks. In the simulations Ag wires with width w, height h and pitch Λ = 500 nm were positioned on a semi-infinite SiO_2 substrate. In the simulations a broad-band (λ = 400–1100 nm) plane wave at normal incidence is used as a source, polarized along one of the wire orientations. Power monitors, positioned 1 nm below the air-SiO_2 interface and 500 nm above the silver network, are used to determine the transmission and reflection at each wavelength. Perfectly matched layer (PML) boundary conditions were used in the vertical direction to prevent unphysical scattering at the edge of the simulation box. Periodic boundary conditions were used in both in-plane dimensions to simulate an infinite network. Optical constants for silver were obtained from a combined Drude, Lorentz, and Debye model fitted to the data from Palik [138]; optical constants for SiO_2 were also taken from Palik.

Figure 2.3a shows the simulated transmittance T (solid) and reflectance R (dashed) as a function of wavelength for a network consisting of wires with h = 50 nm and a width ranging from w = 30–100 nm (different colors). The wavelength equal to the wire pitch (500 nm), is indicated by the dashed vertical line in gray. A high transmittance is observed with several sharp and broad dips, governed by four different scattering mechanisms.

The broad dip in transmission in the 400–500 nm spectral range shows a red-shift for increasing wire width, as was also observed in the experiment (Fig. 2.2a). This dip is attributed to the excitation of the LSPR due to oscillations of free electrons in the transverse direction to the individual NWs (see sketch in inset of Fig. 2.3c). To prove this, we simulate the transmission of an infinitely long single wire in air by introducing PML boundary conditions in the in-plane direction normal to the wire axis. Figure 2.3c shows the transmission of a single wire with w = 80 nm and h = 50 nm, corresponding to the wire geometry for the blue curve in Fig. 2.3a. Both curves show a similar dip in transmittance, and a red-shift

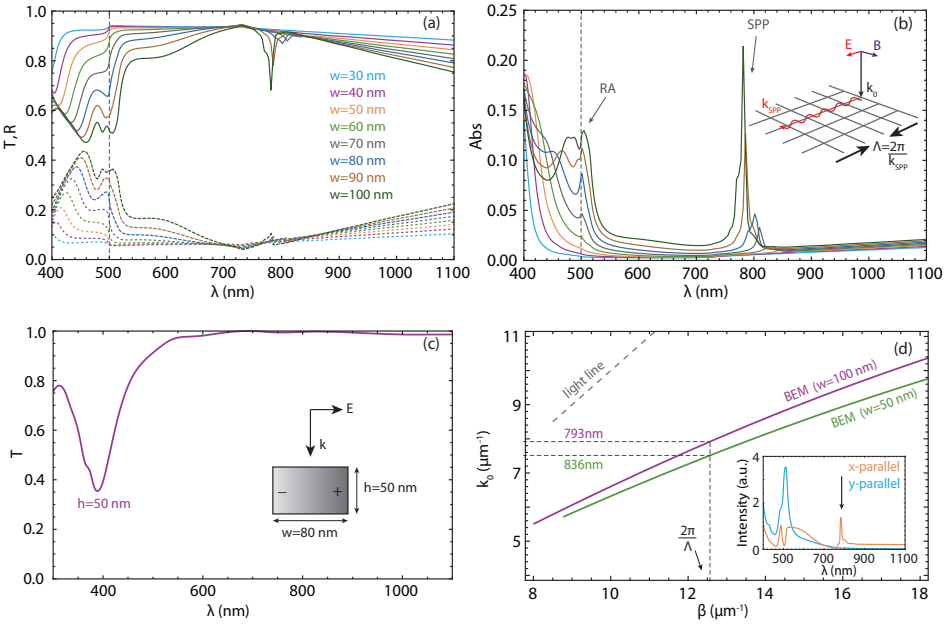

Figure 2.3: (a) Simulated transmission (solid) and reflectance (dashed) as a function of wavelength for a range of wire widths (colors), for h = 50 nm. Also shown is the wavelength equal to the wire spacing (500 nm, vertical gray dashed line). (b) Absorption in the nanowires, calculated as $Abs = 1 - R - T$. Apart from the intrinsic absorption of silver in the blue, two peaks due to the Rayleigh anomaly (RA) and coupling to the surface plasmon polariton (SPP) are observed that are labeled with arrows. A sketch of the network is shown as an inset, with the SPP shown as a red oscillating arrow. (c) Transmission as a function of wavelength for a single nanowire with h = 50 nm and w = 80 nm, located in air (simulated box width 400 nm). The inset shows a sketch of the cross section of the wire with a displaced free electron cloud (+ and − sign) as a result of the transverse free electron oscillation of the LSPR. (d) Dispersion relation for a confined SPP mode on a wire with w = 100 nm (purple) and w = 50 nm (green) as calculated with BEM. The wavelength at which momentum matching occurs is shown (horizontal gray dashed lines). The inset shows the FDTD-calculated near-field intensity as a function of wavelength 5 nm above the wire parallel (orange) and perpendicular (blue) to the electric field component of the incoming light. The orange line shows a peak at the wavelength where light couples to the SPP mode, indicated by the arrow.

of the dip position is observed for the wire network (Fig. 2.3a) compared to a single wire (Fig. 2.3c) due to inter-wire coupling and the presence of the substrate. Further confirmation of the LSPR origin of the dip is the red-shift of the resonant wavelength for larger w observed in Fig. 2.3a, which is caused by the reduced restoring force on the oscillating electrons for larger wire width. This dip was also

observed in ref. [102], where it is attributed to the excitation of two coupled SPP modes that propagate on the top and bottom interface of the wires. However, our analysis shows that instead it is a result of the excitation of the LSPR. This is further confirmed by the fact that it also appears in the transmission of a single wire (Fig. 2.3c) onto which SPPs can not be excited by an incident plane wave because of in-plane momentum mismatch.

The second noticeable feature in the transmission spectra in Fig. 2.3a is a step-like increase in transmission for all wire widths that occurs for wavelengths just above the wire spacing (Λ = 500 nm). This is a result of the excitation of ± 1 diffraction orders that are directed into the substrate for $\lambda > \Lambda$. At λ = 500 nm, the ± 1 diffraction orders are scattered parallel to the surface, giving rise to the strong collective excitation of LSPR modes (Rayleigh anomaly) [139]. This increased interaction between the incoming light and the NWs gives rise to strong absorption of light in the NWs, as confirmed by NW absorption spectra shown for different wire widths in Fig. 2.3b. Strong absorption is observed for all widths at λ = 500 nm as a result of the collective excitation of the LSPR, with the strongest absorption observed for the largest width. The interference of the broad LSPR mode and the spectrally sharp Rayleigh anomaly (RA) gives rise to a Fano-lineshape in the transmission around λ = 500 nm. In the experiment, this feature is small and only observable for the two largest wire widths. This is a direct result of the fact that the sample was illuminated through a microscope objective and the incident light is thus not perfectly collimated. This broadens the RA over a large spectral range.

A third characteristic feature in Fig. 2.3a is the gradually decreasing transmission for wavelengths above ~750 nm; an effect that becomes stronger for larger w. As also described in ref. [102] for one-dimensional networks, this is due to the cut-off of the fundamental TE_0 mode supported by the vertically oriented MIM waveguide formed by the wires and the air in between. The decrease in transmission is relatively weak for two reasons. First, in the square network geometry light can couple to both TE_0 and TM_0 modes. Indeed, a modal dispersion calculation for an infinite MIM waveguide with similar insulator thickness shows a well pronounced cut-off for the TE_0 mode, but not for the TM_0 mode (data not shown here). Second, the cut-off is not well pronounced due to the very limited waveguide length in the normal direction, which is equal to the wire height (50 nm). The decrease in transmittance is also observed in experiments for wavelengths above 800 nm (see Fig. 2.2a).

Finally, a sharp dip in transmission is observed around λ = 800 nm that blue-shifts and is more pronounced for larger wire width. In contrast to the dips in the blue spectral range, this sharp dip is not accompanied by a large peak in reflectance. This indicates strong absorption takes place in the silver NWs, as is confirmed by the spectra in Fig. 2.3b. This dip in transmission is caused by the excitation of SPPs propagating in the longitudinal direction along the wires. The lossy nature of these SPP modes causes the peak in absorption. The two-dimensional periodic nature of our structure provides the in-plane momentum required to excite the SPP mode. The wires oriented perpendicular to the electric field component of the incoming

light act as a grating to provide the in-plane momentum required to couple to a SPP propagating in the direction parallel to the electric field component (see sketch in inset of Fig 2.3b). Larger wire widths lead to an increase in the scattering cross section of the wires such that light can couple more efficiently to the SPP mode, which explains why the dip is more pronounced for larger w. Furthermore, the SPP mode is more confined in the in-plane direction for wires with smaller w, resulting in a higher effective mode index. This explains the red-shift of the SPP transmission dip for thinner wires in Fig. 2.3a.

To further corroborate the SPP excitation mechanism in the Ag NW networks, we use momentum matching calculations to relate the spectral location of the dip to the dispersion curve of the SPP mode. Electromagnetic Boundary Element Method (BEM) calculations were performed using the BEM2D program [140, 141] to calculate the dispersion curves for the confined SPP modes on a 50 nm and 100 nm wide infinitely long wire on SiO_2. The dispersion curve was determined by finding local maxima in the local density of optical states (LDOS) 10 nm above the wire, for a broad range of k_0 and β. The curves are shown in Fig. 2.3d together with light line in air. An increase in mode index is observed for narrower wires, as expected. Coupling to these modes through the periodic NW grating requires momentum matching according to $2\pi m/\Lambda = \beta$, where m = 1,2... The dashed lines in Fig. 2.3d show that coupling to the SPP can occur at λ = 836 nm for w = 50 nm and λ = 793 nm for w = 100 nm. These wavelengths are in good agreement with the wavelengths of the transmission dips in Fig. 2.3a (λ = 849 nm and 781 nm respectively).

Additional proof for the coupling to SPP modes can be obtained from FDTD by monitoring the near field intensity 5 nm above the surface in the middle of wires perpendicular (y-parallel) and parallel (x-parallel) to the electric field orientation. As explained above, the wires perpendicular to the electric field orientation act as a grating that allows coupling to a SPP parallel to the electric field orientation, such that the near field intensity should show a peak at λ = 781 nm for the x-parallel wires only. The near field intensity as a function of wavelength is shown as an inset in Fig. 2.1d, where the blue line corresponds to the y-parallel and the orange line to the x-parallel. Indeed, a sharp peak at λ = 781 nm is observed for the orange line only, confirming that the dip is a result of coupling to the SPP mode (indicated by arrow).

The dip in transmission due to coupling to the NW SPP mode and the blue-shift for thicker wires are also clearly observed in the experiment (Fig. 2.2a). However, in the experiment the dips are spectrally broadened, which we attribute to small variations in wire width and angle of incidence of the light. BEM calculations using the measured wire width and height are used to find the spectral location of the dip as predicted by momentum matching calculations. The results are plotted as the gray dashed line in Fig. 2.2a. The measured data shows good qualitative agreement with the calculation, although the data is slightly red-shifted. We attribute this to small differences in the wire geometry (cross-sectional shape) and optical constants. Finally, the analysis presented here also explains why a dip due to the coupling to

the NW SPP mode was not observed for the larger pitches in Fig. 2.2b. For these networks the momentum matching condition occurs at longer wavelengths outside the spectral range detected in experiments.

2.4 Electrical experiments

The electrical resistance of the Ag NW networks was measured with a four probe experiment such that the probe contact resistance is eliminated. Two probes were positioned on each contact pad and I-V-curves were measured by ramping the current through the network from -1 to 1 mA and measuring the voltage over the network. Typical I-V measurements are shown in the inset of Fig. 2.4. The graph shows measured data (dots) for networks with a w = 45 nm and Λ = 500 (blue), 700 (green) and 1000 nm (orange). Linear fits of the data reflect the Ohmic conduction through the network. The fitted resistances are 17.2 Ω/sq, 27.0 Ω/sq and 38.7 Ω/sq for the Λ = 500, 700 and 1000 nm network respectively. According to Kirchoff's rules, the sheet resistance R_s for a square wire network with $N \times N$ wires is given by

$$R_s = \frac{N}{N+1} R_{wire} = \frac{N}{N+1} \frac{\rho L}{wh}, \tag{2.1}$$

where ρ is the resistivity of silver, L is the length of the wire (equal to network pitch), w is the wire width and h is the height of the wire. For network dimensions used in the experiment (N = 50–100) the first term is close to unity, such that $R_s = \rho L / wh$. Indeed, the measured sheet resistances scale linearly with network pitch (L).

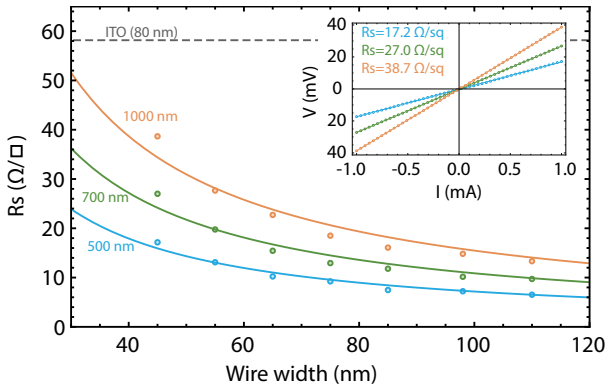

Figure 2.4: Measured sheet resistance (dots) as a function of wire width for different network pitch (500 nm (blue), 700 nm (green) and 1000 nm (orange)). The solid lines represent model fits for each pitch. Also shown is the measured sheet resistance of an 80 nm thick ITO layer sputtered on glass (gray dashed line). The inset shows measured I-V-curves for w = 45 nm for all three pitches (dots) with a linear fit (solid line).

Figure 2.4 shows the measured sheet resistance (dots) as a function of wire width for networks with Λ = 500 (blue), 700 (green) and 1000 nm (orange). The dashed gray line shows the measured sheet resistance for the 80 nm thick ITO layer. We measure a sheet resistance of 58.2 Ω/sq for the 80 nm thick layer of ITO sputtered on glass, in good agreement with literature values [122, 142]. Figure 2.4 shows a decreasing sheet resistance for all networks as w increases, ranging from 38.7 Ω/sq for the Λ = 1000 nm, w = 45 nm network down to 6.5 Ω/sq for the Λ = 500 nm, w = 110 nm network. The measured sheet resistance is well below that of ITO for all measured networks. The solid lines in Fig. 2.4 represent a fit according to $R_s = aw^{-1}$, where $a = \rho L/h$ for perfect Ohmic scaling. Good agreement is observed for the model, except for the networks with smallest w where a higher resistance is found. Indeed, SEM images show higher defect densities and variations in wire width for the thinnest wires w = 45 nm. From the fitted values for a the resistivity of the material ρ is found for each pitch. Averaging the results gives $\rho = (9.3 \pm 0.4) \times 10^{-8}$ Ωm, which is ~5.7 times the bulk resistivity of silver (1.59×10^{-8} Ωm). The difference is attributed to structural wire defects and discontinuities in the wires, variations in the wire width, and electron scattering from grain boundaries.

2.5 Discussion

The optical and electrical measurements demonstrate that Ag nanowire networks are effective transparent conductors, for which optical transmittances and sheet resistances can be tuned by varying the wire diameter and pitch. Figure 2.5 summarizes the measured data, plotting the optical transmission averaged over the AM1.5 solar spectrum versus the sheet resistance for the three network pitches. The transmission and resistance data for the 80 nm ITO layer are also shown as horizontal and vertical gray dashed lines. From this graph three major trends can be observed. First, all NW networks show the inherent trade-off between optical transmittance and low sheet resistance: a lower sheet resistance can only be obtained at the expense of a reduced optical transmittance. Second, smaller-pitch networks have higher optical transmittance for a given sheet resistance. Similarly, for a transmittance that is equal to that of ITO, smaller-pitch networks have lower sheet resistance. Third, the smallest (w = 45 nm) Λ = 500 nm networks shows identical transmittance and lower sheet resistance than ITO; the Λ = 700 and Λ = 1000 nm networks show both higher transmittance and lower resistance than ITO.

Based on the four optical scattering processes described above, the advantage of using small w is due to the fact that this: (1) shifts the LSPR wavelength to the blue where the AM1.5 solar spectrum is less intense; (2) reduces the coupling to the SPP and Rayleigh anomaly due to the smaller scattering cross section; and (3) shifts the MIM cut-off to longer wavelengths. The second loss mechanism; the excitation of NW SPPs is directly related to the NW network pitch. Larger pitch reduces the in-plane momentum obtained from the grating such that coupling to SPPs occurs

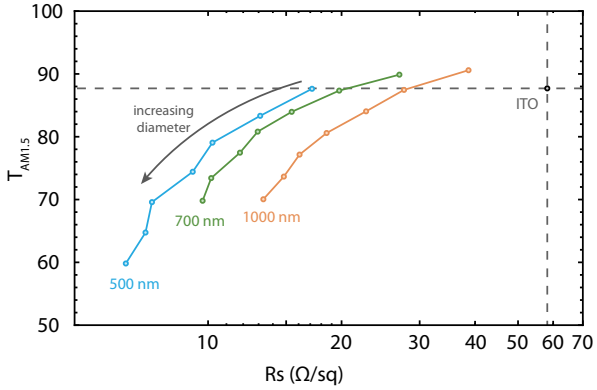

Figure 2.5: AM1.5 averaged transmission as function of sheet resistance for all networks with 500 nm pitch (blue), 700 nm pitch (green) and 1000 nm pitch (orange). The horizontal and vertical gray dashed lines show the transmittance and resistance of an 80 nm thick layer of ITO sputtered on glass. Note the logarithmic horizontal axis.

at wavelengths outside the spectral range of interest. It also increases the clear aperture of the network and increases the MIM cut-off wavelength. However, the increase in optical transmission as a result of the ± 1 diffraction orders directing into the plane for $\lambda > \Lambda$ and the linear relation between the sheet resistance and Λ suggest the pitch should be small.

For photovoltaic applications, the short minority carrier diffusion length in many materials, such as a-Si, suggests that a small pitch would be desirable for better carrier collection. In addition to this, the network pitch determines the amount of in-plane momentum ($m2\pi/\Lambda$) generated by the network, such that efficient light trapping can occur when the pitch is tuned to match the in-plane momentum of waveguide modes in the substrate. This is particularly relevant for thin-film solar cells. In summary, for application of transparent Ag nanowire networks in solar cells, the optimum design depends on the thickness of the substrate (which determines the waveguide modal dispersion), substrate refractive index, carrier diffusion length and absorption length of the solar cell.

Finally, we note that while the EBL technique used in this study provided an excellent tool to systematically study the metal nanowire networks, an inexpensive, large-area technique is needed for practical application. Recently, soft-nanoimprint techniques, such as substrate-conformal imprint-lithography (SCIL) [143, 144], have become available to print metal nanostructures with the required dimensions over large areas in an inexpensive manner (see Chapter 3).

2.6 Conclusions

In conclusion, we have fabricated two-dimensional periodic silver nanowire networks with wire diameters in the range 45–110 nm and pitches of 500, 700 and 1000 nm. From a systematic study of optical transmission spectroscopy and numerical modeling we identify four physical mechanisms that determine the optical transmission of the network: (1) the LSPR on the individual nanowires; (2) diffractive coupling to the Rayleigh anomaly; (3) cut-off of the fundamental TE_0 mode in the MIM waveguides formed by the nanowires; and (4) coupling to SPPs on the wires parallel to the electric field component. Based on this, it is found that the best transparent nanowire network is obtained for thin wires and small pitch. We observe a normalized transmittance up to 91% averaged over the AM1.5 solar spectrum (larger than the clear aperture of network) for the best transmitting network and sheet resistances as low as 6.5 Ω/sq for the best conducting network. Our best performing networks show both better optical transparency and lower sheet resistances than an 80 nm thick ITO layer sputtered on glass. Finally, due to the two-dimensional periodic structure our networks can also function as a scattering layer, thereby combining the functionality of an electrical contact and a light trapping scheme in one design.

3

Large-area soft-imprinted nanowire networks as light trapping transparent conductors

Using soft-imprint nanolithography, we demonstrate large-area application of engineered two-dimensional polarization-independent networks of silver nanowires as transparent conducting electrodes. These networks have high optical transmittance, low electrical sheet resistance, and at the same time function as a photonic light-trapping structure enhancing optical absorption in the absorber layer of thin-film solar cells. We study the influence of nanowire width and pitch on the network transmittance and sheet resistance, and demonstrate improved performance compared to ITO. Next, we use P3HT-PCBM organic solar cells as a model system to show the realization of nanowire network based functional devices. Using angle-resolved external quantum efficiency measurements, we demonstrate engineered light trapping by coupling to guided modes in the thin absorber layer of the solar cell. Concurrent to the direct observation of controlled light trapping we observe a reduction in photocurrent as a result of increased reflection and parasitic absorption losses; such losses can be minimized by re-optimization of the NW network geometry. Together, these results demonstrate how engineered 2D NW networks can serve as multifunctional structures that unify the functions of a transparent conductor and a light trapping structure. These results are generic and can be applied to any type of optoelectronic device.

3.1 Introduction

High-quality transparent conducting electrodes (TCEs) form an essential component of a broad range of optoelectronics devices including LEDs, displays, and solar cells. For solar cells, the inclusion of a transparent conductor is particularly important when the charge carrier diffusion length is short, such as in for example Si heterojunction, perovskite or organic cells. The most commonly used TCE is indium-tin-oxide (ITO). However, high material costs [101, 102], the scarcity of indium [145], brittleness [103, 104], optical absorption [80, 100] and incompatibility of the sputtering process with organic layers [105] strongly motivate the development of a replacement for ITO.

The high conductivity of metals has stimulated interest in metal nanowire (NW) networks and meshes as alternatives to ITO. A wide variety of geometries have been proposed, including random nanowire meshes [100, 106–108, 146], percolated films [110, 111], 1D (nano-)imprinted gratings [103, 104, 109], nanogratings interconnected with mesoscale wires [112], self-assembled microstructures [147], as well as NW-graphene hybrid structures [148]. These nanoscale and multiscale geometries can be designed to provide improved optoelectronic performance relative to ITO, achieving concurrent improvements in both optical transparency and electrical conductivity. Furthermore different metals can be used, which provides tuneability of the workfunction of the contact, and allows for inverted fabrication schemes.

Plasmonic light trapping effects can further improve the absorption in thin absorber layers. For organic photovoltaic devices, plasmonic light trapping has recently become the subject of intense interest due to the short carrier diffusion lengths in these material systems. To facilitate efficient carrier extraction the active layer thickness must be thin, however this limits the optical path length inside the absorbing material. Optical efficiency enhancements have already been demonstrated [149] by employing both localized plasmon resonances [150] and surface plasmon polaritons (SPPs) on the (rear) electrode [151–153]. ITO can be replaced with a conductive plasmonic array made of 1D silver gratings [104, 154] and silver nanohole arrays [155]. Random NW networks provide limited light trapping capabilities through random scattering [156]. However, all these geometries are either strongly polarization dependent (limited or no light trapping for other polarization) or allow no control over the network geometry.

In Chapter 2, we have shown using e-beam lithography (EBL) that 2D networks of silver NWs can match the optical performance of ITO as a transparent conductor, while offering significantly improved sheet resistances. Unlike random networks, controlled network geometries allow engineered spectral transmission by optimizing the effects of excitation of localized and propagating surface plasmon modes, scattering and coupling to guided modes in an underlying semiconductor substrate.

In this Chapter, we employ soft-imprint lithography [157] to transfer this small-area concept into large-area applications of NW networks. The facile fabrication of

large-area NW networks allows us to systematically vary NW width and pitch and study the influence on spectral transmittance and sheet resistance, and to demonstrate centimeter-scale NW network based functional devices. Furthermore, we employ the engineered 2D NW networks to systematically study plasmonic light trapping in an organic solar cell in a fully controlled manner. We demonstrate the unique combination of both mode-matched light trapping and charge collection in a single multifunctional layer using P3HT-PCBM polymer solar cells. The results from this well characterized model system [149, 158] are generic, and applicable to all thin film devices.

3.2 Nanoimprinted nanowire networks as transparent conducting electrodes

Substrate-conformal imprint-lithography (SCIL) is a high-resolution nanoimprint technique that employs a bilayer PDMS stamp to reproducibly transfer high-resolution nanopatterns onto substrates in a fast, facile and inexpensive manner [157]. Here, we use this technique to fabricate Ag NW networks over centimeter-scale areas on a glass substrate with nanometer control over nanowire position, dimension, and spacing (see Supplemental Fig. 3.6). Briefly, a PMMA sacrificial layer and a silica sol-gel layer are deposited on a glass substrate by spin coating. A 6" diameter SCIL stamp containing the nanowire pattern is applied and, after 30 minutes of drying in ambient conditions, removed to leave behind the patterned silica sol-gel layer. Subsequent reactive ion etching of the PMMA, thermal evaporation of Ag through the sol-gel/PMMA apertures, and a lift-off process complete the fabrication of networks of Ag NWs. While this process can be applied to wafer-scale processing, here the stamped pattern consists of 40 square networks (2×2 mm^2 each), with each square containing a 30 nm high network with different NW width and pitch (widths: 55–130 nm, pitches: 300–1000 nm in steps of 100 nm). Electrical contact pads on either side of each network (125 μm $\times$ 2 mm) were fabricated using UV-lithography, followed by thermal evaporation (5 nm Cr, 50 nm Au), and subsequent lift-off (see sketch in Supplemental Fig. 3.7a).

The NW networks resulting from this top-down SCIL process are uniform over large areas (Fig. 3.1a), with the wires exhibiting both smooth interfaces and high-quality interconnections (Fig. 3.1b). Unlike chemically synthesized random NW network meshes, these large-area NW networks are fabricated out of a single metallic sheet with correspondingly low inter-wire junction resistance, as we will show. We use 40 different combinations of pitch and NW width, each with a different metal filling fraction, to explore the trade-off between high optical transmittance and low sheet resistance on each array geometry.

The performance of these NW networks as transparent conducting electrodes was first characterized by measuring both the white-light transmittance and the lateral electrical sheet resistance. Optical transmission spectra were taken of the Ag NW coated glass, with the NWs at the front (incident) side. An integrating sphere

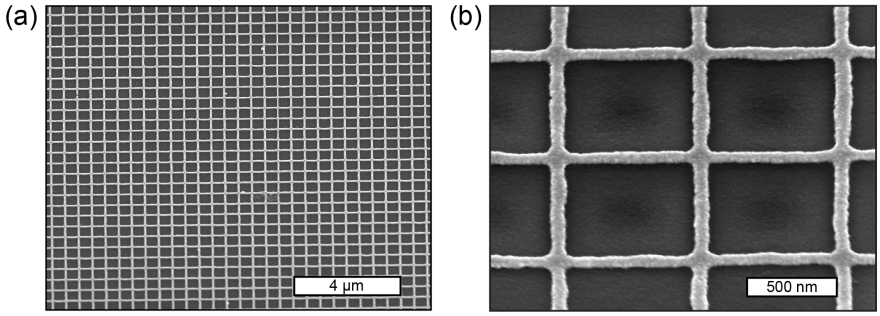

Figure 3.1: (a) SEM image of large-area 500 nm pitch Ag NW network on glass. (b) High resolution SEM image of 800 nm pitched network with NW width ~85 nm.

was used to allow the collection of light diffracted out of the sample under large angles (inset Fig. 3.2b). To isolate the influence of the NW networks, the measured transmission spectra were normalized to the transmittance of a bare glass sample.

All nanowire network spectra exhibit broadband normalized transmittance as a result of guided modes through the apertures [102, 159] with two main perturbations (Fig. 3.2a). The sharp dip in the red spectral range is a result of diffractive coupling of light to propagating surface plasmon polaritons (SPPs) along the nanowires (see Chapter 2). A broad dip in the blue spectral range originating from absorption due to the excitation of the transverse local surface plasmon resonance (LSPR) of the individual wires; and plasmonic light scattering into waveguide modes in the glass substrate.

This diffractive coupling of light into the glass substrate, appearing as a reduction in the transmission spectra (Fig. 3.2a), is a desired feature in light trapping geometries. In a functional device, the guided light couples to the absorber layer and will enhance the absorption, as demonstrated below. To investigate it further we plot the maximum in-plane wavevector $k_{max} = n_{SiO_2} k_0 = 2\pi/p$ that can be obtained in a glass substrate through scattering off a grating with pitch p (Fig. 3.2b, where $n_{SiO_2} = 1.52$). Guided modes lie between the light lines in air and in the glass substrate (Fig. 3.2b, shaded region). Combined, these conditions define the wavelength range for which mode coupling occurs (red line in Fig. 3.2b). For optical frequencies where $\lambda_{min} < \lambda_0 < \lambda_{max}$ (dashed vertical gray lines in Fig. 3.2a) light couples to guided modes in the glass substrate; the density of these optical modes decreases with increasing wavelength, resulting in reduced coupling and a concomitant increase in transmittance through the slide, as is observed.

Finite-difference time-domain (FDTD) simulations [137] were performed to calculate the fraction of light trapped by mode coupling into the glass substrate (see Supplemental Section 3.7.3). To this end, we simulated the transmittance of the top interface with Ag NW network (neglecting the 1 nm Ge seed layer, see

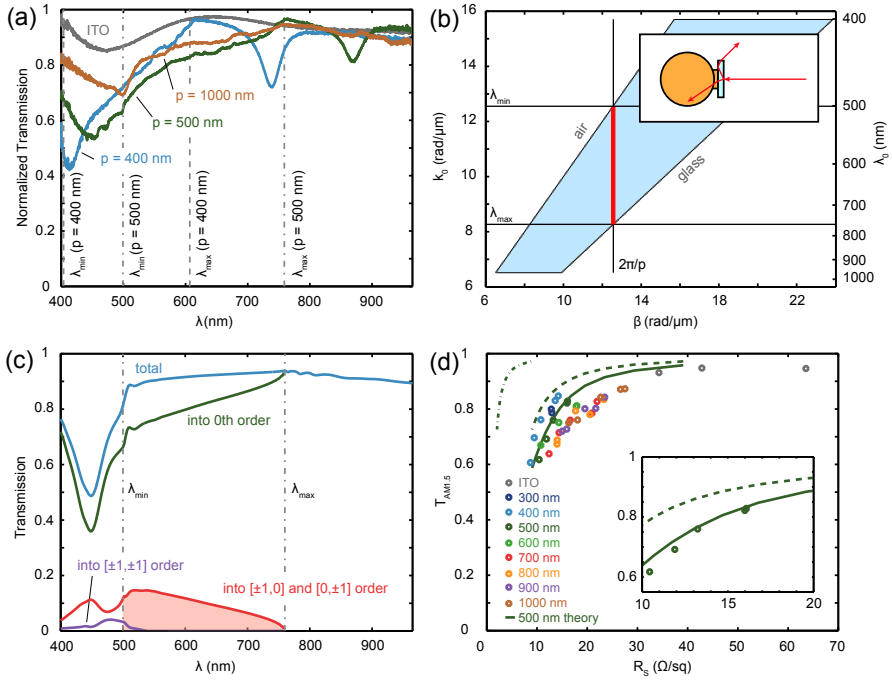

Figure 3.2: (a) Measured normalized transmission of thinnest NWs with 400 (blue), 500 (green) and 1000 nm (orange) pitch (~60, 65 and 80 nm width respectively). Also shown is the transmittance of a 200 nm layer of ITO (gray). Vertical lines indicate the spectral range where mode coupling occurs for p = 400 nm (dashed) and p = 500 nm (dash-dot). (b) Dispersion diagram for 500 nm pitched network, showing light lines in air and glass. The wavelengths for which coupling to guided modes occurs are indicated by the red line. Inset: sketch of integrating sphere setup. (c) Simulated transmittance into different diffraction orders for NW network with 65 nm width, 30 nm height and 500 nm pitch. The shaded area corresponds to the power coupled to guided modes (average 5%). (d) Average transmission (weighted for AM1.5 photon flux) versus sheet resistance of all fabricated NW networks. The different pitches are indicated with different colors. The measured data for 200, 150 and 110 nm thick layers of ITO (light gray, from left to right) are also shown. The green lines show theoretical data for p = 500 nm: total transmission and theoretical resistivity (dash-dot), total transmission and actual resistivity (dashed), transmission excluding light coupling to guided modes and actual resistivity (solid). The inset shows the match to the experimental data for p = 500 nm.

Supplemental Section 3.7.6), and calculated the angular distribution of the light transmitted into the substrate. For the experimental Ag network dimensions (w = 65 nm, p = 500 nm), the results are shown in Fig. 3.2c. The spectral distribution of total transmittance into the substrate (blue) is separated into the 0^{th} order transmittance (green), and the [±1,0] and [0,±1] (red) and [±1,±1]

(purple) diffraction orders in the substrate. Since the simulations only consider the top interface, direct comparison with the measured spectrum (Fig. 3.2a) in absolute terms is incorrect. However, comparing the 0th order transmittance (Fig. 3.2c, green line) with the measured spectrum (Fig. 3.2a, green line) shows good qualitative agreement. The dip in transmission as a result of plasmon absorption ($\lambda_0 \sim 450$ nm), the gradual increase in transmittance due to substrate modes ($500 \leq \lambda_0 \leq 760$ nm), as well as the kink in transmission at $\lambda_0 = 760$ nm are clearly reproduced.

From the angular analysis we find that 5% of the photons in the AM1.5 solar spectrum will couple to guided modes, indicated by the shaded region. In the experiment, this fraction is not collected giving rise to the kink in the measured transmittance at $\lambda_{max} = 760$ nm (see Figs. 3.2a,c). Figure 3.2c shows that the total transmitted spectrum (0^{th} order plus grating coupling into the substrate) is ~90% over the entire spectral range from 500–900 nm (88% averaged over photon flux). This is very similar to the average transmittance through the ITO layers for this spectral range (Fig. 3.2a) despite the large area fraction covered by metal (20–31%, as determined from SEM images). Note that the simulated reflection and parasitic losses in the metal are limited to only 9.7% and 2.3% respectively (averaged over photon flux).

The sheet resistance (R_s) of the NW networks was characterized using four-point-probe measurements. Two probes were placed on each contact pad, and the resulting current-voltage (IV) response measured (see Supplemental Section 3.7.2). For the ITO, the standard geometry of four equally spaced probes was used to measure R_s. All NW networks and ITO samples showed Ohmic behavior, allowing R_s to be extracted from a linear fit.

For all nanowire networks the sheet resistance was measured and found to be significantly lower than the resistance of the ITO reference samples (thicknesses 110, 150 and 200 nm). The data is plotted in Fig. 3.2d for different pitches (shown as different colors) with the corresponding measured average transmittance ($T_{AM1.5}$), weighted for photon density in the AM1.5 solar spectrum (using the experimental spectral range; $400 < \lambda < 965$ nm). For comparison, the measured data for ITO is shown in gray. The NW networks had a measured $T_{AM1.5}$ from 40–87% compared to 93–95% for commercially available ITO. Note that this neglects the ~5% coupled by the NW networks into waveguided modes of the glass substrate. However, the NW networks show sheet resistances in the range of 8.7–27.5 Ω/sq, which is much lower than ITO studied here (34.3–63.6 Ω/sq). This shows that, despite the nanoscale dimensions of the wires, the presence of the highly conductive Ag metal permits a large improvement in sheet resistance.

Comparing the measured data with the theoretical sheet resistance for a square grid we find that the effective resistivity of the material is $(7.0 \pm 0.5) \times 10^{-8}$ Ωm, which is 4.3 ± 0.3 times larger than the bulk resistivity of silver. We attribute this to variations in wire width, surface roughness, and electron scattering from grain boundaries. This is a significant improvement compared to the 5.7 times increase in resistivity observed for NW networks fabricated by e-beam lithography (see

Chapter 2), which we attribute to reduced surface roughness on the individual NWs.

To determine the upper limit in performance that can be achieved with the NW networks, as well as to correct for the fraction of light coupled to guided substrate modes, we simulated the transmittance for p = 500 nm, h = 30 nm and w = 30–130 nm (similar to Fig. 3.2c), converted the spectra to normalized transmittance (see Supplemental Section 3.7.3), and calculated the sheet resistance. First, the theoretical absolute maximum performance for the p = 500 nm networks (Fig. 3.2d dash-dotted line) is obtained from the total transmission and sheet resistance calculated from the bulk resistivity of Ag. Second, the performance of the NW networks including the light coupled to guided modes (dashed line) is calculated by using the realistic resistivity (4.3 times bulk resistivity) instead of bulk resistivity. Third, by excluding the light coupled to guided modes the experimental conditions used in this work are calculated (solid line). Indeed, the theory line (solid) shows good agreement with the measured results (see inset of Fig. 3.2d), showing that the simulations accurately describe the experiments. Finally, we can compare the performance of the NW networks (using full transmission, dashed line) with that of ITO. We find that the NW networks outperform the transmittance and sheet resistance of ITO.

Figure 3.2d clearly shows the trade-off between high transmittance (thin wires, large pitch) and low sheet resistance (wide wires, small pitch). Tuning these parameters - pitch and width - allows the selection of a desired resistance/transmittance combination that can be optimized for specific applications as well as tuning the spectral range of plasmonic enhancement. Note that the spectral range of the plasmonic response strongly depends on the dielectric surrounding, as will be shown below.

3.3 Nanowire network based polymer solar cells

Next, we demonstrate the application of these NW networks as the TCE in functional organic solar cells. Starting with the NW networks printed on glass, P3HT-PCBM polymer solar cells were fabricated on the networks in a superstrate configuration. This well-established cell type was chosen to serve as a model system where ITO serves as the transparent conductor [158]. Also, with the absorption edges of P3HT around $\lambda \sim 650$ nm [158, 160] and that of PCBM at $\lambda \sim 700$ nm, this type of cell can benefit significantly from light trapping in the red and infrared spectral regions where both direct absorption and charge-transfer (CT) absorption are weak.

The experimental cell geometry is shown in Fig. 3.3a. Substrates with NW networks were first coated with a 30 nm layer of PEDOT:PSS as a hole-conduction layer. Next, 230 nm of P3HT-PCBM (1:1 weight ratio) was spin coated, followed by thermal evaporation of 1 nm of LiF to modify the work function of the electrode and facilitate electron collection, 200 nm Al and 500 nm of Ag. The PEDOT:PSS and active polymer layer thicknesses were optimized using transfer matrix calculations

to maximize optical absorption in the active layer of a flat reference cell (note that this is not the optimum for the NW network devices). The standard TCE reference device used a 200 nm thick layer of ITO ($T_{AM1.5}$ = 93.1%, R_s = 34.3 Ω/sq) instead of the Ag NW networks.

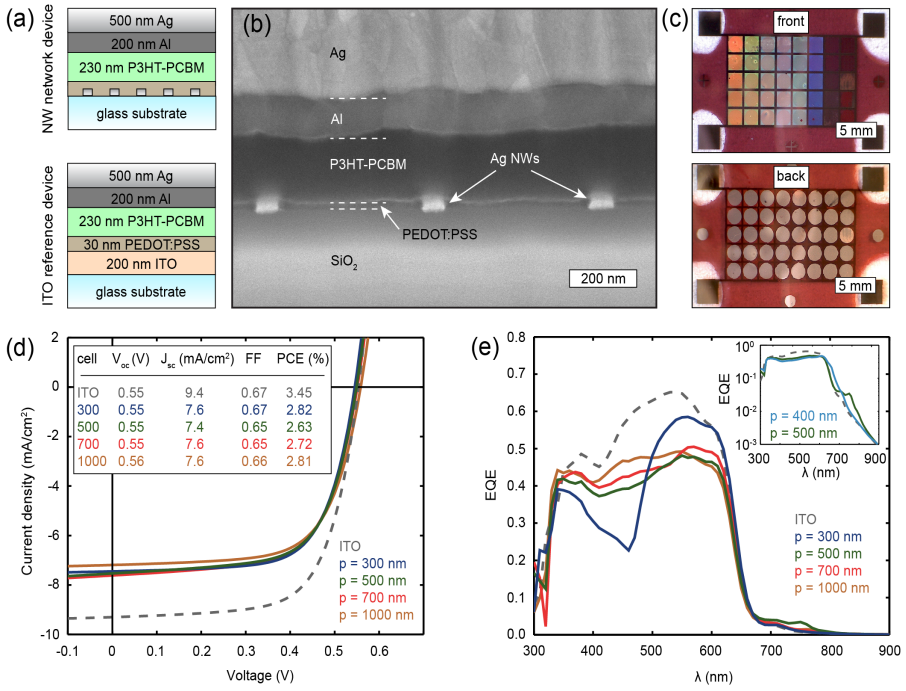

Figure 3.3: (a) Schematic cross sections of the layer stack of the NW network device (top) and ITO reference device (bottom). (b) FIB cross section of a device with p = 500 nm, clearly showing the Ag NW network embedded in the cell. (c) Photograph of front (top) and back (bottom) of the completed devices, showing the 40 different cells on one substrate. (d) Measured IV-curves for a 300 (blue), 500 (green), 700 (red) and 1000 nm pitch device (orange). Silver wire widths were ~65–85 nm. Also shown is the data for the ITO reference device (gray, dashed). The cell parameters are shown as an inset. The J_{sc} listed here is obtained from the EQE measurements. (e) Measured EQE for the same devices. The inset shows the EQE for p = 400 nm (blue) and p = 500 nm (green), and for ITO as a reference (gray, dashed), to emphasize the EQE enhancements in the weakly absorbing spectral range.

Contacting the nanowire networks was achieved using evaporated gold contact pads patterned by UV lithography. The geometry of the front contact is clearly visible through the glass substrate (Fig. 3.3c, front), where the color of individual squares is the result of scattering from the NW networks. Electrical contacts are made by positioning a probe on one of the 4 corner pads (black squares). The

rear contacts (LiF, Al and Ag) are evaporated through a circular physical mask (1.9 mm diameter) such that isolated cells are defined with an area of 0.0284 cm^2 each (Fig. 3.3c, back). The layered structure of these cells can be seen in Fig. 3.3b, which shows a focused-ion beam (FIB) cross section of a representative device. The figure clearly shows the layers including the NWs. Importantly, the 30 nm thin PEDOT:PSS layer conformally coats the NWs, which we found was essential to prevent voltage reduction from current leakage. In total, 3 samples, containing 113 complete cells were fabricated, with an overall yield of 89%. Device failures were a result of current leakage induced by metal residues from incomplete lift-off processes.

To characterize the performance of the Ag nanowire contacted solar cells we performed current density–voltage (JV) measurements under white light illumination (100 mW/cm^2, 1 sun). Typical results are shown in Fig. 3.3d for NW network-based cells with wire widths of ~65–85 nm and pitches ranging from 300–1000 nm (colored lines), along with reference results for an ITO-based cell (gray dashed line). Performance parameters for these cells - open-circuit voltage (V_{oc}), short-circuit current density (J_{sc}, obtained from EQE measurements below), fill factor (FF), and power conversion efficiency (PCE) - are shown as an inset.

These JV-measurements prove that the NW networks function as efficient transparent conductors. The application of the NW networks as a transparent conductor induces no current leakage, as V_{oc} is ~550 mV for all NW network cells, equal to that of the ITO reference cell. Also, the fill factor, which represents the electrical quality of the device, is ~0.66 for all NW network devices, similar to that of the ITO reference device. So, despite the corrugation of the cell surface resulting from conformal coating of the NW network, the networks do not induce additional carrier recombination. Replacing the ITO with NW networks causes a reduction in the short-circuit current density (J_{sc}) from 9.4 mA/cm^2 to 7.4–7.7 mA/cm^2 for the NWs relative to ITO. This difference in J_{sc} can be attributed to several effects. First, the NW networks used here have slightly lower transmittance than the ITO reference samples (Fig. 3.2d). Despite the lower sheet resistance, this results into reduced current generation. Second, the active layer thickness is not optimized for the NW network cells. Third, in the solar cell geometry the NW networks are coated by PEDOT:PSS instead of air. As a result, the refractive index contrast at the position of the NWs is reduced from 1 (air) → 1.52 (glass) to 1.52 (glass) → 1.7 (PEDOT:PSS). This reduces the forward scattering of the NWs and thereby increases the reflection of the cell, as confirmed by reflection measurements on the completed devices (see Supplemental Fig. 3.9). Fourth, the higher refractive index red-shifts the LSPR to longer wavelengths where the solar flux is higher, thereby increasing the absorption in the NWs. From FDTD simulations we estimate the combined absorption losses ($400 \leq \lambda \leq 650$ nm) in the PEDOT:PSS and nanowire network to be 17.4% and 10.7% with and without the 1 nm Ge layer present, respectively (see Supplemental Section 3.7.6 for influence of Ge). The difference in transmittance can be readily minimized by optimizing the nanoimprint process for thinner wires, as shown in Fig. 3.2d. The effects of the increased refractive index however, are inherent to the

device structure.

To characterize the spectral dependence of cell performance, the external quantum efficiency (EQE) was measured by illuminating the cells with a 1 mm diameter spot of monochromatic light (300–900 nm, 10 nm steps) and measuring both the illumination power and resulting photocurrent. The band edge for absorption in the P3HT donor molecule is observed at $\lambda \sim 650$ nm (Fig. 3.3e), in agreement with literature values [158, 160]. In the blue spectral range the NW network cells show a reduced EQE relative to the ITO cell, due reflection (see Supplemental Fig. 3.9b) and absorption in the metal. Furthermore, a clear transition in the shape of the EQE curves can be observed with increasing pitch. For the 300 nm device, the EQE is strongly asymmetric, showing low EQE in the blue and high EQE in the red spectral range. This is a clear sign of strong scattering by the LSPR of the NW network around $\lambda \sim$450 nm. Fano-interference with the non-scattered light causes destructive interference for $\lambda < \lambda_{LSPR}$, and constructive interference for$\lambda < \lambda_{LSPR}$ [72]. For larger NW pitches, the wire density decreases, such that the scattering amplitude of the LSPR also decreases. This reduces the spectral asymmetry, and results in a more spectrally flat response.

Finally, small but significant peaks can be observed in the EQE of the NW devices for $\lambda > 650$ nm, exceeding the EQE of the ITO reference device. To show this more clearly, a logarithmic plot is shown in Fig. 3.3e (inset) for a 500 nm (green) and 400 nm (blue) pitch device. An EQE enhancement is observed for $700 < \lambda < 900$ nm and $650 < \lambda < 800$ nm for these two devices, respectively. We attribute this EQE enhancement to light trapping as a result of the NW networks scattering light into the guided modes of the polymer cells. This EQE enhancement occurs in the weakly absorbing spectral range of the polymer, corresponding to PCBM (acceptor molecule) absorption up to $\lambda \sim 750$ nm, and CT absorption up to $\lambda \sim 1100$ nm [161].

3.4 Light trapping through NW network scattering

To confirm that the EQE enhancement observed at long wavelengths is a result of mode coupling we first calculate the guided modes supported by the solar cell layer structure. Our calculations were performed using a mode-solver to find the complex wavevectors of the eigenmodes propagating in the plane parallel to the polymer layer [162]. The calculations use the layer stack shown in Fig. 3.3a (top), assuming semi-infinite Al and glass layers, and neglecting the NWs. Complex dielectric constants were used for all materials, taken from the literature for P3HT-PCBM [163], PEDOT:PSS [163], Al [36], and from spectroscopic ellipsometry measurements for ITO. We find three waveguide modes, of which dispersion curves showing the propagating wavevector β (real part of complex eigenmode wavevector) for each free-space wavevector k_0 are shown in Fig. 3.4a. Also shown are the light lines in air and glass (gray lines). Two of the modes are strongly bound (TM_0 and TE_0); their dispersion curves lie below the light lines of air and glass. The

corresponding modal field profiles are shown in Fig. 3.4b (in-plane E-component for the TE mode, in-plane H-component for the TM modes). The TM modes show high field intensity on the Al-polymer interface as a result of surface plasmon polaritons. Light scattering from the Ag NWs can result into efficient coupling to these waveguide modes when the in-plane momentum is matched to that of the guided modes:

$$k_0 \sin(\theta) \pm \frac{2\pi}{p} = \beta \tag{3.1}$$

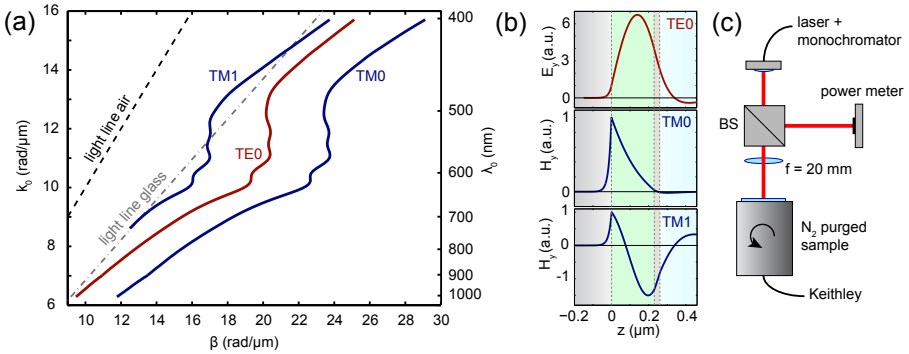

Figure 3.4: (a) Dispersion curves of the guided modes (TE in red, TM in blue) supported by the layer structure shown in Fig. 3.3a (top). Also shown are the light lines in air and glass (gray dashed lines). (b) Corresponding field profiles of the in-plane electric (for TE mode) and in-plane magnetic (for TM modes) components. The layer structure is shown in the background (colors). (c) Experimental setup used for angle-resolved *EQE* measurements.

Angle-resolved *EQE* measurements were performed using the experimental setup is shown in Fig. 3.4c. Monochromatic radiation is sent through a beam splitter. One beam is weakly focused onto the sample, the other beam is used to measure the illumination power. For each wavelength, a rotation stage is used to scan the angle of incidence from 0–45 degrees and the zero-bias photocurrent is recorded.

Figures 3.5a,b show angle-resolved *EQE* measurements for pitches of 400 and 500 nm respectively. They show an overall decrease in *EQE* at wavelengths beyond the absorption edge of the polymer. Both figures show clear bands of enhanced *EQE*, for which the spectral position shifts with angle of incidence. For normal incidence these *EQE* peaks occur at ~660 nm and ~760 nm for p = 400 and 500 nm pitches, respectively, in agreement with the inset in Fig. 3.3e. For p = 500 nm, a second branch can be observed for $700 < \lambda < 750$ nm at larger angles of incidence. This dispersive, angle-dependent behavior directly proves coupling of light scattered by the Ag NW networks to waveguide modes in the polymer layer, in agreement with Eq. 3.1.

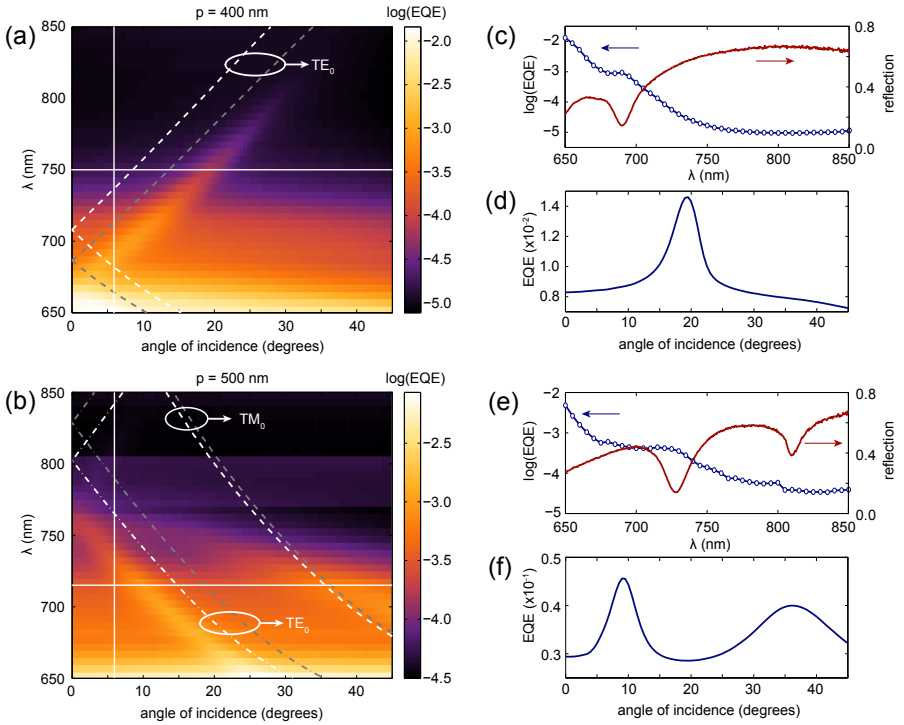

Figure 3.5: (a) Measured EQE (color, log scale) for p = 400 nm. The dashed lines show the calculated dispersion curves for 220 (white) and 285 (gray) nm thick polymer layers. The solid white lines indicate the cross cuts shown in c) and d). (b) Measured EQE for p = 500 nm. Dashed lines correspond to dispersion curves for 225 (white) and 275 (gray) nm thick polymer layers. (c) Cross cut through a) for θ = 6 degrees (blue, left axis), and measured reflection spectrum (red, right axis) for p = 400 nm. (d) Cross cut through a) for λ = 750 nm. (e) Cross cut through b) for θ = 6 degrees (blue, left axis), and measured reflection spectrum (red, right axis) for p = 500 nm. (f) Cross cut through b) for λ = 715 nm.

Figure 3.5b also shows that coupling to the TE_0 mode is more pronounced than to the TM_0 mode. This can be explained by the anisotropic refractive index which influences the efficiency of light trapping. The electric field polarization must be aligned with the strongly absorbing axis in order to maximize light trapping efficiency causing that TE modes absorb more efficiently than either the TM and plasmon modes [164]. However, such a difference in mode amplitudes may also be influenced by strong absorption in the Al (Fig. 3.4b, TM_0 mode), as well as differences in coupling efficiency.

These experimental results are in good qualitative agreement with calculated dispersion curves for the TM_0 and TE_0 modes (Figs. 3.5a,b, dashed lines). However,

an offset is observed for all lines, which can be attributed to three factors. First, the calculations assume perfectly flat layers, while the fabricated devices show variations in thickness (see Supplemental Fig. 3.8b). Using FIB cross sections we measured the range of polymer layer thicknesses, and observed thickness variations on the order of 65 nm. Dispersion curves calculated for both the minimum and maximum layer thicknesses are shown in Figs. 3.5a,b. Second, the calculations neglect the presence of the NWs. Third, the calculations assume a dispersive but isotropic refractive index for P3HT-PCBM; the actual dielectric is known to be anisotropic as a result of vertical segregation [160].

The EQE response of the cells can be further understood by comparing crosscut spectra (taken from Fig. 3.5a,b) with measured reflection spectra. The total reflection of the completed devices was measured using an integrating sphere setup (see Supplemental Section 3.7.5). The angle of incidence is set to 6 ± 1 degrees to prevent the specular reflection from escaping the sphere. A broadband high reflection can be observed above the band edge (Figs. 3.5c,e, right axes) for both $p = 400$ nm and $p = 500$ nm due to the low absorption of the polymer. However, clear dips in reflection can be observed around $\lambda = 690$ nm for $p = 400$ nm and around $\lambda = 730$ nm and $\lambda = 810$ nm for $p = 500$ nm device.

Comparing the reflection spectra with the measured EQE confirms that the absorption in the active polymer is enhanced by coupling to guided modes. First, crosscuts along wavelength axis show a clear peak in EQE where Eq. 3.1 is satisfied, corresponding to an ~1.7 and ~1.5 enhancement for devices with $p = 400$ nm and $p = 500$ nm pitches, respectively (Figs. 3.5d,f). Figure 3.5f clearly shows coupling to both the TE_0 and TM_0 modes at different angles of incidence. Second, crosscuts along angle axis ($\theta = 6$ degrees) show small but clear shoulders on the rapidly decaying background signal above the absorption edge (Figs. 3.5c,e, left axes). Third, the spectral position of the enhanced EQE shows good agreement with reflection minima, demonstrating a concomitant increase in absorption. Note that the two dips observed in Fig. 3.5e are in fact due to the same mode propagating in opposite directions, spectrally separated due to the non-zero angle of incidence.

Finally, the field profile of the guided mode was obtained from full wave FDTD simulations [137]. The simulation (using $p = 500$ nm) shows clear coupling to a guided mode at $\lambda = 788$ nm, with the maximum field intensity located in the polymer layer (see Supplemental Sections 3.7.3 and 3.7.4 for simulation details and field profile respectively). The spectral position of the guided mode shows good agreement with the measured EQE at normal incidence (Fig. 3.5b), and both the propagation vector and the mode profile of the guided mode confirm that light couples to the TE_0 mode.

These results demonstrate how engineered 2D Ag NW networks can serve as multifunctional structures that unify the functions of a TCE and a light trapping structure. Concurrent to the observation of direct evidence for engineered light trapping, the NW networks geometries used in this work resulted into an overall decrease in photocurrent, and thereby power conversion efficiency. The net increase in photocurrent as a result of light scattering and trapping is counteracted

by a larger increase in reflection and absorption losses. These losses can be minimized by further reducing the NW width. As shown in Fig. 3.2d, reducing the NW width from the 65 nm used in this work to 30–40 nm will significantly increase the transmission. By adjusting the physical parameters of the networks, these Ag NW TCEs can be optimized for efficient light incoupling and trapping. Such systematic optimization is not possible for random meshes. Recent work demonstrating such optimization has shown significant absorption enhancements in ultra-thin GaAs layers [165], as well as improved optical transmission into photodiodes using 2D fractal patterns [166].

3.5 Conclusions

In conclusion, we used nano-imprint lithography for the large-area fabrication of two-dimensional networks of Ag nanowires. The SCIL method provides nanometer control over nanowire position, width, height and pitch. The sheet resistances is as low as 8.7 Ω/sq for the best conducting network, an average transmission up to 87% is found for the best transmitting networks. Our analysis shows that optimized NW networks outperform the sheet resistance and transmittance of ITO. Using P3HT-PCBM polymer solar cells as a model system, we demonstrated the use of our NW networks as functioning transparent electrodes. The NW network devices showed no losses in V_{oc} and fill factor, demonstrating good TCE performance. Angle-resolved EQE measurements demonstrate that, in addition to functioning as electrical conductors, the NW networks scatter light into guided modes in the solar cell and enhance absorption. EQE enhancements up to ~1.7 are shown in the weakly absorbing spectral range, including the charge-transfer absorption range. Concurrent to the direct observation of controlled light trapping we observe a reduction in photocurrent as a result of increased reflection and parasitic absorption losses; such losses can be minimized by re-optimization of the NW network geometry. This work demonstrates how engineered 2D networks of silver nanowires can simultaneously function as a transparent electrode to replace ITO and as a light trapping layer to enhance the optical absorption.

3.6 Methods

NW network fabrication

Large glass substrates (69 × 69 × 1 mm) were cleaned with base piranha, followed by a 10–15 min bake-out at 150°C. Next, ~250 nm PMMA 35k (300) was spincoated at 1000 rpm in 45 s, followed by a 15 min bake at 150°C. To make the surface of the PMMA hydrophilic, a 10 s O_2 descum reactive-ion etch (RIE) was applied. Then, liquid silica sol-gel (home-made) was spin coated at 1000 rpm in 10 s to form a uniform layer of 60–70 nm thickness, after which the nano-imprint stamp was applied. After 30 minutes of curing in ambient conditions, the stamp was removed and the nanopatterned sol-gel formed. Next, RIE etching using CHF_3 (25 sccm)

and Ar (25 sccm) was used to anisotropically etch through the residual sol-gel layer (1:45 min, 67 W, 15 mTorr), followed by 12 min of O_2 descum to etch trough the PMMA and create an undercut.

Thermal evaporation was used to deposit 1 ± 0.5 nm of Ge (0.1 Å/s) and 30 ± 2 nm of Ag (0.5 Å/s). The Ge functions as a seed layer to prevent the Ag from growing in large grains, such that very smooth Ag NWs can be grown [128, 129]. To perform lift-off, the samples were soaked in acetone at 50°C for 3–5 hours, followed by 10 min of megasonication and 1 min of ultrasonication. Finally, the samples were rinsed in isopropanol and dried using nitrogen.

The samples were then coated with S1813 (2000 rpm, 32 s) and baked at 110°C for 2 min to protect the NW networks during the cutting of the samples to a smaller size (30 × 30 mm), in order to be compatible with the rest of the processing. After the cutting, the samples were cleaned by rinsing in acetone and isopropanol, followed by blow-drying.

UV-lithography was used to fabricate the Au contacts for the NW networks. After a 5 min bake-out at 100°C, an HMDS primer was applied (4000 rpm, 32 s) for adhesion, followed by a 1 min bake at 100°C. A negative-tone resist (ma-N 1410, 1400 rpm, 32 s, ~925 nm thick) was spincoated, followed by a 90 s bake at 100°C. The samples were then exposed through a flexible foil mask (Selba) for 90 s at 5 mW (450 mJ dose) to create 125 μm × 2 mm large contacts that have 50 μm overlap with the NW networks. To develop, the samples were dipped in ma-D 533S developer for 85 s, dipped in water twice to stop the development and dried using nitrogen. Again, thermal evaporation was used to deposit 5 ± 1 nm of Cr as an adhesion layer (0.3 Å/s), and 50 ± 2 nm of Au (0.5 Å/s). Finally, lift-off was performed by soaking in acetone at 50°C for 1–3 hours, followed by rinsing in isopropanol and blow drying.

Transmission and reflection measurements

White light illumination in combination with an integrating sphere was used to measure the total transmittance of the NW network and ITO samples. A supercontinuum laser (Fianium SC400-4) was attenuated using a glass wedge and a ND 2.0 filter, after which it is focused by a f = 200 mm lens onto the samples. The samples are mounted in front of an integrating sphere (LabSphere). The transmitted light is collected from the sphere using a multi-mode collection fiber and fed into a spectrometer (Acton SpectraPro 300i) equipped with a Si CCD (Roper Scientific 7344-0001, cooled to −45°C). The measured spectral range was 400–964 nm. Each reported spectrum is an accumulation of 250 spectra, each with 100 ms accumulation time. The spectra were normalized to the transmission through the bare glass, right next to the NWs/ITO on the same sample. The total reflection measurements on the completed devices were performed with the same settings. Here, a silver mirror is used as a reference.

Sheet resistance measurements

The sheet resistance is determined from four-point probe measurements. For the NW networks, two probes were positioned on each contact pad. For the ITO the

standard procedure using four equally spaced probes (spacing 1 mm) was used. IV-curves were measured with micro-positioning probes connected to a source meter (Agilent B2902A) by applying current (−10 to 10 mA, in 101 steps) through the samples using the outer probes and measuring the induced voltage with the inner probes. The sheet resistance is found from a linear fit through the data.

Solar cell fabrication

ITO-coated glass substrates (200 nm thick ITO, Naranjo substrates) were cleaned by sonicating in acetone and soap-water followed by rinsing with normal water and sonicating in 2-propanol for few minutes. Silver nanowire substrates were cleaned only by mild rinsing in isopropanol to remove dust particles and were blow-dried using nitrogen.

A commercial formulation of high conductivity poly(3,4-ethylenedioxythiophene): poly(styrenesulfonate) (PEDOT:PSS), PH1000 was mixed with 5 wt% dimethyl-sulfoxide (DMSO) to enhance its conductivity and 0.2 wt% fluorosurfactant Zonyl FS-300 to facilitate wetting. The mixture was sonicated for 30 min. This PEDOT:PSS formulation was then spin coated on top of ITO-coated substrates and Ag-nanowire-coated substrate at 6000 rpm to obtain a 30 nm thick film.

P3HT (>98% head to tail, M_n = 54,000–75,000 g mol^{-1}, Plextronics, purchased from Aldrich) and PCBM (>99%, Solenne BV) in 1:1 weight ratio were dissolved in ortho-dichlorobenzene (o-DCB, 99%, Sigma-Aldrich) at a concentration of 40 mg/mL. The polymer solution was stirred overnight at 70°C and was then filtered using a 1 μm-pore filter. The polymer was spin coated inside a nitrogen filled glovebox at 700 rpm to obtain a 220–230 nm thick film. Substrates were subsequently annealed inside a glovebox at 110°C for 30 min.

To complete the devices, 1 nm LiF, 100 nm Al and 500 nm Ag were evaporated using a circular shaped shadow mask (diameter = 1.9 mm). The thickness of all layers was measured using Veeco Dektak 150 Surface Profiler.

Solar cell characterization

Current vs. voltage curves (I-V) were measured under simulated solar light (100 mW cm^{-2}) from a tungsten-halogen lamp filtered by a Schott GG385 UV filter and a Hoya LB120 daylight filter using a Keithley 2400 source meter. The voltage range was −2 to 2 V. The short-circuit current density (J_{sc}) was determined from the EQE data by multiplying with the AM1.5G solar spectrum and integration [167].

EQE measurements were performed in a homebuilt set-up, with the devices kept in a nitrogen filled box and illuminated through an aperture of 1 mm diameter. Mechanically modulated (Chopper, Stanford Research, SR 540) monochromatic (Monochromator, Oriel, Cornerstone 130) light from a 50 W tungsten halogen lamp (Osram 64610) was used as probe light. A calibrated Si photodiode was used for the reference spectrum. The response was recorded as the voltage using a current preamplifier (Stanford Research Systems, SR570) connected to lock-in amplifier (Stanford Research Systems, SR830).

Angle-resolved EQE measurements
A supercontinuum laser (Fianium, SC400-4) and a home-built prism-based monochromator were used to obtain fiber-coupled (multimode) monochromatic illumination (1.5–5.5 nm bandwidth, 57–65 μW). After the outcoupler, a 50–50 beam splitter was used to direct half of the power to a calibrated power meter (Thorlabs PM300) and half through a f = 200 mm lens onto the sample. The sample is mounted in the same nitrogen-filled box onto an automated rotation stage (HUBER 420-10724), and the generated photocurrent is measured by a source meter (Keithley 2612). In the experiment, the wavelength was scanned from 650–850 nm in steps of 5 nm. For each wavelength, the angle of incidence was scanned from 0–45 degrees in steps of 0.5 degrees. The measured photocurrent values are the average over 10 measurement points.

3.7 Supplementary information

3.7.1 SCIL fabrication procedure

SCIL is a high-resolution soft-imprint technique that uses a bi-layer PDMS stamp together with a silica-based sol-gel with minimized shrinking during the curing process, to obtain both high resolution and make it substrate conformal. Figure 3.6 shows the process steps of the SCIL fabrication of the NW networks. Low-molecular weight PMMA (yellow) is spin coated onto a glass substrate, followed by spin coating of ~65 nm of sol-gel (green). The PMMA will be used to perform lift-off. The PDMS stamp is applied without pressure, capillary forces pull the stamp into the sol-gel. After 30 minutes in ambient conditions, the sol-gel is cured and the stamp is removed. Next, reactive-ion etching (RIE) is used to etch through the residual layer of sol-gel and PMMA. Next, thermal evaporation was used to deposit 1–2 nm of Ge as a seed layer, followed by ~30 nm of Ag. Finally, the redundant metal was removed by dissolving the PMMA in acetone.

The timing of the RIE steps is critical and the optimum strongly depends on the filling fraction of the stamp. Over-etching causes the trenches in the sol-gel to widen due to the non-perfect anisotropy. Our stamp contains 40 patterns with different filling fraction. As a result, a large fraction of the patterns have been over-etched, resulting into wider wires and thus lower transmittance. The patterns can easily be optimized for transmission by reducing the REI etch times.

3.7.2 Four-point probe measurements

To measure the sheet resistance of the networks, we assume that the resistance of the contact pads is very small compared to that of the NW network. To eliminate the effect of the contact resistance, a 4-point-probe experiment was performed (Fig. 3.7a). The outer 2 probes (red, channel 1) are used to apply a current through the network (−10 to 10 mA). The inner 2 probes (blue, channel 2) measure the induced voltage over the network.

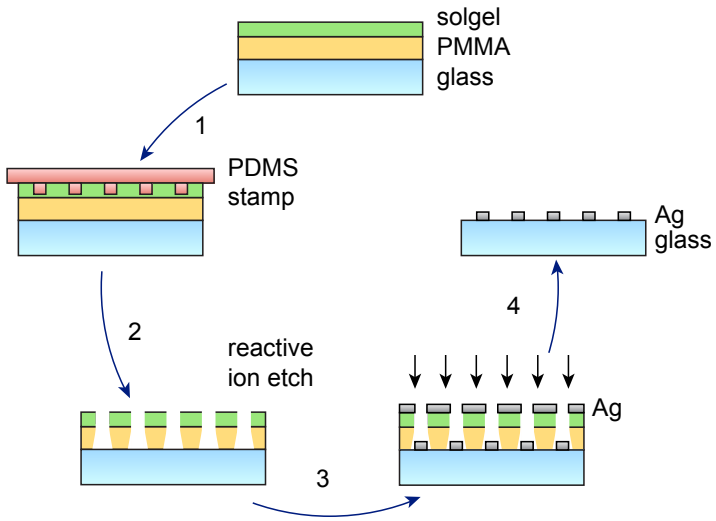

Figure 3.6: Fabrication steps of substrate-conformal imprint lithography (SCIL) to form Ag nanowire networks.

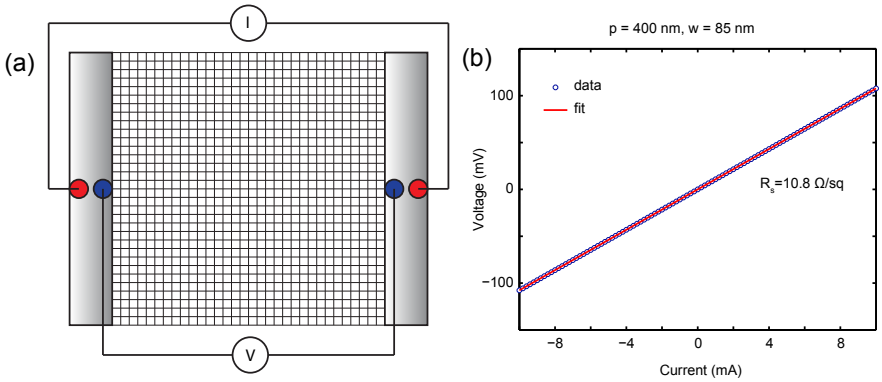

Figure 3.7: Four-point probe measurement procedure. (a) Sketch of geometry for 4-point probe electrical measurements of the NW networks. (b) IV-curve for NW network (400 nm pitch) showing Ohmic behavior.

Figure 3.7b shows a typical IV curve, showing that the networks behave Ohmic (straight line) and the data (blue) can easily be fitted by a linear model (red). The slope gives the sheet resistance. For ITO, a standard four-point probe measurement is performed. For thin films, the sheet resistance can be obtained from the slope of

the measured IV-curve multiplied by $\pi / \log(2)$. The data for ITO are the average of three measurements for each thickness.

3.7.3 FDTD simulation details

Simulations for Figs. 3.2c,d were performed using periodic boundary conditions in the in-plane directions to mimic an infinitely large Ag NW network (30–130 nm width, 30 nm high, 500 nm pitch). For Fig. 3.2c, w = 65 nm was used. Perfectly Matched Layers (PMLs) were used in the vertical direction to simulate a semi-infinite glass substrate and air above the network. A broadband plane wave (400–965 nm) was launched from the top, and the transmittance into the glass substrate and the reflected power were monitored. Using the Lumerical far-field transformation routine, the power in each diffractive order was calculated. A 10 nm mesh, with a 1 nm refinement mesh around the NWs was used. Optical constants were taken from a Drude, Lorentz, and Debye model fitted to the data from Palik [138]. To convert the transmittance of the first interface (studied in Fig. 3.2c) into "normalized transmittance" (shown in Fig. 3.2d), the spectra are multiplied by the transmission coefficient of a glass–air interface for normal incidence and divided by the transmittance of a flat reference substrate.

Simulations of the completed device (w = 65 nm, h = 30 nm, p = 500 nm) were performed using rounded corners at the top of the NWs (radius of curvature 15 nm) to better match the experiment and improve the convergence. Thicknesses for the PEDOT:PSS and polymer layer were taken 30 and 230 nm respectively, similar to the case for the eigenmode calculations. The conformal coating of the PEDOT:PSS over the NW networks is also taken into account (Fig. 3.8c), assuming a 30 nm thick layer on the side of the NWs and a 30 nm thick layer on top. The same optical constants as for the eigenmode calculations were used. A background index of 1.52 is used in order to take into account the presence of the glass superstrate. A 5 nm mesh, with a 1 nm refinement mesh around the NWs and PEDOT:PSS was used.

3.7.4 Angle resolved EQE measurement details

Due to the dispersive nature of the prism in the home-built monochromator, the bandwidth increases for larger illumination wavelengths. Therefore, while scanning from 500–800 nm, the bandwidth is adjusted after scanning ~100 nm, in order to keep it roughly constant. To characterize the bandwidth of the monochromatic illumination in the angle-resolved EQE measurements, we measured the monochromator output at different wavelengths after each adjustment (Fig. 3.8a). We find bandwidths in the range of 1.5–5.6 nm from a Lorentzian fit to the data.

Focused Ion Beam (FIB) cross sections were performed in order to characterize the layer thicknesses of the devices as fabricated, as an input for the dispersion calculations (dashed lines, Figs. 3.5a,b). Large variations up to 65 nm in the thickness of the polymer can be observed (Fig. 3.8b).

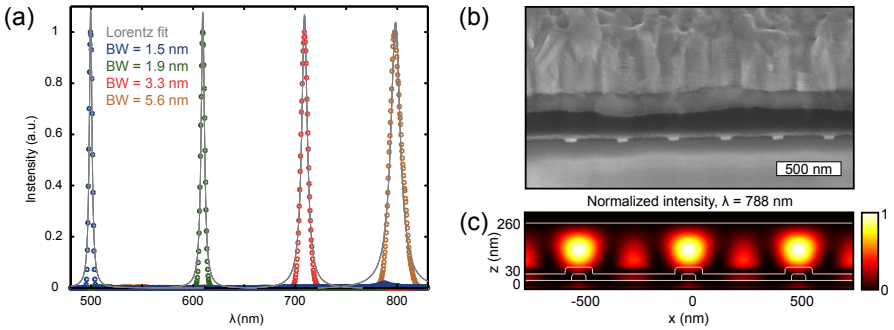

Figure 3.8: Angle-resolved *EQE* details. (a) Measured monochromator output for several wavelengths across the scan range. Gray lines show Lorentzian fits through data. The bandwidth (BW) is listed as an inset, and is obtained from the FWHM of the fit. (b) FIB cross section showing the variations in polymer thickness across the device. (c) Simulated intensity profile, obtained from a y-z cross-cut perpendicular to the polarization (x-direction), through a p = 500 nm device (w = 65 nm). The outline of the layer stack is shown in white. From bottom to top: glass, NWs, conformal coating of PEDOT:PSS, P3HT-PCBM, Al.

Simulations of the field inside the complete devices (w = 65 nm, h = 30 nm, p = 500 nm) shows strong coupling to guided modes (Fig. 3.8c). The cross cut is taken perpendicular to the electric field polarization. Together with the mode profile (compare to Fig. 3.4b), this confirms that light couples to the TE_0 mode.

3.7.5 Total reflection measurement of solar cells

Total reflection measurements on the completed devices were performed for comparison with the measured *EQE* (Fig. 3.9). Comparing the *EQE* of a NW network device (p = 500 nm) with that of the ITO reference device shows a large reduction (up to 0.2) in the visible (Fig. 3.9a). Embedding the NW networks in PEDOT:PSS instead of air makes the dielectric environment of the NW networks nearly uniform. This increases the backscattering of light, and thereby the reflectivity. Figure 3.9b shows that ~0.07 of the ~0.2 difference in *EQE* is a result of the increase in reflection. The remainder is due to enhanced parasitic absorption in the NWs, PEDOT:PSS and rear contact.

For wavelengths above the P3HT absorption edge ($\lambda > 650$ nm), the NW network device shows higher *EQE* (Fig. 3.9a) and lower reflection (Fig. 3.9b). The small peak in *EQE* at λ = 760 nm roughly coincides with the spectral position of a sharp dip in reflection, which is a strong indication for mode coupling (spectral misalignment is a result of non-zero angle of incidence in the reflection measurements).

To further corroborate the role of mode coupling as a light trapping mechanism, Fig. 3.10 shows total reflection measurements for different pitch (Fig. 3.10a,

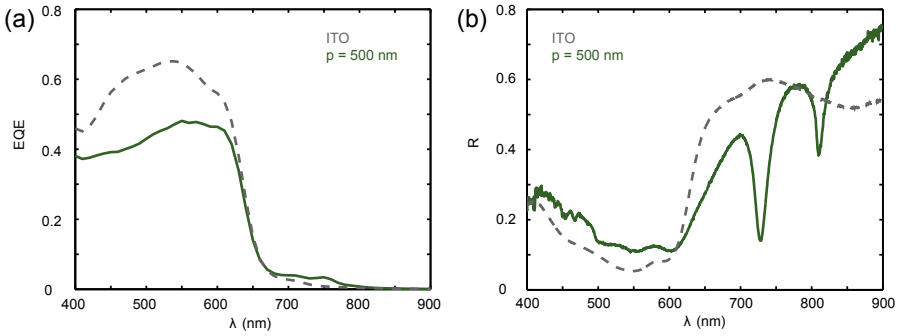

Figure 3.9: Total reflection measurements. Measured EQE under normal incidence (a) and measured total reflection for θ = 6 degrees (b) for the ITO reference device (gray) and p = 500 nm.

w = 65–85 nm) and different wire widths (Fig. 3.10b, p = 600 nm). Varying the NW pitch alters the in-plane momentum obtained from diffractive coupling, giving rise to a spectral shift when coupling to a guided mode with a well-defined wavevector. Indeed, sharp dips at different spectral positions can be observed for different NW pitch (Fig. 3.10a). Note that the non-zero angle of incidence (θ = 6 degrees) causes mode coupling to the same mode at different wavelengths, as apparent in Figs. 3.5b, 3.9b and 3.10a. Increasing the NW width increases the scattering cross section of the individual NWs, giving rise to an increase in backscattering in the visible as well as more efficient coupling to the guided mode in the NIR (Fig. 3.10b).

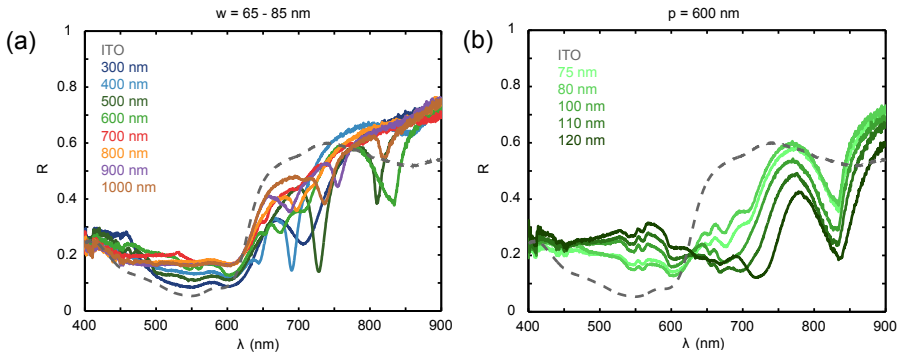

Figure 3.10: Total reflection measurements for varying pitch and wire width. (a) Measured total reflection (θ = 6 degrees) for different pitched NW network devices (w = 65–85 nm). (b) Measured total reflection for different wire width (p = 600 nm).

3.7.6 Influence of Ge seed layer on optical properties

The simulations in Fig. 3.2 neglect the presence of the 1 nm Ge seed layer, since this figure aims to describe the theoretical optimum performance that can be obtained with Ag NW networks (Fig. 3.2d). The inclusion of the Ge is an experimental necessity, which may be circumvented by further optimization of metal deposition methods (see Chapter 4). However, for low-aspect ratio structures such as those used in this work, the optical absorption of the Ge can be non-negligible. To demonstrate this, we simulate the optical absorption in the NWs with and without the 1 nm Ge layer. The results for a network with p = 500 nm, w = 65 nm, and h = 30 nm is shown in Fig. 3.11. Due to the strong absorption of Ge in the blue spectral range, the averaged absorption losses increase from 2.3% without to 5.4% with Ge seed layer (weighted for the AM1.5 photon density). This demonstrates that further optimization of the metal deposition techniques to relieve the necessity of the Ge seed layer is an important direction for future research.

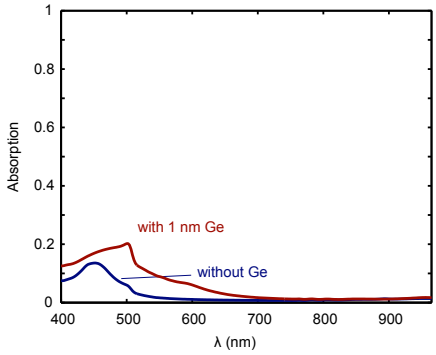

Figure 3.11: Simulated absorption losses in nanowire networks with (red) and without (blue) 1 nm Ge seed layer.

4

Solution-grown silver nanowire ordered arrays as transparent electrodes

High-quality transparent conductors are a key component in the optoelectronics industry, with applications in photovoltaics, organic light-emitting diodes and displays. We demonstrate the fabrication of a transparent conducting film composed of a regular network of silver nanowires, obtained by a combination of a soft solution process at room temperature in a mild aqueous environment and substrate-conformal imprint-lithography. The solution-grown nanowire networks show a three-fold higher conductivity than grids obtained by metal evaporation (3.5 Ω/sq vs 10.7 Ω/sq at 76% transmission weighted for AM1.5 photon density). We demonstrate that the better performance is due to the larger grain size obtained in the solution-grown nanowire grid compared to the evaporated grid, which results in a strong reduction of electron scattering by grain boundaries. This procedure allows for the replacement of high-vacuum technologies required in the conventional evaporation step used for metal deposition, with a low-cost solution-based process.

4.1 Introduction

Transparent conductors are crucial components in optoelectronic devices, such as touch screen displays, organic light-emitting diodes (OLEDs), and solar cells.

Transparent conducting oxides (TCOs) are the most commonly used in these applications, with indium-tin-oxide (ITO) leading the market [168]. However, the costly deposition process of TCOs, along with brittleness and incompatibility with organic materials [169, 170], have triggered intensive research towards alternative schemes that can simultaneously provide high electrical conductivity and high optical transmittance. Materials that have recently been investigated include carbon nanotubes [169, 171–173], conducting polymers [169, 174, 175] percolated metal films [103, 111, 112], graphene [125, 169, 176], and metal nanowire networks [99, 100, 102, 122, 159, 169, 177–180].

Metal nanowire networks composed of e.g. Ag, Cu and Al have proven to be excellent transparent conductors [100, 102, 159, 177, 178, 181]. The bulk conductivity of these metals is high, and nanostructured wires effectively couple light into an underlying substrate through the excitation and scattering of plasmons [102, 122, 159, 177]. Several approaches to realize metal nanowire networks with high transmittance and low sheet resistance that can be made at low costs have been explored so far. These include nanowire meshes prepared by metal evaporation on various templates, such as electrospun fibers [100, 182, 183], self-cracking templates [179], or lithography-defined nanopatterns (see Chapters 2 and 3). Such approaches typically require thermal evaporation in order to deposit metal. Although vacuum processes allow to deposit high quality materials, they are energy intensive, time consuming, and make inefficient use of metal. Cost-effective alternatives based on deposition and welding of metal nanowires prepared in solution have proven effective to achieve transparent electrodes with remarkable performance [106, 107, 122, 170, 180]. This shows that solution processes can yield material of similar quality compared to vacuum-based methods. Although this method provides a relatively simple fabrication scheme, the random geometry limits control over the optical transmission characteristics, which are determined by the subtle interplay between plasmons on the interacting nanowires. To achieve such control, ordered arrays of nanowires have been made by lithographic techniques [109, 159, 177]. Using these arrays, accurate control over the excited plasmon modes and their interaction has led to performance beyond that of ITO (see Chapter 2). Furthermore, it has been shown that the accurate design of patterns at the nanoscale (such as fractal geometries), can yield electrodes with superior optoelectronic performance [166]. In fact, this enables (i) minimum sheet resistance (for a certain transmittance) via tuning of the geometry, (ii) coupling to specific optical modes and (iii) light trapping or directional emission. As such optimal features are only achievable with an engineered pattern, the successful integration of nano patterning with solution processing techniques would be an important step towards replacing expensive metal oxide films as transparent electrodes.

In this Chapter, we demonstrate a strategy that bridges the gap between the efficiency of solution phase processes, and the control of light-matter interaction at the nanoscale using nano patterning. We combine substrate-conformal imprint-lithography (SCIL) with a soft solution process to fabricate highly controlled two-dimensional networks of silver nanowires without metal evaporation steps. First,

SCIL is used to make a square array of trenches in a poly(methyl methacrylate) (PMMA) film that is spin-coated on glass (trench width 50–130 nm, pitch 300–1000 nm). Second, the reduction of a silver salt ($AgNO_3$) by a sugar (glucose) in an aqueous solution is used to locally infill the trenches with silver, following a chemical route commonly employed as a simple test for the presence of aldehydes (Tollens' test). Using this method, we obtain a solution-grown nanowire network on glass with a well-controlled geometry. We find that the electrical performance outperforms that of evaporated networks with an almost three-fold decrease in resistivity (3.5 Ω/sq vs 10.7 Ω/sq at a transmission of 76%, weighted for AM1.5 photon density). The controlled two-dimensional network allows us to confidently compare different metal deposition pathways and derive conclusions about their performance. Based on detailed characterization and a simple conductivity model, we show that the high conductance of the solution-grown networks can be explained by a large increase in the grain size of silver crystallites within the nanowires, compared to the evaporated wires. This shows that the material quality achievable with solution deposition methods can match or even exceed that obtained with vacuum-based techniques.

4.2 Fabrication and characterization

The fabrication of solution-grown nanowire networks is summarized in Fig. 4.1a. It involves four steps (see Section 4.6 for more details): (i) use of SCIL to imprint nanosized trenches in a PMMA template, organized in a grid fashion; (ii) use of the Tollens' reaction to nucleate and grow crystalline silver on the substrate surface; (iii) lift-off of the PMMA template to obtain a transparent and conductive nanowire network; (iv) use of rapid thermal annealing (RTA) to reduce surface roughness. Silver was chosen as the material for the solution grown nanowire networks because of its exceptional conductivity and better chemical stability compared to copper. The Tollens' reaction [184], causes the formation of silver nanocrystals when a sugar with an aldehyde group, such as glucose, is present in a solution containing diamminesilver(I) complexes (see Eqs. 4.1–4.3).

$$2\,AgNO_3 + 2\,NaOH \longrightarrow Ag_2O_{(s)} + 2\,NaNO_3 + H_2O \tag{4.1}$$

$$Ag_2O_{(s)} + 4\,NH_3 + 2\,NaNO_3 + H_2O \longrightarrow 2\,[Ag(NH_3)_2]NO_3 + 2\,NaOH \tag{4.2}$$

$$2\,[Ag(NH_3)_2]^+ + RCHO + H_2O \longrightarrow 2\,Ag_{(s)} + 4\,NH_3 + RCO_2H + 2\,H^+ \tag{4.3}$$

Nanocrystals preferentially form at the substrate surface due to the lower nucleation barrier. Some partial nucleation occurs also on the PMMA template surface, at a much lower rate compared to that at the glass substrate. This allows for successful lift-off on the entire sample because the nanowires growing in the trenches and nanoparticles nucleating on the template are physically separated. The SCIL stamp contained several fields with different nanowire width and pitch, each field having a total size of 2×2 mm^2.

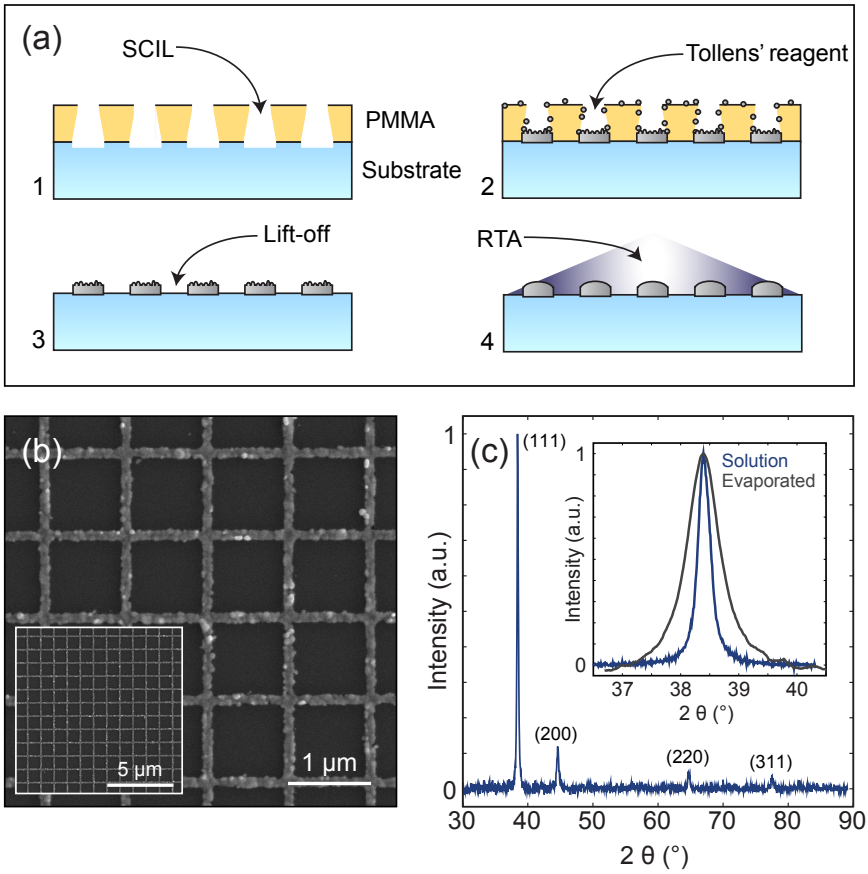

Figure 4.1: (a) Schematic of the solution grown nanowire network fabrication process: (1) SCIL to produce a grid nanopattern in PMMA; (2) solution phase growth of Ag nanowires in the trenches defined by the template via the Tollens' reaction; (3) lift-off and (4) RTA to smoothen the nanowire surfaces. (b) SEM images of an as-grown nanowire network before RTA treatment, showing the confinement of the growth over a large area. (c) XRD before RTA treatment of solution grown nanowire network measured in the range 30–90° with the θ–2θ configuration, showing the crystalline nature of the nanowire. The inset shows the comparison of the (111) Ag reflection peak for solution grown and evaporated silver, indicating the larger average grain size in the former.

Figure 4.1b shows SEM images of a solution grown nanowire network after lift-off. The images show the confined growth of silver only on the exposed glass surface, and indicate the continuity of the network over a large area. A dark-field optical image of the network is displayed in Supplemental Fig. 4.5. The surface texture of the silver nanogrid suggests that nucleation takes place at many different

positions in the trench on the substrate surface, followed by growth of individual nanocrystals until merging with neighbors. As a result, a continuous network of crystalline silver is formed. The x-ray diffraction (XRD) pattern presented in Fig. 4.1c shows the characteristic reflection peaks of crystalline silver with no secondary phases.

The average Ag grain size for the solution-grown nanowires, estimated from the x-ray diffraction peak width using the Scherrer equation [185], is ~60 nm (inset in Fig. 4.1c). X-ray diffraction peak width measurements were also performed on silver evaporated using the method described in Chapter 3, and show a silver grain size of ~15 nm. Clearly, the solution-growth method leads to larger Ag grains and thus a smaller density of grain boundaries.

The surface topography of the solution-grown silver nanowire networks was characterized by atomic force microscopy (AFM) on a 100 μm^2 area (see Supplemental Fig. 4.6a). The average height across a Ag nanowire network is shown in Supplemental Fig. 4.6b, indicating for this particular sample a typical nanowire height of 30–40 nm. The nanowire height can be controlled by adjusting the growth time.

4.3 Rapid-thermal annealing

Because of the formation process, i.e. random nucleation and growth, the surface of as grown nanowire networks is rough. This causes strong scattering and absorption of light, which limits optical transmittance and therefore reduces performance. It has been shown that solution synthesized silver nanowires can be plasmonically welded by rapid thermal annealing (RTA) [178], at temperatures below the melting point of silver, preserving the nanowire shape. High intensity broad-band light is absorbed by the metal nanowires, causing heating; silver atoms become highly mobile well below the melting point [178], and diffuse to minimize the surface to volume ratio. Furthermore, the electromagnetic field can be locally enhanced due to roughness, resulting in hot spots that create additional heating where the surface is rougher. This effectively contributes to the reduction of the surface to volume ratio, therefore leading to a smoother surface. Following this paradigm we performed RTA on solution grown nanowire.

Figures 4.2a-d compare SEM and AFM images of solution grown nanowire networks before and after 7 s of RTA. The difference in surface texture observed in the figure, indicates a smoothing of the nanowires as a result of RTA. Cross-cuts of AFM data show that indeed after RTA, the nanowires display a rounded cross-section compared to as grown nanowires (Figs. 4.2e,f), and become smoother. Statistical analysis of the entire AFM scan was performed, by computing the probability density function of the nanowire height distribution. This allows us investigate trends representative of a larger area. Figure 4.3a compares the height distribution of the nanowires before (red) and after (blue) RTA. It shows that after RTA the distribution is slightly narrower, indicating that the nanowires become more

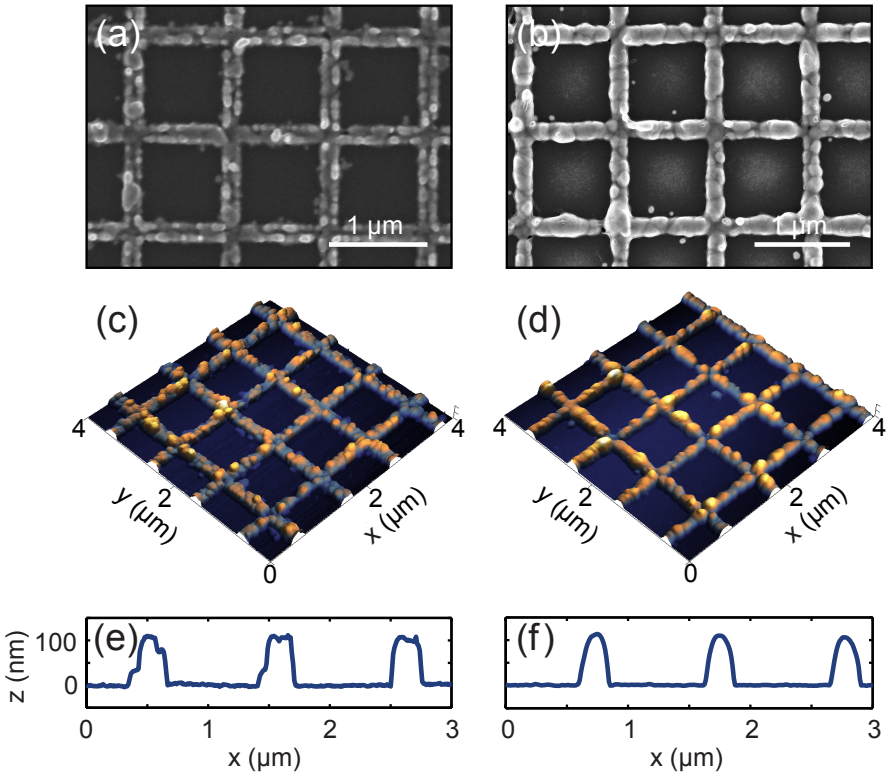

Figure 4.2: (a-d) SEM and AFM images of solution grown nanowire networks samples before (a,c) and after (b,d) RTA; the aspect ratio of AFM image is 1. (e,f) Cross-cuts of the AFM map of (c) and (d) respectively.

uniform in height. Figure 4.3b compares XRD data of the (111) silver peak before (red) and after RTA (blue). It shows that a narrower peak is obtained after RTA, corresponding to an average grain size of ~200 nm, calculated using the Scherrer equation (see Section 4.6). Considering the relatively low temperature achieved during the process [178], which is expected to be well below the melting point (T_{mp}) of silver, we exclude melting of the nanowires followed by solidification to achieve recrystallization with larger grains. This increase in average grain size can however be explained in terms of gain of interfacial free energy as a result of grain boundary migration, which has been reported to occur at temperatures as small as 0.2 T_{mp} in metals [186].

We next characterized electrical and optical response of RTA-processed solution-grown nanowire networks. This is presented in Fig. 4.3c, which compares

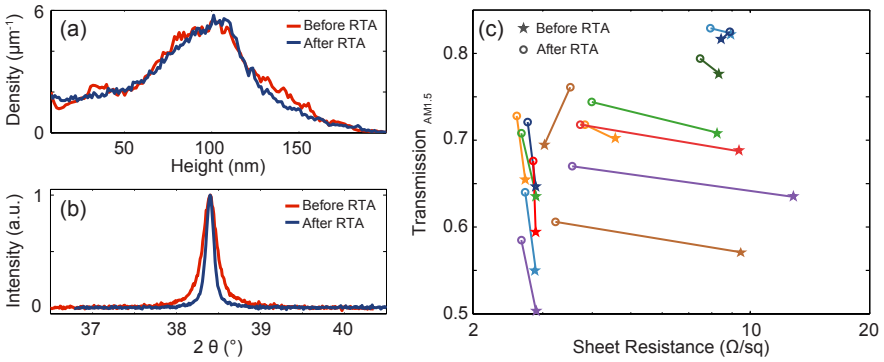

Figure 4.3: (a) Probability density function of the height distribution computed from Figs. 4.2c-d, showing a slightly narrower peak after RTA annealing, as a result of smoothing and homogenization of the nanowires. (b) XRD of solution grown nanowire networks before and after RTA, showing a narrower (111) silver reflection peak as a result of the larger average grain size due to RTA. (c) Evolution of the optical/electrical performance of solution grown nanowire networks of various height, as a result of RTA; star and circle markers indicate the sample before and after RTA respectively.

performance before RTA (star) and after RTA (circle), for networks of various height, pitch and width. The performance of the networks improves upon RTA processing, independent of the array geometry. The transmittance (T) of the network improves significantly, up to 10% absolute. Furthermore, an improvement of sheet resistance (R_{sh}) is observed as well in almost every sample, due to the enlargement of the average grain size and the concurrent homogenizations of the nanowire height distribution.

4.4 Transparent electrode performance

Having demonstrated the efficacy of RTA to improve the performance of solution grown nanowire networks, we summarize in Fig. 4.4a optical transmission and sheet resistance measurements of best performing samples. The solid blue points represent solution-grown nanowire networks with different nanowire widths in the range 90–180 nm, periodicities of 800, 900 and 1000 nm and heights in the range 30–100 nm. The transmittance data were calculated by weighting the transmission spectra over the photon density in the AM1.5 spectrum (see Supplemental Fig. 4.7 for transmission spectra), and normalized to the transmission of a bare, flat substrate. We note that the transmittance derived this way is underestimated, as this analysis does not take into account light coupled into guided modes in the substrate (see Chapter 3); such scattered and trapped light does contribute to power generation in a photovoltaic device. The sheet resistance was obtained from

four-point-probe measurements.

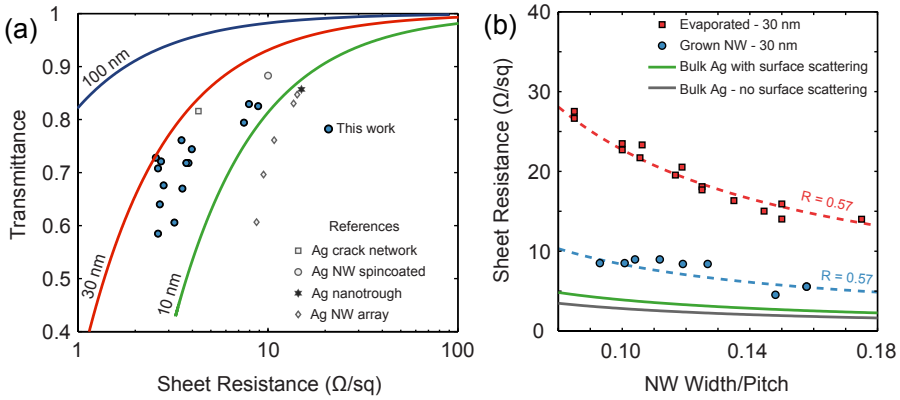

Figure 4.4: (a) Optical vs electrical performance of solution grown nanowire networks, represented by blue solid markers, for different nanowire width, height and pitch of the array. The performance of Ag nanowire array [177], Ag nanotrough [100], Ag crack network [179], and Ag nanowire spincoated [180] are reported for comparison after weighting for the AM1.5 spectrum. Solid lines represent the performance of ideal nanowire grids of different thicknesses. (b) Sheet resistance of 30 nm thin nanowire grids as a function of nanowire width/pitch, according to the Mayadas-Shatzkes model described in Supplemental Eq. 4.5a, that accounts for electron scattering at the surface and by grain boundaries, with a $p = 0.5$ specularity parameter and $R = 0.57$ reflection coefficient. The average grain size employed in the model was calculated from XRD measurements and corresponds to 15 nm for evaporated (black dashed line) and 60 nm for solution grown nanowire networks (blue dashed line). The solid curve represents the sheet resistance of a defect-free nanowire grid, accounting for surface scattering ($p = 0.5$, green curve) and assuming values for bulk materials ($p = 1$, gray curve). Data points represent measured sheet resistance of solution-grown (blue dots) and of evaporated nanowire networks (red squares) with a thickness of 30 nm. The smaller sheet resistance measured for solution-grown networks compared to evaporated networks is due to the larger average grain size in the former (60 nm vs 15 nm). This is accurately described by the Mayadas-Shatzkes model.

As reference, the lines drawn in Fig. 4.4a represent the calculated performance for defect-free metal nanowire grids of three different thicknesses based on a simple geometrical transmission model. The curves are obtained by varying the nanowire width to pitch ratio. The calculated transmittance accounts for both transmission through the voids and transmission through the metal (this is important for thin films). The transmittance is weighted for the AM1.5 spectrum. While no plasmonic effects are included in the calculation, this simple model accurately represents experimental transmittance data (see Supplemental Fig. 4.8), which we attribute to the fact that the relatively narrow resonances only have a small effect on the average broadband response. The sheet resistance accounts for electron scattering at the

surface but assumes no grain boundaries, and was calculated by employing the Mayadas and Shatzkes model [187] (see Supplemental Section 4.7.1). The curves show the typical trade-off between T and R_{sh}, which can be accurately controlled by varying pitch, width and thickness of the nanowire networks.

Next, the performance of our solution-grown nanowire networks is compared to that of nanowire-based transparent electrodes fabricated in other ways reported in the literature; the data are shown for reference in Fig. 4.4a. We find superior performance for the solution-grown networks compared to the same nanowire networks obtained by metal evaporation (gray diamonds, data from Chapter 3). Ag crack networks are obtained by metal evaporation on a cracked gel film template [179]; Ag nanotroughs are obtained by metal evaporation on suspended electrospun fibers [100]; spincoated Ag nanowires are obtained by spincoating Ag nanowires prepared in solution with the polyol process [180]. This shows that our solution grown nanowire networks have outstanding performance. Note that the values reported for the reference networks were calculated by applying the AM1.5 weighting function to the wavelength dependent transmittance data available in the references. Also, all data in Fig. 4.4a are referenced to the transmission of a glass substrate; this results in absolute 8% overestimation of the transmittance. We chose not to overlay in Fig. 4.4a the widely used figure of merit (defined as the ratio between dc conductivity to optical conductivity) [99, 106, 173, 179] because it is not applicable in the optical frequency regime studied here.

In order to understand the superior performance of solution deposited Ag nanowire compared to those made by evaporation, we employed the model developed by Mayadas and Shatzkes [187], which describes the relation between conductivity of nanoscale metallic films and electron scattering at grain boundaries and at the surface (see Supplemental Eq. 4.5). The sheet resistance of solution-grown nanowire networks and evaporated networks (both with a thickness of 30 nm) is reported in Fig. 4.4b as a function of the ratio between the nanowire width and the pitch of the array, showing the trend that larger filling fractions correspond to smaller sheet resistances. It also shows that for a fixed nanowire width/pitch ratio, the conductivity of solution grown nanowire networks is on average 2.5 times better than that of evaporated networks.

Fig. 4.4b shows the modeled sheet resistance of the grid calculated from Supplemental Eq. 4.5a, for 60 nm grain size (dashed blue line) and 15 nm grain size (dashed red line), in accordance with the average grain size obtained from XRD data (Fig. 4.1c). The excellent match between the model and experimental data for solution processed and evaporated films, indicates that the larger conductivity of the solution processed wires originates from the larger grain size. Note that the data reported in Fig. 4.3b for solution-grown nanowire networks were measured before RTA processing. Using the same grain boundary and surface scattering model parameters (see Supplemental Section 4.7.1 for full description), we could achieve good fits to the experimental data for both solution-grown and evaporated nanowire networks simply by inputting the grain size calculated from XRD. The calculated sheet resistance of the same silver nanowire grid without grain bound-

ary scattering (i.e. monocrystalline Ag) is also given in Fig. 4.4b for comparison, both with and without surface scattering contributions (green and gray solid lines, respectively). This shows that our solution grown nanowire networks are less than a factor of 2 from the sheet resistance expected from a defect-free grid. Detailed characterization of the nanowire networks thus indicates that solution deposition methods can match or even exceed the material quality of vacuum-based deposition, in stark contrast to the conventional wisdom in the field.

4.5 Conclusions

We demonstrate high-quality silver nanowire networks fabricated by a combination of soft-imprint lithography and soft-solution processing (Tollens' reaction). This relatively simple method yields ordered metal nanowire grids as transparent electrodes, without the need for energy intensive vacuum metal evaporation processes. We show that the solution process, combined with a short RTA treatment, yields superior performance compared to the thermally evaporated networks. This important result shows that solution-based methods can lead to material quality comparable or even superior to vacuum-based deposition methods, in contrast with common assumptions. We demonstrate that the lower material resistance is due to the larger average grain size, which decreases electron scattering from grain boundaries. The simplicity of this solution approach can be extended to other types of template-assisted metal nanowire network transparent electrodes, thus providing a general pathway for further improvement of transparent conductor performance at low cost.

4.6 Methods

Nanowire network fabrication

4-inch borosilicate wafers (0.7 mm thick) were cut and subsequently cleaned with base piranha. After a 2–5 min bake-out at 150°C the samples were cooled with N_2. Next, ~250 nm Poly(methyl methacrylate) (mr-I PMMA, micro resist technology) 35 kDa (300) was spincoated at 1000 rpm in 45 s, followed by a 15 min bake at 150°C. After cooling, the substrates were exposed to a 10 s O_2 plasma reactive-ion etch (RIE) to make the surface of the PMMA hydrophilic. Then, a 60–70 nm thick uniform layer of liquid silica sol-gel (details can be found in Chapter 11) was spincoated at 1000 rpm (10 s), after which the nano-imprint stamp (containing multiple 2 × 2 mm nanopatterns) was applied. After 30 minutes of drying in ambient conditions, the stamp was removed and nanoscale trenches were formed in the solidified sol-gel layer. RIE was then used to anisotropically etch through the residual sol-gel layer (25 sccm CHF_3, 25 sccm Ar, 15 mTorr, 67 W, 1:45 min), followed by a 4 min O_2 plasma etch (25 sccm, 5 mTorr, 50 W) to etch through the PMMA layer and expose the glass substrate. Finally, another 6 min etch step (same CHF_3-based recipe as above) was performed to remove any residual sol-gel from

the sample. This last step also etches shallow trenches into the glass substrate and leaves behind a clean PMMA template.

Metal deposition via solution phase
The reducing solution was prepared by dissolving 6.84 g of D-glucose in 20 mL of deionized water. After complete dissolution of glucose, 10 mL of absolute methanol was added. The silver solution was prepared by adding 0.815 g of silver nitrate ($AgNO_3$) to 20 mL of deionized water and stirring at 400 rpm for 20 min. 40 μL of potassium hydroxide (KOH) 0.25 M was added, producing a cloudy solution due to the precipitation of solid silver oxide particles (Ag_2O). Ammonium hydroxide (NH_4OH) (28–32%) was added drop wise until the solution became clear and transparent again, as a result of the formation of diamminesilver(I) complex $(Ag(NH_3)_2)^+$. The amount of NH4OH added was typically around 950 μL. After 5 min, 20 mL of the reducing solution was added to the silver solution, while vigorously stirring to ensure homogeneous mixing of the reagents. The resulting solution was quickly poured into a plastic petri-dish containing the nanopatterned glass substrate. The reaction time was controlled to produce nanowire networks with different heights. After the desired growth time, the sample was rinsed first in a 20:1 H_2O:NH_4OH solution for 30 s, to quench the reaction, and subsequently in deionized water.

Lift-off procedure
The sample was first transferred into an aqueous solution containing 0.2 M Polyvinylpyrrolidone (PVP) (55 kDa) for 1 h, then rinsed in deionized water and dried. The sample was then placed in a 1:3 H_2O:Ethanol solution with 0.2 M PVP at 65°C, while stirring at 500 rpm. The solution dissolved the PMMA template, while PVP ensured the encapsulation of Ag nanoparticles present on PMMA, to avoid irreversible adhesion to the glass substrate by Van der Waals forces, and affect the transmission properties of the electrode. After 2 h, the sample was sonicated for 30 s to remove any residual PMMA from the surface, rinsed in isopropanol and N_2 dried.

Contact fabrication
Thick Ag contacts on either side of the nanowire networks were fabricated using UV-lithography. After 2–5 min bake-out at 100°C, the samples were spincoated with a HMDS primer (4000 rpm, 32 s) to improve the adhesion of the photoresist. After a 1 min bake at 100°C, the samples were cooled and a ~925 nm thick layer of negative-tone photoresist (ma-N 1410 micro resist technology) was spincoated at 1400 rpm in 32 s, followed by a 90 s bake at 100°C. The samples were then exposed for 22.5 s at 20 mW (450 mJ) through a flexible mask (Selba) to create 125 μm × 2 mm large contacts that have 50 μm overlap with the nanowire networks. The exposed resist was developed by rinsing in ma-D 533S (micro resist technology) for 85 s to create an undercut, followed by extensive rinsing in deionized water to stop the development, and dried using N_2. Next, thermal

evaporation was used to deposit a 5 nm Cr adhesion layer (0.3 Å/s) and 150 nm of Ag (2.0 Å/s). Finally, lift-off was performed by soaking the sample in acetone (53°C) for 1–2 hours, followed by rinsing in isopropanol and blow drying.

Transmission measurements
A white-light super-continuum laser (Fianium SC400-4), attenuated using the reflection of a glass slide and a ND 2.0 filter, was used to illuminate the substrates. A f = 40 mm lens (Thorlabs, AC254-040-B-ML) was used to weakly focus the light onto the nanowire networks. The samples were mounted in front of an integrating sphere (LabSphere) such that also the diffusely scattered light is collected. The transmitted light is collected by a multi-mode collection fiber (105 μm core, Thorlabs FG105ACU) and sent to a spectrograph (ACTON spectrapro 2300i) and CCD camera (Pixis 400, cooled to −70°C). The measured spectral range was 430–930 nm. Each reported spectrum is the result of 100 accumulated spectra, each with a 250 ms integration time. To isolate the transmittance of the nanowire networks, the spectra were normalized to the transmission of a flat and clean reference glass wafer. This normalization procedure, often employed in the field of transparent electrodes, overestimates the transmittance by 8% absolute. Spectra collected in three different positions on each network were averaged to account for any spatial variation on the sample.

Sheet resistance measurements
Four-point-probe sheet resistance measurements were performed by applying a current in the range −0.1 to 0.1 A (external terminals) and measuring the voltage drop across the network with two different probes (internal terminals). All the terminals were on the big Ag photolithography pads. The sheet resistance for the square networks was calculated as the ratio of the two quantities.

X-ray diffraction
The average grain size can be estimated using the well-known Scherrer equation [185];

$$L = \frac{K\lambda}{Bcos(\theta)} \tag{4.4}$$

Here, L is the average crystallite diameter, K is the Scherrer constant (a typical value is 0.9), λ is the x-ray wavelength (λ = 0.154 nm for Cu Kα), B is the 2θ XRD FHWM peak (in radians) corrected for the instrumental broadening, and θ is the Bragg angle. The Bruker D2-phaser instrument was used to collect the XRD spectra, in the θ–2θ configuration. An acquisition time of 0.2 s per step was used and more than 100 spectra were averaged to increase signal to noise ratio. The B values were obtained after correcting for instrumental intrinsic broadening; this was done by measuring XRD of a Corundum standard sample and subtracting the FHWM of the peak at 2θ = 35.1°, from the FHWM of the (111) reflection 2θ = 38.4° in the Ag nanowire network sample.

Rapid thermal annealing
Rapid thermal annealing was performed in Sitesa addax RM6. The sample was placed on the silicon wafer susceptor, spaced by two 1 mm thick glass slides employed as insulator from the underlying substrate. The light source was turned on for a fixed amount of time (7 s), and Ar (5 L/min) was flowed during the experiment up to 60 s after the exposure, to allow for cooling down without oxidation of the nanowires. The temperature setpoint was 600°C with a ramp rate of 250°C/s but the pyrometer never reached a stable value as it is not accurate below 600°C.

Atomic force microscopy
Surface topographies were measured using a Digital Instruments Dimension 3100 atomic force microscope. 4 × 4 micron areas (384 × 384 pixels) were scanned using tapping mode (163.344 kHz tapping frequency) and a horizontal scan speed of 2 s/line. For Fig. 4.6, a 10 × 10 micron area was scanned using tapping mode (140.48 kHz tapping frequency) and a horizontal scan speed of 5 s/line.

4.7 Supplementary information

4.7.1 Mayadas and Shatzkes' model

In the Mayadas-Shatzkes' model the ratio of the conductivity of a polycrystalline sample (σ_g) and that of bulk material (σ_0) is given by:

$$\frac{\sigma_g}{\sigma_0} = \frac{1}{f(\alpha) - g(p,k,\alpha)} \tag{4.5a}$$

$$\alpha = \frac{l_0}{d}\frac{R}{1-R} \tag{4.5b}$$

$$f(\alpha) = 3\left[\frac{1}{3} - \frac{1}{2}\alpha + \alpha^2 - \alpha^3 ln\left(1 + \frac{1}{\alpha}\right)\right] \tag{4.5c}$$

$$g(k,p,\alpha) = \frac{6(1-p)}{\pi k}\int_0^{\pi/2}\int_0^{\pi/2}\frac{\cos(\theta)\sin(\phi)^3\cos(\phi)^2}{H^2}\frac{1-e^{-kH/\cos(\theta)}}{1-pe^{-kH/\cos(\theta)}}d\phi d\theta \tag{4.5d}$$

$$H = 1 + \frac{\alpha}{\cos(\theta)\sin(\phi)} \tag{4.5e}$$

$$k = \frac{t}{l_0} \tag{4.5f}$$

Here, θ and ϕ are the angles in polar coordinates, t is the film thickness, l_0 is the electron mean free path (~58 nm for silver, calculated with the Drude model), d the average crystallite diameter, and $0 < R < 1$ a coefficient describing the likelihood for an electron to be reflected by a grain boundary (which is assumed to be perpendicular to the drift velocity). Losses due to electron scattering at the surface

are taken into account in the specularity parameter $0 < p < 1$, with $p = 0$ meaning diffuse scattering and $p = 1$ specular scattering.

4.7.2 Supplementary figures

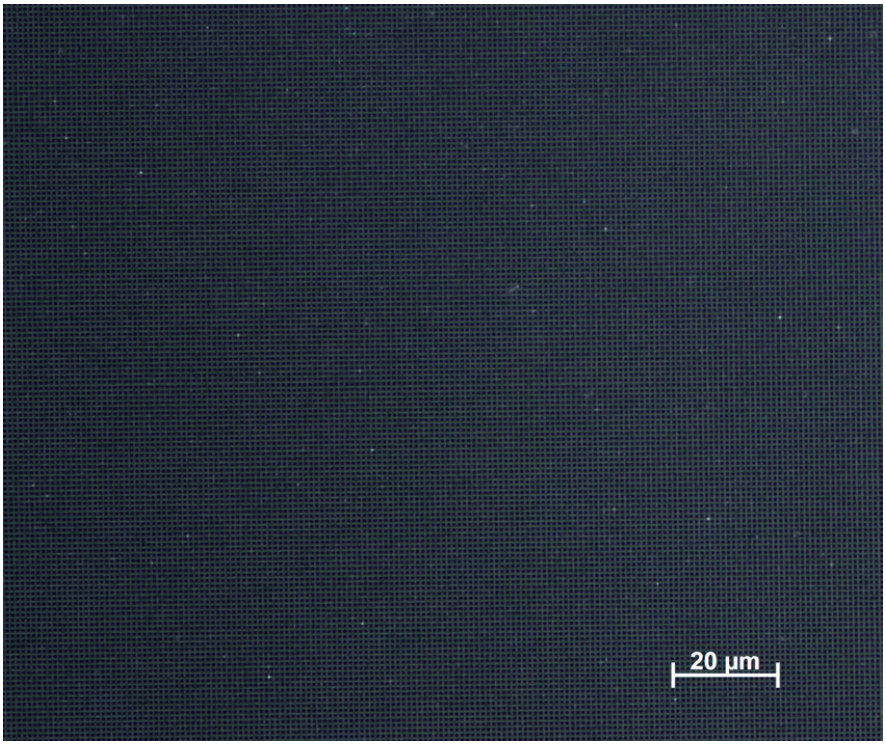

Figure 4.5: Dark-field optical microscope image of Ag nanowire network. The pitch of the array is 1000 nm.

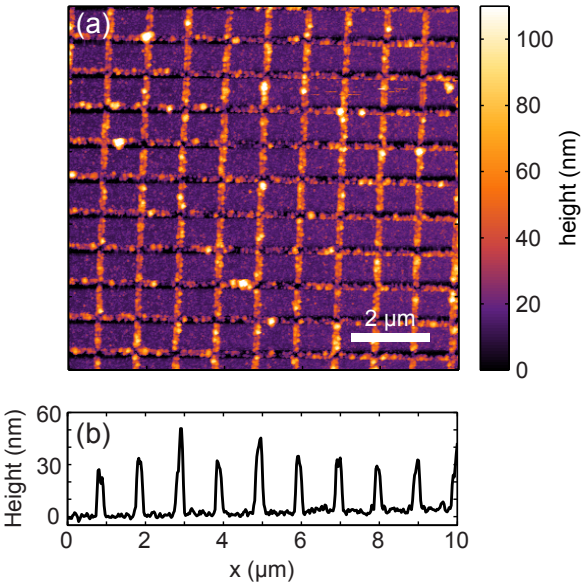

Figure 4.6: (a) 10 × 10 μm AFM scan of Ag nanowire networks. (b) Cross-cut of the image.

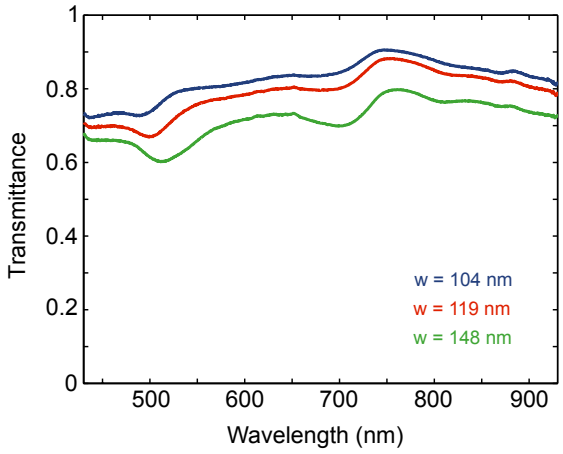

Figure 4.7: Transmittance of solution-grown nanowire network with an average height of 30 nm, normalized to the transmittance of the glass substrate. The array pitch is 1000 nm.

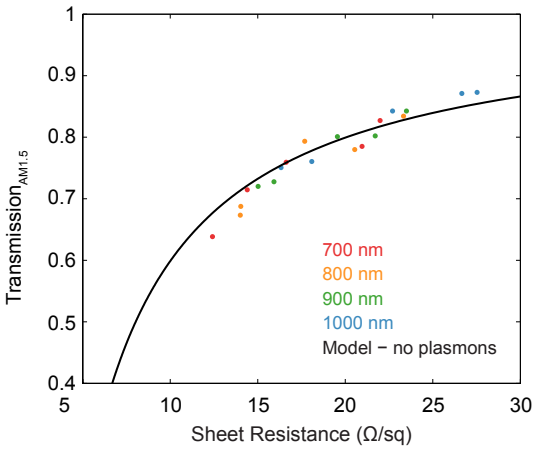

Figure 4.8: Optical vs electrical performance of evaporated Ag nanowire networks with a thickness of 30 nm for different nanowire width. The different colors represent a different pitch of the array. The solid black line represents the theoretical performance of 30 nm thick nanowire networks of various pitch/width ratio; the sheet resistance is calculated from the Mayadas-Shatzkes model ($p = 0.5$, $R = 0.57$, $d = 15$ nm) and the transmittance is calculated by adding the transmission through voids and the wavelength dependent transmission through the 30 nm metal film (weighted for AM1.5 spectrum). Plasmonic effects are not taken into account. This shows that this simple model describes well the experimental data.

5

Plasmoelectric potentials in metal nanostructures

The conversion of optical power to an electrical potential is of general interest for energy applications, and is typically obtained via optical excitation of semiconductor materials. Here, we introduce a new method using an all-metal geometry, based on the plasmon resonance in metal nanostructures. In arrays of Au nanoparticles on an indium-tin-oxide substrate and arrays of 100-nm-diameter holes in 20-nm-thick Au films on a glass substrate, we show negative and positive surface potentials during monochromatic irradiation at wavelengths below or above the plasmon resonance respectively. We observe such plasmo-electric surface potentials as large as 100 mV under 100 mW/cm^2 illumination. Plasmoelectric devices may enable development of entirely new types of all-metal optoelectronic devices that can convert light into electrical energy.

5.1 Introduction

Noble metal nanostructures display remarkable optical properties that arise from the coupling of incident light to the collective motion of the conduction electrons. The excitation, propagation and localization of these plasmons can be tailored by nanoscale control of metal size, shape and architecture [190]. Metal nanostructures

exhibiting subwavelength optical confinement [191] have enabled nanoscale photonic waveguides [192, 193] modulators [194], and surface plasmon amplification by stimulated emission of radiation (SPASERs) [195, 196], light trapping structures for photovoltaics [78, 197], field enhancement for Raman spectroscopy, and biological labeling techniques [198, 199]. Coupling of laser light to plasmonic structures can also result in efficient localized heating, because the resonant absorption cross section for plasmonic nanostructures is much larger than their physical cross section [200].

Recent work has demonstrated control over the plasmon resonance frequency (ω_p) of metal nanostructures when an external electrostatic field alters the carrier density in the metal [201, 202]. Increasing the carrier density in a noble metal nanoparticle leads to a blue shift of the resonance, while decreasing it leads to a red shift, as illustrated for a 20-nm-diameter Ag nanoparticle in vacuum (Fig. 5.1). Interestingly, the reverse effect, the optical generation of an electrostatic potential due to an optically driven change in carrier density in a plasmonic nanostructure has so far not been observed. Thermodynamically, however, such a plasmoelectric effect is expected to occur. We demonstrate direct experimental evidence of plasmoelectric potentials in the range 10–100 mV on colloidal assemblies and plasmonic light harvesting device geometries, in qualitative agreement with a thermodynamic model. The results may provide a new route to convert optical energy into electrical power.

5.2 Au colloids on ITO

Figure 5.2a shows the measured scattering spectrum for 60 nm Au colloids on ITO/glass, showing a clear plasmon resonance around λ = 550 nm. Kelvin-probe force-microscopy (KPFM) [203] with a conductive AFM tip in non-contact mode was used to probe the local static potential difference between the tip and sample surface at room temperature (Fig. 5.2). While the illumination wavelength is gradually scanned through the plasmon resonance spectrum, from 480–650 nm (~1 nm s^{-1}), we probe the potential on the illuminated Au nanoparticle array (see Supplemental Section 5.6.2). A clear optically induced surface potential is observed, that varies with illumination wavelength (Fig. 5.2b). We observe negative induced potentials during excitation to the blue side of the neutral-particle plasmon resonance wavelength near 550 nm, and positive potentials during excitation on the red side of the resonance, with the measured potential changing sign near the peak of the plasmon resonance.

To model the experimentally observed plasmoelectric effect we consider a metal nanostructure placed on a grounded conducting substrate that is illuminated with monochromatic radiation at a wavelength just below the plasmon resonance λ_p. Random charge fluctuations between particle and substrate will cause the plasmon resonance spectrum to vary by minute amounts (Fig. 5.1). If an electron is randomly added to the particle, the resonance will blueshift, leading to a

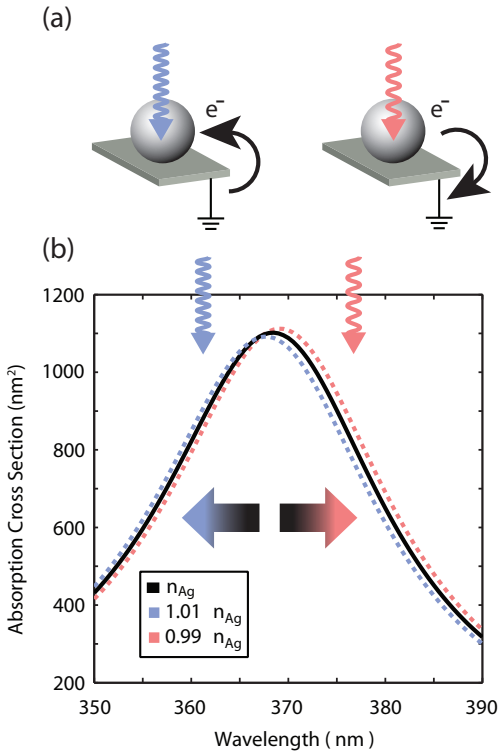

Figure 5.1: Absorption cross section spectrum of a Ag nanoparticle and the plasmoelectric effect. (a) Schematics: Spontaneous charge transfer to or from the nanoparticle is thermodynamically favored when the consequent spectral shift increases the absorption, raising the temperature. Irradiation on the blue side of the resonance leads to a negative charge on the particle, irradiation on the red side to a positive charge. (b) Calculated absorption cross section for a 20-nm-diameter Ag nanoparticle in vacuum with bulk carrier density n_{Ag} and carrier densities that are reduced or increased by 1%.

concomitant increase in light absorption of the particle, which in turn leads to a small increase in the nanoparticle temperature. The changes in number of electrons N and temperature $T(N)$ change the free energy F of the particle, and an equilibrium charge density is achieved when the free energy is minimum:

$$\frac{\partial F(N,T)}{\partial N} = \left(\frac{\partial F}{\partial N}\right)_T + \left(\frac{\partial F}{\partial T}\right)_N \frac{dT}{dN} = 0 \tag{5.1}$$

Here, we assume that both the intensity and wavelength of the illumination is constant. Using, by definition, $(\partial F/\partial N)_T \equiv \mu$, where μ is the electrochemical potential,

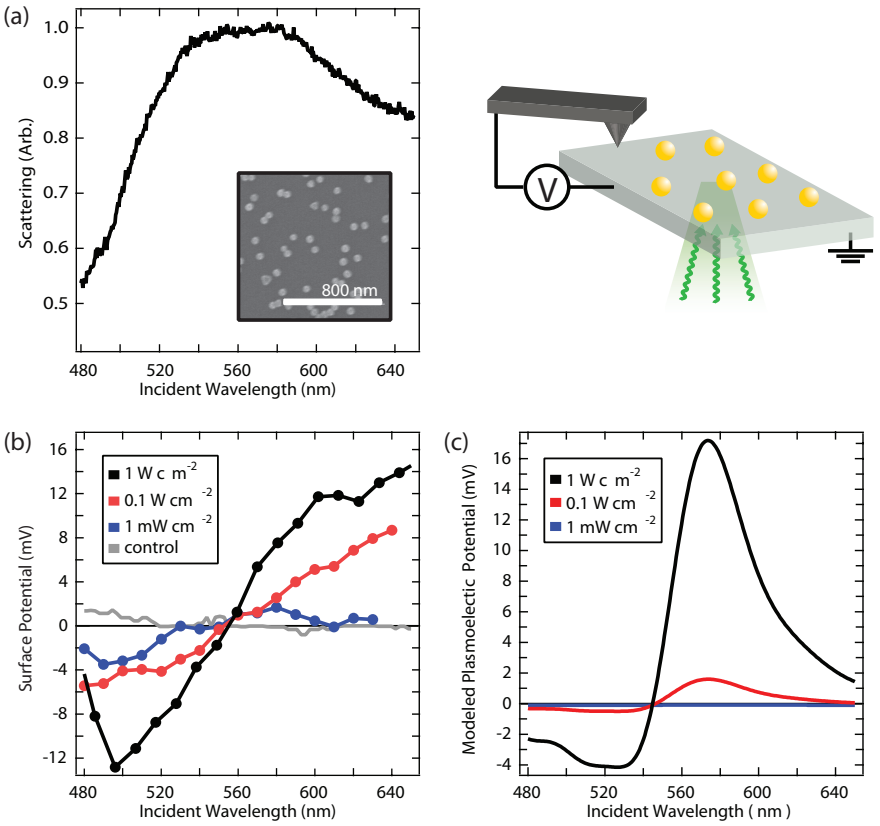

Figure 5.2: Plasmoelectric effect on dense Au nanoparticle arrays on ITO/glass. (a) Dark-field scattering spectrum of 60-nm-diameter Au nanoparticles on ITO/glass. The inset shows an SEM image of the nanoparticle array. (b) Kelvin probe force microscopy measurements of the surface potential as a function of illumination wavelength (15-nm-bandwidth) for three different illumination intensities. The surface potential of a flat region of ITO/glass adjacent to the nanoparticle array was monitored during scanned monochromatic illumination (see schematic geometry). A control measurement of an ITO/glass substrate without nanoparticles (1 W/cm^2) is also plotted (grey). (c) Modeled plasmoelectric potential for 60-nm-diameter Au nanoparticles on ITO/glass for the three illumination intensities in (b).

and $-(\partial F/\partial T)_N \equiv S$, where S is the entropy of the particle, we find:

$$\mu = S\frac{dT}{dN} \tag{5.2}$$

Equation 5.2 shows that under illumination the plasmonic particle adopts a electrochemical potential that is proportional to dT/dN. This quantity, which is only determined by the plasmon resonance spectrum and the heat flow from the particle

to the substrate, provides the unique thermodynamic driving force in this system. It favors charge transfer to or from the particle that increases absorption, and thereby temperature, in order to lower the free energy. The factor dT/dN is largest on the steepest parts of the resonance spectrum; it is positive for irradiation on the blue side of the resonance, leading to a positive chemical potential for the electrons, and hence a negative voltage; the reverse is observed for irradiation on the red side of the resonance. All these trends are exactly as observed in the experimental spectra of Fig. 5.2b: the surface potential vanishes at the peak of the resonance where dT/dN is zero; the largest (negative) potential is observed at a wavelength of 500 nm, coinciding with the steepest slope in the resonance spectrum of Fig. 5.2a.

Equation 5.1 can be used to quantitatively estimate the equilibrium plasmoelectric potential, writing $F(N,T)$ as the sum of the free energies of electrons and phonons, using the well-known free energy functions of an electron and phonon gas [42, 204, 205]. The electronic term is composed of a contribution due to the chemical potential of the electrons which is directly given by the Fermi function, and an electrostatic contribution due to charging of the metal nanosphere; the phonon term is given by the Debye model. Taking the derivatives to N and T we find analytical expressions for $\mu(N,T)$ and $S(N,T)$, that are then input in Eq.5.2 (see Chapter 6).

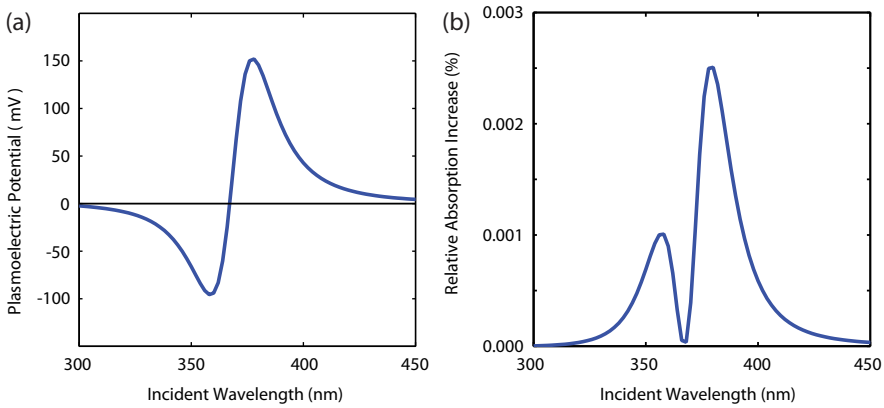

Figure 5.3: Modeled plasmoelectric response for Ag nanoparticles. A 20-nm-diameter Ag particle in vacuum is illuminated with monochromatic light (1 mW/cm^2). (a) Plasmoelectric potential and (b) relative absorption increase as a function of incident wavelength.

Before applying the model to the experimental geometry in Fig. 5.2 we calculate the plasmoelectric potential, i.e. the electrochemical potential gained by the particle from the electron transfer induced by optical absorption, for a spherical 20-nm-diameter Ag nanoparticle in vacuum under monochromatic illumination. For

these particles analytical Mie theory can be used to calculate the absorption cross section spectrum, $C_{abs}(\lambda, n)$, for a given electron density in the nanoparticle, by taking into account the dependence of the bulk plasma frequency, ω_p, in the complex dielectric function of the metal on carrier density, $\omega_p \propto n^{1/2}$ (see Supplemental Section 5.6.1). To calculate the nanoparticle temperature we use a steady-state heat-flow model in which heat is dissipated from the nanoparticle by radiation. Figure 5.3a shows the calculated plasmoelectric potential of the Ag nanoparticle as a function of illumination wavelength at an incident flux of 1 mW/cm^2, under which the particle obtains a maximum temperature of ~400 K (see Supplemental Section 5.6.3A). The model predicts a clear negative surface potential below the plasmon resonance and a positive one, up to 150 mV, above it. The asymmetry in the plasmoelectric potential below and above the resonance wavelength is due to the intrinsic non-resonant interband absorption in the metal. Figure 5.3b shows the corresponding relative absorption increase for the Ag nanoparticle, it ranges up to 2.5×10^{-5}.

The model for the simple geometry in Fig. 5.3 describes the key factors in the plasmoelectric effect: an increase in carrier density under illumination at wavelengths shorter than the resonance peak, inducing a negative plasmoelectric potential and enhanced absorption compared with the neutral particle. Similarly, radiation at longer wavelengths induces a lower carrier density, a positive plasmoelectric potential, and enhanced absorption. These results demonstrate that an excited plasmonic resonator behaves as a heat engine that can convert absorbed off-resonant optical power into a static electrochemical potential.

Next, we use the model to calculate the wavelength-dependent and power-dependent plasmoelectric potential for the experimental geometry in Fig. 5.2, a spherical 60-nm-diameter Au particle on an ITO/glass substrate. We calculated the factor dT/dN in Eq. 5.2 using finite-difference time-domain (FDTD) simulations [137] of the absorption spectra for an Au particle on an ITO/glass substrate to take into account radiative damping from the substrate not captured by simple Mie theory and a 1D model for heat conduction into the substrate (see Supplemental Sections 5.6.3–5.6.4 and 5.6.7). Due to variations in interparticle coupling and clustering (see SEM in Fig. 5.2a), and possible adsorption of water on the particle-ITO interface, the ensemble dielectric environment is complex. The broadened, red-shifted scattering spectrum in Fig. 5.2a is evidence for some particle aggregation. In the FDTD simulations we model these effects by assuming a background index of $n = 1.4$ for the medium above the ITO substrate, such that the absorption spectrum matches the experimentally observed spectrum. As can be seen in Fig. 5.2c for the high-power data, the modeled trends correspond well with the experimental trends: the modeled minimum potential occurs at 530 nm (experimental: 500 nm), the modeled zero potential at 545 nm (experimental: 560 nm), and a large positive potential is observed for wavelengths above the resonance, both in model and experiment. The extent of the measured potential to wavelengths up to 640 nm in Fig. 5.2b is in agreement with the long-wavelength tail in the spectrum of Fig. 5.2a. At 555 nm the modeled particle

temperature peaks at 308 K, 15 K above ambient (see Supplemental Section 5.6.3B), in good agreement with other experimental observations [27, 206].

To aid interpretation of our findings, we comment briefly on other mechanisms for generating photopotentials with metals. A thermoelectric effect is several orders of magnitude weaker ($\sim \mu V\ \Delta K^{-1}$) than the observed potentials [207]. Hot-carrier induced effects would require rectifying contacts which are not present in our geometry. Moreover, both these effects would not result in a bisignated signal [14]. "Plasmon drag" or similar direct photon-to-electron momentum transfer mechanisms on Au colloids would not produce a bisignated signal; nor for symmetric hole arrays under normal-incidence irradiation [208–210]. Future work will focus on obtaining further insight in the microscopic mechanisms that contribute to the observed effect.

5.3 Hole arrays in thin Au films

To demonstrate the generality of the observed plasmoelectric effect we measured the plasmoelectric potential on 10-micron-sized arrays of sub-wavelength holes in an optically thin Au film on a glass substrate. In these micro-arrays, light is absorbed by the resonant excitation of interacting surface plasmon polaritons that propagate between the holes on the Au-air and Au-glass interface [131, 211, 212] (see Supplemental Section 5.6.8). The absorption spectrum of a single array is determined by the coherent interaction of plasmons within the array, and the study of such arrays thus enables probing the plasmoelectric effect on a single absorber geometry. Moreover, the metal hole array architectures provide a first step towards future plasmoelectric integrated circuitry in which plasmoelectric power is harvested.

Figures 5.4a,b show a fabricated 10 × 10 μm hole array composed of 100-nm-diameter holes in a square array with a pitch of 200 nm, made in a 20-nm-thick Au film on a glass substrate. Figure 5.4c shows the measured absorption spectra of hole arrays with a pitch of 175–300 nm (see Supplemental Section 5.6.6). Increasing the pitch leads to a clear redshift in the absorption spectrum. Figure 5.4d shows the corresponding measured surface potential as a function of the wavelength of illumination (100 mW/cm^2), as measured with KPFM. A transition from negative to positive surface potential is seen for each array geometry. Also, the measured potential spectra show a clear redshift with increasing array pitch, in accordance with the trend in the absorption spectra. The maximum plasmoelectric potential observed for each measurement shows a gradually decreasing trend with increasing pitch, also in agreement with the trend in the absorption spectra. A slight difference is observed between the zero-crossing in the potential measurements and the peak in the corresponding absorption spectrum, which is attributed to the difference in numerical aperture (*NA*) of the microscope objective used for the two measurements (see Supplemental Section 5.6.9). All surface potential spectra show clear minima and maxima and then decrease as the wavelength is tuned further

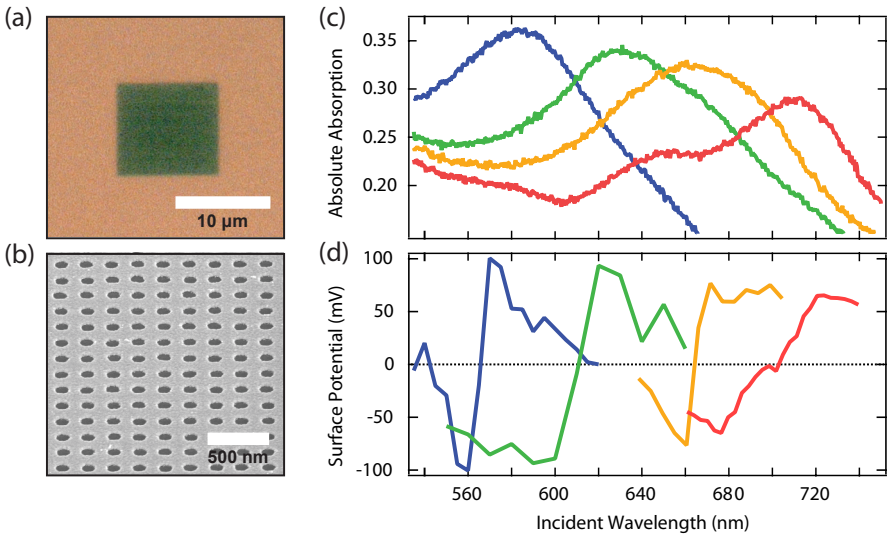

Figure 5.4: Plasmoelectric effect on Au nano-hole arrays on glass. (a) Bright-field optical microscope image showing a 200-nm-pitch array of 100-nm-diameter holes in a 20-nm-thick Au film on glass. The dark green color directly shows the strong absorption in the hole array. (b) SEM image of a 200-nm-pitch hole array imaged under 52 degrees with respect to the normal. (c) Measured optical absorption spectra for hole arrays with a pitch of 175 nm (blue), 225 nm (green), 250 nm (yellow) and 300 nm (red) (NA = 0.8). (d) Surface potential as a function of excitation wavelength measured using Kelvin force probe microscopy at 100 mW/cm^2 for the four hole arrays in (c) (NA = 0.25).

away from the resonance, as expected. The measurements in Fig. 5.4d show a plasmoelectric potential as large as ±100 mV and demonstrate the generality of the plasmoelectric effect for arbitrary plasmonic absorbers.

5.4 Conclusions

The observed plasmoelectric phenomenon takes advantage of the remarkable spectral tailorability of plasmonic nanostructures and can be extended to a variety of material systems, absorber geometries, and radiation environments. Plasmoelectric devices may enable development of entirely new types of all-metal optoelectronic devices that can convert light into electrical energy by replacing the usual function of doped semiconductors with metal nanostructures that are optically excited off-resonance.

5.5 Methods

Colloid materials and preparation
60-nm-diameter Au colloids (BBI International, EM.GC60 Batch #15269, OD1.2) were used for optical and electrical measurements. Samples for electrical characterization were prepared on indium tin oxide (ITO) coated glass substrates (SPI brand, 30–60 Ω, 06430, ITO layer thickness: 100 nm) that were first ultrasonicated overnight in a solution containing an equal volume of acetone, methanol, toluene, and isopropyl alcohol and then dried with N_2. Substrates were placed individually in glass scintillation vials (ITO-side up) with 600 μL Au colloid diluted by 1.2 mL of deionized (DI) water; for control samples, DI water was used instead of the Au colloid solution. Then 60 μL 0.1 M HCl was added, and the vials were immediately centrifuged at 2000 rpm (~670 g-force) for 40 minutes. After centrifuging, the solution had become clear and the ITO film had a noticeable red color due to Au nanoparticles deposited on the surface. Subsequently, the substrates were rinsed thoroughly with DI water and heated to 290°C by placing a heat gun 5 cm above the sample surface for 20 minutes. The scattering spectra of the deposited samples (as in Fig. 5.2a) were obtained using a Zeiss Axio Observer inverted microscope equipped with a 20× dark-field objective, with illumination from a halogen lamp.

Hole array fabrication
10 × 10 micron sized hole arrays in 20 nm thick Au, with 100 nm hole diameter and pitch in the range of 150–300 nm, were fabricated on 1-mm-thick glass using electron-beam lithography. A three-layer process was used to fabricate a shadow mask for Au evaporation. First, 240 nm PMMA 35k300 was spincast on a clean glass substrate, and baked at 180°C for 15 min. Next, 25 nm of Ge was thermally evaporated (0.5 Å/s) to make the substrate conductive and to protect the PMMA during further processing. Finally, 65 nm of hydrogen silsesquioxane (HSQ) negative tone resist (2 MIBK : 1 Fox 15 dilution) was spincoated and baked at 180°C for 2 min. Proximity-corrected square arrays of disks were written in the HSQ (20 kV, 7.5 μm aperture, 10.7 pA beam current) using area exposure with a dose of 200–500 μAs/cm^2 (depending on pitch). The HSQ was developed by submerging in MF-319 (Microposit developer) at 50°C for 60 s, followed by thorough rinsing with dH20. The disk patterns were transferred into the PMMA by subsequent anisotropic reactive-ion etching of the Ge (using SF_6 and O_2) and PMMA (using O_2). Next, 20 ± 2 nm of Au was thermally evaporated at 0.5 Å/s. Finally, lift-off was performed by dissolving the PMMA in acetone at 50°C for 3 hours, followed by 10 min of megasonification and 1 min of ultrasonification, both in acetone.

Hole array optical characterization
Transmission and reflection spectra of the hole arrays were measured using a WiTec-αSR optical microscope. A fiber-coupled white light source (Ando AQ-4303B) in combination with a 9 μm-core fiber was used to illuminate the hole arrays through a 60× objective (Nikon, *NA* = 0.8, WD = 0.3 mm), resulting in a

3–4 μm diameter spot (unpolarized). The transmission was collected by a 50× objective (Nikon, CFI L-Plan EPI CR, *NA* = 0.7, WD = 3 mm corrected for substrate thickness). Both the transmitted and reflected light was coupled into a 100-μm-core collection fiber and analyzed by a spectrograph (Acton 300i) and Si CCD, which was cooled to −45°C (Roper Scientific, model 7344-0001). Each spectrum is an average of 100 frames with 250 ms accumulation time each.

5.6 Supplementary information

5.6.1 Complex dielectric function of Ag and Au

To calculate the absorption cross section spectra of a Ag nanoparticle (Fig. 5.1), we apply a 6th-order, multiple oscillator Lorenz-Drude model of the complex dielectric function of silver, fit to data from Palik [138]. For the dielectric function of Au we use a Brendel-Bormann Gaussian oscillator model. We use the method outlined by Rakic and coworkers [213]. These dielectric functions accurately reproduce the observed extinction spectra of spherical silver or gold nanoparticles when input into the exact analytic solutions to Maxwell's equations provided by Mie theory [113]. To introduce the explicit dependence on electron density, n, we assume that all terms in the dielectric function that depend on the bulk plasma frequency, ω_p^* , depend on electron density, n, according to a simple Drude model relation,

$$\omega_p^* = \left(\frac{ne^2}{\varepsilon_0 m_e^*} \right)^{1/2} \tag{5.3}$$

where e is the electron charge, ε_0 is the permittivity of free space, and m_e^* is the electron effective mass [214]. This strategy is consistent with other work that examined carrier density-dependent plasmon shifts, for example in doped semiconductors, electrochemical cells, or at metal surfaces during ultrafast pump-probe measurements [194, 215–217]. Figure 5.5 shows the calculated relative change of the absorption cross section of a 20-nm-diameter Ag nanoparticle in vacuum, as a function of wavelength and electron density, n, compared with the absorption cross section for a neutral Ag silver particle with electron density n_{Ag}.

5.6.2 Kelvin-probe force-microscopy (KPFM) of Au colloids on ITO/glass and Au hole arrays

For KPFM characterization of colloid particles on ITO/glass, the sample was measured at the limit of highest possible particle coverage, and it was anticipated that the measured region of ITO/glass adjacent to the Au particles was equipotential with the particles. Direct illumination of the AFM tip was avoided, and there was no dependence of the magnitude of signal based on the distance from the optical spot, within ~10's of μm. A control measurement of ITO/glass free of Au colloids is shown in Fig. 5.6 and shows no detectable wavelength-dependent signal. The absolute

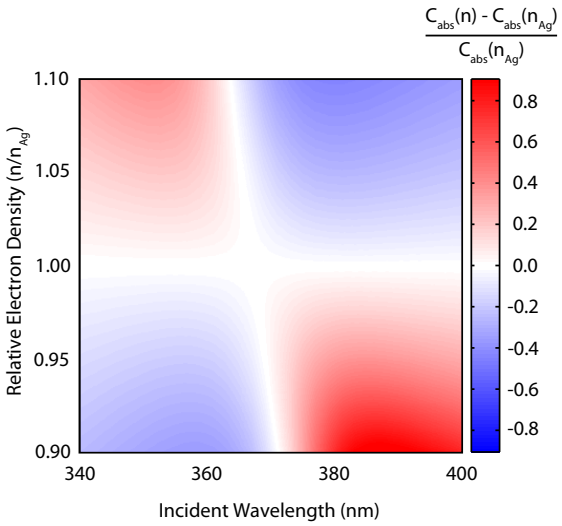

Figure 5.5: Relative change of the absorption cross section, $C_{abs}(n,\lambda)$, (color scale) of a 20-nm-diameter Ag nanoparticle in vacuum, as a function of wavelength and electron density, n, compared with the absorption cross section for a neutral Ag silver particle with electron density n_{Ag}.

surface potential determined by the KPFM technique is always a convolution of the work function difference between the sample and a particular tip, and factors relating to the tip-sample geometry that define capacitance. Therefore, to emphasize wavelength-dependent changes of potential, the reported data (Fig. 5.2b) are plotted relative to the surface potential in the same spot measured in the dark before optical excitation.

For KPFM measurements of hole arrays, an optical spot encompassing the entire array was incident directly beneath the AFM tip. The plotted data (Fig. 5.4d) are the average response of the entire 10 × 10 μm array integrated over ~20 min with a single wavelength incident. This procedure allowed the sample to stabilize from any drift during the course of the measurement, and, by measuring a structure much larger than the tip, maximized the accuracy of the KPFM technique [218]. Because the tip was illuminated, even control measurements of smooth Au films detected uniform changes in the KPFM signal based on whether the tip was illuminated or in the dark. This signal results from optical heating of the tip, while other contributions to the measured potential, such as photo-carrier generation in the tip, may also be manifest. The magnitude of the light vs. dark response, though independent of incident wavelength, was dependent on the incident power as well as the particular tip used. Therefore we could not employ the same simple subtraction procedure used to offset the data during the colloid measurements on ITO, as described above.

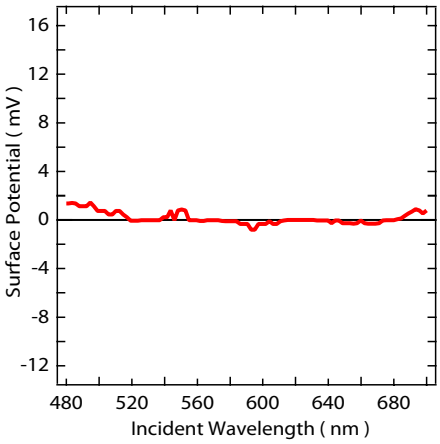

Figure 5.6: KPFM-measured surface potential from a control experiment of bare ITO/glass under 1 W/cm^2 scanned monochromatic illumination, plotted on the same scale as Fig. 5.2b.

However, relative changes in the surface potential of the hole arrays that were dependent on the wavelength of illumination were stable and reproducible, and were independent of the tip employed or the tip distance from the sample, over a range of tip distances spanning ~1 to 100 nm. For this reason, the curves from different arrays in Fig. 5.3d are plotted to emphasize the comparison between wavelength-dependent changes, with zero set by the mid-point of the maximum and minimum surface potential measured from that array.

5.6.3 Temperature calculations

(A) Ag nanoparticle in vacuum

To calculate the plasmoelectric potential for a Ag nanoparticle in vacuum we calculate the temperature of the nanoparticle, T, given the absorption cross section $C_{abs}(n,\lambda)$ from section 5.6.1 and incident power density. Under steady state illumination, the power absorbed by the particle must equal the power going out:

$$P_{in} = P_{out} \tag{5.4}$$

P_{in} constitutes the absorbed monochromatic optical radiation plus the absorbed thermal radiation from the ambient background (at T_{amb} = 293 K).

$$P_{in} = C_{abs}(N,\lambda) I_{\lambda} + \sigma A \varepsilon T_{amb}^4 \tag{5.5}$$

Here, σ is the Stefan Boltzmann constant, A is the surface area of the nanoparticle, and ε is the emissivity. The nanoparticle emissivity ε = 0.01 was experimentally determined using FTIR absorption spectroscopy on gold colloids, assuming

reciprocity of the absorption and emission in the 2–5 μm wavelength range of the measurement. This value is close to that of bulk gold and silver in the infrared, as reported elsewhere [27] and predicted by Mie theory. For Ag nanoparticles in vacuum the only loss channel for the power is thermal radiation, defining

$$P_{out} = \sigma A \varepsilon T^4 \tag{5.6}$$

Solving Eq. 5.4 for the temperature of the particle then gives

$$T(N,\lambda) = \left(\frac{C_{abs}(N,\lambda) I_\lambda + \sigma A \varepsilon T_{amb}^4}{\sigma A \varepsilon} \right)^{1/4} \tag{5.7}$$

Figure 5.7 shows the calculated temperature for a 20-nm-diameter Ag nanoparticle in vacuum as a function of illumination wavelength for an incident power densities of 1 mW/cm^2; it peaks at 400 K. The calculated temperature and its dependence on N, $dT(N)/dN$ (for a given λ and I_λ) are then used as input in solving Eq. 5.2 for the case of a Ag nanoparticle in vacuum (see Chapter 6).

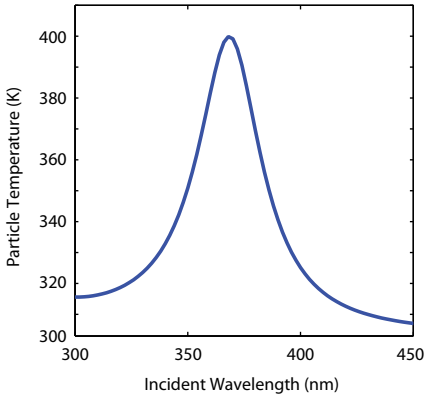

Figure 5.7: Calculated temperature for a 20-nm-diameter Ag particle in vacuum as a function of illumination wavelength (1 mW/cm^2).

(B) Au nanoparticles on ITO

To calculate the temperature of Au nanoparticles on ITO/glass we first calculate the absorption cross section spectrum $C_{abs}(n,\lambda)$ using finite-difference-time-domain (FDTD) full wave electromagnetic simulations. In the experiment, the exact dielectric surrounding of the nanoparticle is very complex. As shown in Fig. 5.2a, there are large variations in inter-particle spacing as well as clusters with different configurations, both inducing near-field coupling and thereby red-shifted resonance wavelengths. Furthermore, the KPFM experiments were performed in ambient conditions, such that adsorption of water to the particle-ITO interface is likely. Since the

exact influence of such conditions on the plasmoelectric potential is beyond the scope of this paper, we simplified the geometry to a single 60 nm Au nanoparticle on an ITO substrate. We assumed a uniform background index of $n = 1.4$ to take into account the red-shift due to the dielectric surrounding described above, such that the modeled scattering spectrum represented the measured scattering spectrum. We then calculate the steady-state power balance to obtain the nanoparticle temperature. Heat flow into the substrate is modeled using a 1D heat transfer model, as sketched in Fig. 5.8, with the particle on a glass substrate with thickness $d = 1$ mm covered by a thin layer of ITO. We use the thermal heat conductivity for glass of $\sigma_T = 1.05$ $\mathrm{Wm^{-1}K^{-1}}$ [219]. The heat of the particle can be transferred from the particle (at T_{part}) through a cylinder of glass with cross sectional area equal to the contact area $A_{contact}$ between the glass and the particle, to the bottom of the substrate (at ambient temperature, $T_{amb} = 293$ K). The heat flow is given by [219]

$$P_{diff} = \sigma_T \frac{T_{part} - T_{amb}}{d} A_{contact} \tag{5.8}$$

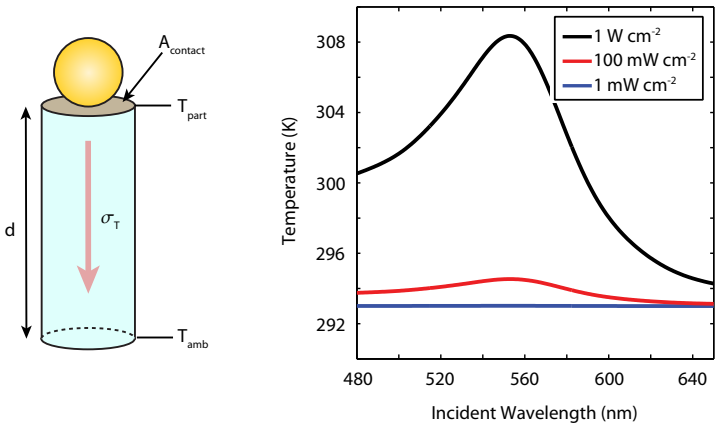

Figure 5.8: (Left) Sketch of 1D heat diffusion model for a Au nanoparticle on ITO/glass. (Right) Au nanoparticle temperature as a function of illumination wavelength, corresponding to the experiments in Fig. 5.2b.

Figure 5.8 shows the calculated temperature of the Au nanoparticle as a function of incident wavelength for the three different intensities used in Fig. 5.2b. In these calculations the parameter $A_{contact}$ is tuned such that the calculations of the surface potential (see Section 5.6.4) best match the experimentally observed surface potential for the largest power densities. The best fit for the contact area is 2.5 times the geometrical particle cross section, a reasonable value given the simple heat flow model. The same contact area is then used for the lower power densities to calculate the temperature profiles in Fig. 5.8 and the surface potentials

in Fig. 5.2c. We find the same power-dependent trend for slightly more complicated 2D and 3D heat diffusion models, with the assumed contact area between the particle and ITO dominating the magnitude of the temperature. The maximum temperature calculated in Fig. 5.8 amounts to 308 K, 15 degrees above ambient temperature, which is a reasonable temperature to sustain for an Au nanoparticle on a substrate. Note that the increase of temperature due to the plasmoelectric effect compared with a neutral particle is only of order of up to 10s of mK, depending on geometry and illumination intensity. The calculated temperature and its dependence on N, $dT(N)/dN$ (for a given λ and I_λ) are used as input in solving Eq. 5.2 for the case of Au nanoparticles on ITO/glass (see Section 5.6.4).

5.6.4 Calculation of steady-state nanoparticle surface potential and charge

Using the temperature and values for $dT(N)/dN$ described in 5.6.3 we solve Eq. 5.2 to determine the steady-state surface potential and corresponding charge on the nanoparticle as a function of irradiation wavelength (see Chapter 6 for details to solve Eq. 5.2). Figure 5.9 shows the calculated charge density $N - N_0$ for Au nanoparticles on ITO/glass, for the highest experimental power density of Fig. 5.2b (I_λ = 1000 mW/cm^2). The calculations use 6.67×10^6 Au atoms for a 60-nm-Au sphere.

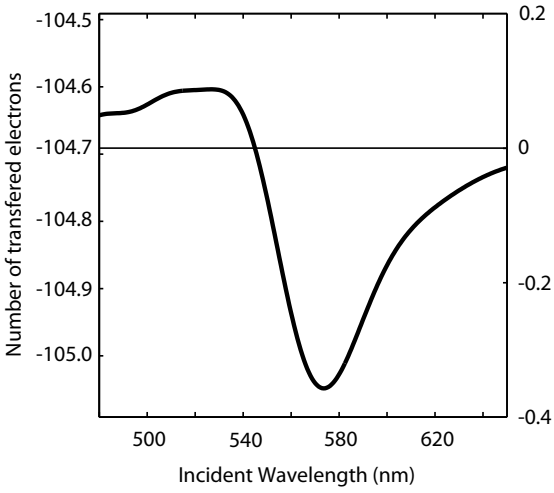

Figure 5.9: Calculated excess electron number $N - N_0$ (left-hand scale) for a 60-nm-diameter Au particle on ITO/glass as a function of illumination wavelength (1000 mW/cm^2). The average number of electrons generating the plasmoelectric effect is shown by the right-hand scale.

As can be seen, the excess electron number $N - N_0$ is modulated around a value of $N - N_0 = -104.69$ electrons, observed at the peak of the resonance (no plasmoelectric effect, $dN/dT = 0$). This corresponds to the number of electrons for which the total electrostatic charging energy equals the Fermi energy for Au $\epsilon_F = 5.02$ eV. In the dark, the offset between the Fermi level of the particle and the substrate will induce a compensating electrostatic charge on the particle, which is the usual condition for electrochemical equilibration between two dissimilar conductors. Note that the presence of the ITO substrate can be easily accounted for by subtracting the Fermi energy of the ITO substrate, such that the offset observed in Fig. 5.9 is in fact the difference in Fermi energy between the particle and the ITO. Correcting for this "dark charge" (right-hand scale in Fig. 5.9) we see that in the time-averaged situation, less than one electron on average is added or removed from the nanoparticle to generate the observed plasmoelectric potential. The data in Fig. 5.9 can be converted to surface potential, as shown in Fig. 5.2c. Additionally, we note that the thermoelectric effect (omitted in our analysis) induces only a minor contribution to the potential state of the particle, even for large temperature gradients between the substrate and particle, because of the small Seebeck coefficient of metals, $\sim\mu$V/ΔK [207].

5.6.5 Charge accumulation shell model

The calculations described above assume that any additional charge carriers that are transferred to the particle are uniformly distributed throughout the nanoparticle. However, electrostatic models require that any surplus charges reside on the surface of a metal object (less than 1 nm thickness), since no static electric fields can exist inside the metal [220]. On the other hand, the surface plasmon resonance is a dynamic phenomenon, with electromagnetic fields that penetrate into the metal as defined by the electromagnetic skin-depth, which is ~3–10 nm for Ag and Au at optical frequencies, and an electron mean free path that is larger than the Fermi screening length. Additionally, the plasmon resonance frequency is predominately determined by the electron density of the very outer layer within the optical skin depth of the metal, as reported experimentally [221] and verified by us using FDTD simulations. Therefore, electrostatic arguments suggest that any additional charges will reside near the surface of the nanoparticle, and electrodynamic arguments suggest that only the electron density near the outer surface needs to be increased in order to blue-shift the plasmon resonance. If excess charge resides only near the surface, the plasmoelectric effect thus requires a smaller number of electrons to obtain the same frequency shift, and thereby $dT(N)/dN$ in Eq. 5.2 is larger.

To study the influence of non-uniform distributions of charge density in the particle, we consider a simplified shell model, in which we assume that all the additional charge carriers transferred due to the plasmoelectric effect reside in the outer shell with thickness δ (see inset of Fig. 5.10). To implement the shell in the calculations, one has to express the Fermi energy, temperature, and N and V in

terms of the number of electrons in the shell and the shell volume rather than the whole particle. Eq. 5.2 can then be solved for the number of electrons in the shell, assuming a certain shell thickness.

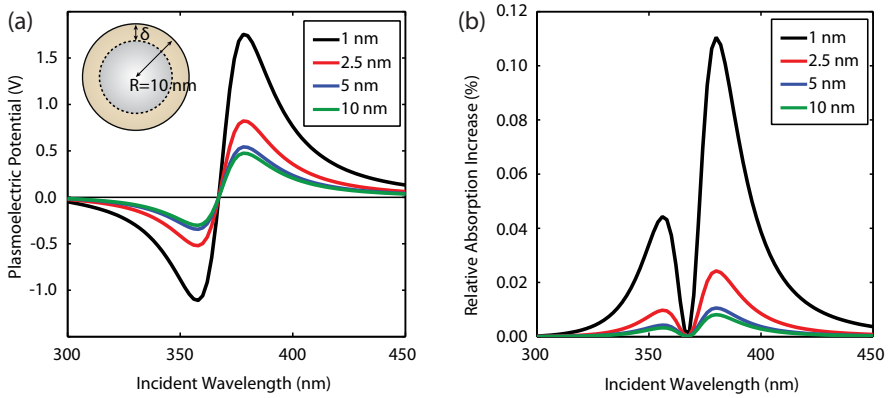

Figure 5.10: Calculated induced potential (a) and relative increase in absorption compared with a neutral particle (b) for a 20-nm-diameter Ag nanoparticle in vacuum as a function of illumination wavelength for shell thicknesses of 1.0, 2.5, 5.0 and 10 nm (black, red, blue and green trace respectively). The illumination power density is 10 mW/cm^2.

Figure 5.10 shows the plasmoelectric potential (a) and the relative increase in absorption (b) for a 20-nm-diameter Ag particle in vacuum, as a function of illumination wavelength (10 mW/cm^2), for different shell thicknesses. Figures 5.10a,b clearly show the effect of a thinner shell: the transferred electrons induce a relatively larger increase in electron density and thereby a larger increase in absorption (Fig. 5.10b). Note that for shell thicknesses larger than 1 nm, the magnitude of the potential rapidly converges to that obtained with uniform charge distribution (δ = 10 nm, green curves). Uniform charge distribution is assumed for calculations throughout this manuscript. Further arguments for assuming a uniform distribution of charge include the fact that the area under the absorption spectrum of a dipolar plasmon mode should only scale with the total number of valence electrons in the metal, irrespective of their location inside the particle.

5.6.6 Transmission and reflection experiments on hole arrays

The absorption spectra for the hole arrays in Au in Fig. 5.4 are derived from transmission and reflection spectra measured in an optical microscope. Light from a broadband light source (Ando AQ-4303B) was focused onto the 10×10 μm hole arrays to a ~4 μm diameter spot using a 0.8 *NA* microscope objective. Transmitted and reflected light intensities were recorded using a fiber-coupled spectrometer equipped with a Si CCD array detector. To calibrate the measured transmitted

and reflected intensity spectra, the transmission spectrum was measured for a bare region of the gold film, next to the hole arrays, and normalized this to the measured transmission of bare glass. Figure 5.11a shows the resulting transmission spectrum for the bare Au film (dark blue). For comparison, the transmission obtained from Fresnel calculations of a air-Au-glass layer system (light blue) is shown, assuming a Au layer thickness of 18 nm and optical constants from Johnson and Christy [222]. The calculated transmission was multiplied by a factor 0.96 to correct for the 4% reflection on the bottom interface in the experimental geometry. Figure 5.11a shows very good agreement between the measured and calculated spectra which provides further confidence in the normalization procedure for the transmission measurements.

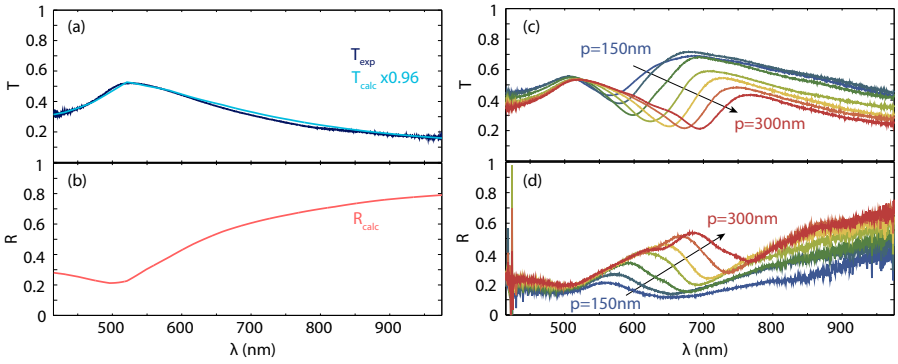

Figure 5.11: (a) Measured (dark blue) and calculated (light blue) transmission spectrum for a 18 nm thick bare Au film on glass. (b) Calculated reflection spectrum for the same geometry. Measured transmission (c) and reflection spectra (d) of square arrays of 100 nm diameter holes in a Au film with pitch ranging from 150–300 nm, in 25 nm steps (blue to red).

Reflection measurements were normalized using the calculated reflection spectrum for the bare gold film, which is shown in Figure 5.11b, as a reference. This procedure does not take into account the small reflection from the bottom interface of the glass substrate. Therefore, derived reflectivities are slightly overestimated. The accuracy of all derived transmittance and reflectance spectra is within 5%.

Figures 5.11c,d show measured transmission and reflection spectra for all hole arrays, with pitch ranging from 150 nm to 300 nm in steps of 25 nm. A clear dip is observed both in transmission and reflection spectra resulting from the resonant absorption in the hole array. The dips show a clear red shift with increasing pitch, as expected. The wavelength of the dip in transmission is significantly blue shifted with respect to the dip in reflection, which is due to interference between directly transmitted light and forward scattered light (Fano-effect) [135].

The absorption spectra for the hole arrays in Fig. 5.4c were calculated from the measured spectra as $Abs = 1 - R - T$. This analysis slightly overestimates the actual

absorption, as it neglects the small amount of light scattered in angles beyond the *NA* of the collection aperture. However, this fraction will be small, since no diffraction orders can occur in the visible spectral range for the used array pitch.

5.6.7 FDTD simulation details

We performed full wave modeling using Lumerical finite-difference time-domain (FDTD) [137] simulations to determine the scattering and absorption spectra for Au particles on ITO and to simulate the transmission and reflection spectra for Au hole arrays. Optical constants for Au are as described in 5.6.1, taken from Johnson and Christy [222] for Fig. 5.11, and using the Brendel and Bormann model [213] for all other calculations. For ITO they were taken from spectroscopic ellipsometry measurements of sputtered ITO films.

For simulations of Au colloids on ITO, we modeled a 60-nm-diameter Au sphere on top of an ITO slab and a background index of n = 1.4 (see Section 5.6.3B). The simulations employed perfectly matching layer (PML) boundary conditions on all boundaries. We used a Total-Field Scattered-Field (TFSF) source to launch and extinguish broadband plane waves (λ = 460–650 nm). The scattering and transmission due to the sphere were recorded and used to calculate the absorption and extinction spectra.

For the hole array geometry, we modeled a 20-nm-thin Au film on top of a glass substrate (index n = 1.46), and applied PML boundary conditions at the top and bottom interfaces of the simulation box to mimic semi-infinite media for both the glass substrate and air. A 100-nm-diameter hole is positioned in the center of the simulation box. The lateral size of the box is set equal to the desired pitch, and periodic boundary conditions are used to simulate an infinite array. A broad-band (λ = 400–900 nm) plane wave is launched from the top. Power monitors above the source and 50 nm below the Au-SiO_2 interface are used to monitor the reflection and transmission respectively. Since the gold is the only absorbing material in the simulation box, the absorption of the hole array is calculated as $1-R-T$. The mesh size is set to 10 nm, with a 1.0–2.5 nm refinement mesh around the hole.

5.6.8 Mechanism of resonant absorption in hole arrays

Resonant absorption of light in the hole arrays results from the diffractive coupling of incident light to surface plasmon polaritons (SPP) propagating at the metal-dielectric interface [211, 212]. For the thin (18 nm) Au films used, SPPs on the Au-air and the Au-glass interface are strongly coupled [223], giving rise to symmetric and anti-symmetric insulator-metal-insulator (IMI) SPP modes. Figure 5.12a shows the calculated mode profile of the in-plane magnetic field component of the anti-symmetric mode for the glass-Au-air layer geometry at a free-space wavelength λ = 600 nm. In the calculations, optical constants for Au were taken from the Brendel and Bormann model [213], which show good correspondence with data from Johnson and Christy [222]. The index of glass was taken as n = 1.46. The dispersion

for the anti-symmetric IMI SPP is shown in Fig. 5.12b. For comparison, the light line in air and the dispersion of single-interface SPPs on a semi-infinite Au substrate are also shown. As can be seen, the strong coupling of SPPs across the Au films leads to large wave vectors compared to the free-space or single-interface SPPs.

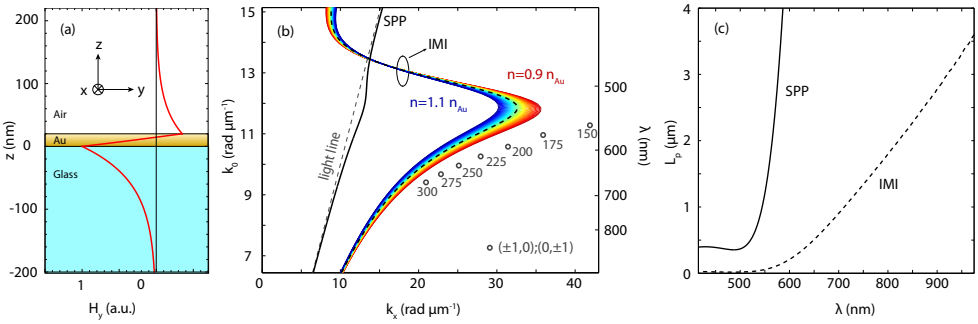

Figure 5.12: (a) Field profile (in-plane magnetic field component) of the anti-symmetric IMI mode for a glass-Au-air layer geometry at a free-space wavelength λ = 600 nm. (b) Calculated dispersion for the anti-symmetric IMI SPP (black dashed line), and the SPP for a semi-infinite Au substrate (black solid line). Also shown is the light line in air (gray dashed). The colored lines show the calculated IMI dispersion curves for modified electron densities n in Au, ranging between 0.9–1.1 times the bulk density (red-blue). Also shown are the wavelengths of the peaks in the absorption spectra obtained from FDTD simulations plotted against wave vectors corresponding to (±1,0) and (0,±1) grating orders (open dots). The numbers next to the dots refer to the pitch (in nm) of the arrays for which these numbers were determined. (c) SPP intensity propagation length of the IMI (dashed line) SPP and of the SPP mode on a semi-infinite substrate (solid line).

Figure 5.12c shows the propagation length of the IMI SPP as a function of wavelength. Data for a semi-infinite Au substrate are also shown. Clearly, the IMI mode has a strongly reduced propagation length due to the strong absorption in the metal [223], the latter obviously a desired feature to achieve a strong plasmoelectric effect.

Incident light can couple to the IMI SPPs through diffractive coupling via (±1,0), (0,±1), (±1, ±1) and higher order grating orders. To investigate which coupling order is dominant we performed FDTD simulations of the absorption in hole arrays (225 nm pitch) for angles of incidence $\theta = 0°$ and $\theta = 25°$ in a plane along the (0,1)-axis of the array, for polarization angles ξ ranging from 0° (p-polarized) to 90° (s-polarized, see Fig. 5.13a). Figure 5.13b shows that we find identical absorption spectra for the two angles of incidence (θ) for s-polarized light, whereas the spectra for p-polarized light differ significantly. From this we conclude that the in-plane component $k_0 \sin(\theta)$ of the incoming wave vector is orthogonal to k_{IMI}, which implies the incident light couples to the (0,±1) and (±1,0) orders.

The peak resonance wavelengths λ_{res} for the absorption spectra simulated by FDTD for different array pitch Λ are plotted in Fig. 5.12b as $2\pi/\lambda_{res}$, with the x-

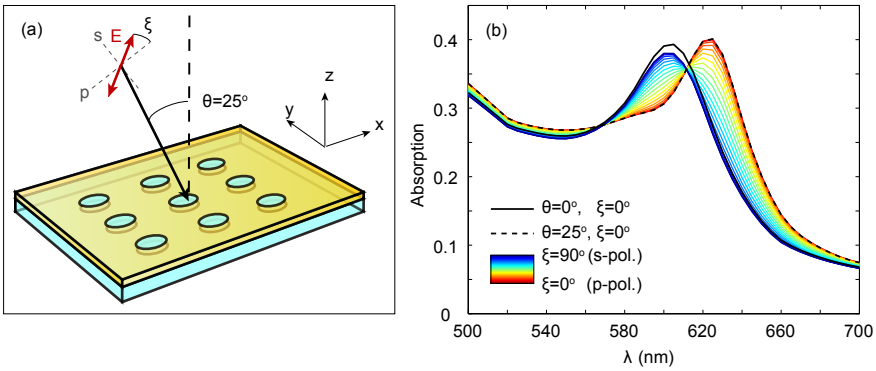

Figure 5.13: (a) Sketch indicating the angle of incidence $\theta = 25°$ in the plane along the (0,1)-axis of the hole array. Light is polarized with an angle ξ with respect to the plane of reflection. (b) Simulated absorption in the hole array (225 nm pitch) for $\theta = 0°$ (degenerate in ξ) and $\theta = 25°$ with $\xi = 0$–$90°$ (red through blue).

coordinate given by $2\pi/\Lambda$, corresponding to coupling through (±1,0) and (0,±1) orders (open circles). The data points lie quite close to the calculated dispersion curves indicating that absorption of incident light occurs through the (±1,0) and (0,±1) orders, with good agreement observed for the wavelength at which the experiments were done ($\lambda = 600$–700 nm, $k_0 \sim 10\ \mu m^{-1}$). Note that the large discrepancy for 150–175 nm pitch can be attributed to a second branch of the dispersion curve as described in refs. [224–226], a detailed discussion of which goes beyond the scope of this paper [225, 226].

The dispersion data in Fig. 5.12b provide guidelines for the design of the array pitch in order to achieve efficient diffractive coupling from the normal-incident light beam to the in-plane IMI SPPs for a given incident wavelength. Due to the strong dispersion, the array pitches required to couple to the IMI SPP are much smaller than the free-space wavelength (e.g. 200 nm at $\lambda = 600$ nm) [212].

Next, we calculated the effect of a variation of the electron density in the Au film on the IMI SPP dispersion. Variations in carrier density n were included in the optical constants for Au as described in Section 5.6.1. Figure 5.12b shows the dispersion curves for electron densities in the range of $n = 0.9 \times n_{Au}$ (red) to $n = 1.1 \times n_{Au}$ (blue). A decrease in electron density redshifts the dispersion curve, analogous to what is observed for the localized resonances in the colloidal nanoparticles. In the spectral range where the resonant absorption occurs, a 1% change in electron density gives rise to a spectral shift of ~1.5 nm. This matches well with the spectral shift observed in the FDTD simulated absorption spectra for the different electron densities (not shown here). It is this dependence of the dispersion on the electron density, that in turn modifies the absorption efficiency, that is the driving mechanism for the plasmoelectric effect in the hole arrays.

Note that the absorption mechanism described here is very similar to the phenomenon of extraordinary transmission (EOT) in sub-wavelength hole arrays in optically thick films [131, 211], the only difference being that for EOT the SPPs on the air-Au and glass-Au interface do not couple, such that the SPP absorption losses are minimized rather than maximized, as is desired for the plasmoelectric effect [223].

5.6.9 Spectral broadening and red shift in measured spectra

Figure 5.4d shows that the wavelength of the zero-crossing in the KPFM spectrum is slightly blue shifted with respect to the measured absorption maximum in Fig. 5.4c. This blueshift is more pronounced for hole arrays of smaller pitch. Based on the absorption mechanism described above, this discrepancy can readily be explained by the difference in numerical aperture (*NA*) of the objectives used for the two measurements. Transmission and reflection experiments were made using an $NA = 0.8$, corresponding to a wide range of angles of incidence up to 53°. This gives rise to a large spread in the in-plane component of the wave vector of the incoming light, which translates into a large spread in spectral position along the dispersion curve. KPFM measurements were made using a lens with $NA = 0.25$, giving rise to much sharper absorption peaks.

To quantify the effect of angular spread on the absorption spectra we performed FDTD simulations for a hole array (225 nm pitch), for different angles of incidence. Single-wavelength simulations were performed in the spectral range of λ = 500–700 nm, in steps of 5 nm. A plane-wave source was launched with an angle of incidence θ, p-polarized along one of the axis of the hole array. Bloch boundary conditions were used in the lateral direction of propagation.

Figure 5.14a shows the simulated absorption for $0° \leq \theta \leq 14°$ (blue to red), corresponding to the angles of incidence for $NA = 0.25$ for the KPFM measurement. Also shown is the calculated absorption spectrum for normal incidence (solid black line) and the absorption averaged over all angles (dashed black line). Figure 5.14a shows only a small effect of angular spread for the $NA = 0.25$ lens. Figure 5.14b shows the absorption spectra for an angular range ($0° \leq \theta \leq 53°$) corresponding to the $NA = 0.8$ objective used in the transmission and reflection experiments. A pronounced redshift is observed for larger angles of incidence. Figures 5.14a,b also show the angle-averaged absorption spectrum, for the $NA = 0.8$ geometry it shows a strong red shift compared to the absorption for normal incidence, as well as significant spectral broadening. The observation of a red shifts indicates light couple to the (-1,0)-order, consistent with what was observed by Braun et al. in absorption measurements on Au hole arrays [223]. Note that to calculate a properly angle-weighted absorption spectrum the intensity profile on the back focal plane of the objective, and the transfer function of the objective must be taken into account. Nonetheless, the data in Fig. 5.14 explain that the resonant absorption manifest in the KPFM signal in Fig. 5.4d is blue shifted and spectrally narrower compared with the measured absorption spectra in Fig. 5.4c. Finally, we note that for unpolarized

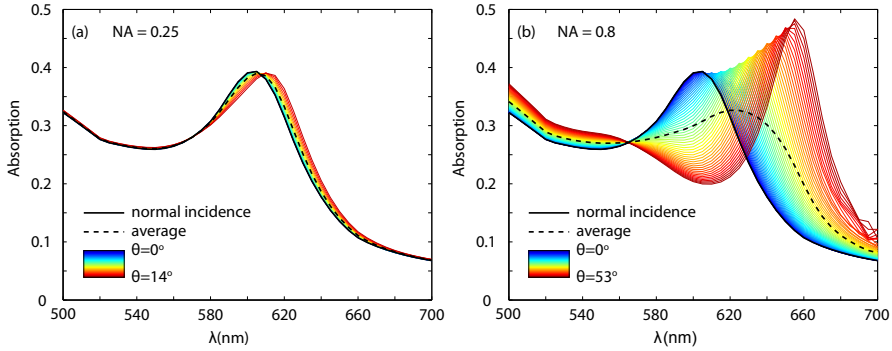

Figure 5.14: Absorption spectra for a 225 nm pitched array, illuminated at different angles of incidence (colors) corresponding to the angles within the range of a *NA* = 0.25 (a, used for KPFM measurements) and *NA* = 0.8 (b, used for transmission and reflection experiments). A clear red-shift is observed for larger angles of incidence. The spectrum for normal incidence (solid black) and the average over all angles (dashed black) are also shown, clearly showing the effective redshift and broadening for the larger *NA*.

light, variations in incident angle will lead to a further broadening of the absorption spectrum due to the different coupling conditions for different polarizations at different incident angles (see Fig. 5.13).

6

Theory of the plasmoelectric effect

Resonant metal nanostructures exhibit an optically induced electrostatic potential when illuminated with monochromatic light under off-resonant conditions. This plasmoelectric effect is thermodynamically driven by the increase in entropy that occurs when the plasmonic structure aligns its resonant absorption spectrum with incident illumination by varying charge density. Here, we study in detail the thermodynamic theory underlying the plasmoelectric effect by analyzing a simplified model system consisting of a single silver nanoparticle. We find that surface potentials as large as 473 *mV are induced under* 100 W/m^2 *monochromatic illumination, as a result of a* 11 *mK increases in the steady-state temperature of the nanoparticle. Furthermore, we discuss the applicability of this analysis for realistic experimental geometries, and show that this effect is generic for optical structures in which the resonance is linked to the charge density.*

6.1 Introduction

Surface plasmons are collective oscillations of charge density in metal nanostructures during optical excitation. Recently, there has been significant interest in the relationship between plasmonic and electrical phenomena [14, 115, 227–233]. For

example, localized plasmon resonances have been shown to influence the photoconductivity of films of metal nanoparticles coated with self-assembled monolayers [234, 235], and plasmon-induced hot electrons have been shown to generate macroscopic currents in plasmonic energy conversion devices [228]. Furthermore, it has been demonstrated that electrostatic charging influences the plasmon resonance frequency [233]. The plasmon resonance frequency of metal nanoparticles is determined by geometry, dielectric surrounding and material properties [3]. In the visible spectral range the dielectric function of the metal can often be well described by a Drude model. In this model the plasmon resonance frequency depends on electron density, n_e, via the bulk plasma frequency ω_p [216, 236]:

$$\omega_{plasmon} \propto \omega_p = \sqrt{\frac{n_e e^2}{m^\star \varepsilon_0}}. \tag{6.1}$$

Here, e is the electron charge, $m^\star$ is the effective electron mass [214], and ε_0 is the free-space permittivity. Equation 6.1 shows that the plasmon resonance frequency is directly linked to the electron density n_e, and thus may be tuned by varying n_e. Indeed, recent experiments have demonstrated spectral shifts up to 43 nm in the plasmon scattering spectrum of Au nanoparticles by adding chemical reductants to the nanoparticle solution that induce a negative charge at the surface of the particles [236]. Also, spectral shifts up to 11 nm have been demonstrated using electrostatic biasing of Au nanoparticles in electrochemical cells [201, 202, 237]. Electron density changes as high as 11% relative to the electron density in the uncharged state were observed. These experiments show a clear relationship between the optical properties of metal nanoparticles and their electron density, as predicted by the Drude model.

In Chapter 5, we have demonstrated a *plasmoelectric effect* in which an optically induced electrostatic potential is generated if a metal nanostructure is illuminated off-resonance [238]. This effect is driven by a thermodynamic increase in entropy, which originates from the dependence of the plasmon resonance on electron density. Here, we discuss in detail the thermodynamic theory underlying the plasmoelectric effect. We first explore a simplified model consisting of a single plasmonic nanoparticle in vacuum to describe the fundamental theory, and subsequently discuss implications for realistic experimental geometries.

6.2 Plasmoelectric effect

To introduce the plasmoelectric effect, we explore the reciprocal phenomenon of electrostatic modulation of a plasmon resonance via the dependence on electron density [201, 202, 237]. Consider a silver nanoparticle in vacuum with radius, R, that is electrically connected to ground (Fig. 6.1a). Thermal fluctuations will cause electrons to randomly enter or exit the nanoparticle, thereby inducing minute fluctuations of electron density. In the dark and under equilibrium conditions the net electron flux is zero. For the analysis here, we first assume radiation provides

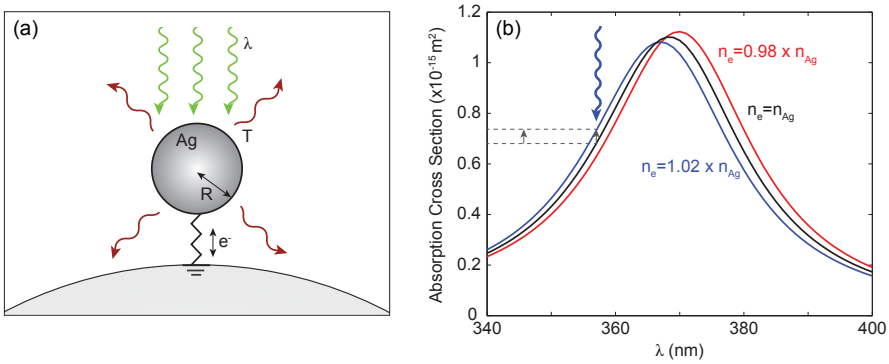

Figure 6.1: (a) Schematic of the model: a silver nanoparticle with radius R in vacuum in electrically connected to ground. Monochromatic illumination with wavelength λ and intensity I_λ is absorbed and excites a plasmon resonance, heating the particle to temperature T. Thermal radiation is the only power loss channel. (b) Calculated absorption cross section for a Ag nanoparticle ($R = 10$ nm) in vacuum with an electron density 2% higher (blue), lower (red), or equal to that of neutral silver (black). Under off-resonance monochromatic illumination, changes in the electron density increase the absorption cross section (gray arrows).

the only pathway for transferring thermal energy in or out of the particle. Now, consider if the nanoparticle is illuminated with monochromatic radiation at wavelength λ and intensity I_λ that is blue shifted with respect to the plasmon resonance of the nanoparticle. Small thermal fluctuations in electron density will cause small fluctuations in the absorption cross section at the illumination wavelength $C_{abs}(\lambda)$ (Fig. 6.1b). Since optical absorption induces heating of the nanoparticle, these small fluctuations result in small changes of the nanoparticle temperature T and, in turn, thermodynamic quantities such as entropy and internal energy. For the situation with blue shifted incident light, thermal fluctuations that add electrons to the nanoparticle thus increase temperature and entropy, which implies that spontaneous *increases* of charge density are thermodynamically favored. Vice versa, if the incident light is red shifted with respect to the plasmon resonance, a *decrease* of electron density increases entropy. At the same time, Coulombic interactions induce a counteracting force against charging of the nanoparticle. To calculate the charge of the nanoparticle during illumination in steady state, we consider the thermodynamic free energy of the system F_{tot}, and minimize it with respect to the number of electrons in the nanoparticle N.

$$\frac{\partial F_{tot}}{\partial N} = 0. \tag{6.2}$$

As the nanoparticle temperature T also depends on N, Eq. 6.2 can be expanded as

$$\frac{\partial F_{tot}(N,T)}{\partial N} = \left(\frac{\partial F_{tot}(N,T)}{\partial N}\right)_T + \left(\frac{\partial F_{tot}(N,T)}{\partial T}\right)_N \frac{dT(N)}{dN} = 0. \tag{6.3}$$

Next, we recognize the general definition for the chemical potential μ

$$\left(\frac{\partial F_{tot}(N,T)}{\partial N}\right)_T \equiv \mu(N,T), \tag{6.4}$$

and for the entropy S

$$-\left(\frac{\partial F_{tot}(N,T)}{\partial T}\right)_N \equiv S(N,T), \tag{6.5}$$

so that Eq. 6.3 can be written as

$$\mu(N,T) = S(N,T)\frac{dT(N)}{dN}. \tag{6.6}$$

Equation 6.6 demonstrates the essence of the plasmoelectric effect: a non-zero electrochemical potential results from the dependence of temperature on electron number in a plasmonic nanoparticle. This analysis is based upon the minimization of the thermodynamic free energy of the system, which we argue to be accurate for the steady-state conditions considered here (see Section 6.11.2). Note that electron density n_e and number of electrons in the nanoparticle N are related by $N = n_e V$, where V is the (constant) particle volume.

The amplitude and spectrum of the plasmonically induced electrochemical potential (i.e. the *plasmoelectric potential*, V_{PE}) can be calculated, fully analytically, in five steps. First, we use Mie theory to calculate the dependence of the absorption cross section $C_{abs}(n_e,\lambda)$ on electron density. Second, we use this cross section in a steady-state power balance to calculate the particle temperature $T(N,\lambda)$. The derivative of this function with respect to N for fixed λ yields $dT(N)/dN$ in Eq. 6.6. Third, we determine the total free energy of the system using well-known definitions for the free energy of a free electron gas and crystal lattice. Fourth, we use Eqs. 6.4 and 6.5 to derive definitions for $\mu(N,T)$ and $S(N,T)$ in Eq. 6.6. Finally, Eq. 6.6 can be solved for N for a range of λ to determine $N(\lambda)$, from which we calculate the surface potential $V_{PE}(\lambda)$. In the remainder of the paper, we will discuss each step in detail and finally explore the influence of geometrical parameters and illumination conditions on V_{PE}.

6.3 Absorption cross section and steady-state temperature

We use Mie theory [29] to calculate the the electron density dependent absorption cross section $C_{abs}(n_e,\lambda)$. For the dielectric function of Ag, we apply a sixth-order multiple Lorentz-Drude fit (see Supplemental Section 6.13.1) to data from Palik [138], analogous to the method outlined by Rakic et al. [213]. This dielectric function depends explicitly on the electron density n_e through the bulk plasma frequency, as described in Eq. 6.1. This method has been demonstrated to accurately describe charge carrier-dependent shifts of the plasmon resonance in both metal nanoparticles [202, 236], and doped semiconductor quantum dots [215, 216].

Figure 6.2a shows the calculated absorption cross section for a Ag particle (R = 10 nm) in vacuum. A clear peak in absorption as a result of the lowest order dipolar plasmon resonance can be observed around λ = 367 nm for the neutral particle; it shows a monotonic blue shift with increasing electron density, as expected from Eq. 6.1. Next, we use the results from Fig. 6.2a to calculate

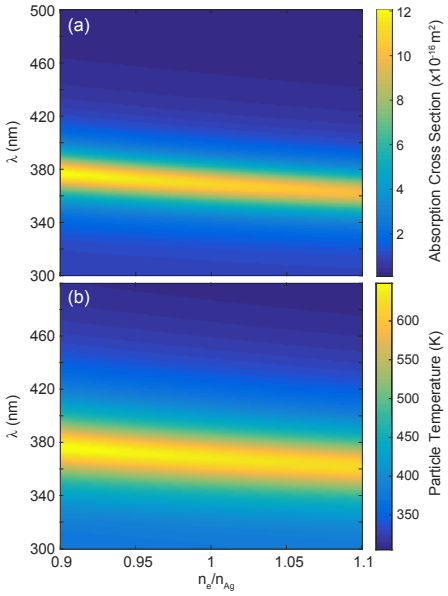

Figure 6.2: (a) Calculated electron density dependent absorption cross section (color) for a Ag nanoparticle (R = 10 nm) in vacuum, for $0.9 \leq n_e/n_{Ag} \leq 1.1$. (b) Steady-state particle temperature (color) for $I_\lambda = 100\,\mathrm{W/m^2}$ (monochromatic).

the steady-state particle temperature $T(n_e, \lambda)$. Note that for the illumination powers considered here, the electron temperature equals the phonon temperature due to the fast electronic relaxation rate and electron-phonon coupling rate in a metal [113]:

$$T_{electron} \approx T_{phonon} = T \tag{6.7}$$

In steady state, the power absorbed by the particle is balanced by the power going out:

$$P_{in} = P_{out} \tag{6.8}$$

The absorbed power includes both the absorbed monochromatic radiation and the ambient thermal background radiation (T_{amb} = 293 K), which is given by the Stefan-Boltzmann law:

$$P_{in} = C_{abs}(N, \lambda) I_\lambda + \sigma A \varepsilon T_{amb}^4. \tag{6.9}$$

Here, σ is the Stefan-Boltzmann constant, A is the particle surface area, and ε is the emissivity. The nanoparticle emissivity is taken to be equal to that of bulk silver, $\varepsilon = 0.01$, as no modulation to the bulk properties is predicted by Mie theory in the spectral range of thermal radiation. Indeed, despite that plasmonic nanoparticles can be strong absorbers at wavelengths close the the plasmon resonance, the low emissivity of the bulk material results in a low IR emissivity [27]. In vacuum, the only power loss channel is through thermal radiation:

$$P_{out} = \sigma A \varepsilon T^4. \tag{6.10}$$

Using Eqs. 6.9 and 6.10 to solve Eq. 6.8 for T yields the steady-state particle temperature

$$T(N,\lambda) = \left(\frac{C_{abs}(N,\lambda) I_\lambda + \sigma A \varepsilon T_{amb}^4}{\sigma A \varepsilon} \right)^{1/4}. \tag{6.11}$$

Figure 6.2b shows the calculated steady-state particle temperature for $I_\lambda = 100\,\mathrm{W/m^2}$. A peak temperature of 634 K is observed for a neutral particle at resonance, and the temperature profile clearly follows the absorption profile as expected from Eq. 6.11. Finally, converting the x-axis from n_e to N and taking the derivative with respect to N at a given wavelength yields $dT(N)/dN$, the last term in Eq. 6.6.

6.4 Free energy calculations

The free energy of the system can be obtained by considering the separate contributions of the electrons F_e, and phonons, F_p in the nanoparticle as well as those of the substrate (the electrical ground, subscript s):

$$F_{tot}(N, T(N)) = F_e(N, T(N)) + F_p(T(N)) + F_{e,s}(N) + F_{p,s}. \tag{6.12}$$

Note that $F_{e,s}$ is a function of N through the conservation of total charge N_{tot} = N + N_s: i.e. if $N > N_0$, with N_0 the number of electrons in a neutral nanoparticle, the chemical and electrostatic potential of the substrate also changes ($N_s < N_{0,s}$). F_e is composed of the electron chemical potential μ_e, and the electrostatic potential, Φ:

$$F_e(N, T(N)) = \int_0^N \mu_e(N', T(N'), V) dN' + \int_0^{N-N_0} \Phi(N') dN'. \tag{6.13}$$

Here, μ_e is the temperature dependent chemical potential of a free electron gas [205]:

$$\mu_e(N, T(N,\lambda), V) = \epsilon_F(N,V) \left(1 - \frac{1}{3} \left(\frac{\pi k_b T(N,\lambda)}{2\epsilon_F(N,V)} \right)^2 \right), \tag{6.14}$$

where k_b is Boltzmann's constant, and ϵ_F is the Fermi energy

$$\epsilon_F(N,V) = \frac{\hbar^2}{2m} \left(\frac{3\pi^2 N}{V} \right)^{2/3}, \tag{6.15}$$

with $\hbar$ the reduced Planck constant. The temperature-dependent term in Eq. 6.14 is < 0.01% at the temperatures considered here [205]. The electrostatic potential is easily obtained from the self-capacitance of a sphere $c = 4\pi R\varepsilon_0\varepsilon_m$, where ε_m is the relative permittivity of the surrounding medium. The work W required to charge a capacitor with charge $Q = N'e$ is

$$W = \frac{1}{2}\frac{Q^2}{c} = \frac{1}{2}\frac{N'^2e^2}{4\pi R\varepsilon_0\varepsilon_m}, \tag{6.16}$$

where $e = -1.602 \times 10^{-19}$ C is the electron charge, so that

$$\Phi(N') = \frac{N'e^2}{4\pi R\varepsilon_0\varepsilon_m}. \tag{6.17}$$

F_p is expressed in terms of the speed of sound in the particle v_s, as obtained from the high-temperature classical limit of the Debye model [42, 204]:

$$F_p(T(N)) = 3k_bT(N)A_0 ln\left(\frac{\theta}{T(N)}\right) - k_bT(N)A_0, \tag{6.18}$$

where A_0 is the number of atoms in the nanoparticle (equal to N_0 for Ag), and θ the Debye temperature [204]:

$$\theta = \frac{\hbar v_s}{k_b}\left(\frac{6\pi A_0}{V}\right)^{1/3}. \tag{6.19}$$

We use $\theta_{Ag} = 215$ K [42].

To quantify the free energy of the substrate, we assume the substrate (electrical ground) is a macroscopic silver sphere with radius R_s and volume V_s at fixed ambient temperature (T_{amb}), containing $A_{0,s}$ atoms and $N_{0,s}$ electrons in a neutral state. If the number of electrons transfered from the substrate to the nanoparticle is $N - N_0$, $F_{e,s}$ and $F_{p,s}$ are given by

$$F_{e,s}(N) = \int_0^{N_{s,0}-(N-N_0)} \mu_e(N', T_{amb}, V_s)dN' + \int_0^{-(N-N_0)} \frac{N'e^2}{4\pi R_s\varepsilon_0\varepsilon_m}dN' \tag{6.20}$$

and

$$F_{p,s} = 3k_bT_{amb}A_{0,s} ln\left(\frac{\theta}{T_{amb}}\right) - k_bT_{amb}A_{0,s} \tag{6.21}$$

respectively.

6.5 Electrochemical potential and entropy

Equation 6.4 is applied to Eq. 6.12 to obtain the electrochemical potential. Starting with $F_e(N, T(N))$, we use

$$\frac{d}{dy}\left(\int_0^y f(x)dx\right) = f(y) \tag{6.22}$$

to get

$$\left(\frac{d}{dN}F_e(N,T(N))\right)_T = \epsilon_F(N,V)\left(1-\frac{1}{3}\left(\frac{\pi k_b T(N,\lambda)}{2\epsilon_F(N,V)}\right)^2\right)+\frac{(N-N_0)e^2}{4\pi R\varepsilon_0\varepsilon_m}. \tag{6.23}$$

Next, since F_p does not depend on N for constant T,

$$\left(\frac{d}{dN}F_p(T(N))\right)_T = 0. \tag{6.24}$$

Using the fact that the substrate is macroscopic (e.g. $R_s > 1$ cm, $N_{s,0} \gg (N-N_0)$ and $c_s \gg c$), the effect of electrostatic charging of the substrate is negligible and the derivative of $F_{e,s}$ can be simplified to

$$\left(\frac{d}{dN}F_{e,s}(N)\right)_T = -\epsilon_F(N_{s,0},V_s)\left(1-\frac{1}{3}\left(\frac{\pi k_b T_{amb},\lambda)}{2\epsilon_F(N_{s,0},V_s)}\right)^2\right). \tag{6.25}$$

Note that Eq. 6.25 simplifies to $-\epsilon_F(N_0,V)$ if the temperature dependence is neglected. Finally,

$$\left(\frac{d}{dN}F_{p,s}\right)_T = 0, \tag{6.26}$$

such that the complete definition for $\mu(N,T(N))$ in Eq. 6.6 is given by:

$$\begin{aligned}\mu(N,T(N)) = \epsilon_F(N,V)&\left(1-\frac{1}{3}\left(\frac{\pi k_b T(N,\lambda)}{2\epsilon_F(N,V)}\right)^2\right)\\ &+\frac{(N-N_0)e^2}{4\pi R\varepsilon_0\varepsilon_m}-\epsilon_F(N_{s,0},V_s)\left(1-\frac{1}{3}\left(\frac{\pi k_b T_{amb},\lambda)}{2\epsilon_F(N_{s,0},V_s)}\right)^2\right)\end{aligned} \tag{6.27}$$

Next, we obtain a definition for the entropy of the system by applying Eq. 6.5 to Eq. 6.12. Since the electrostatic potential does not depend on T,

$$-\left(\frac{d}{dT}F_e(N,T(N))\right)_N = \int_0^N \frac{\pi^2 k_b^2 T(N',\lambda)}{6\epsilon_F(N',V)}dN'. \tag{6.28}$$

The nanoparticle phonon entropy is easily obtained as

$$-\left(\frac{d}{dT}F_p(T(N))\right)_N = -3k_bA_0 ln\left(\frac{\theta}{T(N)}\right)+4k_bA_0. \tag{6.29}$$

Finally, since the grounded substrate has constant temperature $T_s = T_{amb}$,

$$-\left(\frac{d}{dT}F_{e,s}(N)\right)_N = -\left(\frac{d}{dT}F_{p,s}\right)_N = 0, \tag{6.30}$$

such that

$$S(N,T(N)) = \int_0^N \frac{\pi^2 k_b^2 T(N',\lambda)}{6\epsilon_F(N',V)}dN' - 3k_bA_0 ln\left(\frac{\theta}{T(N)}\right)+4k_bA_0. \tag{6.31}$$

6.6 Master equation

Based of the definitions of μ (Eq. 6.27), S (Eq. 6.31) and dT/dN (Eq. 6.11 and Fig. 6.2a), the free energy minimization can now be applied to find the steady-state (time-averaged) charge state of the nanoparticle for each illumination wavelength λ. As it is instructive to explore the terms in Eq. 6.6 individually we first calculate μ, S and dT/dN for the 20 nm Ag nanoparticle model system. Figure 6.3 shows the electrochemical potential (a), entropy (b) and plasmonically induced temperature dependence dT/dN (c) for $I_\lambda = 100\,\mathrm{W/m^2}$.

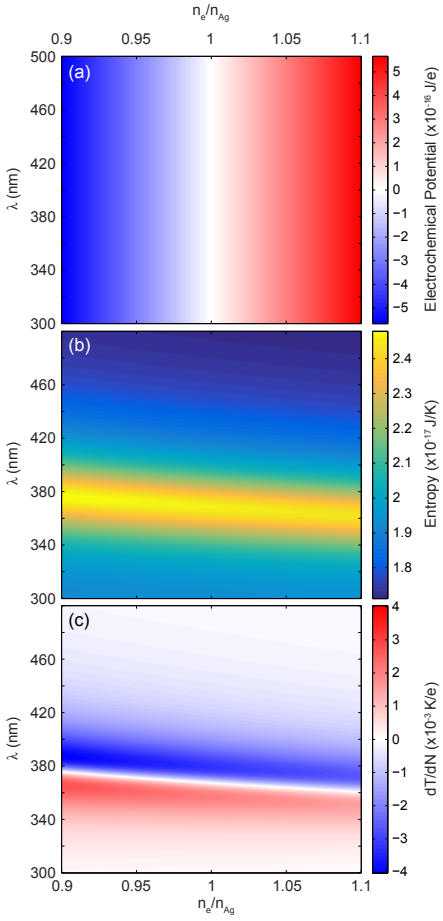

Figure 6.3: Electrochemical potential μ (a), entropy S (b), and plasmonically induced temperature dependence dT/dN (c) for a Ag particle (R = 10 nm) in vacuum under 100 W/m^2 monochromatic illumination as a function of electron density and wavelength.

The electrochemical potential (Fig. 6.3a) shows a monotonic, wavelength independent increase with electron density. Comparing this trend with the particle temperature in Fig. 6.2b, which shows a clear wavelength dependence as a result of the resonance, indicates that the temperature dependence of μ is indeed negligible. Furthermore, from the linear increase with n_e (and thus N), is it clear that the electrostatic Coulombic interaction dominates over the Fermi energy, which scales with $\propto N^{2/3}$ (see Eq. 6.15). Indeed, comparing the increase in Fermi energy (Eq. 6.15) and electrostatic potential (Eq. 6.17) as a result of the addition of a single electron to the neutral particle shows that the effect on the electrostatic potential is 4 orders of magnitude larger than that on ϵ_F.

Equation 6.31 shows a dependence of S on N through the first and second term. The first term corresponds to the entropy of the electron gas, which is negligible compared to the lattice entropy. The second term scales with $\propto \log(T(N))$. Finally, the third term in Eq. 6.31 is constant and only determined by the number of atoms A_0 in the nanoparticle. Hence, the entropy will be constant with a small modulation that scales logarithmically with the particle temperature (Fig. 6.2b). This is confirmed by the trend in Fig. 6.3b, which clearly follows that of T. The entropy of the system is thus clearly dominated by the entropy of the lattice.

Figure 6.3c shows $dT(N)/dN$, calculated from Fig. 6.2b. Three distinct features can be observed. First, $dT/dN = 0$ at the resonance wavelength of the neutral particle. Since $S \times dT/dN$ is the thermodynamic driving force for the plasmoelectric potential, this implies that $V_{PE} = 0$ at the resonance wavelength of the neutral particle. Second, it is important to realize that V_{PE} is calculated for fixed incident wavelength. Hence, it is the horizontal cross cut through Fig. 6.3c that determines the magnitude of the thermodynamic driving force. Third, with this in mind it is clear from Fig. 6.3c that it is beneficial to have plasmonic resonances with high quality factor (Q), but it is the sensitivity of the resonance wavelength to the electron density that determines the magnitude of V_{PE} in the end. This sensitivity is characterized by the slope of the white line in Fig. 6.3c.

Equation 6.6 shows that the free energy minimum can be found by equating μ to $S \times dT/dN$, corresponding to where data in Fig. 6.3a equals the product of data in Figs. 6.3b and 6.3c. Considering the order of magnitude of the different terms in Figs. 6.3b and 6.3c shows that $S \times dT/dN < 9 \times 10^{-20}$ J/e. Comparing this with the magnitude of the electrostatic potential in Fig. 6.3a (up to 5×10^{-16} J/e) shows that the free energy minimum will occur very close to charge neutrality. Indeed, adding a single electron to a 20 nm nanoparticle leads to a change in surface potential of 144 mV.

Finally, note that the master equation can be greatly simplified. Neglecting the temperature dependence in the chemical potential (Eq. 6.27), using that $N_{s,0} \gg (N - N_0)$, and neglecting the electron entropy (Eq. 6.28), simplifies the

equation to

$$\epsilon_F(N,V) - \epsilon_F(N_0,V) + \frac{(N-N_0)e^2}{4\pi R\varepsilon_0\varepsilon_m} = -3k_bA_0 ln\left(\frac{\theta}{T(N)}\right)\frac{dT(N)}{dN} + 4k_bA_0\frac{dT(N)}{dN} \quad (6.32)$$

with < 0.25% error in the maximum calculated potential. All results in this work are calculated using the full equation rather than the simplified one.

6.7 Results

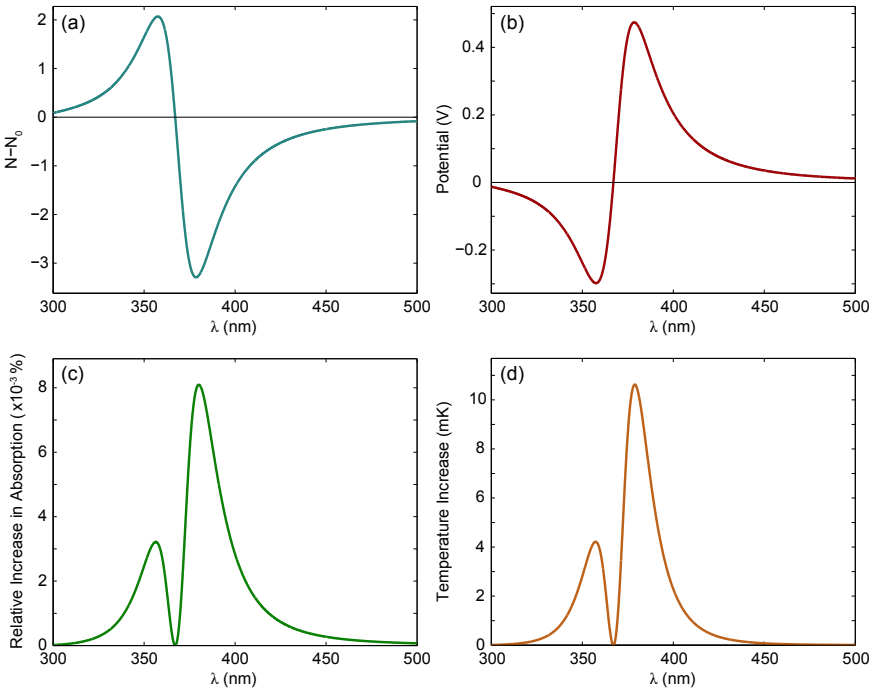

Figure 6.4: Steady-state configuration as a function of wavelength of a 20 nm Ag particle in vacuum under $I_\lambda = 100$ W/m^2 monochromatic illumination. (a) Time-averaged number of electrons transfered from the substrate into the nanoparticle. (b) Induced plasmoelectric surface potential. (c) Relative increase in absorption as result of plasmoelectric effect. (d) Corresponding increase in particle temperature.

Solving Eq. 6.6 for N for a range of λ yields $N(\lambda)$. Figure 6.4a shows the time-averaged number of electrons transfered from the substrate to the nanoparticle

$(N - N_0)$ as a function of wavelength for a 20 nm Ag particle (I_λ = 100 W/m^2). Three trends are worth noting in Fig. 6.4a. First, a clear bisignated signal is observed which is positive on the blue side and negative on the red side of the neutral particle resonance wavelength (λ_{res} = 367 nm). The shape of the signal clearly indicates the trend of the plasmoelectric effect: electrons are added to the nanoparticle for $\lambda < \lambda_{res}$ to blue shift the absorption resonance and thereby increase the entropy. Vice versa, electrons are removed from the particle for $\lambda > \lambda_{res}$ to red shift the absorption resonance. Second, the signal is maximized when $S \times dT/dN$ is maximum, which roughly corresponds to where the slope in the absorption spectrum is maximum. Third, the signal is asymmetric: the amplitude of the signal is larger above λ_{res} than below. This is caused by: 1) the non-resonant intrinsic interband absorption in the silver, and 2) the fact that $C_{abs} \propto \lambda^2$ according to Mie theory.

Three observables can be derived from $N(\lambda)$. First, a static surface potential will be induced on the nanoparticle if $N \neq N_0$, which is defined by both the difference in Fermi energy as well as the potential due to electrostatic charging of the self-capacitance:

$$V_{PE}(\lambda) = \frac{\epsilon_F(N(\lambda), V) - \epsilon_F(N_0, V)}{e} + \frac{(N(\lambda) - N_0)e}{4\pi R \varepsilon_0 \varepsilon_m}. \tag{6.33}$$

Second, the plasmoelectric effect is driven by an increase in absorption as a result of electron transfer. Therefore, the relative increase in absorption compared to a neutral particle can be calculated as

$$\Delta C_{abs}^{rel}(N(\lambda), \lambda) = \frac{C_{abs}(N(\lambda), \lambda) - C_{abs}(N_0, \lambda)}{C_{abs}(N_0, \lambda)}. \tag{6.34}$$

Finally, the increase in absorption results in an increase in the particle temperature:

$$\Delta T(N(\lambda), \lambda) = T(N(\lambda), \lambda) - T(N_0, \lambda) \tag{6.35}$$

Figures 6.4b-d show the calculated plasmoelectric potential (b), relative increase in absorption (c) and corresponding increase in temperature (d) as a result of the plasmoelectric effect. V_{PE} scales with $-N$ since the electrostatic potential dominates the amplitude of the potential. Therefore, the potential has the same but negative trend as Fig. 6.4a. As a result of the small capacitance of the nanoparticle the potential reaches several 100 mV for the transfer of only a few electrons.

Due to the small number of electrons transfered, the spectral shift of the plasmon resonance is very small. Therefore, the relative increase in absorption is limited to a maximum of 8×10^{-3}%, corresponding to a maximum increase in temperature due to the charge transfer of ~ 11 mK. Note that this small increase in temperature is with respect to that of a neutral particle under steady-state illumination. Starting from a neutral particle in the dark, T increases from T_{amb} to $T \sim 630$ K due to steady-state absorption of monochromatic radiation. Then, by adding or subtracting on average 2–3 electrons (Fig. 6.4a) the temperature is further increased by ~ 11 mK (Fig. 6.4d). Finally, unlike the potential, the increase in absorption and

temperature is always positive due to the requirement of entropy maximization. Interestingly, the increase in absorption and temperature vanishes at λ_{res}, which distinguishes the plasmoelectric effect from e.g. the thermoelectric effect, which would be maximum at $\lambda = \lambda_{res}$ due to the maximum induced temperature at that wavelength.

6.8 Illumination conditions

The intrinsic thermodynamic nature (entropy maximization and free energy minimization) of the plasmoelectric effect indicates that it is not a linear optical phenomenon. However, the amplitude of the potential is not directly described by higher-order non-linear susceptibility terms $\chi^{(i)}$, as is, for example, plasmon-enhanced second harmonic generation [239]. The scaling of V_{PE} with I_λ is determined by the steady-state particle temperature, and thereby the power gain and loss channels available to the system. For a nanoparticle in vacuum, P_{in} is linear with I_λ. However P_{out} is limited to thermal radiation, which scales with $\propto T^4$ (Eq. 6.10). Therefore, V_{PE} initially shows a rapid increase with increasing I_λ, but saturates as P_{out} increases $\propto T^4$. To demonstrate this, we calculate the induced potential for the same 20 nm Ag nanoparticle as considered in Figs. 6.2-6.4, but now for $0 \leq I_\lambda \leq 250$ W/m^2.

Figure 6.5 shows the calculated V_{PE} (a) and maximum particle temperature (b) as a function of I_λ. Both the potential and the steady-state temperature show a strong increase at low intensities, which is clearly visible from the closely spaced iso-potential lines (a). The saturation as a result of the rapid increase in thermal radiation is also clearly visible in both figures. Furthermore, the iso-potential lines in Fig. 6.5a show a strong spectral shift away from λ_{res} with increasing I_λ. As a result, the thermodynamic driving force increases with I_λ such that dT/dN increases at the shoulders of the resonance spectrum, thereby increasing the spectral bandwidth of the plasmoelectric effect.

Note that for realistic experimental geometries (i.e. particles on a substrate in air), thermal diffusion and convection rather than radiation dominate the thermal response, thereby changing the proportionality of $V_{PE} \propto I_\lambda$. The thermal power balance also dictates the maximum intensity that can be used in experiments, since the power loss channels determine the damage threshold of the resonant structure.

6.9 Particle size

Next, we study the influence of particle size on the plasmoelectric potential. The localized plasmon resonance is strongly sensitive to the particle geometry [3], and shows a red shift with increasing particle diameter [72]. Furthermore, the electrostatic capacitance of the nanoparticle scales with R, such that the number of electrons transferred to/from the nanoparticle will increase for a given potential. Figure 6.6a shows the calculated extinction efficiency, which is defined as $\sigma_{ext}/\sigma_{geo}$,

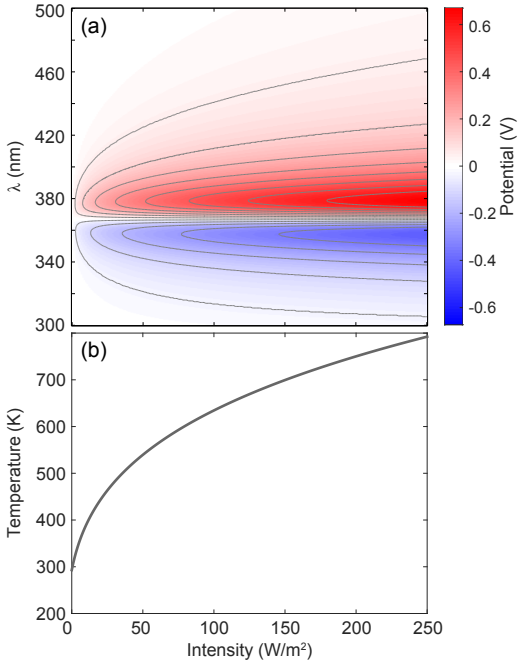

Figure 6.5: (a) Plasmoelectric potential on a 20 nm Ag sphere in vacuum as a function of monochromatic illumination intensity and wavelength. The gray lines show iso-potential lines. (b) Corresponding maximum temperature of the nanoparticle.

where $\sigma_{geo} = \pi R^2$ is the geometrical cross section of the nanoparticle. The dipolar (D) resonance, observed at $\lambda_{res} = 367$ nm for the 20 nm particle (Fig. 6.1b), shows a clear red shift and increase in extinction efficiency with increasing diameter. For $d > 100$ nm, a higher order quadrupolar resonance (Q) occurs, which also red shifts with increasing particle diameter. A maximum extinction efficiency of 9.38 is observed for $d = 68$ nm, showing the strongly resonant behavior of the nanoparticle. Comparing the trends in Fig. 6.6a with the 20 nm particle considered in Figs. 6.1–6.5 could suggest that larger plasmoelectric potentials can be obtained for $d \sim 70$ nm than for $d = 20$ nm. However, the albedo ($\sigma_{scat}/\sigma_{ext}$) of the resonance also increases with particle size [71]. Hence, a smaller fraction of the extinction is due to absorption by the nanoparticle. Figure 6.6b shows the absorption efficiency ($\sigma_{abs}/\sigma_{geo}$) as a function of particle size. It shows both the dipolar and quadrupolar resonance, and a strong reduction in the absorption efficiency is observed for $d > 70$ nm as a result of the increased scattering rate. An optimum absorption efficiency of 6.37 is observed for $d = 48$ nm. Note that this is not necessarily the optimum geometry for the plasmoelectric effect either, since it is the increase in ab-

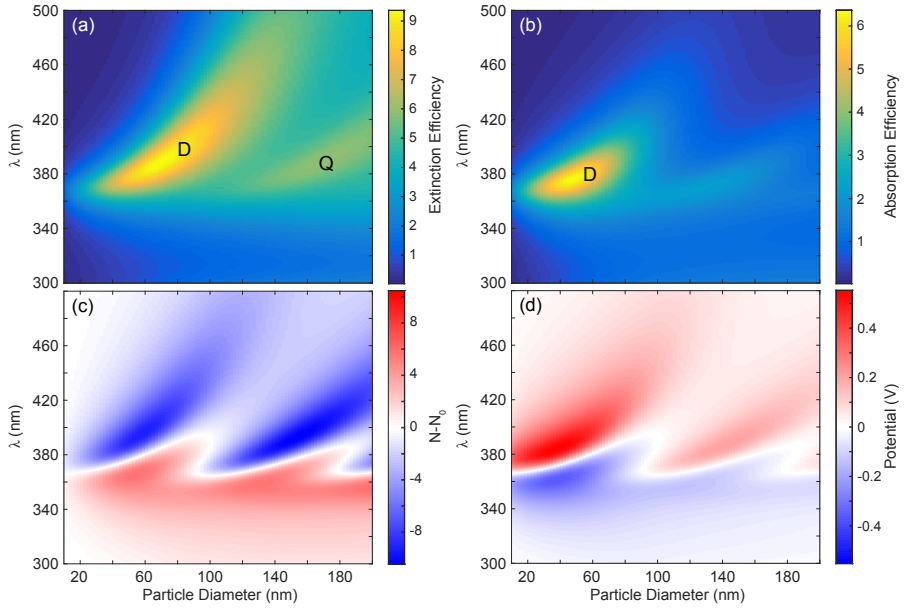

Figure 6.6: (a) Calculated extinction efficiency ($\sigma_{ext}/\sigma_{geo}$) for a Ag sphere in vacuum as a function of particle diameter. The dipolar (D) and quadrupolar (Q) resonant modes are labeled accordingly. (b) Calculated absorption efficiency ($\sigma_{abs}/\sigma_{geo}$) showing the increase in albedo for larger particle diameters. (c,d) Transferred average number of electrons (c) and induced plasmoelectric potential (d) as a result of the dipolar and quadrupolar resonance under 100 W/m^2 monochromatic illumination.

sorption per added electron (dT/dN), which depends on radius, that determines the magnitude of the potential rather than the absolute absorption.

The average number of electrons transferred to the nanoparticle (Fig. 6.6c) shows a general positive trend for $\lambda < \lambda_{res}$, and a negative trend for $\lambda > \lambda_{res}$, for all particle sizes. The zero-point crossing line (i.e. where $N - N_0 = 0$) clearly follows the dipolar and quadrupolar resonances observed in Fig. 6.6b, indicating that the plasmoelectric effect is not limited to the dipolar nature of the lowest order plasmon resonance. Furthermore, a significant increase in $N - N_0$ is observed for increasing particle diameter. Since $Ne = cV_{PE}$ and $c \propto R$, the number of charges strongly increases as a result of the reduced electrostatic repulsion on larger particles. Note that the capacitance, and thereby the number of transfered number of electrons can be drastically enhanced by embedding the nanoparticle in a water-based electrolyte, as a result of the large static dielectric constant of water and the double-layer screening by counter ions [202]. Finally, the charge transfer induced by the dipolar and quadrupolar resonance counteract each other

for $\lambda_{res}^{Q} < \lambda < \lambda_{res}^{D}$. The dipolar resonance induces an increase in charge density, whereas the quadrupolar resonance induces a reduction. This balance causes a "dead" region in between the two resonances around $d = 100$ nm.

Next, we calculate the potential induced on the nanoparticle by the charge transfer (Fig. 6.6d). The potential follows roughly the same trends as the charge transfer (Fig. 6.6c), except that a strong reduction is observed with increasing particle diameter. Comparing Fig. 6.6d with Fig. 6.6b shows why: the absorption efficiency shows a strong decrease with increasing particle size, suggesting that the increase in $N - N_0$ in Fig. 6.6c is dominated by the increase in c. A maximum potential of 554 mV is observed for $d = 38$ nm and $\lambda = 384$ nm. Figures. 6.6c,d show that the particle geometry can be tuned to optimize the plasmoelectric effect for maximum charge transfer (large particle) or maximum potential (small particle).

6.10 Thermodynamic potential

Figure 6.6 shows that the absorption profile (Fig. 6.6b) does not unambiguously predict the plasmoelectric potential (Fig. 6.6d); i.e. the potential is not maximum where absorption is maximum. To explain this we consider S and dT/dN separately as a function of particle size. Similar to Fig. 6.4d, the increase in temperature as a result of the plasmoelectric effect can be studied by considering the intuitive quantity $\Delta T = \int_{N_0}^{N} dT/dN' dN' = T(N,\lambda) - T(N_0,\lambda)$. Figure 6.7a shows ΔT ($\log_{10}$, color) obtained from the results of Fig. 6.6. A small overall increase in temperature is observed for wavelengths close to the λ_{res} (corresponding to the dark blue line). The oscillations in the dark blue line with increasing particle diameter correspond to the subsequent transitions from dipole to quadrupole, and quadrupole to octopole plasmon resonance modes dominating the plasmoelectric effect, respectively. Although the increase in temperature is significant for small particles (up to 25.4 mK for $d = 10$ nm), it rapidly decreases with increasing particle diameter. In fact, for $d = 200$ nm ΔT peaks at only 6 μK, which indicates a three orders of magnitude reduction in ΔT compared to small particles. Yet still, a significant potential ($V_{PE}^{max} = 107$ mV) is observed for such large particles (Fig. 6.6d).

To understand why, Fig. 6.7b shows the entropy of a neural nanoparticle $S(N_0)$ (color) as a function of particle size and incident wavelength. Note that $S(N) \approx S(N_0)$ due to the logarithmic dependence on the very small variations in $T(N)$. The particle entropy shows a drastic increase with particle size, as $A_0 \propto R^3$ (Eq. 6.31). Indeed, S increases from $\sim 10^{-17}$ J/K for $d = 20$ nm with three orders of magnitude up to $\sim 10^{-14}$ J/K for $d = 200$ nm. Note that the small variation of S with λ originates from the dependence of the temperature on N: $S(T(N))$, see Eq. 6.31 and Fig. 6.3b.

Finally, Fig. 6.7c shows $S(N_0) \times dT(N)/dN\big|_{N=N_0}$, which corresponds to the thermodynamic potential experienced by a neutral particle under monochromatic illumination. Figures 6.7a,b show that for larger particles the increase in temperature drops by three order of magnitude, whereas the entropy increases by three orders

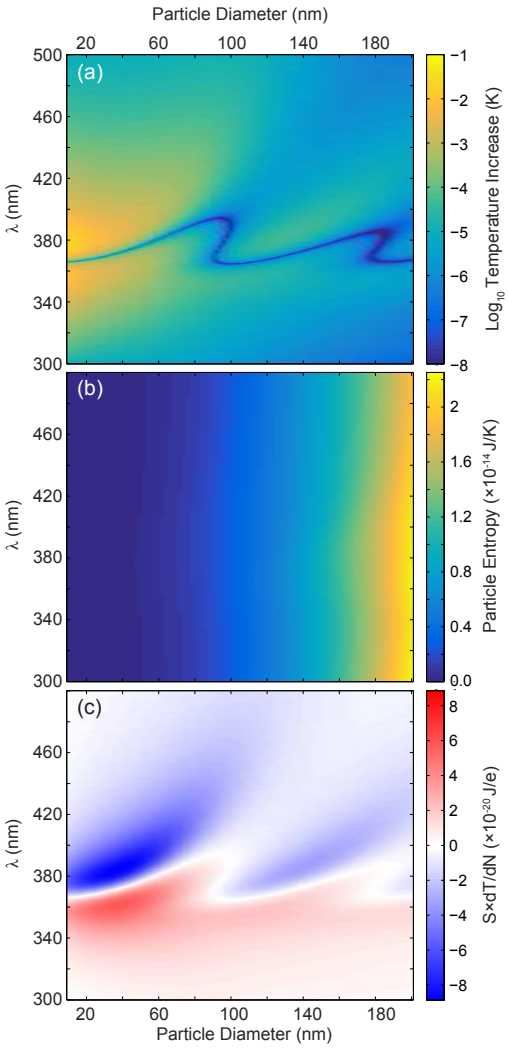

Figure 6.7: (a) Log_{10} of increase in temperature (in K, color) as a function of particle diameter and wavelength for $I_\lambda = 100$ W/m^2, showing a rapid decrease with increasing particle size. (b) Entropy of the nanoparticle (for $N = N_0$), showing a strong increase with increasing particle size. (c) Thermodynamic potential $S \times dT/dN$ (evaluated at $N = N_0$) driving the plasmoelectric effect.

of magnitude. As a result, the product (Fig. 6.7c) has the same order of magnitude for the entire range of particle diameters. Indeed, comparing Fig. 6.7c with Fig. 6.6d shows that the product $S \times dT/dN$ scales with the calculated potential (converted

from J/e to V). This example demonstrates that for large systems, the increase in temperature as a result of the plasmoelectric effect can be very small. However, due to the large entropy of the system, the energetic pay-off of this small increase in temperature is sufficiently large to induce significant surface potentials. Thus more realistic experimental geometries can still be expected to exhibit appreciable plasmoelectric potentials, e.g. particles on a substrate in air, where thermal convection and conduction may significantly lower the temperature obtained under illumination.

6.11 Discussion

6.11.1 Generalization

The plasmoelectric effect is not limited to plasmonic resonators. It is generic for a resonant optical cavity that tends to spectrally align its resonance with the pump light to optimize absorption. Conditions to achieve this are: First, the system has an optical resonance that exhibits non-radiative losses, i.e. absorption. The absorption generates heat and thereby entropy, which is the underlying thermodynamic driving force. Second, there exist a feedback mechanism between the resonance frequency and the electron density of the structure. Essential for the bisignated signal is that the feedback mechanism works in both ways: e.g. an increase (decrease) in electron density causes a blue- (red) shift of the optical resonance. Third, the system is electrically connected to ground or a (large) electron bath, which allows exchange of electrons with the resonator. These requirements can also be met with non-plasmonic resonators such as for example whispering gallery cavities based on doped semiconductor or transparent conductive oxides structures, which can be heavily doped [240]. Significant changes in the refractive index of such materials have been demonstrated through electrical gating [241], and electrically tunable resonances in these devices using this effect have been realized [242]. This offers great potential for the use of these structures in plasmoelectric circuitry.

6.11.2 Free energy minimization for local-equilibrium systems

The thermodynamic analysis discussed in Section 6.2 is based upon the minimization of the thermodynamic free energy of the system. By definition, this analysis is strictly warranted when describing the equilibrium state of a closed system with fixed total energy [243]. Although the system we model here does not approach a true thermodynamic equilibrium, i.e. we do not consider a closed system which includes the thermodynamic state of the optical source, we argue that free-energy minimization still gives an accurate description. The steady-state power balance dictates a well defined particle temperature: in Fig. 6.2b, a maximum temperature of 634 K was observed. For the optical intensities considered, the electronic and phononic distribution of the particle is not driven to a non-thermal state, but is expected to be well described by conventional Fermi-Dirac and Boltzmann statistics,

respectively [113]. We stress that similar arguments hold for the well-established detailed-balance calculation of the limiting efficiency of a photovoltaic cell [244], which also considers a steady-state system that is not in thermal equilibrium with a source but assumes the validity of a thermal distribution among the excited carriers in the conduction band.

6.12 Conclusions

In conclusion, we present a thermodynamic theory of the plasmoelectric effect using a model system composed of a 20 nm Ag sphere in vacuum. We show that minimization of the thermodynamic free energy of the system leads to an electrostatic surface potential on a resonant metal nanoparticle, driven by the increase in absorption - and thereby entropy production - as a result of electron injection. We find that for our model system, potentials up to 473 mV are induced under 100 W/m^2 monochromatic illumination as a result of an 11 mK increase in the steady-state particle temperature. Furthermore, the plasmoelectric potential is found to be non-linear with the illumination intensity, as the amplitude of the potential is dictated by the steady-state thermal balance. We determine how the plasmoelectric potential scales with particle size, and find that for large systems, minute increases in temperature can induce significant surface potentials as a result of the large entropic pay-off. Finally, we discuss the conditions required for manifestation of the plasmoelectric effect, and predict that the effect is generic for any resonant system in which optical absorption and charge density are coupled.

6.13 Supplementary information

6.13.1 Complex dielectric function of Ag

We use a sixth-order Lorentz-Drude fit to the data from Palik [138], using the approach outlined by Rakic et al. [213]. The detailed procedure and the fit parameters are obtained from ref. [245]. In short, the model used is

$$\varepsilon_{LD}(\omega) = 1 - \frac{f_0\omega_p^2}{\omega^2 + i\Gamma_0\omega} + \sum_{j=1}^{5} \frac{f_j\omega_p^2}{\omega_j^2 - \omega^2 - i\Gamma_j\omega}, \tag{6.36}$$

where f_0 and Γ_0 are the amplitude and damping rate of the Drude (intraband) term, describing the free-electron contribution to the dielectric function. Similarly, f_j, ω_j and Γ_j are the amplitude, resonance frequency, and damping rate of the j-th Lorentz oscillator describing the interband part of the dielectric function. The fitting parameters used are:

Term	f	ω_p (rad/s)	ω_j (rad/s)	Γ_j (rad/s)
$j = 0$	0.845	13.69×10^{15}	0.000	0.0729×10^{15}
$j = 1$	0.065	13.69×10^{15}	1.240×10^{15}	5.904×10^{15}
$j = 2$	0.124	13.69×10^{15}	6.808×10^{15}	0.6867×10^{15}
$j = 3$	0.011	13.69×10^{15}	12.44×10^{15}	0.0988×10^{15}
$j = 4$	0.840	13.69×10^{15}	13.80×10^{15}	1.392×10^{15}
$j = 5$	5.646	13.69×10^{15}	30.83×10^{15}	3.675×10^{15}

Table 6.1: Fitting parameters used in Eq. 6.36, obtained from ref. [245]

7

Integrated circuits for AC plasmoelectric power conversion

We present first steps towards the experimental demonstration of plasmoelectric power conversion in a circuit-based micro-capacitor device. Using finite-difference time-domain simulations, we design and study a plasmonic hole array in a 20 nm thick Au film that shows near-unity absorption as a result of diffractive coupling to a damped symmetric surface plasmon polariton mode. Using electron beam lithography and focused-ion beam milling, we fabricate Au–Al_2O_3–Ag parallel-plate micro-capacitors with top plates that are partially patterned with a strongly absorbing hole array. We experimentally study the optical absorption spectra of the hole arrays and the spatial absorption profiles of the micro-capacitor devices. Finally, towards the first demonstration of plasmoelectric power conversion, we design an AC optoelectronic experiment to measure the charging/discharging current of the micro-capacitor as a result of the plasmoelectric effect.

7.1 Introduction

The miniaturization of optoelectronic devices allows for faster and more complex data processing at reduced power consumption. Enabled by rapid improvements in nanopatterning and material processing techniques over the past decade, a wide range of micro-scale optoelectronic devices has been demonstrated. These

include nanolasers [246, 247], nanoscale power sources [64, 65], and micro-scale optoelectronic circuits [248]. Typically, nanoscale photodetectors and power sources are based on the cross band gap excitation of semiconductor materials [57, 58, 249, 250]. While semiconductor materials are well studied for these applications, the performance of micro-scale optoelectronic device is strongly sensitive to semiconductor material quality and surface states [65]. Therefore, micro-scale functional devices often require complex fabrication methods. The ability to use all-metal (resonant) geometries in optoelectronic devices would relax these constraints and preempt the use of sensitive semiconductor interfaces. Furthermore, photo-voltages induced by resonant metal nanostructures are tunable from the visible spectral range to the deep IR, rather than fixed by the semiconductor band gap. This tunability allows for the optimization of the spectral response for specific device applications. Finally, the low electrical resistivity of all-metal structures yields an intrinsically low RC-time, which allows for ultra-fast devices.

In Chapter 5 we demonstrated how all-metal nanostructures can be used to induce local electrostatic potentials as a result of the plasmoelectric effect. Using Kelvin-probe force-microscopy (KPFM), ~100 mV potentials were measured on metal hole arrays in non-contact mode. Although such local surface potentials are promising, the realization of micro-scale plasmoelectric power conversion devices requires the demonstration of plasmoelectric currents in a circuit-based device.

Here, we show the first steps towards the experimental demonstration of such circuit-based plasmoelectric currents. We use finite-difference time-domain simulations to design a hole array with near-unity absorption at resonance, and explore its suitability for the plasmoelectric effect. Next, using electron beam lithography (EBL) and focused-ion beam (FIB) milling, we fabricate micro-scale devices with strongly absorbing hole arrays as active plasmonic elements. We experimentally study both the absorption spectra of the hole arrays and the spatial absorption maps of the devices. Next, we design an AC experiment which exploits the transient currents generated by the plasmoelectric effect. Micro-capacitors are important on-chip micro-scale power sources [251]. Therefore, we combine the plasmonic hole arrays with lithographically defined parallel-plate capacitors and design an experiment to measure the charge/discharge current of this micro-capacitor, driven by the plasmoelectric effect. The results presented here demonstrate a clear experimental route towards the first demonstration of plasmoelectric power conversion.

7.2 Fabrication

Figure 7.1 shows a schematic cross section (a) and top view (b) of the sample layout. A strongly absorbing hole array (dark red) in a 20 nm thick Au film is used as an active plasmonic element. The lateral size of the hole array is 10 × 10 μm, large enough to provide a homogeneous environment for a typical focused laser beam. This hole array is integrated in the top layer of a Au–Al_2O_3–Ag layer stack.

The function of the three-layer geometry is two-fold. First, it resembles a parallel-plate capacitor geometry, which enhances the electrical capacitance of the hole array, and thereby the charging/discharging current. Second, the Ag is a low-loss high-quality optical back reflector which is separated from the hole array using a dielectric spacer. The back reflector blocks the downward optical path. Moreover, the thickness of the Al_2O_3 is optimized using finite-difference time-domain simulations (see Section 7.3) to achieve critical coupling to the absorption resonance in the hole array, causing a strong increase in the absolute absorption efficiency [252]. Al_2O_3 was chosen as the material for the dielectric spacer as it is commonly used as a high-quality electrical isolator in integrated circuits, and exhibits no optical absorption in the visible spectral range due to its high band gap energy (6.4 eV) [253].

Samples were fabricated on 12 × 12 × 1 mm glass substrates, to prevent any electrical interaction with the substrate. Substrates were first cleaned with a base piranha recipe, rinsed in isopropanol, and blow dried. Next, the substrates were sputter coated with a 5 nm Cr adhesion layer (0.3 nm/s), followed by 500 nm of Ag (1.9 nm/s). After this, 125 nm of Al_2O_3 was deposited by thermal atomic layer deposition (150°C) using trimethylalmuninium (TMA) and H_2O as a precursor and reactant respectively (1580 cycles, 0.8 Å/cycle). In-situ spectroscopic ellipsometry was used to monitor the thickness and measure the optical constants (see Supplemental Fig. 7.8).

Next, electron beam lithography was used to fabricate 10 × 10 μm sized hole arrays in a 20 nm thick Au film on top of the Al_2O_3. A three-layer process is used to fabricate the shadow mask for the Au evaporation. First, after a 3 min bake out at 150°C, the samples are cooled and spincoated with 230 nm of mr-I PMMA (35kDa, 1500 rpm, 45 s), and baked for another 3 min at 150°C. Second, a 25 nm sacrificial layer of Ge was thermally evaporated (0.5 Å/s) onto the samples in order to protect the PMMA layer during the rest of the process. Third, hydrogen silsesquioxane (HSQ, Fox 15) was diluted with methylisobutylketon (MIBK) in a 1:2 ratio and spincoated onto the sample (3000 rpm, 45 s), and subsequently baked for 2 min at 180°C. After the bake out, the resist was measured to be 60 nm thick using profilometry. Proximity-corrected two-dimensional arrays of disks (320 nm pitch) were written in the HSQ (20 kV, 7.5 μm aperture, 3.4 pA beam current) using area exposure with a dose of 250–450 $\mu As/cm^2$. The resulting disk diameters ranged from 110–150 nm. The patterned HSQ was developed by immersion in MF-319 (Microposit developer) at 50°C for 60 s, subsequently rinsed in deionized water, and blow dried.

The disk pattern was transferred into the PMMA layer by subsequent reactive-ion etching (RIE) of the Ge layer (12.5 sccm SF6 and 2.5 sccm O_2, 30 W, 3:00 min) and the PMMA layer (25 sccm O_2, 50 W, 4:30 min). Next, 20 nm Au was thermally evaporated (0.5 Å/s). Finally, lift-off of the shadow mask was performed by dissolving the PMMA in acetone at 50°C for 3 hours, followed by 45 min in N-methylpyrrolidon (NMP) at 65°C. Then, 10 min of megasonification and 5 min of ultrasonification in NMP, followed by 10 min of megasonification in deionized water was used to remove residuals of the shadow mask.

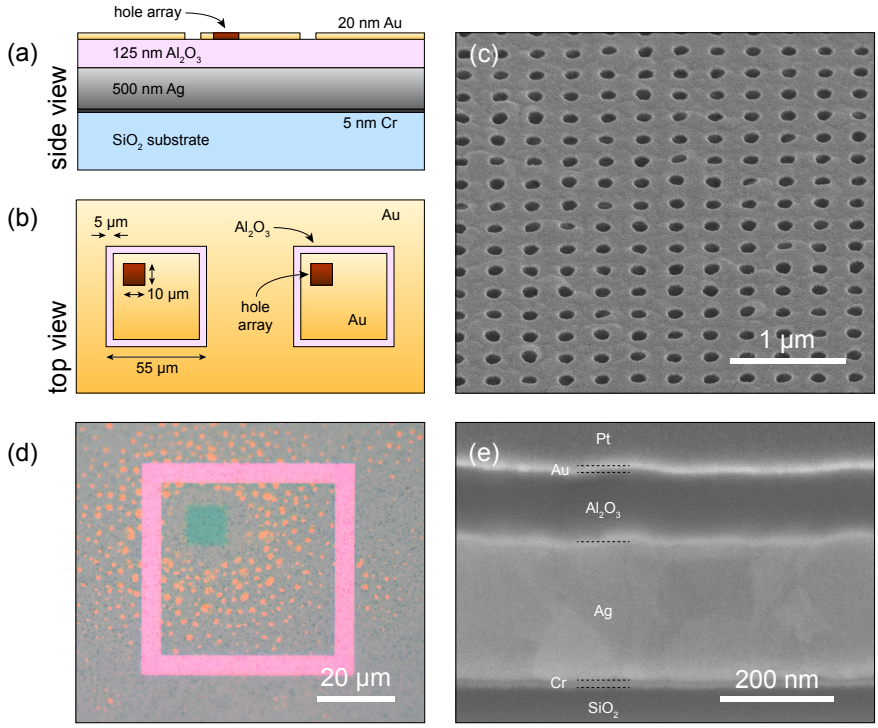

Figure 7.1: Schematic cross section (a) and top view (b) of the plasmoelectric device. (c) SEM image of the 320 nm pitch hole array, imaged under 52°. The hole diameter is ~125 nm. (d) Bright-field optical microscope image of a plasmoelectric device. The dark green square is the 10 × 10 μm hole array. (e) SEM image of a FIB cross section of the layer stack. The black dashed lines and labels indicate the corresponding layers. Note that the Pt layer on top is not part of the device.

Electrical contact pads to the hole arrays were fabricated by introducing a 5 μm wide electrical isolation around the hole arrays (see Figs. 7.1a,b). Focused-ion beam (FIB) milling was used to locally remove the Au top layer. 55 μm long trenches (5 μm wide, 60 nm deep) were milled to locally expose the Al_2O_3 layer. These dimensions were optimized for electrical isolation. As a result, 45 × 45 μm squares (containing the hole arrays) were electrically isolated from the surrounding gold, providing ample room for electrical contacting.

Figure 7.1c shows a SEM image of the fabricated 320 nm pitched hole array. The holes clearly resemble the designed cylindrical shape, although small height variations can be observed in the Au film as a result of roughness in the layers underneath. A bright-field optical microscope image (Fig. 7.1d) shows a completed device. The electrically isolating surrounding is clearly visible, showing the exposed

Al_2O_3 (pink). Also, the hole array can be observed in the top left corner of the device as a result of optical absorption (dark green). The orange spots surrounding the hole array are attributed to minor damage to the Al_2O_3 and Ag back reflector as a result of exposure to the NMP during the lift-off procedure. Figure 7.1e shows a FIB cross section of the layer structure. All layers can be clearly observed. Note that the Pt layer on top is not part of the device, but deposited to enhance the quality of the cross section.

7.3 Optical simulations

The sample geometry was optimized for strong resonant absorption in the hole array using finite-difference time-domain simulations [137]. Arrays of cylindrical holes (d = 120 nm) in a 20 nm thin Au film were simulated using periodic boundary conditions in the in-plane directions and perfectly-matched layers (PMLs) in the vertical direction. The hole array was positioned on an Al_2O_3 layer with thickness t, on top of a semi-infinite Ag substrate. A broadband plane-wave (λ = 500–900 nm) was used as a source. Using power-flux monitors the fraction of the incident power reflected from the layer stack, and the fraction transmitted into the substrate were calculated. A 10 nm mesh with a 1 nm refinement mesh around the Au layer containing the hole and the Al_2O_3–Ag interface was used. (Electron-density dependent) optical constants for the Au were obtained from a Brendel-Bormann Gaussian oscillator model, using the method outlined by Rakic et al. [213] (see also Supplemental Section 5.6.1). Optical constants for the Al_2O_3 (see Supplemental Fig. 7.8) and Ag were obtained from spectroscopic ellipsometry.

Figure 7.2a shows the simulated absorption in the hole array (color) as a function of wavelength and Al_2O_3 thickness t for a hole diameter of d = 120 nm. Three clear bands of strong absorption can be observed; one strongly dispersive with t, and two weakly dispersive with t. The strongly dispersive band of enhanced absorption is due to a Fabry-Pérot resonance in the layer stack, which was also observed for a flat non-patterned layer stack. The weakly dispersive bands around λ = 650 nm and λ = 800 nm are due to diffractive coupling to strongly absorbing SPP modes. SPPs in ultra-thin Au films have been demonstrated to give rise to strong localized absorption, as a result of the high field intensities in the metal associated with the coupling between SPPs on the top and bottom interface [223]. Furthermore, light scattered by the SPP modes in the downward vertical direction is reflected by the Ag reflector. By accurate tuning of the Al_2O_3 thickness, the phase of the reflected light can be controlled. As a result, the coupling between vertical plane-waves and the SPP modes can be engineered. Critical coupling occurs when the internal loss rate and the radiative loss rate are equal [98, 254], yielding perfect (100%) absorption in the layer stack [252, 255]. Moreover, coupling between SPPs on the thin Au film and Al_2O_3–Ag interface results into a symmetric and anti-symmetric SPP mode (see Supplemental Figs. 7.9b-c), giving rise to two bands of strong absorption in Fig. 7.2a.

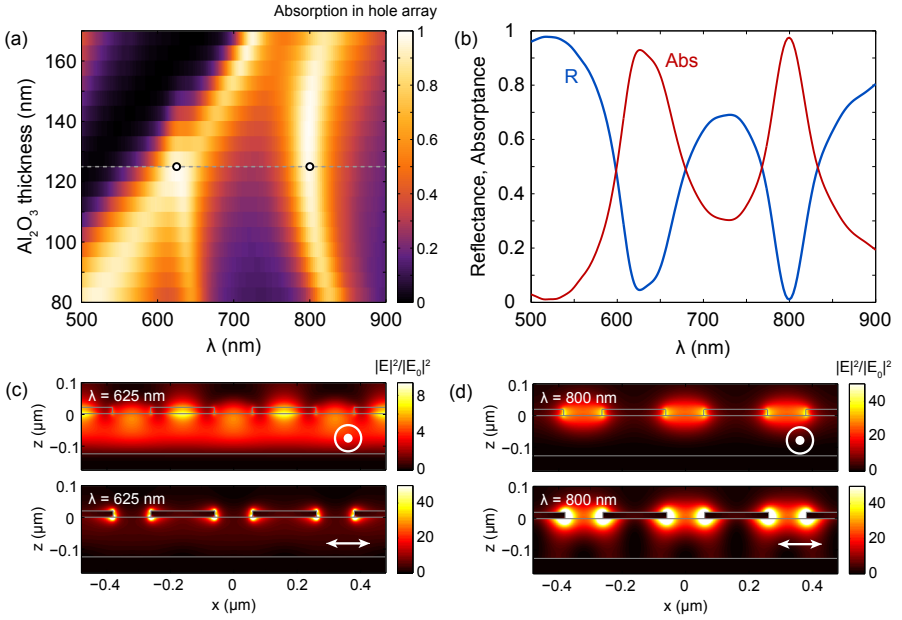

Figure 7.2: (a) Simulated absorption in the Au hole array (d = 120 nm) as a function of wavelength and thickness of the Al_2O_3. The gray horizontal line indicates the cross cut shown in (b, red). The black circles indicate the wavelength of the cross cuts shown in (c–d). (b) Absorption in hole array (red) and reflection (blue) for t = 125 nm, showing 97.5% absorption at λ = 800 nm. (c) Cross cut of the intensity distribution for λ = 625 nm in the plane perpendicular (top) and parallel (bottom) to the axis of the incident polarization (indicated by white arrow). Both the Fabry-Pérot (top) and SPP (bottom) modes are clearly visible. (d) Cross cut of the intensity distribution for λ = 800 nm in the plane perpendicular (top) and parallel (bottom) to the axis of the incident polarization, showing the strongly absorbing SPP mode. Note that the color scale of the latter is saturated for improved visibility.

Near-unity absorption occurs at λ = 800 nm for t = 125 nm, with a large free spectral range (Fig. 7.2b). In fact, 97.5% of the incident light is absorbed in the 20 nm thin hole array as a result of efficient coupling to the symmetric SPP mode. The concurrent low overall reflection (1.1%) shows that only 1.4% of the incident light is absorbed by the back reflector. The high amplitude and high Q of the absorption resonance are both advantageous for the observation of the plasmoelectric effect (see Chapter 6).

To further examine the origin of the strong absorption, Figs. 7.2c-d show cross cuts of the intensity distribution along the planes perpendicular (top) and parallel (bottom) to the electric field polarization of the incident light (white arrow), for λ = 625 nm and λ = 800 nm respectively. Figure 7.2c shows both field intensities delocalized throughout the Al_2O_3 (top) and confined to the Au film (bottom). This

is caused by the simultaneous excitation of the Fabry-Pérot mode and the anti-symmetric SPP mode. The lack of an avoided crossing (Fig. 7.2a) indicates weak coupling between these modes. Figure 7.2d on the other hand, merely shows a field distribution that is strongly confined to the Au film as a result of the symmetric SPP mode, thereby giving rise to very strong absorption in the thin Au. Note that coupling to SPPs can occur along both axes of the hole array, depending on the incident polarization (see Section 5.6.8).

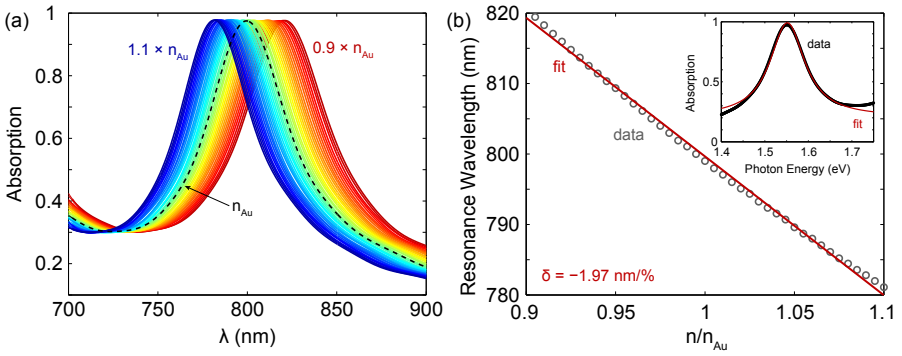

Figure 7.3: (a) Absorption in hole array (d = 120 nm) for Au with an electron density ranging from 0.9 (red) to 1.1 (blue) times that of neutral Au (black dashed). A clear blue shift in the SPP resonance wavelength is observed with increasing electron density. (b) Resonance wavelength (gray dots) obtained from Lorentzian fits to the data in (a) as a function of electron density. A linear fit through the obtained resonance wavelengths (red line) is used to estimate the spectral sensitivity, which is found to be -1.97 nm/% increase in electron density. As an example, the fit for $n/n_{Au} = 1$ is shown as an inset.

To examine the applicability of the resonant structure in Figs. 7.2b-d to generate plasmoelectric potentials, we study the spectral sensitivity with respect to electron density in the hole array. As the plasmoelectric effect is driven by the increase in entropy as a result of electron injection, a strong spectral sensitivity is beneficial. Figure 7.3a shows the simulated absorption in the hole array for electron densities ranging from 90% (red) to 110% (blue) of that of neutral Au. As a reference, the absorption spectrum of the neutral hole array is also shown (black dashed line). A strong blue shift (red shift) is observed for increased (decreased) electron density, while the peak absorption is larger than 97% for all electron densities. To quantify the spectral sensitivity with electron density, a Lorentzian fit in energy space (see inset of Fig. 7.3b for example) is used to determine the resonance wavelength of each spectrum in Fig. 7.3a. The results are displayed in Fig. 7.3b (gray dots), and indicate a 39 nm spectral shift for the lowest electron density (λ_{res} = 821 nm) compared to the highest (λ_{res} = 782 nm). Motivated by the linear relation between resonance wavelength and electron density observed for metal nanoparticles [202, 236], we apply a linear fit to the gray dots to retrieve the spectral sensitivity (red line).

Although there is a non-zero residual error in the fit, the −1.97 nm/% obtained from the linear approximation gives a good indication of the spectral sensitivity. This strong spectral sensitivity with electron density provides the essential feedback mechanism required for the observation of the plasmoelectric effect, analogous to the case for plasmonic nanoparticles (see Chapters 5 and 6). Note that although the spectral sensitivity observed here is slightly lower than that observed for Au nanorods in solution (>3 nm/%) [202], the relative absorption enhancement as a result of electron injection is significantly larger for the hole array (see Supplementary Fig. 7.10).

7.4 Optical experiments

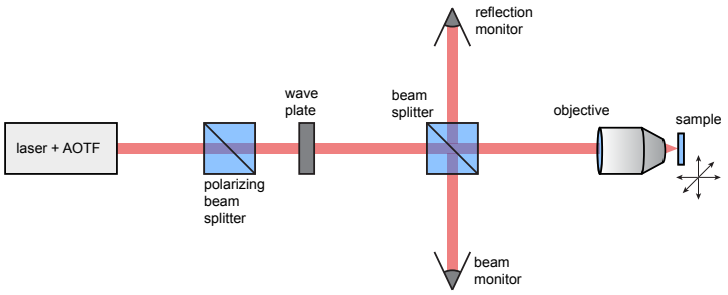

Figure 7.4: Schematic representation of the optical setup.

Optical reflection spectra of the fabricated hole array devices were measured in order to determine the absorption spectra. A sketch of the setup is shown in Fig. 7.4. A white-light supercontinuum laser (Fianium WL-SC-400-4) was sent through an acousto-optical tunable filter (AOTF, Crystal Technologies, ~4 nm bandwidth) and digitally modulated at 20 kHz (block pulse, 50% duty cycle). The measurements were performed in two separate spectral ranges and subsequently stitched; visible ($450 < \lambda < 700$ nm) and NIR ($700 < \lambda < 900$ nm). The polarization was controlled using a polarizing beam splitter (Thorlabs PBS-101 and PBS-102) and a broad band half-wave plate (AHWP05M-600 and AHWP05M-980). The polarized light was sent through a 50-50 beam splitter (Thorlabs CM1-BS013). One beam is used to illuminate the sample, the other was directed onto a Thorlabs amplified Si photodetector which was used as a beam monitor in order to correct for power fluctuations in the source. The light was subsequently focused onto the hole arrays using a Mitutoyo M Apo Plan NIR 50× 0.42 *NA* objective (17 mm working distance, <2 μm spot size). The same beam splitter was used to send the reflected light onto a second amplified Si photodetector. Stanford Research Systems SR830 lock-in amplifiers were used to read out the photodetectors. The sample was mounted on a 3D piezo stage (Piezo-

jena Tritor 400) to allow for spatial mapping of the reflectivity. A protected silver mirror (Thorlabs PF10-03-P01) was used as a reference sample for the reflection measurements, to correct for the system response. The absorption in the hole array is approximated as $1-R$. Note that the devices were electrically isolated during the optical reflection measurements, thereby preventing spectral broadening due to the plasmoelectic effect.

Figure 7.5a shows the measured absorption spectra for devices with hole arrays with diameters ranging from 110 nm (blue) to 150 nm (red). The spectra are stitched at $\lambda = 700$ nm. The small stitching mismatch indicates an absolute uncertainty of ~0.02 in the measurements of the absorption amplitude. Also shown is the absorption of a flat non-patterned reference device (gray). A strong peak in absorption around $\lambda = 800$ nm is observed for all hole diameters as a result of the absorption resonance, which is not present for the flat reference. The broad peak around $\lambda = 640$ nm as a result of the combined Fabry-Pérot resonance and anti-symmetric SPP mode is also clearly reproduced. Furthermore, both a distinct red shift and broadening of the resonant absorption peak is observed with increasing hole diameter.

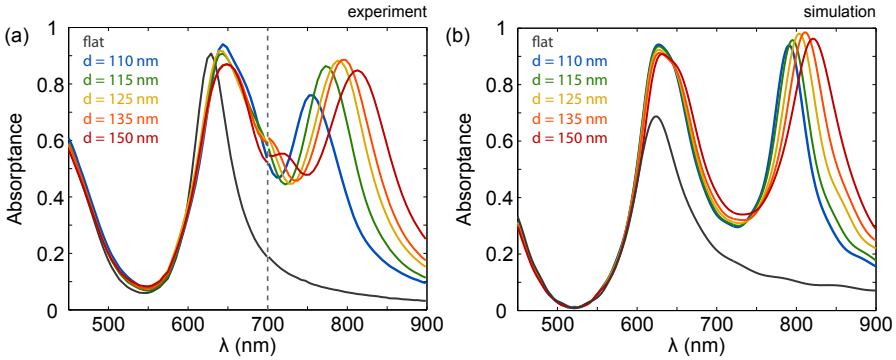

Figure 7.5: (a) Measured absorption spectra (calculated as $Abs = 1-R$) for devices with hole diameters ranging from 110 nm (blue) to 150 nm (red). The absorption spectrum measured on a flat device is also shown in gray. (b) Simulated absorption in the hole array for the same hole diameters (color) and flat device (gray).

To further explore the influence of hole size, Fig. 7.5b shows the simulated absorption spectra for the experimentally obtained hole diameters. The overall trends show good comparison with the experimental spectra: both resonant peaks are reproduced. Also the red shift and broadening of the absorption resonance with increasing hole diameter is visible in the simulated spectra, although significantly weaker. We attribute this broadening to enhanced radiation losses as a result of the increased scattering cross section of larger holes. Moreover, further comparison between the experimental and simulated spectra shows three more observations. First, the detailed trends in the absorption peaks are well-reproduced: both

the simulated and the experimental spectra show maximized absorption for d = 135 nm. Second, the experimental spectrum for the flat reference device reaches a maximum absorption of 0.91 compared to 0.69 for the simulated curve. This indicates increased absorption losses in the gold film, which may be caused by surface roughness and other non-idealities in the geometry. Third, the experimental absorption spectra show a significantly reduced amplitude and increased width for the resonance around λ = 800 nm, compared to the simulated spectra. This indicates that the internal absorption loss rate and radiative loss rates are unbalanced. This can be attributed to small differences in geometry and material properties compared to the theoretical structure. Despite these dissimilarities, the absorption spectra shown in Fig. 7.5a show a very distinct and strong absorption resonance that can be utilized to induce plasmoelectric potentials.

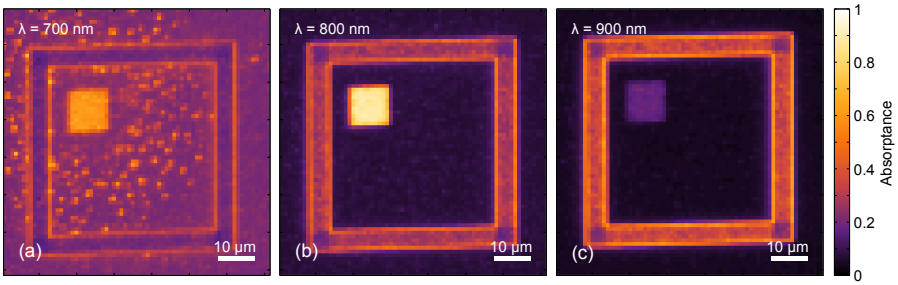

Figure 7.6: Measured spatial absorption profiles of a device with d = 135 nm for λ = 700 nm (a), λ = 800 nm (b), and λ = 900 nm (c). The strong locally enhanced absorption by the hole array is clearly visible for λ = 800 nm, whereas the contrast is strongly reduced off resonance (λ = 900 nm). Moreover, the optical absorption as a result of the minor damage is observed for λ = 700 nm. The spatial step size during the scans was 1 μm.

To further demonstrate the strong absorption in the active plasmonic element of the devices, we measured spatial absorption maps of the complete devices for different incident wavelengths. Figure 7.6 shows the absorption (color) of a device with d = 135 nm for λ = 700 nm (a), λ = 800 nm (b), and λ = 900 nm (c). The device geometry (Fig. 7.1b) is evident in all three spatial maps. Both the electrically isolating surrounding and the absorbing hole array can be recognized. The resonant absorption is apparent from the strong contrast for λ = 800 nm, and weak contrast for λ = 900 nm (see spectra in Fig. 7.5). Moreover, the minor damage to the Al_2O_3 and Ag shows enhanced absorption for λ = 700 nm, but is insignificant for λ = 800 nm. The regions of low absorption in the corners of the surroundings are caused by local overexposure during the FIB milling, thereby slightly changing the Al_2O_3 thickness. Figures 7.6a-c clearly show how the hole array functions as an active plasmonic element in the device layout. Next, we will discuss the experimental procedure for the optoelectronic experiments.

7.5 Optoelectronic experimental design

Upon off-resonance monochromatic illumination of the hole array the plasmoelectric effect will locally induce a non-zero thermodynamic potential in the Au film. As a result, electrons will flow into or out of the hole array. The change in electron density in the hole array induces a non-zero electrostatic potential, which will counteract the plasmoelectric potential. The redistribution of charge will stop when the effective potential is zero (i.e. electric and plasmoelectric potential cancel). The new equilibrium condition will be sustained as long as the illumination conditions remain unchanged, such that no current will flow under continuous illumination.

To exploit the transient currents induced by the plasmoelectric effect, we designed an AC experiment in which the charging/discharging current of the hole array is measured over time. The proposed experimental procedure is summarized in Fig. 7.7. First, wire bonding is used to provide electrical contacts, both to the device and to the Ag ground plane (wire A and B in Fig. 7.7a respectively). To contact the Ag, the Al_2O_3 is locally scratched away, and Al wires are subsequently bonded to the scratch. A simplified circuit diagram of the experimental setup is shown in Fig. 7.7b. The hole array is assumed to form a parallel-plate capacitor with the Al_2O_3 dielectric spacer and Ag back reflector, characterized by a capacitance C. Note that the potential over the Au film will not be uniform as the plasmoelectric potential is zero outside the illumination spot. The bottom Ag plate is grounded (wire B). Under pulsed illumination the active plasmonic hole array functions as an AC potential source, inducing a time-varying thermodynamic potential V_{PE} on the top plate. Driven by this potential, electrons can flow from ground through a current meter (through wire A) into the top plate. This charging/discharging pathway is characterized by a series resistance R_C, which is determined by the resistance of the wire, bond and sheet resistance of the Au film. Furthermore, the Au–Al_2O_3–Ag multilayer capacitor is characterized by a leakage resistance R_L. Effective charging of the capacitor is restricted by the condition $R_L \gg R_C$. Current-voltage measurements on the experimental device showed that $R_C < 20\ \Omega$ whereas $R_L \sim 100\ \text{G}\Omega$, limited by the lateral conductivity across the isolating surrounding.

To estimate the order of magnitude of the currents that can be expected, we consider the charging of a capacitor with N electrons under voltage V: $N = CV/e$, where e is the electron charge. Assuming a parallel-plate geometry, a 2 μm laser spot (defining the area of the capacitor), and a static relative dielectric permittivity of $\epsilon_s = 9$ for the Al_2O_3, we find that $C \approx 2$ fF. Furthermore, assuming $V_{PE} = 100$ mV (see Chapter 5), the total number of electrons transferred from ground to the top plate upon charging is roughly 1250. Assuming a $(1/e)$ 10 μs rise time of the capacitor, this corresponds to a peak transient current of 20 pA. Note that the capacitance, and thereby the current can be drastically enhanced by applying a water-based electrolyte on top of the device (see Fig. 7.7a), as a result of the large static dielectric constant of water and the double-layer screening by counter ions [202]. The presence of the electrolyte changes the dielectric surrounding of the hole array,

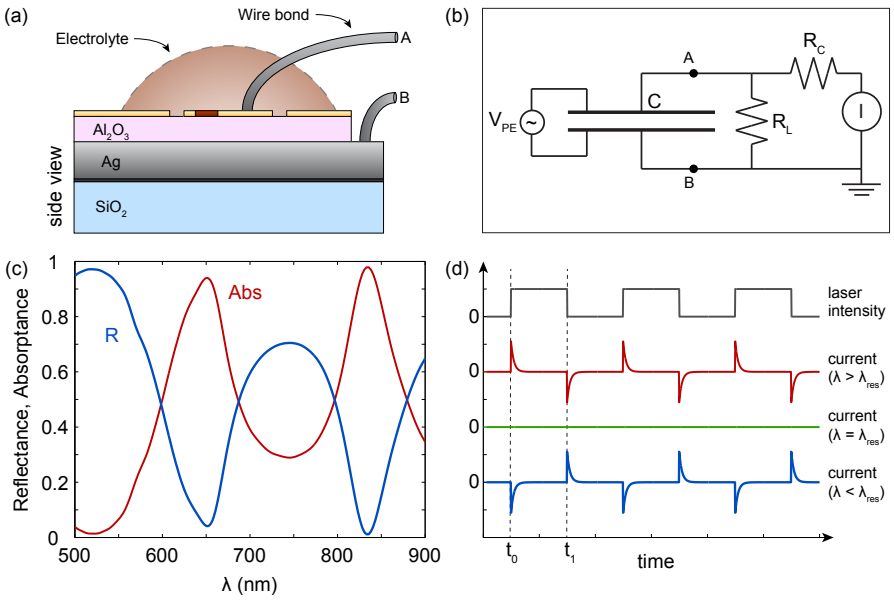

Figure 7.7: (a) Side view of the proposed electrical experiment. Both the Au device and the Ag back electrode are contacted by wire bonding with thin Al wires. The surface is covered by a droplet of electrolyte to enhance the capacitance of the device. (b) Simplified electrical circuit diagram of the experiment. I represents a current meter (e.g. oscilloscope), R_L corresponds to the capacitor leakage resistance, and R_C to the series resistance experienced during charging/discharging. The points A and B correspond to the ends of the wire bonds (indicated in (a)). (c) Simulated absorption in the hole array (red) and reflection (blue) for a device with $d = 120$ nm in a water environment (electrolyte). (d) Sketch of expected current measurements upon pulsed illumination (gray top), for $\lambda > \lambda_{res}$ (red), $\lambda = \lambda_{res}$ (green), and $\lambda < \lambda_{res}$ (blue).

which may change the resonance wavelength of the hole array. To investigate the resonant response under the presence of an electrolyte, Fig. 7.7c shows the absorption (red) and reflection (blue) spectra for a hole array with $d = 120$ nm in a water environment ($n = 1.33$). Although a clear red-shift of the absorption peak from $\lambda = 800$ nm to $\lambda = 830$ nm is observed, the resonance is still characterized by strong absorption and a high Q.

Figure 7.7d shows a schematic of the expected charging and discharging current measured by the current meter as function of time. Monochromatic illumination is modulated and used to locally illuminate the hole array. At the onset of an optical pulse (t_0), the capacitor is charged and a current I flows through the meter. Due to the exponential charging of a capacitor under constant plasmoelectric potential, the current decays exponentially while a new equilibrium is obtained. As soon as the optical pulse ends (t_1), $V_{PE} = 0$ and the capacitor will discharge, giving

rise to the same current pulse with opposite sign. Depending on the wavelength of the pulsed illumination, the current pulse at t_0 will be positive ($\lambda > \lambda_{res}$, red), zero ($\lambda = \lambda_{res}$, green), or negative ($\lambda = \lambda_{res}$, blue). This bisignated response is characteristic for the plasmoelectric effect (see Chapter 5), and distinctly different from thermoelectric currents which scale linearly with absorption and will be maximum for $\lambda = \lambda_{res}$. This experimental procedure provides the ability for the first demonstration of plasmoelectric currents and power conversion. Moreover, the lithography-generated circuits are a first step towards functional integrated plasmoelectric circuits.

7.6 Conclusions

We show the first steps towards the experimental demonstration of circuit-based plasmoelectric power conversion devices. Using finite-difference time-domain, we design a plasmonic hole array in 20 nm thin Au with near-unity absorption at $\lambda = 800$ nm. We demonstrate that this optical absorption is a result of resonant coupling to a symmetric SPP mode, and study the applicability of this hole array for the generation of plasmoelectric potentials. Next, we use electron-beam lithography and focused-ion beam milling to fabricate plasmoelectric devices that function as micro-scale capacitors. We experimentally investigate the absorption spectra of the hole arrays and the spatial absorption profiles of the devices, and find that the hole arrays cause strongly localized absorption at resonance. Finally, we design an AC experiment to measure the charging/discharging current of the micro-capacitors as a result of the plasmoelectric effect. This experiment is the first step towards the experimental demonstration of plasmoelectric power conversion.

7.7 Supplementary information

7.7.1 Spectroscopic ellipsometry on Al_2O_3

Figure 7.8 shows the real part of the refractive index of the Al_2O_3, obtained from in-situ spectroscopic ellipsometry during the thermal ALD process. The oxide is very weakly dispersive in the visible spectral range with $n = 1.64$ at $\lambda = 800$ nm, and shows no optical absorption as a result of the high band gap of the material (6.4 eV).

7.7.2 SPP dispersion and mode profiles

Dispersion curves and modal field profiles of the coupled SPP modes on the flat layer stack were calculated using a mode-solver analogous to ref. [162]. Using the geometry and the corresponding dielectric constants of the Au–Al_2O_3–Ag layer stack, the complex wave vectors of the plasmonic eigenmodes are calculated. To do this, the optically thick Ag and the air above the Au are assumed to be semi-infinite, and the layers are assumed to be perfectly smooth (presence of holes is

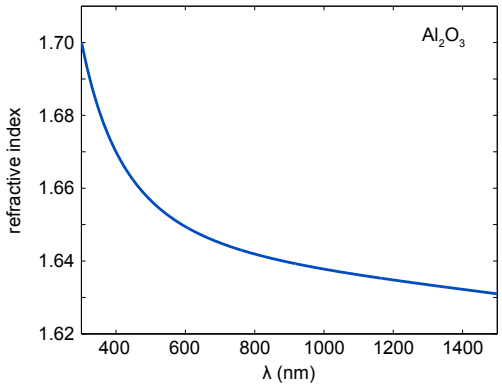

Figure 7.8: Measured refractive index of the Al_2O_3 layer, obtained from in-situ spectroscopic ellipsometry.

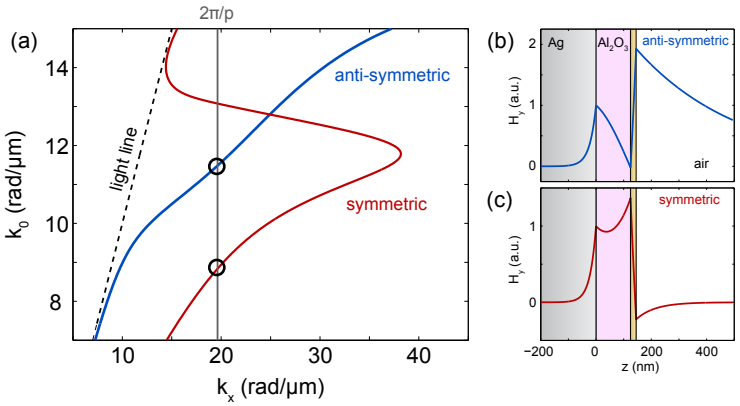

Figure 7.9: Calculated dispersion curves (a) and field profiles (b-c) for the symmetric and anti-symmetric MIM plasmon mode supported by the layer structure. Also shown is the light line in air (black dashed) and the momentum obtain from diffraction off the hole array (gray). The black dots indicate the wavelengths where the incident light couples to the plasmon modes. Note that the holes are not taken into account in the calculation.

neglected). Figure 7.9 shows the dispersion curves (a) and field profiles of the anti-symmetric (b, blue) and symmetric (c, red) SPP modes. The displayed field profiles correspond to the out-of-plane magnetic component (H_y), and clearly show the (anti-)symmetric coupling between the SPP on the Ag–Al_2O_3 interface and that on the Au film. Also shown in (a) is the light line in air (black dashed), and

the momentum obtained from the [±1,0] diffraction order of the hole array with $p = 320$ nm (vertical gray line).

Diffractive coupling to the SPP modes under normal incidence occurs when the wave vector of the mode matches the in-plane momentum of the grating order; $k_{SPP} = 2\pi/p$ (i.e. where the gray line intersects the dispersion curves). In the spectral range considered in Fig. 7.2, coupling to the anti-symmetric and symmetric mode occurs at 547 nm and 711 nm, respectively (black circles in Fig. 7.9a). We attribute the spectral mismatch with the experimental resonance wavelengths (640 nm and 800 nm) to the absence of the holes and surface roughness in the calculations. Indeed, simulations show that the resonance wavelength is sensitive to the size of the holes, and thereby the filling fraction of the Au layer. Despite the spectral mismatch, Fig. 7.9 clearly illustrates the plasmonic nature of the resonant modes observed in Fig. 7.2 and Fig. 7.5.

7.7.3 Electron-density dependent absorption

Figure 7.10 shows the relative increase in absorption as a function of electron density and wavelength $Abs(n,\lambda)$, compared to the absorption in a neutral hole array:

$$\frac{Abs(n,\lambda) - Abs(n_{Au},\lambda)}{Abs(n_{Au},\lambda)}. \tag{7.1}$$

The spectral sensitivity (see Fig. 7.3b) is clearly visible as the slope in the white horizontal line. Moreover, a relative increase in absorption as large as 75% can be observed as a result of charge injection (e.g. for $\lambda = 835$ nm the absorption increases from 0.48 to 0.84 due to the reduction of the electron density). This large increase in absorption shows the excellent suitability of the geometry for observation of the plasmoelectric effect.

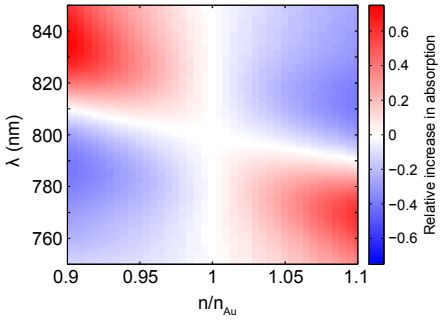

Figure 7.10: Simulated relative increase in absorption compared to the neutral hole array, as a function of relative electron density (n/n_{Au}) and wavelength.

8

Resonant modes of single silicon nanocavities excited by electron irradiation

High-index dielectric or semiconductor nanoparticles support strong Mie-like geometrical resonances in the visible spectral range. We use angle-resolved cathodoluminescence imaging spectroscopy to excite and detect these resonant modes in single silicon nanocylinders with diameters ranging from 60 to 325 nm. Resonances are observed with peak-wavelengths in the range of 400–700 nm, and show a strong red shift with increasing cylinder diameter. The photonic wave function of all modes is determined at deep-subwavelength resolution and shows good correspondence with numerical simulations. An analytical model is developed that describes the resonant Mie-like optical eigenmodes in the silicon cylinders using an effective index of a slab waveguide mode. It shows good overall agreement with the experimental results and enables qualification of all resonances with azimuthal (m = 0–4) and radial (q = 1–4) quantum numbers. The single resonant Si nanocylinders show characteristic angular radiation distributions in agreement with the modal symmetry.

8.1 Introduction

Nanoparticles and nanowires made from high-index semiconductor or dielectric materials have the ability to strongly confine and scatter light [28, 256–258]. These

properties make them interesting for a large range of applications including solar cells [33, 60, 85, 89, 91, 92, 259–262], lasers [263], and nanoscale photodetectors or sensors [57, 58, 61, 264, 265]. Unlike their metallic counterparts, where light is confined to the surface in the form of surface plasmons, in semiconductor/dielectric nanostructures, light is mostly confined within the nanostructure. The resonant eigenmodes of these cavities are often referred to as Mie resonances, after the Lorentz-Mie-Debye solution to Maxwell's equations, which can be used to describe scattering by wavelength-scale spherical nanoparticles in a uniform dielectric environment [28]. They can also be referred to as geometrical resonances because of their similarity to whispering gallery modes [89, 266].

Silicon is an ideal base material for resonant Mie cavities. Due to its high refractive index, it can strongly confine light, while its indirect electronic band gap leads to relatively low absorption losses. Due to the compatibility with CMOS fabrication processes, resonant Si Mie scatterers can be readily integrated into optoelectronic devices based on silicon. The first applications of silicon Mie scatterers in metamaterials [43, 53, 54], optical antennas [33, 39, 41, 43, 44], and anti-reflection coatings [33] are appearing just recently and show the great potential of Mie scatterers as optical building blocks in nanophotonic nanostructures and devices. To fully unleash the potential of these nanoscale Si light scatterers, detailed understanding of their fundamental scattering properties is essential. However, standard optical techniques have been unable to fully resolve the Mie resonant modes due to lack of spatial resolution.

In this Chapter, we study the resonant optical properties of individual silicon cylinders using angle-resolved cathodoluminescence (CL) imaging spectroscopy [267–269]. With this technique, a 30 keV electron beam acts as a broad-band point source of light that can be employed to probe the optical properties of nanostructures with deep-subwavelength spatial resolution [270, 271]. We determine the spectral and spatial characteristics of the resonant optical eigenmodes for single silicon nanocylinders with different diameters. We compare our results with finite-difference time-domain (FDTD) simulations and an analytical model, and we identify the fundamental and higher-order radial and azimuthal modes of the cavities. In addition, we present experimental data on the angular distribution and polarization of light emission from single resonant Mie cavities.

8.2 Sample fabrication

Figure 8.1a shows the geometry of the sample. Single Si nanocylinders were fabricated on a thin SiO_2 layer, supported by a Si substrate. The fabrication starts with a silicon-on-insulator (SOI) wafer with a 100 nm Si layer on a 300 nm SiO2 layer. Electron beam lithography (EBL) is used to write circular pads as an etch mask in a negative tone resist. Next, anisotropic reactive ion etching (RIE) is used to etch down the top Si layer of the SOI wafer, such that Si nanocylinders are formed

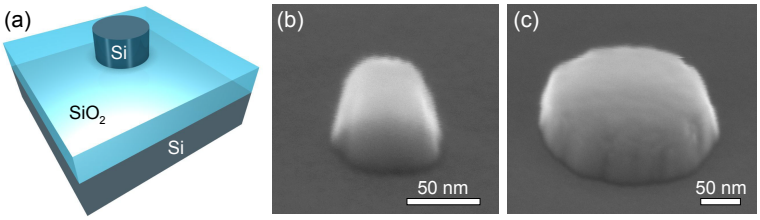

Figure 8.1: (a) Sketch of the sample geometry. Single silicon cylinders are fabricated on a thin silica layer, supported by a silicon substrate. SEM images of fabricated cylinders with base diameters of (b) 80 nm and (c) 200 nm. The cylinders are slightly tapered toward the surface.

on top of the silica layer. Residual resist is removed using an oxygen plasma etch. The resulting cylinders have diameters ranging from 60 to 325 nm and are 100 nm high. Scanning electron micrographs of a small (d = 80 nm) and large (d = 200 nm) cylinder are shown in Figs. 8.1b,c, respectively. From the electron micrographs, it can be seen that the cylinders are slightly tapered due to the non-perfect anisotropy of the Si etch but clearly resemble the intended cylindrical structure.

8.3 Imaging Mie modes in silicon cylinders

To measure the resonant optical properties of single cylinders, we use angle-resolved cathodoluminescence (CL) imaging spectroscopy [267–269]. The electric field generated by a high-energy electron passing through a dielectric nanoparticle induces a transient vertically oriented polarization that results in the coherent excitation of the resonant modes supported by the Si nanocylinder at a rate that is proportional to the out-of-plane component of the local density of optical states (LDOS) [270, 271]. The excited local modes radiate into the far field; the radiation is collected by a parabolic mirror placed between the sample and the electron column, after which both the spectrum and the angular distribution are analyzed. Since the electron beam can be scanned at very high spatial resolution and the electron range is well beyond the thickness of the Si nanostructures, spatial information about the optical modes inside the nanostructures can be obtained far below the diffraction limit of light.

To probe the resonant optical response we raster-scan a 30 keV electron beam in 10 nm steps over a Si cylinder and collect a CL spectrum for each position. In parallel, we collect the secondary electron (SE) signal to obtain geometrical information about the cylinder (see insets in Figs. 8.2a,b). These data are used to define a spatial mask for the CL data, based on a threshold in SE counts, in order to select the pixels in the CL map corresponding to the Si cylinder.

The CL from the Si cylinders is superimposed on a broad background signal peaking at λ_0 = 650 nm due to CL from intrinsic defects in the SiO_2 matrix, which

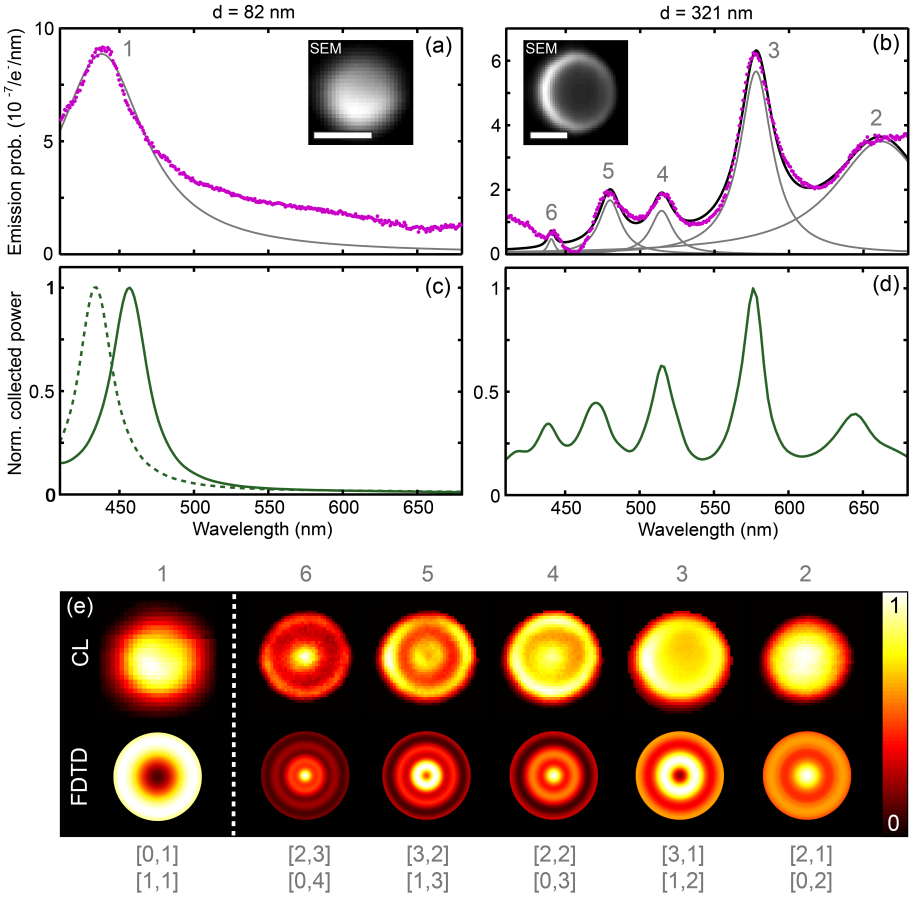

Figure 8.2: (a) Spatially integrated cathodoluminescence spectrum (purple dots) for an 82 nm diameter cylinder. A Lorentzian line shape is fitted to the spectrum (gray curve). The inset shows the secondary electron map collected simultaneously with the CL data collection (scale bar: 50 nm). (b) Similar measurement for a 321 nm diameter particle. The spectrum is fitted with a sum of five Lorentzians (black curve) that are also plotted individually (scale bar SEM image: 150 nm). (c) Normalized FDTD simulation of collected power as function of wavelength for 80 nm (solid green curve) and 70 nm (dashed green curve) cylinders. (d) Same as (c) for a 321 nm cylinder (solid green curve). (e, Top row) Two-dimensional CL intensity maps shown at resonance wavelengths indicated in (a) and (b), displaying the photonic wave functions of the different resonances. (e, Bottom row) Corresponding time-averaged intensity maps calculated using FDTD. The labels $[m,q]$ indicate the corresponding branches in Fig. 8.3b from the analytical model.

can vary slightly in intensity over time under electron beam irradiation [272]. We use a triangular interpolation routine to subtract this variable background from the CL signal from the cylinders (see Section 8.10). In the experimental geometry, the thickness of the SiO_2 layer was chosen as a compromise between minimizing background from the SiO_2 layer on the one hand and optical isolation of the Si cylinder from the high-index silicon substrate on the other hand.

Figure 8.2a shows the spatially integrated CL spectrum for an 82 nm diameter nanocylinder. A clear peak is observed in the spectrum at $\lambda_0 = 439$ nm corresponding to an optical resonance in the nanoparticle. For accurate determination of the peak wavelength, we fit a Lorentzian line shape to the spectrum, using a least-squares fitting routine (solid gray curve). From the width of the Lorentzian, we determine the quality factor of the resonance to be $Q = 6$. The magnitude of Q is determined both by absorption of light by the Si cylinder and radiative loss. Figure 8.2b shows the CL spectrum for a 321 nm diameter cylinder, which shows multiple peaks at $\lambda_0 = 440$, 480, 515, 578, and 662 nm (labeled 2–6 in the figure, as will be discussed further on). Due to the larger diameter, this cylinder supports multiple resonant modes of different order within the experimental spectral range. The spectrum is fitted with a sum of five Lorentzians (black curve) which corresponds well to the measured spectrum. The quality factors derived from the individual fits are $Q = 77$, 27, 29, 22, and 9 for modes with increasing wavelength. Note that the high quality factor of the first peak at $\lambda_0 = 440$ nm has a large uncertainty due to the low intensity with respect to the background signal. To study the spatial characteristics (*i.e.* the "photonic wave functions" of the resonant modes), we determined the two-dimensional excitation distribution at each resonance wavelength. To obtain sufficient signal-to-noise ratio, we integrate the spectra over a 20 nm bandwidth. Figure 8.2e (top row) shows these maps for the numbered peak wavelengths indicated in Figs. 8.2a,b. For the small nanoparticle, the CL emission is observed from the entire nanoparticle, with an antinode (maximum) observed in the center. For the large cylinder, the spatial maps are more complex and consist of multiple rings and dots with alternating minima and maxima in the center, corresponding to resonances with higher radial mode orders, as will be discussed below.

8.4 Numerical modeling

Numerical modeling is performed using finite-difference time-domain (FDTD) simulations [137]. Single Si cylinders (diameter $d = 50$–350 nm, height $h = 100$ nm) are placed on a 300 nm thick SiO_2 layer on a Si substrate. In the simulations, the electron source is approximated by a single broad-band vertically oriented electric dipole positioned at 50 nm height inside the cylinder. Radiation from the cylinder into the upper hemisphere is collected using transmission monitors. To simulate a resonant spectrum, the dipole position is varied from the center ($r = 0$) to the outer radius of the cylinder ($r = d/2$), in steps of 5 nm. The collected power spectrum for each radius is then multiplied by $2\pi r$ to account for the cylindrical geometry; all

power spectra are summed, and the result is normalized to its maximum. Optical constants for Si and SiO_2 are taken from Palik [138].

The results for the 80 and 320 nm diameter cylinders are shown in Figs. 8.2c,d, respectively, where the spatially integrated collected power (green solid lines) is shown as a function of free space wavelength. As in the experiment, the 80 nm cylinder clearly shows one single peak (Q = 16), corresponding to the lowest-order resonance, whereas the 320 nm cylinder shows many peaks due to higher-order resonances. Compared with the experiment for the 80 nm cylinder, the simulated peak wavelength is off by 18 nm. We attribute this to the small tapering of the cylinders, resulting in a slightly reduced diameter at the surface, as can be observed in Figs. 8.1b,c. Indeed, the simulated spectrum for a 70 nm diameter (dashed line) matches the measured spectrum quite well. This indicates that the effective diameter of a particle with an 80 nm diameter base is 70 nm, in good correspondence with the SEM image in Fig. 8.2a. The simulated spectrum for the 320 nm diameter particle in Fig. 8.2d shows good agreement with the different resonances with the experiment. In agreement with the experiment, the simulated peak at λ_0 = 575 nm has the highest intensity. The simulated quality factor for the five modes is Q = 21, 19, 24, 30, and 15, which is in the same range as the experimental values, except for the small lowest-wavelength peak. The observed Q is determined by both absorption in the particle and the radiative coupling to the far field. Absorption losses are larger in the blue spectral range due the higher absorption of silicon in that wavelength range.

Figure 8.2e, bottom row, shows the simulated time-averaged photonic wave functions. Analogous to the experiment, the peak intensity is integrated over a 20 nm bandwidth around the peak wavelength for each dipole position, giving the peak intensity as a function of radial position. The data set is then rotated to obtain the two-dimensional photonic wave function maps. Simulations are shown for the 80 and 320 nm diameter cylinders for each resonance. The simulated photonic wave function of the lowest-order mode for the 82 nm cylinder (peak 1) shows a bright ring, while the measurement shows a more uniform distribution peaking in the center. For the 320 nm cylinder, the simulations show good agreement with the measured trends. For lower resonance wavelengths (going from peak 2 to peak 6), more nodes and antinodes are observed in the radial direction, corresponding to higher-order radial modes. For the highest-order mode (peak 6), a bright dot is observed in the center, surrounded by two bright rings. The alternating dark and bright center of the cylinder observed for subsequent resonances is also reproduced in the simulations.

8.5 Mode evolution as a function of particle diameter

From Fig. 8.2, it is clear that the resonant behavior of the cylinders strongly depends on the diameter. To gain more insight into the spectral mode evolution of the resonances for different sizes, we collected the CL spectra from 88 different cylinders

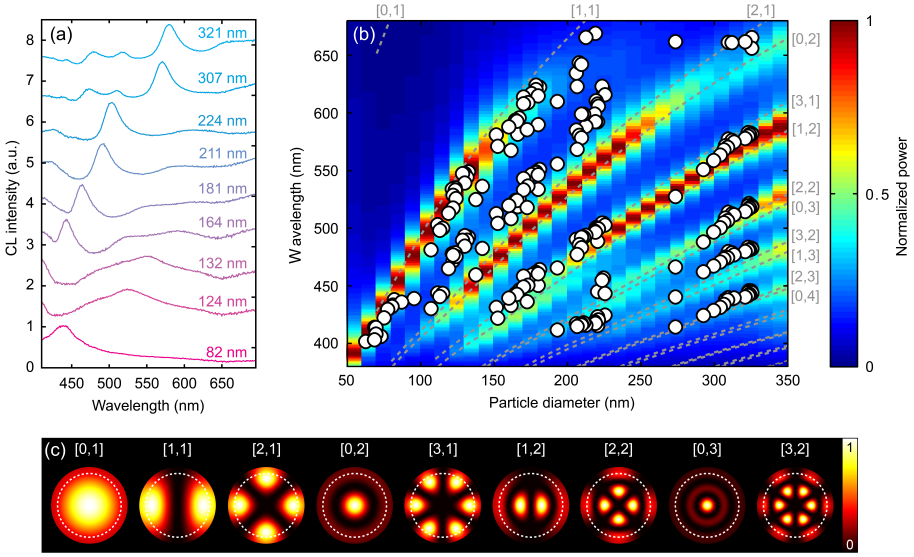

Figure 8.3: (a) Spatially integrated CL spectra for different cylinder diameters. The normalized spectra have been vertically offset for clarity. All resonances show a clear red shift for larger diameters. (b) Resonance peak wavelengths for different cylinder diameters obtained by fitting the CL spectra with Lorentzians (white dots). The color map shows the emitted power as function of particle diameter and wavelength, calculated using FDTD (normalized to its maximum for each particle diameter). The dashed gray curves correspond to the eigenvalues found for different diameter cylinders using the analytical 2D disk resonator model. Each curve is associated with a particular radial and azimuthal quantum number, indicated by the $[m,q]$ notations on the top and side of the figure. (c) Photonic wave functions for a d = 320 nm cylinder obtained from the analytical model. The time-averaged amplitude $|E_z(r,j)|^2$ is plotted. The white dashed circles indicate the edge of the particle.

with diameters ranging from 60 to 325 nm. Figure 8.3a shows a representative subset of this data set with spectra for different diameters. As the diameter increases, higher-order resonances emerge and all resonances progressively red shift as is expected for geometrical resonances [28].

By using the Lorentzian fitting shown in Figs. 8.2a,b, we determined the resonance peak wavelength for all measured cylinders. In Fig. 8.3b, these peak wavelengths are shown as a function of diameter. This figure clearly shows how each resonance mode gradually red shifts for increasing diameter. To compare the experimental resonances with the results from numerical modeling, we also plot the collected power as a function of diameter and wavelength in a 2D color plot (Fig. 8.3b). Here, every vertical slice in the color plot corresponds to a normalized spectrum, as shown in Figs. 8.2c,d. The FDTD simulations show multiple branches, each of which corresponds to a particular resonant mode in the cylinders. Both the

number of peaks as well as their peak wavelength show good agreement with the measurements, except the second branch from the top, for which the simulation is blue shifted with respect to the measurements.

8.6 Analytical disc model

To study the nature of these resonances in more detail, we developed an analytical 2D disc resonator model [273–277]. In this model, we solve for the cylindrical modes of an infinitely long cylinder, which can be analytically calculated using Maxwell's equations. Confinement in the normal direction is then included using a planar waveguide model. This is a reasonable assumption for cylinders with a diameter (much) larger than the thickness. Figure 8.4a shows the 2D slab waveguide geometry with the Si/SiO_2/Si layer stack. The 100 nm thin Si slab supports both a fundamental transverse electric (TE_0) and transverse magnetic (TM_0) mode. The incoming electrons mainly couple to vertical electric field (E_z) and in-plane transverse magnetic field components (H_T) [270], which both match the field orientations of the TM mode (see Fig. 8.4a), so that only this mode is considered further. We use a numerical method to solve for the dispersion curve of the TM_0 mode and derive from it the mode index n_{eff} at each wavelength. The result is shown in Fig. 8.4b (magenta), along with the refractive index of Si (cyan), SiO_2 (red), and air (black dashed line). For reference, the effective mode index of the TE_0 mode is also shown (blue). Figure 8.4b shows that the effective index of the TM_0 mode gradually decreases from a value close to that of Si at short wavelengths to an index approaching that of SiO_2 for long wavelengths. This can be understood from the increasing overlap of the evanescent tail of the mode profile with the silica and air cladding layer, as the wavelength is increased. We now use this effective index of the Si slab modes as input for the index of the cylinder [275–277] in the 2D Helmholtz wave equation [273, 274]

$$(\nabla_T + n^2 k_0^2 - \beta^2)\Psi = 0) \tag{8.1}$$

to solve for the radial modes. Here, Ψ is the wave function of the out-of-plane field, ∇_T is the transverse gradient, n is the refractive index in the medium, k_0 is the free space wave vector, and β is the propagation constant in the vertical direction. The solution for Eq. 8.1 is given by

$$\Psi(r,\phi) = \begin{cases} a\frac{J_m(\sqrt{n_c^2 k_0^2 - \beta^2}\, r)}{J_m(\sqrt{n_c^2 k_0^2 - \beta^2}\, R)} e^{\imath m\phi} & 0 < r < R \\ b\frac{K_m(\sqrt{\beta^2 - n_s^2 k_0^2}\, r)}{K_m(\sqrt{\beta^2 - n_s^2 k_0^2}\, R)} e^{\imath m\phi} & R < r < \infty \end{cases} \tag{8.2}$$

Here, a and b are constants, J_m is the Bessel function of the first kind, K_m is the modified Bessel function of the second kind, m is the azimuthal mode number, n_c is the effective refractive index of the cylinder, n_s the refractive index of the

surrounding medium (vacuum), r the radial position, ϕ the azimuthal angle, and R the radius of the cylinder. We consider the 2D solutions for the TM modes, $\beta = 0$ and $\Psi = E_z$. The transverse field components can easily be derived from Eq. 8.2 [273, 274]. The eigenvalue equation can be obtained from Eq. 8.2 by applying the boundary conditions $E_{z,c}(R) = E_{z,s}(R)$ and

$H_{\phi,c}(R) = H_{\phi,s}(R)$ (c = cylinder, s = surrounding), which can then be solved for different particle radii to give the eigenvalues, corresponding to the resonance wavelengths. For a given azimuthal mode number m (where $m = 0, \pm 1, \pm 2, ...$ and $m = \pm i$ are degenerate), multiple solutions are found. These correspond to higher-order resonances in the radial direction, with radial mode numbers $q = 1, 2, ...$

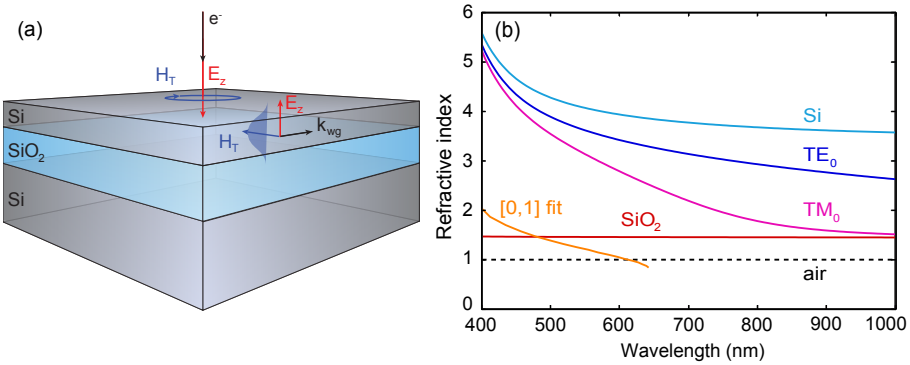

Figure 8.4: (a) Sketch of the layer structure used in the 2D analytical model to calculate the effective mode index of the TM_0 waveguide mode. Also shown are the electromagnetic field components induced by an incoming electron and those of the TM_0 waveguide mode. (b) Real part of the (effective) refractive index of the TM_0 mode (magenta), compared with the index of bulk Si (cyan curve), SiO_2 (red curve), air (dashed black curve), and the TE0 mode (blue curve). The orange line shows the index obtained when fitting the $m = 0$, $q = 1$ mode to the top resonance branch obtained from numerical modeling. It shows a cutoff above $\lambda_0 = 620$ nm.

Resonant modes calculated using the above model are shown in Fig. 8.3 as gray dashed lines. The quantum numbers $[m, q]$ of each branch are indicated on the top and side of the graph, with the lowest-order mode [0,1] occurring for the longest wavelengths. The corresponding mode profiles $|E_z(r,\phi)|^2$ are shown in Fig. 8.3c for the first nine branches, where the dashed white circle indicates the edge of the cylinders. These mode maps also show the azimuthal variations in the photonic wave functions that remain unobserved in the experiment, due to the cylindrical symmetry of the nanoparticle. The model shows good qualitative agreement with the measured data (white dots) and the numerical modeling (colormap); that is, experimental and numerical modal branches each lie close to one or two calculated branches. By comparing the model with the experimental and numerical data, we gain several insights.

First, the increasing number of peaks with increasing diameter observed in

Figs. 8.3a,b reflects the excitation of higher-order resonances. When increasing the particle diameter at a fixed wavelength, both the azimuthal (m) and the radial (q) mode orders increase stepwise. In particular, for the higher-order resonances, the analytically calculated resonances match well with the numerically calculated ones. For example, the [2,1] and [0,2] branches that could not be resolved experimentally show a close match between the analytical model and numerical simulations.

Second, we can now label the complex photonic wave function maps observed in Fig. 8.2e as a superposition of the two photonic wave functions corresponding to the resonances that match the FDTD branches in Fig. 8.3b. For example, the [3,1] and [1,2] modes in Fig. 8.3c together correspond to the map of peak 3 in Fig. 8.2e, with a dark center and two bright rings. The eigenmodes assigned to the simulated profiles in Fig. 8.2e are indicated at the bottom of that figure. The good correspondence between experiment, numerical model, and analytical model is also reflected by the fact that for the 320 nm diameter disk only those with an azimuthal order $m = 0$ show an antinode in the center (peaks 2, 4, and 6).

Third, the analytically calculated modes show strong dispersion (curved resonance branches), in agreement with both the measurements and the FDTD data. This originates from the dispersive effective refractive index n_c of the cylinder due to the strong modal confinement in the vertical dimension. Indeed, the strongly decreasing index as a function of wavelength, as observed in Fig. 8.4b for the TM_0 mode proves to be essential to predict the shape of the measured and FDTD simulated resonance branches. In fact, if the cylinder would be described using the (dispersive) index of bulk Si or using the TE_0 mode, the analytically calculated modal branches in Fig. 8.3b would increase superlinearly rather than sublinearly for longer wavelengths as is observed in the experiment and FDTD simulations. This directly proves that the modal dispersion due to the vertical confinement strongly influences the resonant behavior.

While the analytical model thus predicts many of the key features and trends in both the experiments and FDTD simulations, one discrepancy is observed: the calculated lowest-order resonance [0,1], which is visible in the top left corner of Fig. 8.3b, does not match with any branch observed in the experiment or simulations. This implies that either the lowest-order resonance is not excited in the experiment or that the assumptions of the simple 2D analytical model break down in the range where the wavelength is large compared to the particle diameter. Indeed, the waveguide model assumes an infinitely wide disk.

8.7 Angular patterns

To resolve this issue, we measured the angular emission profiles of individual Si cylinders in the CL system. Here, the light radiated by the cylinders is collected by the parabolic mirror and projected onto a CCD imaging camera; each pixel corresponds to a unique azimuthal/zenithal angle. Using this technique, it is possible

to determine the angular emission properties for such a 3D structure on a layered substrate, which is difficult if not impossible to predict either analytically or with numerical methods such as the boundary element method (BEM), FDTD, or finite-element methods (FEM).

Figure 8.5 shows the measured radiation patterns for four different cylinders measured on different resonance branches in Fig. 8.3b. The pattern strongly depends on the resonance mode order. For the smallest cylinder (Fig. 8.5a), which has a resonance lying on the top experimental branch in Fig. 8.3b, we observe a toroidal "doughnut-like" emission pattern at $\lambda_0 = 400$ nm, which has no light emission along the normal [278–280]. This pattern corresponds to that of a vertically oriented dipole [0,1] mode, which directly proves that the top measured branch corresponds to the [0,1] branch. Note that the [1,1] mode is not excited in the angular CL experiment as the cylinders are excited in the center, where the [1,1] mode has a node (see Fig. 8.3c). We explain the large discrepancy between the experimentally observed top branch and the analytically calculated [0,1] mode by the fact that the analytical waveguide model breaks down when the diameter is small compared to the wavelength. With the experimental data for the top branch in Fig. 8.3b, identified as the [0,1] mode, we conclude that the [0,1] and [1,1] modal branches are closely spaced and overlap with the top experimental branch, as in the case for all other experimental branches, which also correspond to combinations of two modes (see Fig. 8.3b).

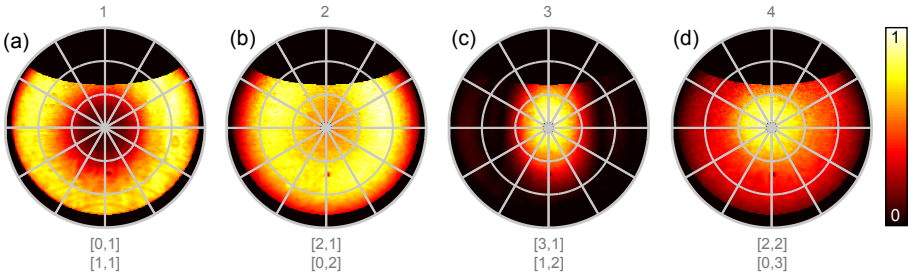

Figure 8.5: Measured angular patterns for the first four modal branches showing the CL emission intensity as function of zenithal angle θ and azimuthal angle φ for (a) d = 70 nm, (b) d = 153 nm, (c) d = 176 nm, and (d) d = 304 nm collected at λ_0 = 400, 500, 450, and 500 nm, respectively. The specific diameters were chosen to optimally match a band-pass color filter. For all of the images, the cylinders were excited in the center, except for (c), where the cylinder was excited at the edge to optimize the excitation efficiency since this resonance has a node in the center.

The angular profile for the second branch (Fig. 8.5b) shows a toroidal shape, as well, consistent with the electron beam selectively exciting the [0,2] mode (the [2,1] mode has a node in the center; see Fig. 8.3c), which also has a vertical dipole moment. The modes in the third branch cannot be excited in the center ($m > 0$ for both modes), and therefore, the beam was placed on the edge of the cylinder,

exciting a superposition of the [1,2] and [3,1] modes. In this case, clear upward beaming is observed, in agreement with the in-plane character of this mode (see Fig. 8.3c). The angular pattern for the fourth branch (Fig. 8.5d) appears to be a combination of a toroidal and upward emission. This corresponds to the excitation of the toroidally emitting [0,3] mode and a small contribution of the upward radiating [2,2] quadrupolar mode; while the latter has a node in the center, given the close proximity of its first radial antinode to the center (see Fig. 8.3c), it can be excited by the finite-size electron beam.

The large difference in radiation profile between the resonance orders shows that, depending on the angular scattering profile that is desired for specific applications, the cylinder geometry can be tuned to obtain such a scattering profile in the appropriate spectral range. Note that the angular distribution is also influenced by the wavelength-dependent interference with the silicon substrate 300 nm below the nanoparticle [280].

8.8 Nature of lowest-order mode

To investigate whether the lowest-order [0,1] dipolar resonance is electric or magnetic in nature [39, 41, 43, 44, 54], we perform polarization-filtered angular measurements, using a linear polarizer in the beam path. Figure 8.6 shows the angular pattern with the polarizer parallel (a) and transverse (b) to the optical axis of the paraboloid (see blue dashed lines) for the smallest cylinder (d = 70 nm) at λ_0 = 400 nm. In the paraboloid, the emission polarization remains almost unaltered along the center line of the mirror (the line going through $\varphi = 0°$ and 180°). We observe that the light intensity is high along this line when the polarizer is aligned, while it is low when it is transversely oriented. This indicates that the emission is p-polarized, which is consistent with the radiation from an m = 0, q = 1 electric dipole mode. For a more elaborate description on why these polarization- filtered angular patterns have this specific shape and how the parabolic mirror affects the emission polarization for different electric dipole orientations, we refer the reader to ref. [269].

Finally, we use the knowledge that the upper experimental/numerical branch corresponds to a [0,1] resonance to fit its appropriate effective index. To do this, we again solve the eigenvalue equation, but now we fix the resonance wavelength to the resonance wavelengths obtained for the top branch from numerical modeling and solve for n_c, given that m = 0 and q = 1. In this way, we force the [0,1] branch of the model to match the experimental data and use this to obtain the effective index of the cylinder. The resulting index is shown as an orange line in Fig. 8.4b and is indeed significantly lower than the TM_0 index that was originally used and gives rise to a significant blue shift of the resonance wavelength. The fitted index steadily decreases with increasing wavelength from n_c = 2.0 at λ_0 = 400 nm to $n_c < 1$ for $\lambda_0 > 620$ nm. This implies that the lowest-order resonance approaches cutoff and becomes a leaky mode that no longer strongly confines light inside the cavity. Close

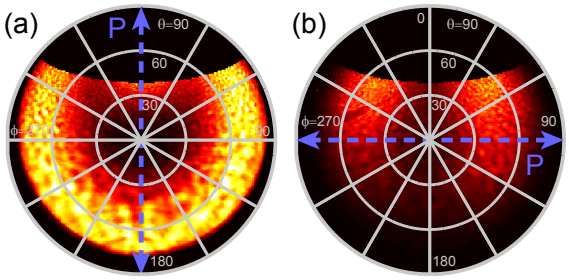

Figure 8.6: Measured polarization-filtered angular patterns for a $d = 70$ nm cylinder measured at $\lambda_0 = 400$ nm with the polarizer positioned (a) vertically (aligned with the optical axis of the paraboloid) and (b) horizontally (transverse to the optical axis). The patterns suggest that this resonance is an electrical dipolar $m = 0$, $q = 1$ resonance.

observation of Fig. 8.3b shows that both the experimental and simulation data of the top resonance branch fade away around this wavelength, in agreement with this cutoff argument. We note that the decrease in effective mode index for the cutoff mode with increasing wavelength is due to both the reduced confinement and the lower index of bulk silicon at larger wavelengths. The strong reduction in Q for the [0,1] mode with increasing diameter is also clearly visible in Fig. 8.3a.

8.9 Conclusions

In conclusion, the resonant optical modes of silicon nanocylinders with diameters between 60 and 325 nm can be excited and studied using a 30 keV electron beam. Well-defined fundamental and higher-order azimuthal ($m = 0$–4) and radial ($q = 1$–4) modes are observed with relatively narrow ($Q = 9$–77) emission peaks and complex photonic wave functions. The data agree with finite-difference time-domain simulations and analytical calculations, in which we solve the Helmholtz wave equation using an effective modal index for the corresponding TM_0 waveguide mode to find the in-plane eigenmodes. Characteristic angular emission patterns are observed for each resonant mode, ranging from an upward dipole-like pattern for the lowest-order modes to distributions that show clear beaming in the upward direction for higher-order modes. Using polarization spectroscopy, we identify the lowest-order resonance as an ($m = 0$, $q = 1$) electrical dipole mode; it becomes leaky for long wavelengths.

Our measurements demonstrate that the optical properties of silicon nanocylinders are highly tunable through the visible spectral range. Further tunability may be achieved by varying the nanoparticle shape. With the fundamental resonant optical properties of single Si Mie resonators now determined, the door is open to studies of more complex geometries of arrays of coupled resonators, in

which the directionality and spectra of emitted light can be tuned further. This work also shows that cathodoluminescence spectroscopy, which so far has been used mostly on metallic nanostructures, can be used to study the fundamental resonant properties of single dielectric or semiconductor nanostructures in great detail. In the future, this enables rapid prototyping of semiconductor or dielectric nanostructures, where the spectral and angular emission properties can be fine-tuned for specific applications.

8.10 Methods

Fabrication
Small chips (12 × 12 mm) of SOI wafer (100 nm Si device layer, 300 nm SiO_2 buried oxide layer) are baked for 5 min at 180°C before spin coating the sample with a thin HMDS adhesion layer (4000 rpm, 30 s). The HMDS layer is baked for 1 min at 180°C to evaporate the solvents. Next, the sample is spin coated with approximately 65 nm of negative tone resist (ma-N 2401, 2000 rpm, 30 s) and baked for 60 s at 90°C. Au colloids with a diameter of 50 nm are deposited in the corner of the sample to allow accurate focusing of the electron beam.

Electron beam lithography is performed in a Raith e-LINE system, using a 30 kV acceleration voltage and 7.5 μm aperture, resulting in a beam current of 14 pA. Single dot exposure is used for the smallest cylinders ($d < 240$ nm), whereas area exposure is used for the larger cylinders ($d > 270$ nm). The resist is developed by rinsing in ma-D 332 S for 15 s, followed by rinsing in deionized H_2O to stop the development. The resulting disks of resist function as an etch mask in the reactive ion etching (RIE) step. A gas mixture of CHF_3 (35 sccm) and SF_6 (5 sccm) is used to anisotropically etch down the Si layer of the SOI wafer (100 nm) in 3.5 min (forward power = 125 W). Subsequently, the residual resist is removed using a 10 min oxygen plasma etch (20 sccm O_2, 50 W forward power).

Cathodoluminescence experiments
For the spectral images, 0.3 s integration time per pixel was used at a current of 10 nA. The CL data are corrected for system response using a measured transition radiation spectrum from gold and comparing that to theory [270, 281], so that the absolute excitation efficiency is determined per electron per unit bandwidth. For the angle-resolved measurements, we used dwell times between 15 and 30 s depending on wavelength. For the polarization-filtered angular measurements, we used an integration time of 60 s. Spectral sensitivity was achieved by filtering the CL beam with 40 nm band-pass color filters. In all cases, the background CL signal from the substrate was subtracted from the measured data, which includes the transition radiation of the SiO_2 layer and Si substrate. To correctly subtract the variable background from the CL signal, we use a triangular interpolation routine, which interpolates the background intensity between the four corners (averaged over nine pixels in each corner) of the scan.

FDTD simulations

The finite-difference time-domain simulations are performed using the commercial software package Lumerical FDTD Solutions [137]. An 800 nm cubed simulation box is used, with perfectly matching layer (PML) boundary conditions on all sides. The simulation box ranges from 150 nm into the Si substrate to 250 nm above the top of the cylinders. A constant current broad band (λ_0 = 300–900 nm) vertically oriented electric dipole, positioned at half the height of the cylinder (50 nm), is used as a source. To simulate the spectrum for a given cylinder diameter, the dipole position is varied from the center to the edge of the cylinder in steps of 5 nm, such that the number of simulations N per cylinder is given by $N = R/5 + 1$, with R being the particle radius in nanometers. Two-dimensional flux box transmission monitors, the top one positioned 100 nm above the top interface of the cylinder, the side ones 360 nm from the center of the cylinder, monitor the power of the light emitted into the upper hemisphere. Note that interference with the Si substrate is taken into account, but that light reflected from the SiO_2-Si interface under large angles may be radiated into the upper hemisphere without being detected. Automatic non-uniform meshing is used, resulting in mesh sizes ranging from 4 to 7 nm in the Si cylinder or air, respectively.

9

Designing dielectric resonators on substrates: combining magnetic and electric resonances

High-performance integrated optics, solar cells, and sensors require nanoscale optical components at the surface of the device, in order to manipulate, redirect and concentrate light. High-index dielectric resonators provide the possibility to do this efficiently with low absorption losses. The resonances supported by dielectric resonators are both magnetic and electric in nature. Combined scattering from these two can be used for directional scattering. Most applications require strong coupling between the particles and the substrate, which strongly influences the resonant behavior of the particles. Here, we systematically study the influence of particle geometry and dielectric environment on the resonant behavior of dielectric resonators in the visible to near-IR spectral range. We show the key role of retardation in the excitation of the magnetic dipole (MD) mode, as well as the limit where no MD mode is supported. Furthermore, we study the influence of particle diameter, shape and substrate index on the spectral position, width and overlap of the electric dipole (ED) and MD modes. Also, we show that the ED and MD mode can selectively be enhanced or suppressed using multi-layer substrates. And, by comparing dipole excitation and plane wave excitation, we study the influence of driving field on the scattering properties. Finally, we show that the directional radiation profiles of the ED and MD modes in resonators on a substrate are similar to those of point-dipoles close to a substrate. Altogether, this work is a guideline how to tune magnetic and electric resonances for specific applications.

9.1 Introduction

High-performance integrated optics, solar cells, sensors and many other optical devices require the ability to concentrate, redirect and manipulate light at the surface of the device, in order to optimize the coupling and trapping of light. Resonant nanostructures can have large scattering cross sections at visible wavelengths, and therefore are suitable candidates for this purpose. Plasmonic nanostructures have proven to be very successful in this field, and have been used for light focusing and scattering in sensing and imaging [35, 282], solar cells [74, 78] and light emitting devices [16, 283]. However, the performance of plasmonic nanostructures is always limited by parasitic absorption in the metal. High-index dielectric or semiconductor nanostructures support (Mie-like) geometrical resonances in the visible spectral range [28, 31, 54, 284]. Unlike in plasmonic particles, these are driven by displacement currents rather than actual currents [30]. Therefore, these resonances are characterized by (very) low losses. Scattering from spherical dielectric particles in a homogeneous medium has already been described in great detail using Mie theory [29, 37, 43, 256], and particles weakly coupled to the substrate have also been analyzed [41]. This work has shown that silicon nanoparticles support both electrical and magnetic resonances in the visible and near-infrared spectral range [37–39, 41, 43, 44]. Recently, it has also been shown that the interplay between electrical and magnetic resonances can be used to control the angular radiation pattern of the resonant cavities [30, 45, 46], and that using cylinders instead of spheres allows for tuning of the spectral spacing between the electric and magnetic lowest order resonances [38, 45]. For all practical applications particles are placed on a substrate and in most cases strong coupling to the substrate is even desired (e.g. absorption in photodiodes [15], solar cells [33, 73], etc.). This interaction with the substrate strongly influences the resonant behavior, as well as the interaction between the magnetic and electric resonances. So far, there has been no systematic study on the influence of particle geometry and dielectric environment on the resonant properties of dielectric nanoparticles on a substrate.

Here, we use numerical simulations to systematically study the resonant properties of high-index dielectric particles in the visible spectral range for different particle geometries and dielectric environments. We show how electric and magnetic resonances are supported, and that retardation plays a key role in the driving of the magnetic resonances. Also, we show how varying the height and diameter of resonant nanocylinders placed on a dielectric substrate provides the possibility to spectrally tune the electric dipole (ED) and magnetic dipole (MD) resonances. Furthermore, we study how the presence of a (high-index) substrate dramatically alters the resonant properties, as well as the interplay between the different eigenmodes. We show that by tuning the substrate geometry, the ED and MD resonances can be selectively enhanced or suppressed. Also, we find that such resonators can be used as low-loss antennas that exhibit directional emission into the substrate. Altogether, this Chapter shows how, by engineering the particle shape and dielectric environment, the scattering properties of single resonators placed on a dielectric

substrate can be tailored for specific applications.

9.2 Magnetic and electric modes in dielectric particles

The ability to excite magnetic (dipolar) resonances in silicon particles, as well as the driving mechanism, has been described recently [39, 41, 43]. In short, the in-plane magnetic dipole is driven by the electric field of light that couples to displacement current loops, vertically oriented in the particle (see inset in Fig. 9.1a). This displacement current loop (orange) induces a magnetic dipole moment (blue), oriented perpendicular to the electric field polarization. Efficient driving of this displacement current loop requires significant retardation of the driving field (red) throughout the particle, as the electric field should undergo a significant phase shift in order to match the opposing electric field orientation in the top and bottom part of the particle. The excitation of electric (dipolar) resonances on the other hand, only requires collective polarization of the material inside the resonator by the electric field component of the incident light.

Here, we systematically study the nature of the resonances supported by (mostly cylindrical) nanoparticles while changing the particle height, diameter, shape, presence and refractive index of a substrate, thickness of multi-layered substrates and driving field. To this end, we use finite-difference time-domain simulations [137] to calculate the normalized scattering cross section (scattering cross section normalized to geometrical cross section) $Q_{scat} = \sigma_{scat}/\sigma_{geo}$ and modal field profiles inside the particles. A total-field scattered-field source (TFSF) source is used, which launches a broad-band (λ = 400–1000 nm) plane wave from the top under normal incidence and filters out all the light that has not been scattered. Power transmission monitors are positioned around the TFSF source to monitor the power of the scattered field, and field monitors are positioned in and around the particle to monitor the local field intensity. Substrates (when used) have a purely real refractive index n_{sub}, to prevent absorption of the scattered light before reaching the power monitors. Perfectly matching layers (PMLs) are used to prevent any unphysical scattering from the simulation boundaries, and to mimic semi-infinite substrates. Optical constants for Si and SiO_2 are taken from Palik [138]. Automatic non-uniform meshes are used, and a 2.5 nm refinement mesh around the particle when monitoring the near-field intensities. Identification of the modes (MD, ED) is done by studying the field profiles inside the particle and identifying the corresponding current loops.

9.3 Retardation and particle height

We start by investigating the role of particle height on the excitation of resonant modes in crystalline Si cylinders in a homogeneous air environment. We choose Si since this is a high-index material with relatively low absorption losses in the visible and near-IR, and has been used in most previous work on magnetic resonances

[30, 33, 39, 41, 43, 45]. The necessity of field retardation for the excitation of the MD mode suggests that if the particle is shallow enough, there should not be enough retardation to drive a displacement current loop, and therefore a MD resonance cannot be supported. The ED mode however, does not need retardation *inside* the particle: since $\mu = 1$ both inside and outside the particle, the magnetic current loop induced by the dipole moment can also extend outside the particle.

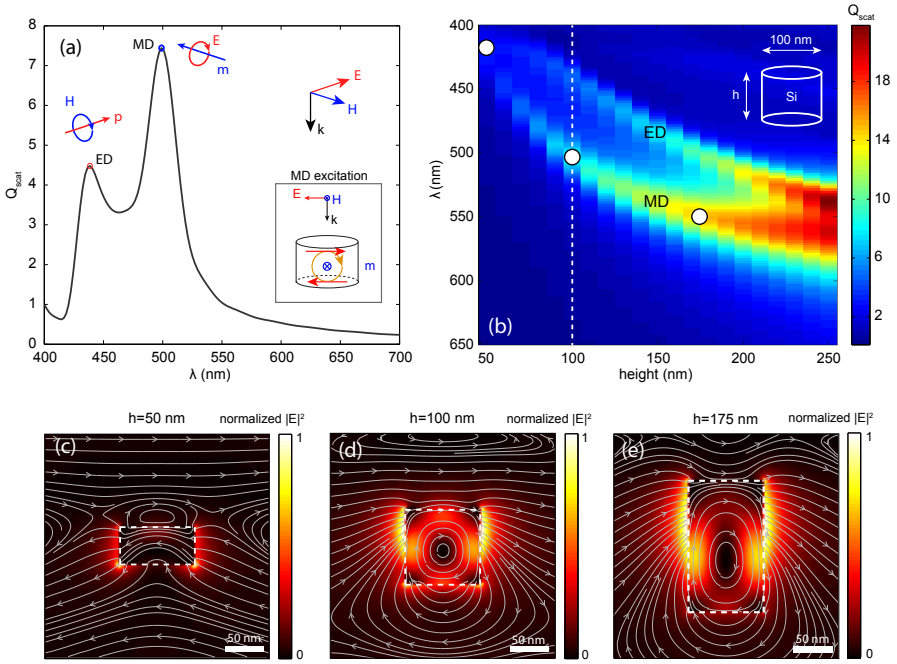

Figure 9.1: (a) Q_{scat} as a function of wavelength for a Si cylinder in air with $h = 100$ nm and $d = 100$ nm for optical excitation under normal incidence. The peaks correspond to the ED and MD mode, and the corresponding dipole moments and current loops are shown. The polarization of the driving field is shown in the top right. The inset shows the excitation mechanism of the MD mode. (b) Q_{scat} (color) as a function of λ and h for $h = 50$–250 nm. The particle geometry is shown as an inset. The vertical white line is the crosscut corresponding to the spectrum shown in (a). The white dots correspond to the λ - h combinations used for (c-e). (c-e) Normalized electric field intensity $|E|^2$ (color) and electric field lines (gray) in vertical crosscuts through particles with $h = 50$ nm (c), $h = 100$ nm (d) and $h = 175$ nm (e), parallel to the electric driving field.

To study the effect of particle height on retardation, we calculate Q_{scat} for a Si cylinder in air, with diameter $d = 100$ nm and height $h = 100$ nm. Figure 9.1a shows Q_{scat} as a function of wavelength. Two clear peaks are observed which correspond to the ED mode at $\lambda = 440$ nm and the MD mode at $\lambda = 503$ nm. As mentioned above, identification of the modes (MD, ED) is done by studying the field profiles

inside the particle and identifying the corresponding current loops. Figure 9.1b shows Q_{scat} spectra for particle heights in the range h = 50–250 nm. The vertical dashed line represents the crosscut shown in Fig. 9.1a. The two maxima, labeled ED and MD, show a clear red shift and increase in Q_{scat} for increasing h. Note that two peaks can be observed for the entire range of h, even down to 50 nm. Thus, even a cylinder only 50 nm high supports a vertically-oriented displacement current loop generating a MD resonance. The strong increase in Q_{scat} for larger height is due to the fact that the volume of the particle increases and thus the polarizability and thereby σ_{scat}, while the geometrical cross section σ_{geo} does not change. Unlike plasmonic particles, where an increase in h gives rise to a small blue shift for an in-plane dipole mode due to an increased restoring force, higher Si cylinders give rise to a large red shift that saturates above $h \sim 220$ nm. This can be understood from Figs. 9.1c-e, which show vertical crosscuts parallel to the polarization of the driving field of the normalized electric field intensity distribution $|E|^2$ (color) for h = 50 nm (c), h = 100 nm (d) and h = 175 nm (e). Electric field lines (gray) in this plane at resonance are also plotted. The three combinations of h and λ from Figs. 9.1c-e are indicated by white dots in Fig. 9.1b. In Figs. 9.1d-e, both the intensity profiles and the field lines clearly show the loop induced by the driving field, which in turn drives the out-of-plane MD mode. In (c) however, this loop is not clearly visible. Detailed analysis of crosscuts through other planes (not shown here) do show that there is a current loop. But, a large fraction of the current loop is inside the evanescent near field in the air below the particle, where n = 1 (hence the high field intensity at the bottom corners). As the particle gets taller, Figs. 9.1d-e, the current loop fits better inside the particle and a larger fraction of the field is in the high index medium, giving rise to a red shift which saturates when the current loop easily fits inside. A similar argument holds for the ED mode, where a larger fraction of the field is inside the cylinder for larger h, giving rise to a red shift.

Concomitant with the strong blue shift for smaller h, the index of Si also strongly increases for smaller wavelengths (from n = 4 at λ = 550 nm to n = 5.1 at λ = 420 nm). This makes the particles "optically" higher, thus creating more space for a current loop and as a result, the MD mode does not disappear. Note that for a non-dispersive medium this might not be the case.

Figure 9.2a shows Q_{scat} as a function of wavelength for a d = 250 nm cylinder in air, made of a non-dispersive dielectric with n = 2 for different heights in the range h = 50–200 nm. For h = 50–100 nm, one very broad peak is observed, which corresponds to the ED mode. When $h > 100$ nm, there is enough retardation to support a displacement current loop and the MD resonance is supported as well, which then red shifts for larger h, as explained above. Note that the Q-factor of the resonances is much lower than observed in Fig. 9.1a since the lower index of the particle results in poor mode confinement and thus a large radiative loss rates γ_{rad}. Therefore, the ED and the MD spectrally overlap and one broad ED/MD peak is observed. Also note that the identification of the modes is again done by studying the field profiles. In this case however, the ED and MD modes spectrally overlap, such that in the near-field profiles both dipolar field profiles and corresponding current loops can

be distinguished. The relatively sharp peak that appears in the blue spectral range for larger heights corresponds to the magnetic quadrupole mode (MQ), as will be shown later. Thus, in the limit that there is not enough retardation of the driving field inside the particle (low n and h), the MD mode is not supported, whereas the ED mode is always supported.

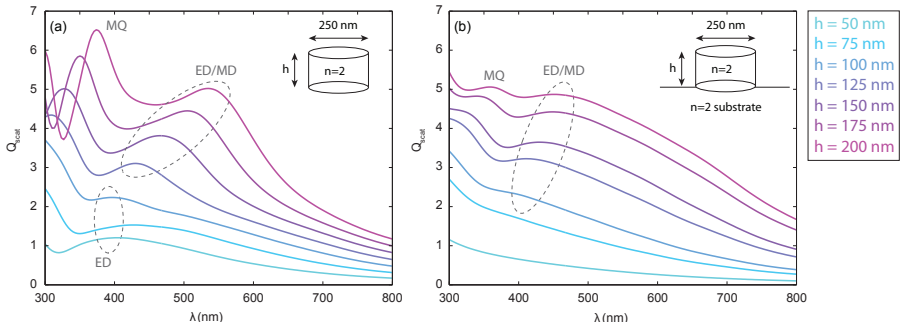

Figure 9.2: (a) Q_{scat} as function of wavelength for $d = 250$ nm particles made of a non-dispersive dielectric with $n = 2$, plotted for heights in the range $h = 50$–200 nm. The geometry is shown as an inset. The peaks are labeled according to the resonance they correspond to (MD, ED, MQ). For $h < 125$ nm, no MD is supported. (b) Q_{scat} for the same particles as in (a), but now on a semi-infinite substrate with $n = 2$ (see inset for geometry).

It has been shown that when a dielectric resonator is positioned on a substrate with similar index as the resonator, the displacement current loop can extend into the substrate [33] (also see Section 9.5). The substrate effectively provides additional "optical" height to the resonator, such that the MD mode can be supported for shallow particles that do not show this resonance when positioned in air. Figure 9.2b shows Q_{scat} for the same resonator as in (a), but now positioned on a semi-infinite substrate with $n_{sub} = 2$ (see inset). Comparison of (a) and (b) clearly shows that all resonances have significantly broadened, due to the fact that part of the mode profile extends into the substrate. This increases the radiative loss rate γ_{rad} into the substrate, resulting in a reduced resonance Q-factor. Although combining shallow particles ($h < 100$ nm) with a substrate provides enough retardation and space to support a current loop, the degree of confinement is insufficient to support any resonance. However, as soon as resonant behavior occurs by increasing h, the resonant peak corresponds to a combination of the ED and MD eigenmodes.

9.4 Particle diameter and higher order modes

Increasing the particle diameter d enables the excitation of resonant modes at larger wavelengths. A rule of thumb for the resonant wavelengths of the dipolar modes of resonant nanocylinders in air is $\lambda/n \sim d$. Furthermore, when the

diameter is large enough, higher-order modes will also be supported in the visible spectral range. In Fig. 9.3 we investigate the spectral spacing of the ED and MD modes. Figure 9.3a shows Q_{scat} (color) for h = 100 nm Si cylinders in air, with varying diameter in the range d = 50–250 nm.

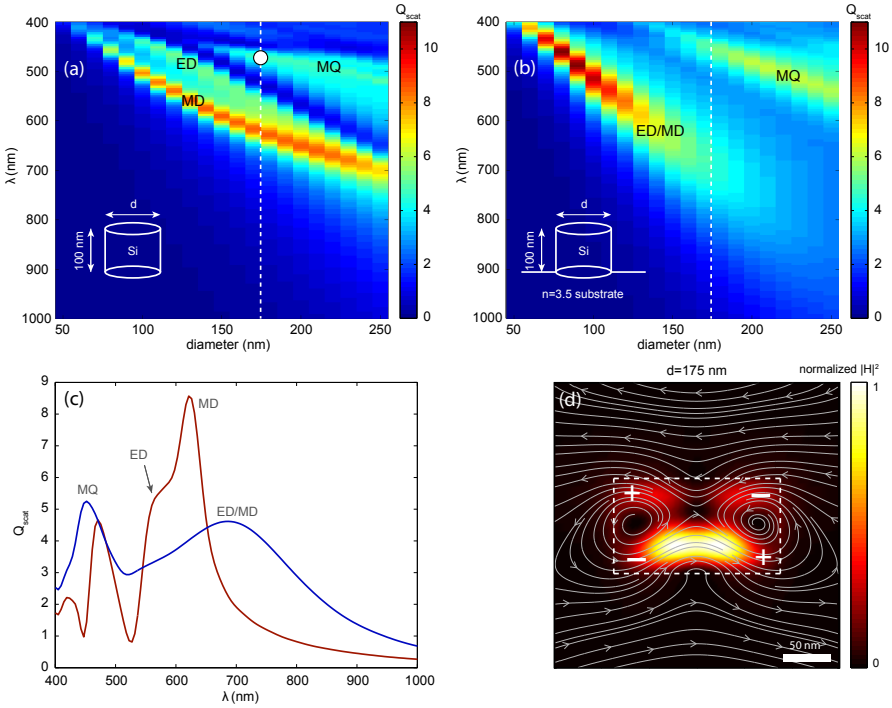

Figure 9.3: (a) Q_{scat} (color) as a function of wavelength for a h = 100 nm Si cylinder in air, for diameters in the range d = 50–250 nm. The geometry is shown as an inset. The peaks are labeled according to the resonance they correspond to (ED, MD, MQ). (b) Q_{scat} (color) for the same resonator as in (a), but now on a semi-infinite substrate with n = 3.5 (see inset). (c) Spectra corresponding to crosscuts indicated by white vertical dashed lines in (a) and (b) showing the spectra for d = 175 nm, in air (red) and on a n = 3.5 substrate (blue). The labels indicate the corresponding resonant modes. (d) Vertical crosscut through the resonator in air (d = 175 nm, see white dot in (a)) in the plane parallel to the H-field of the driving field for λ = 466 nm. Plotted is the normalized $|H|^2$ (color) and the magnetic field lines (gray), showing the MQ mode profile. The corresponding poles are labeled with + and − signs (white).

For d < 130 nm two clear resonances are present, which correspond to the ED and MD modes, as was observed in Fig. 9.1 where the particle height was varied. As d increases, both modes strongly red shift and start to overlap spectrally as d > 160 nm, while the peak value of Q_{scat} stays roughly constant (~8). The curvature of the

MD branch is a result of the dispersive nature of the Si. Note that the red shift for the ED mode with increasing d is much stronger than that of the MD mode, such that tuning the particle aspect ratio allows for control over the spectral spacing between the ED and MD mode. In fact, a further increase in diameter will cause the ED and MD branch in Fig. 9.3a to cross as shown in [45]. The vertical crosscut in Fig. 9.3a indicated by the white line at $d = 175$ nm, is shown as the red spectrum in Fig. 9.3c. The spectrum shows how the ED mode appears as a shoulder on the dominant MD resonance. Thus, in air, the ED and MD peaks are spectrally separated for small d and spectrally overlapping for large d. A third peak is observed for around $\lambda = 466$ nm, which also red shifts with increasing d. This peak is due to a magnetic quadrupole (MQ) as appears from Fig. 9.3d, which shows a vertical crosscut, parallel to the H-field of the driving field, of the normalized magnetic field intensity $|H|^2$ (color) and the magnetic field lines (gray lines) in a $d = 175$ nm particle at the MQ resonance wavelength ($\lambda = 466$ nm). The combination of d and λ used for this plot is indicated with a white dot in Fig. 9.3a. The crosscut shows four bright lobes in the corners of the particle (the bottom two overlap, giving a bright spot in the center), corresponding to the four poles of a quadrupole. The field lines show which pole is positive (field lines going out of the particle) and negative (field lines going in), indicated by white + and − signs. The observed mode sequence MD-ED-MQ with decreasing resonance wavelengths in Figs. 9.3a and 9.3c is in agreement with the well established mode hierarchy of magnetic and electric modes in spheres [29, 41]. Note that a strong reduction in the cylinder aspect ratio can cause the MD mode to be positioned at lower wavelength than the ED mode, thereby changing this mode hierarchy [45].

Figure 9.3b shows Q_{scat} for the same resonators as in (a), but now on a semi-infinite substrate with $n_{sub} = 3.5$ (roughly equal to n_{Si}, see inset for geometry). Comparing (a) and (b), four characteristic differences are observed. First, the ED and MD modes in (b) are spectrally broader and overlapping, now also for small d, which is a result of the increase of γ_{rad} into the substrate. Second, the peak values for Q_{scat} are much higher for small d (~11 instead of ~8) and for the MQ mode (~7 instead of ~5). Both the first effect (broadening) and second effect (increase in Q_{scat}) are attributed to the increased local density of optical states ($LDOS$) accessible to the resonator when located on a substrate: there are more radiative states available to couple to, thus increasing γ_{rad} and therefore Q_{scat}. Third, for $d > 160$ nm the ED/MD peak becomes very broad, scattering light over the entire visible spectral range, since a larger fraction of the mode profile extends into the substrate for larger λ. Figure 9.3c (blue) shows the spectrum for $d = 175$ nm. Clearly, the ED/MD peak ranges all the way from $\lambda = 400$ nm up to $\lambda = 1000$ nm. These modes can serve to achieve efficient light coupling into a high-index substrate over a broad spectral range, as shown in refs. [33, 73]. Fourth, the red shift of the ED/MD peak is more dramatic than in (a), which is a result of the fact that a large fraction of the near-field of the resonance is inside the $n = 3.5$ substrate instead of air ($n = 1$).

9.5 Substrate index and particle shape

Sections 9.3 and 9.4 have shown that when a cylindrical resonator is positioned on a substrate with $n_{sub} \sim n_{part}$, the ED and MD resonances broaden and spectrally overlap. Next, we investigate the case of $1 < n_{sub} < n_{part}$. We study how the spectral positions of the resonances depend on substrate index and particle shape. Figure 9.4a shows Q_{scat} for the same resonator as in Fig. 9.1a, a Si cylinder with $d = 100$ nm and $h = 100$ nm, but now on a semi-infinite substrate with an index in the range $1 \leq n_{sub} \leq 3.5$, varying in steps of 0.25.

Figure 9.4a shows three characteristic features. First, as was observed in Figs. 9.2b and 9.3b, increasing n_{sub} from 1 to 3.5 gradually broadens the resonance peaks (due to an increase in γ_{rad}) and causes the ED and MD peaks to overlap spectrally, such that the ED mode becomes a shoulder of the MD mode for high index. For $n_{sub} > 2.25$, the ED is no longer visible as a separate peak. Second, a significant increase in Q_{scat} is observed for increasing n_{sub}, which is attributed to the increase in the *LDOS* at the position of the particle. Third, a small red shift is observed with increasing n_{sub}: $\lambda_{MD} = 499$ nm for $n_{sub} = 1$ and $\lambda_{MD} = 515$ nm for $n_{sub} = 3.5$. This is caused by the index experienced by the near-field of the resonance. Note that this small shift of only 16 nm is in sharp contrast with the dramatic 600 nm red shift observed for a plasmonic dipolar resonance of a similar cylinder made of Ag [72]. This contrast is a direct result of the different nature of the resonance. While in plasmon resonances most light is concentrated at the interface (in direct contact with the substrate), in case of dielectric resonators most light is concentrated inside the resonator, making it less sensitive to substrate index.

To investigate the influence of particle shape, Fig. 9.4b shows Q_{scat} as a function of wavelength for the same cylinder as in (a) (red), a $d = 114$ nm sphere (green), and a cube with sides of length $l = 92$ nm (blue). The particles have the same volume, are all made of Si and the geometries are shown below (a) and (b). The dashed lines in Fig. 9.4b correspond to particles in air, the solid line to particles on a semi-infinite substrate with $n_{sub} = 3.5$. Note that the sphere is sticking 7 nm into the substrate (center is at 50 nm height above the substrate) to prevent unphysical hot spots at the infinitely sharp contact area (see sketched geometry). Figure 9.4b shows that both in air and on a substrate, the shape of the particle has only a small influence on the resonance wavelengths of the ED and MD modes. Both resonances are supported for all shapes, and the cylinder proves to be the most efficient scatterer. Furthermore, for all shapes Q_{scat} increases significantly due to the enhanced *LDOS*, when put onto a substrate. However, comparing the solid lines with the dashed lines shows that both the cylinder (red) and the cube (blue) show the dramatic broadening of the ED and MD resonances when compared to the case in air, causing the ED to appear as a shoulder on top of the MD mode. For the sphere (green), the broadening is significantly less and the ED remains to be a separate peak.

To understand this difference, we plot vertical crosscuts (parallel to the E-field

of the driving field) through the center of all particles on the $n_{sub} = 3.5$ semi-infinite substrate, at the MD resonance wavelength. Figures 9.4c-e show the normalized $|E|^2$ (color) and the electric field lines (gray), while Figs. 9.4f-h show the normalized $|H|^2$ (color). The magnetic field lines are not plotted because $H \sim 0$ in this plane, which is perpendicular to the H-field orientation of the driving field. Figures 9.4c-e clearly show the displacement current loops that induce the magnetic dipole $\vec{m}$ of the MD mode. Both (c) and (e) show that for the cylinder and the cube a significant fraction of the displacement current loop extends into the substrate. For the sphere, despite the fact that it sticks into the substrate, this effect is much smaller.

As a result, the coupling to the substrate is much weaker for the sphere than for the cylinder and cube. This is also clearly observable in Figs. 9.4f-h, which show that the magnetic field profile of the MD mode inside the substrate is much brighter for the cylinder and the cube, when compared to the sphere. The contact area of the resonator with the substrate is thus very important to get strong coupling to the substrate and provides tunability of the radiation rate γ_{rad} into the substrate. Note that in Figs. 9.4c-e a second (reversed) current loop can be observed in the substrate below the particles. We attribute this to image dipoles induced by the dipole moments in the particles.

9.6 Selective mode enhancement with multi-layer substrates

Based on the results from Sections 9.3–9.5 it is possible to design any resonator geometry such that the particle is resonant at the desired wavelength. Furthermore, by tuning the diameter and height separately it is possible to either have two spectrally separated ED/MD resonances (using a small diameter, large height) or spectrally overlapping resonances (large diameter, small height). However, for specific applications it may be useful to selectively select one of the two modes to dominate the response of the resonator; the ED or the MD mode.

This may be particularly relevant if the radiation pattern of the resonator is important, such as for example in light trapping geometries in photodiodes and solar cells, as will be shown in Section 9.8. Here we will show that this can be done using a multi-layer substrate. The inset of Fig. 9.5a shows the proposed geometry: a Si cylinder with $d = 100$ nm and $h = 100$ nm is positioned on a SiO_2 layer with thickness t, which is on top of a $n_{sub} = 3.5$ substrate (e.g. Si). We vary the SiO_2 layer thickness from $0 \leq t \leq 500$ nm in steps of 20 nm and for each t we calculate Q_{scat}.

The results are shown in Fig. 9.5a, where Q_{scat} is shown (color) as a function of t and λ. For $t = 0$, we observe one very broad peak: the resonator is strongly coupled to the substrate and the ED and MD mode broaden and overlap as in Fig. 9.4. However, as t increases Q_{scat} of the MD mode and ED mode are subsequently suppressed and enhanced. The horizontal dashed black lines indicate crosscuts near the resonance wavelength for the MD mode ($\lambda = 499$ nm) and the ED mode ($\lambda = 440$ nm), which are shown as blue dots in Figs. 9.5b and 9.5c respectively. Note

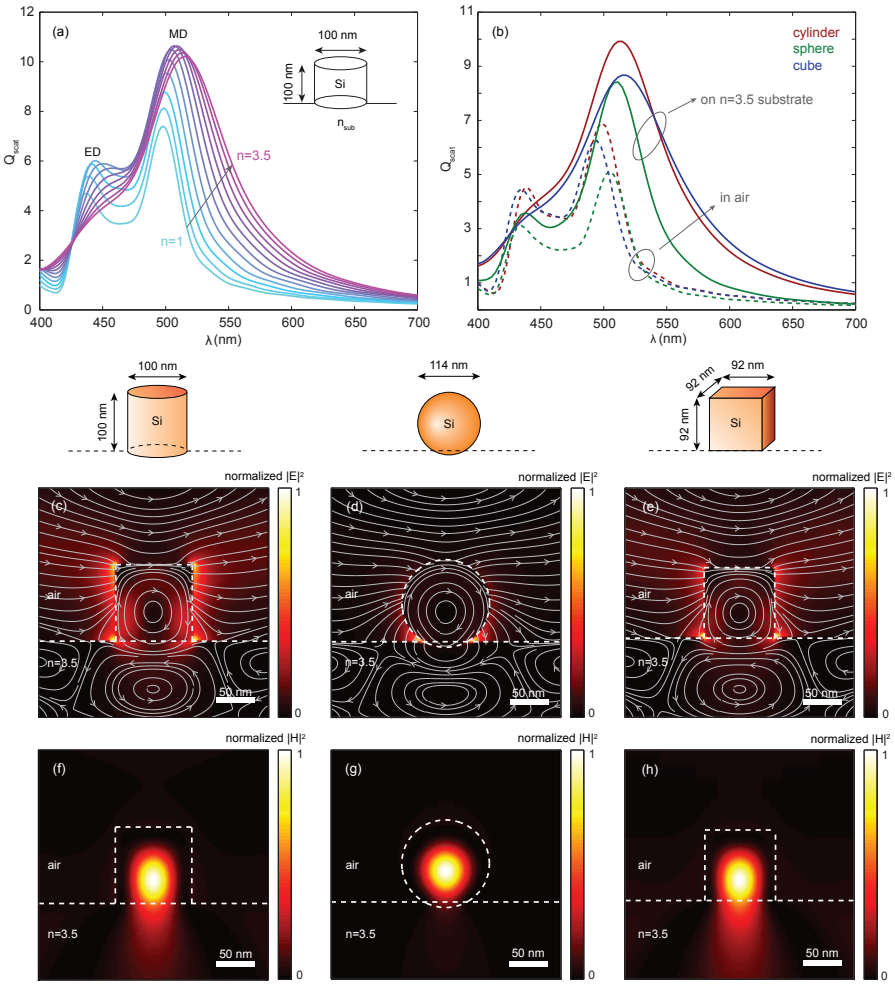

Figure 9.4: (a) Q_{scat} as a function of wavelength for a Si cylinder with h = 100 nm, d = 100 nm, on a semi-infinite substrate with $1 \leq n_{sub} \leq 3.5$, in index steps of 0.25. The geometry is shown as an inset. (b) Q_{scat} for the same cylinder (red), a d = 114 nm sphere (green), and a l = 92 nm cube (blue) in air (dashed), all on a n_{sub} = 3.5 semi-infinite substrate (solid). All particles consist of Si and have the same volume. The three geometries are sketched below (a) and (b). Note that the sphere sticks 7 nm into the substrate to prevent an infinitely sharp contact area. (c-e) Vertical crosscuts through the center of all three particles in the plane parallel to the E-field of the source, showing the normalized $|E|^2$ (color) and electric field lines (gray). The particle surroundings and air-substrate interface are indicated with white dashed lines. The respective geometries are shown above the figures. The displacement current loops are clearly visible. (f-h) The same crosscuts as in (c-e), now showing the normalized $|H|^2$ (color) of the MD modes. The magnetic field lines are not plotted since $H \sim 0$ in this plane (perpendicular to source $\vec{H}$)

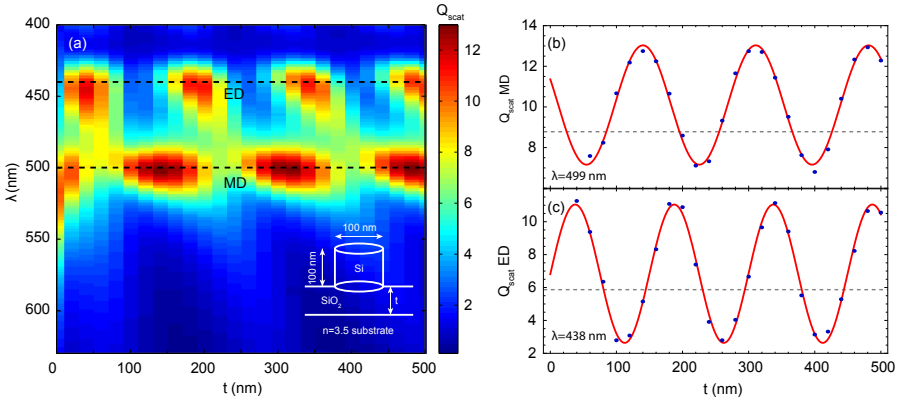

Figure 9.5: (a) Q_{scat} as a function of wavelength and oxide thickness t, for a d = 100 nm, h = 100 nm Si cylinder, positioned on top of an oxide layer with thickness t, on top of a semi-infinite substrate with n_{sub} = 3.5. The inset shows the geometry. The horizontal black dashed lines indicate crosscuts at resonance wavelengths: λ = 440 nm (ED) and λ = 499 nm (MD). (b,c) Blue dots show the cross sections from (a), red lines show the fits from the interference model. The free-space wavelengths found from the fit are shown on the bottom left of the figures. The gray dashed lines show the peak value of Q_{scat} for the same particle on a semi-infinite SiO_2 substrate (limit of $t \to \infty$).

that the oscillation period is different for the ED and MD modes as they appear at different wavelengths, such that any combination of MD/ED amplitude within the oscillation can be chosen: at $t \sim 400$ nm both modes are in phase while at $t \sim 60$ nm they are out of phase. This effect is caused by constructive and destructive interference of the incident light reflected from the SiO_2 layer, resulting in strong variations in the driving field in the resonator, as follows from a simple interference model. Indeed, the oscillation periods found in Figs. 9.5b and 9.5c correspond to the half-wavelength of light in the oxide layer.

To prove that this effect allows for both suppression and enhancement of one of the modes, the gray dashed lines in (b) and (c) show the peak value of Q_{scat} of the same particle on a semi-infinite substrate ($t \to \infty$) with index n_{sub} = 1.5 (roughly equal to n_{SiO_2}), which is 8.8 for the MD mode and 5.9 for the ED mode. As can be seen from both (b) and (c), the amplitude of Q_{scat} can both be lower and higher than these values. The modes are not fully suppressed since the amplitudes of the incoming light and the light scattered from the Fabry-Pérot cavity do not completely cancel each other.

9.7 Plane wave versus dipole excitation

All the above describes the resonant behavior of cylinders, illuminated by plane-waves under normal incidence. However, in many practical applications or experiments the driving field may be light under large angles of incidence (e.g. illumination through a large *NA* objective [30, 41]), or even a local source like an electron beam excitation [285], which corresponds to a vertically oriented electric dipole [270, 271]. Therefore, we investigate the resonant behavior of cylinders excited by a point dipole. We study the scattering cross section of a d = 100 nm, h = 100 nm Si cylinder in air and compare the data with those for plane wave illumination from the top (like in Sections 9.3–9.6). Efficient driving occurs when the fields of the electric dipole source overlap those of the eigenmode. Thus, when the dipole is positioned in an anti-node if the eigenmode field profile. Here, we average over all dipole positions to find all eigenmodes that are efficiently excited by a vertical dipole. Note that this experimental configuration corresponds to that of cathodoluminescence spectroscopy, as we have recently shown for dielectric cylinders [285]. To simulate this, a vertically oriented electric dipole is positioned in the center of the particle, and then scanned to the edge of the particle in steps of 5 nm. For each step, a simulation is performed and the light scattered from the particle is collected using transmission monitors. Next, because of cylindrical symmetry, the dataset is rotated around the axis, and the total particle spectrum is obtained by adding all the individual spectra (using the proper Jacobian). Since the dipole driving power and plane wave base amplitude can be arbitrarily chosen, the spectra from both simulations are normalized for comparison. The results are shown in Fig. 9.6a, where the blue line corresponds to dipole excitation and the red line to plane wave excitation. Both spectra show two peaks, corresponding to the MD mode at long wavelengths and the ED mode at short wavelengths. Interestingly, the figure indicates that both excitation mechanisms induce a similar MD mode, at the same wavelength, whereas the ED energies are distinctively different.

To further characterize this difference, we show in Fig. 9.6b the driving mechanisms of both the MD mode (top row) and the ED mode (bottom row), for the in-plane excitation using a plane wave (left column) and vertical dipole (right column). The driving field orientations are shown on top. For the plane wave driving field (left column), the excitation of the in-plane MD (labeled MD_{hor}) is a result of the E-field of light (red) coupling to a vertically oriented displacement current loop (orange), as was discussed in Section 9.2. The projection of the driving field on the current loop determines the driving efficiency, which occurs on the top and bottom of the current loop in this case. Coupling of the plane wave to the in-plane ED (labeled ED_{hor}) mode (bottom left) occurs due to the in-plane polarization of the material by the driving field. The vertically oriented dipole excitation (right column) has the E-component of the driving field in the vertical direction. However, this driving field has good field overlap with the sides of the vertical displacement current loop, on the left and right of the particle (see top right in Fig. 9.6a. Therefore, the same *in-plane* $\vec{m}$ (MD_{hor}) can be induced with both vertical and in-plane

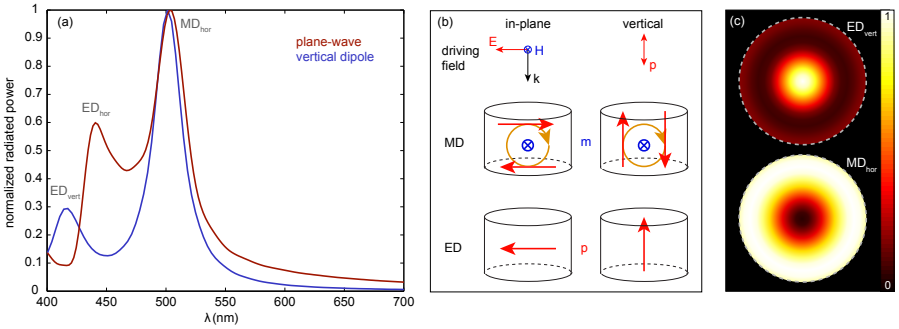

Figure 9.6: (a) Normalized Q_{scat} for a Si cylinder with $d = 100$ nm, $h = 100$ nm in air under plane wave excitation (red), and excited by a vertically oriented electric dipole, calculated by integrating spectra obtained from scanning the dipole position over a horizontal crosscut through the middle of the particle (blue). The modes are labeled in gray. (b) Excitation mechanism for the in-plane polarized plane wave source (left column) and vertically oriented electric dipole source (right column). The driving mechanism is shown for both the MD mode (top row) and ED mode (bottom row). The driving field orientation is shown on top. The orange circles indicate the displacement current loop inducing $\vec{m}$, the red arrows the E-field of the driving field (top row) and $\vec{p}$ orientation (bottom row). The blue crosses indicate the out-of-plane orientation of $\vec{m}$. (c) Excitation efficiency maps of the ED_{vert} (top) and MD_{hor} (bottom) modes driven by a vertically oriented electric dipole. The cross sections are taken at the particle half-height.

E-fields, which explains why the peaks occur at the same resonance wavelength ($\lambda = 503$ nm).

The ED mode, however, is excited differently for the two cases. The ED mode excited by the vertical dipole source is vertically oriented (ED_{vert}), instead of horizontally. The different alignment of the dipole moment $\vec{p}$ within the particle causes the eigenmode to occur at different wavelengths: ED_{vert} (417 nm) occurs at shorter wavelengths than ED_{hor} (440 nm), as can be seen in (a). Note that if a horizontal point dipole would be coupled to the particle, the ED_{hor} mode occur at the same resonance wavelength, while the MD mode will change. Under these conditions, an in-plane current loop will be excited rather than a vertical one. So, the peak corresponding to MD_{hor} mode would occur in the spectrum, with a different resonance energy.

To further corroborate the excitation mechanisms by the vertical point dipole, Fig. 9.6c shows the excitation efficiency maps (corresponding to horizontal crosscuts of the mode profiles at the particle half-height) for the ED_{vert} (top) and MD_{hor} mode (bottom). These maps show how much light is scattered by the particle at resonance wavelength (20 nm bandwidth) as a function of the excitation position (position of the dipole). This corresponds to the coupling efficiency, which is determined by the field overlap of the eigenmodes and the E-fields of the dipole. Figure 9.6c shows that the ED_{vert} (top) is excited most efficiently when the dipole

is positioned in the center (bright spot), which corresponds to the position of the vertically oriented $\vec{p}$ (see bottom right in (a)). Note that the slightly brighter ring on the outside is caused by inefficient coupling to the vertical component of the field lines of the ED_{hor} mode [67]. The MD_{hor} mode is excited most efficiently when the dipole is positioned in the bright ring on the edge of the particle, in agreement with the top right sketch in (a). Note that a ring is observed because the MD_{hor} mode is infinitely degenerate with respect to ϕ, which is a result of the cylindrical symmetry of the particle.

9.8 Radiation patterns

One of the most important characteristics of dielectric resonators is the angular radiation pattern. As specific eigenmodes are often characterized by distinct radiation profiles [285], this allows for the design of angular or spectrally sensitive photodetectors, and solar cell geometries with optimized light trapping. For resonators that are strongly coupled to a high-index substrate, a large fraction of the scattered light is emitted into the substrate due to the enhanced *LDOS* [286]. Here, we use the far-field transformation routine of Lumerical [137] to calculate the radiation patterns of single silicon scatterers on a substrate under plane wave illumination. We use a large (2.2 µm × 2.2 µm × 0.8 µm) simulation volume and apply the far-field transformation to the light propagating downward into a semi-infinite substrate with index n_{sub}, collected by a monitor outside the TFSF source (150 nm below the air-substrate interface). In this way, the radiation patterns only include the scattered light and not the incident light.

Figure 9.7a shows Q_{scat} of a Si cylinder with d = 100 nm, h = 100 nm on a semi-infinite substrate with n_{sub} = 1.5 (red) and n_{sub} = 3.5 (blue). The geometry is shown as an inset, where we define θ as the angle with respect to the surface normal pointing downward. For n_{sub} = 1.5, we observe two distinct resonances due to the ED mode (labeled 1) and the MD mode (2). For n_{sub} = 3.5, both peaks have broadened such that they spectrally overlap and the resonant response is dominated by the MD mode (3).

Figure 9.7b shows the fraction of the scattered power that is scattered into the substrate as a function of n_{sub}, integrated over all wavelengths (red) and at the MD resonance wavelength (blue). Both lines show an increase in downward scattering with increasing n_{sub} due to the increased *LDOS* [286]. For n_{sub} = 3.5 (close to n_{Si}) more than 80% of the scattered light goes into the substrate. Indeed, arrays of Si nanocylinders have shown to act as efficient anti-reflection coatings [33]. Surprisingly, this scattering fraction is lower at resonance than it is for the total power, which shows that the directionality is not optimum at the resonances wavelength itself. However, the absolute power scattered into the substrate *is* determined by Q_{scat} and does peak at resonance (also see Fig. 9.8).

To show that the individual resonances can be used as directional antennas, we show in Fig. 9.7c the angular radiation profiles into the substrate for the Si cylinder

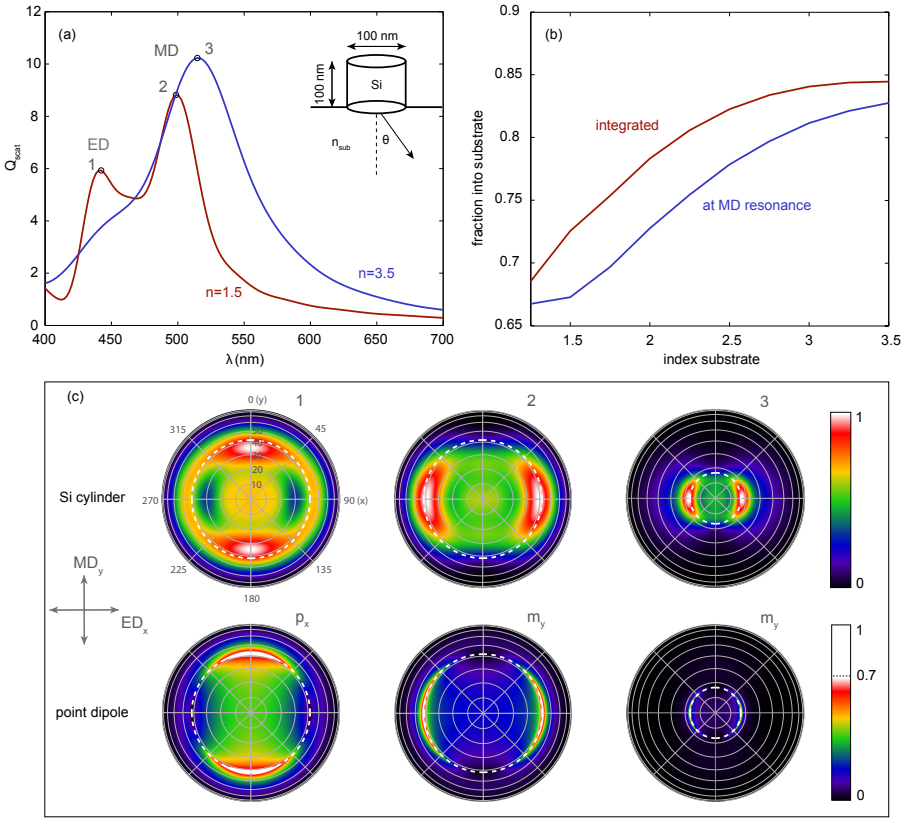

Figure 9.7: (a) Q_{scat} for a Si cylinder with d = 100 nm, h = 100 nm positioned on a semi-infinite substrate with n_{sub} = 1.5 (red) and n_{sub} = 3.5 (blue). The geometry is shown as an inset. The peaks are labeled according to the corresponding resonance (ED/MD) and numbered for reference in (c). (b) Fraction of scattered power into the substrate as a function of n_{sub}, at resonance wavelength (blue) and integrated over the entire spectral range (400–700 nm). A clear increase in downward scattered power is observed with increasing n_{sub}, attributed to the enhanced *LDOS* in the substrate. (c) Far-field radiation patterns for the numbered peaks from (a) corresponding to the ED and MD modes of the Si cylinder (top row). 1–2 correspond to the ED and MD mode on a n_{sub} = 1.5 respectively, 3 to the MD mode on n_{sub} = 3.5. The gray circles correspond to constant θ with equidistant spacing $\Delta\theta = 10°$. The white dashed circles correspond to the critical angle θ_c in the substrate. The orientation of the ED and MD dipole moments are shown on the left. The bottom row shows the calculated radiation patterns of the corresponding point-dipoles (p_x and m_y), positioned 50 nm above the substrates with n_{sub} = 1.5 (left, center) and n_{sub} = 3.5 (right). Note that the colorbar of the bottom row has been saturated at 0.7 for visibility.

(top row), as a function of azimuthal angle and zenithal angle. From left to right, the patterns correspond to peaks 1–3 in Fig. 9.7a, respectively. Incident light is polarized along $\hat{x}$, i.e. the $\theta = 90°$ direction. The orientation of the ED and MD dipole moments is shown by the gray arrows on the left. Furthermore, the critical angle for light trapping in guided modes is plotted as a white dashed line in each radiation pattern.

Radiation pattern 1 shows clear beaming from the ED mode into two specific angular lobes along $\hat{y}$, close to the critical angle. The radiation pattern of the MD mode (pattern 2) shows similar directional beaming close to the critical angle, but now along $\hat{x}$. The orientation of the radiation patterns correspond to that of an electric dipole and magnetic dipole on a substrate, oriented in the $\hat{x}$-direction (p_x) and $\hat{y}$-direction (m_y) respectively. To show this, we also plot the radiation profiles into the substrate of point dipoles (p_x, bottom left, and m_y, bottom center and bottom right) positioned 50 nm above a substrate with $n_{sub} = 1.5$ (bottom left and bottom center) and $n_{sub} = 3.5$ (bottom right). The radiation patterns are obtained from classical theory [280, 287]. Comparing radiation patterns 1 and 2 with those of p_x and m_y we find qualitative agreement, indicating that 100 nm high cylindrical particles at resonance have radiation patterns similar to point dipoles. Finally, radiation pattern 3 in Fig. 9.7c shows how the radiation pattern of the $\hat{y}$-oriented MD (MD_y) resonance is influenced by an increase in refractive index of the substrate to $n_{sub} = 3.5$. The same directional beaming is observed, but now more pronounced (stronger beaming) and under smaller θ as the critical angle has decreased to $\theta_c = 16.6°$. Again, good qualitative agreement is observed with the point dipole model (bottom right).

The patterns observed in Fig. 9.7c show that selective excitation of eigenmodes (ED or MD) allows for directional emission in the $\hat{x}$ or $\hat{y}$-direction. Therefore, the combination of spectrally separated ED/MD modes can be used for wavelength demultiplexing of polarized light: short wavelengths are scattered along $\hat{y}$ by the ED mode, long wavelengths along $\hat{x}$ by the MD mode. The height and diameter can be tuned to obtain the desired spectral response, the index of the substrate defines the bandwidth and scattering angle (i.e. SiO_2 gives large angles). Furthermore, the strong emission around the critical angle has direct implications for the use of such resonators for light trapping in weakly absorbing substrates, such as solar cells. Note that Fig. 9.7 only considers the radiation patterns of the lowest order dipolar modes. It has been observed that higher order modes show strong beaming around the normal [285]. Furthermore, the patterns observed in Fig. 9.7c change when the particle gets taller. In this case, the effective dipole moments are positioned further away from the substrate, such that a larger fraction of the emission is below the critical angle. Simulations show that increasing the particle height from 100 nm to 200 nm significantly changes the radiation patterns from dipolar like emission profiles as observed in Fig. 9.7c, to strong beaming along the normal due to the increased distance of the effective dipole moments to the substrate. Altogether, this indicates that tuning the geometry of the resonator can give accurate control over the radiation properties of the scattered light.

Figure 9.8a shows a comparison of the forward (green) and backward (blue) scattered power for a d = 100 nm, h = 100 nm Si cylinder on a substrate with n_{sub} = 1.5. Also shown are the ratio P_{down}/P_{up} (red), and the spectral range of the ED (shaded red) and MD (shaded blue) resonances. Note that the oscillations in the red line for $\lambda > 580$ nm are due to numerical noise. The scattering ratio peaks at 14.8, which indicates strong directional scattering into the substrate. This is a result of the interference of light scattered by the ED and MD modes, as was theoretically predicted by Kerker et al. [288] and recently demonstrated experimentally for spheres [30, 46] and cylinders [45]. For Si spheres, the peak ratio observed was ~8 [30], which shows that particles that have strong coupling to a substrate can exceed this ratio significantly.

However, in the latter case the directionality also originates from the high *LDOS* of the substrate. To differentiate these two effects, Fig. 9.8b shows the ratio P_{down}/P_{up} as a function of wavelength for $1.25 \leq n_{sub} \leq 3.5$ in steps of 0.25. As was observed in Fig. 9.4a, with increasing n_{sub} both the ED and MD resonance peaks significantly broaden and the total scattered power increases. The peak scattering ratio is significantly reduced for larger n_{sub}. Thus, the contrast from the ED/MD interference is strongly suppressed, whereas the average value is similar (6.4 for n_{sub} = 3.5, 6.8 for n_{sub} = 1.5). Therefore, this graph clearly shows the trend from scattering dominated by Kerker-type interference (high peaks and dips, low n_{sub}) to scattering dominated by *LDOS* (flat and high response, for high n_{sub}). The reason for this transition can be understood from the requirements for Kerker-type interference: as n_{sub} increases, the overlap in the far-field radiation patterns is reduced and the relative phase difference is less well defined. The combination of Kerker-type interference and *LDOS* dominated scattering can be tuned to get optimum directionality for one specific wavelength, or reduced directionality over a broad spectral range. Note that the optimum in forward scattered power always occurs at the MD resonance (see also Fig. 9.7b) [45].

9.9 Conclusions

In conclusion, we have systematically studied the influence of particle geometry and dielectric environment on the resonant behavior of single dielectric particles, both isolated and strongly coupled to a substrate. We found that the lowest energy mode is an in-plane MD mode, driven by a vertical displacement current loop inside the particle. In the limit of low n and low h, there is not enough retardation to form a current loop, such that no MD mode is supported. The excitation of the ED mode is not limited by such constraints. At larger diameters, the ED and MD spectrally overlap, and the higher order MQ mode appears in the blue spectral range. Furthermore, we observe that strong coupling to (dielectric) substrates requires a large contact area between the resonator and the substrate. This allows the displacement current loop to extend partially into substrate, yielding high radiative losses into the substrate. More complex multi-layer substrate allow selective

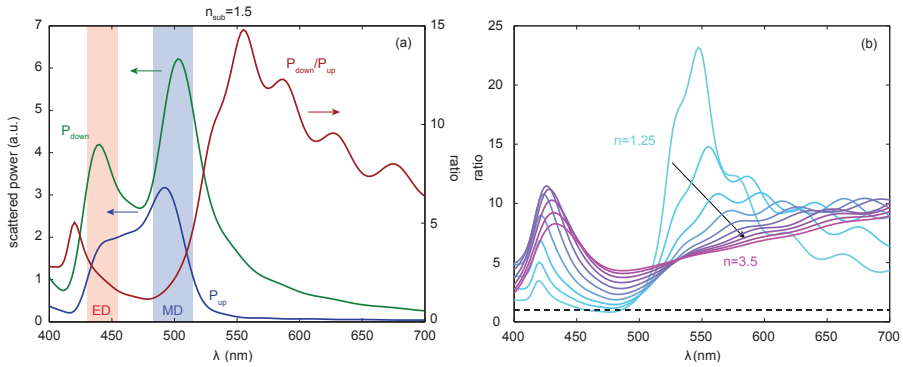

Figure 9.8: (a) Back scattered power (blue), forward scattered power (green) and forward/backward ratio (red) for a $d = 100$ nm, $h = 100$ nm Si cylinder on $n_{sub} = 1.5$. The red and blue shaded regions indicate the spectral range of the ED and MD resonances respectively. Note that the oscillations in the red curve for $\lambda > 580$ nm are due to numerical noise. (b) Forward/backward scattering ratio as a function of wavelength for different n_{sub} ranging from 1.25 to 3.5 in steps of 0.25.

enhancement and/or suppression of ED and MD modes through coupling with a Fabry-Pérot mode in the multi-layer substrate. Also, by comparing dipole and plane wave sources, we found that both vertical and horizontal E-fields can excite the in-plane MD mode, whereas the ED modes have orthogonal dipole moments and different resonance energies. Finally, by studying radiation patterns into the substrate we found that the ED and MD modes have radiation patterns similar to point dipoles above substrate, showing strong directional beaming around the critical angle. Altogether, this work is a guideline for the engineering of dielectric resonators, which allows one to use the combined scattering from ED and MD modes to taylor the scattering properties for specific applications.

10

Direct imaging of hybridized eigenmodes in coupled silicon nanoparticles

High-index dielectric nanoparticles support strong leaky geometrical resonances in the visible spectral range. Coupling between resonant nanoparticles in close proximity can give rise to enhanced directionality and confinement. We combine dark-field scattering spectroscopy with cathodoluminescence (CL) imaging spectroscopy to study hybridization of resonant modes in coupled silicon nanoparticles and directly image the modal field profiles of hybridized eigenmodes. The dark-field measurements show a strong influence of the gap size on the scattering spectrum as a result of hybridization. Using finite-element modeling we calculate the eigenmodes of the dimer and identify the hybridized eigenmodes in the scattering spectrum. CL imaging spectroscopy is used to directly map the modal field profiles of single particles and dimer structures with deep-subwavelength resolution. Detailed comparison with eigenmode calculations shows that the measured modal field profiles correspond to the hybridized electric bonding and magnetic anti-bonding modes.

10.1 Introduction

Dielectric nanostructures with a high refractive index exhibit geometrical resonances that allow for strong scattering and confinement of light at the nano-

scale [28, 31, 256]. These properties have resulted into widespread application of dielectric resonators in nanoscale devices, including photodetectors [57, 58], lasers [62, 263, 289], and solar cells [33, 60, 85, 259]. High-index dielectric particles support both electric and magnetic modes in the visible and near-IR spectral range [28, 39, 41, 43, 44]. Interference of the magnetic dipolar (MD) and electric dipolar (ED) modes can be used to engineer strongly directional scattering profiles [30, 46, 288], and realize all-dielectric low-loss metamaterials [53, 54, 290, 291] and metasurfaces [56, 292].

To fully exploit the potential of dielectric resonators in more complex structures and devices, fundamental understanding of the resonant properties of individual nanoparticles is essential. In Chapter 8 we used cathodoluminescence (CL) imaging spectroscopy to study the resonant properties of single Si nanoparticles. Using the high spatial resolution of CL we systematically mapped the resonant modes in single silicon nanocylinders as a function of particle diameter. In this Chapter, we take the next step and study how resonant particles that are placed in close proximity interact and how their resonant modes are modified. Recently, coupled dielectric resonators have attracted wide-spread attention due to their ability to enhance the scattering directionality and concentration of light compared to a single particle. For example, Si dimers and trimers have been demonstrated to exhibit strongly directional scattering as a result of coupled resonances [47, 48]. Furthermore, electric and magnetic field enhancements in the gap of dielectric dimers have been studied theoretically [47, 49] and demonstrated experimentally using scanning near-field optical microscopy (SNOM) [52]. Similar to hybridization of the electric modes in plasmonic dimers [293, 294], coupling between electric and magnetic magnetic dipolar modes in dielectric resonators can give rise to hybridization, resulting into bonding and anti-bonding modes [49, 51]. The hybridization of ED and MD modes in Si spheres on glass has been studied experimentally using dark-field spectroscopy [51].

Here, we combine dark-field spectroscopy with CL imaging spectroscopy to directly image the field profiles of the hybridized eigenmodes *inside* coupled Si nanoparticles. In dielectric dimers hybridization of eigenmodes occurs for smaller gap sizes than in plasmonic dimers, as a result of the reduced near-field intensity [49]. We fabricate both isolated and coupled Si cubes instead of spheres to reduce the effective gap size and thereby enhance the inter-particle coupling. Using dark-field spectroscopy, we study the influence of gap size on the scattering spectrum and show strong spectral splitting as a result of mode hybridization. We use finite-element modeling to calculate the eigenmodes of the single cubes and dimers, and identify the hybridized eigenmodes. Next, we use CL imaging to directly map the field profiles of the isolated particles and hybridized modes in coupled nanoparticles. Finally, we image the field profiles of larger rectangular dimers and map the complex hybridization modes with deep-subwavelength resolution.

10.2 Fabrication

Single crystalline Si cubes and dimers with spacings in the range of 0–100 nm were fabricated on a thin SiO_2 layer, supported by a thick Si wafer. Starting with a silicon-on-insulator (SOI) wafer (100 nm Si layer and 300 nm SiO_2 layer on a Si substrate), the top layer was patterned into nanostructures. First, electron beam lithography (EBL) was used to write squares and dimers into a negative-tone electron beam resist to form an etch mask. Second, the pattern was etched into the Si top layer using anisotropic reactive-ion etching (RIE). Third, the etch mask is removed using a short wet etch in hydrofluoric (HF) acid. See Section 10.6 for the details of the fabrication process.

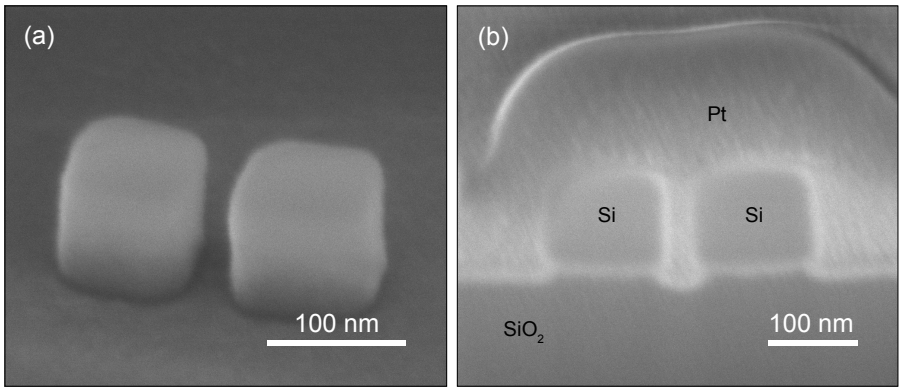

Figure 10.1: (a) SEM image of Si dimer on oxide layer (imaged under 52°). (b) FIB cross section of the Si dimer, showing the rounded square shape of the particles and the small under etch. The different layers are labeled. The particles are surrounded by Pt, which is deposited to improve the quality of the FIB cross section.

The resulting Si cubes are 90 nm wide, 100 nm tall, and have rounded edges. Figure 10.1 shows scanning-electron micrographs (SEM) of the particles (a) and of a focused-ion beam (FIB) cross section (b) of the resulting dimer. A protective layer of Pt was deposited using electron-beam induced deposition (EBID) to improve the quality of the FIB cross section. The cubical shape of the individual nanoparticles is clearly visible. Furthermore, a small under-etch of the SiO_2 layer as a result of the HF etch can be observed. The nanostructures were spaced 5 μm apart, such that experiments could be performed on isolated particles and dimers.

10.3 Dark-field spectroscopy

To study the hybridization of the eigenmodes, we start by using dark-field (DF) backscattering spectroscopy to measure the scattering spectra of the single particles and the dimers with different particle spacing. Single particles and dimers were

illuminated with unpolarized white light, and scattered light in the 430–570 nm spectral range was collected by a 100× microscope objective (0.9 *NA*), and analyzed using a spectrograph and a CCD camera (see Section 10.6 for experimental details). Figure 10.2 shows the DF spectra and corresponding SEM images for a single particle (blue), and for dimers with a spacing of 100 nm (green), 25 nm (yellow), and 0 nm (orange). The spectra for a rectangle (red) and the flat substrate next to the particles (gray) are also shown for reference.

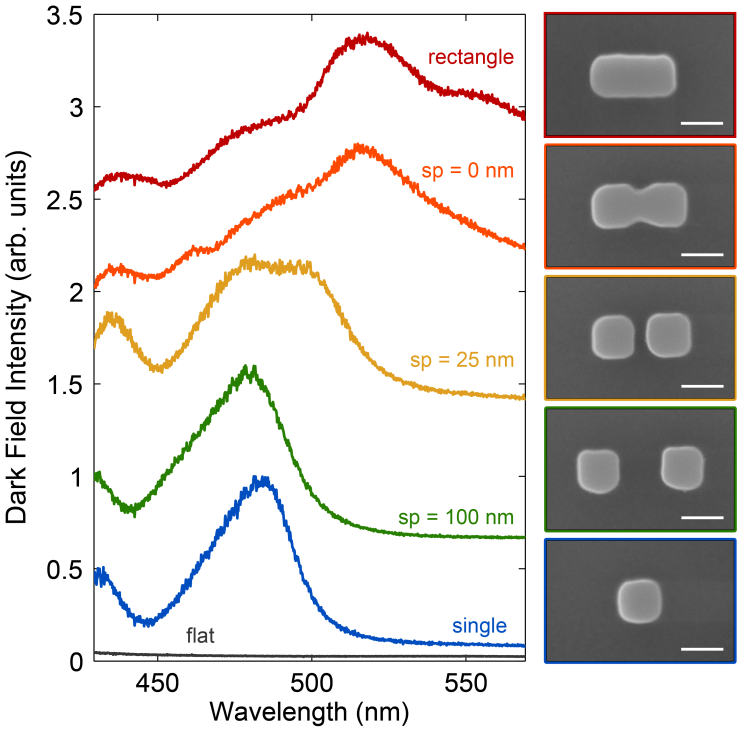

Figure 10.2: Dark-field scattering spectra for single square (blue), dimers with various spacings, and rectangle (red). The spectrum for the flat background is also shown (gray). Note that each spectrum is normalized separately and displayed with a vertical offset for visibility. SEM images of the corresponding particles are shown on the right. The scale bar in all images is 100 nm.

Two clear resonant peaks at $\lambda = 430$ nm and $\lambda = 485$ nm can be observed for the single particle. It is well known that these peaks originate from resonant scattering by the in-plane magnetic dipole (MD, $\lambda = 485$ nm) and in-plane electric dipole (ED, $\lambda = 430$ nm) modes [41, 49, 51, 52, 295] (also see Chapter 9). These modes are degenerate in both in-plane directions as a result of symmetry. For a dimer with spacing $sp = 100$ nm, defined as the size of the gap in between particle, the

scattering spectrum strongly resembles that of the single particle, which indicates the lack of coupling. However, the resonance wavelengths strongly shift when the spacing is reduced to 25 nm. The peak at λ = 485 nm broadens and splits into two separate peaks, which indicates hybridization of the localized modes [51]. A red shift to λ = 435 nm is observed for the ED mode, and the MD mode is split into two modes at λ = 480 nm and λ = 495 nm as a result of hybridization, leading to a 5 nm blue shift and 10 nm red shift compared to the single particle spectrum, respectively. A drastic transformation of the scattering spectrum is observed as the spacing is further reduced to 0 nm (orange). The lowest energy mode strongly red shifts to λ = 515 nm, and higher order modes appear. These correspond to the resonant modes of the new structure formed by the touching cubes, which is confirmed by the strong resemblance with the scattering spectrum of the rectangle (red).

To explain the origin of the splitting observed for 25 nm spacing (yellow spectrum in Fig. 10.2), we use finite-element calculations [296] to find the eigenmodes of the dimer structure. We assume the cubes are non-dispersive and lossless with $\epsilon_r = 20$, and neglect the substrate. Although a multilayer substrate can significantly modify the line width [297] and excitation efficiency of modes (see Chapter 9), the influence of the substrate on the eigenmode field profile was found to be minor. Note that due to these assumption, the calculated eigenfrequencies do not directly match the measured resonance wavelengths. See Section 10.6 for details on the finite-element calculations.

We focus on the coupling between the in-plane MD modes, and neglect the asymmetry introduced by the DF illumination conditions. As a result, only symmetric modes that can be excited by incident plane waves are considered. This assumption has been demonstrated to accurately describe DF scattering spectra of hybridized spherical Si particles on a glass substrate [51]. Under these conditions, two hybridized bonding modes are found which both can be excited directly by incident plane waves. Figure 10.3a,b show schematic representations of the m_x-m_x and m_y-m_y bonding modes respectively, where m_i represents a magnetic dipole moment along the i-axis. The eigenfrequencies are found to be $f_{m_x-m_x} = (561+19i)$ THz ($Q \sim 30$). and $f_{m_y-m_y} = (579+31i)$ THz ($Q \sim 19$). The large imaginary part indicates that these modes exhibit strong radiative damping. The spectral spacing between the calculated eigenmodes is 16.5 nm, which corresponds well with the experimentally observed splitting in Fig. 10.2. To corroborate the magnetic nature of the hybridized eigenmodes, Figs. 10.3c-f show in-plane (x-y) cross cuts of the electric field intensity (c,d) and magnetic field intensity (e,f) inside the particles. The spots of high electric field intensity on either side of the particles in (c-d) correspond to cross-cuts of the displacement current loops, which are characteristic for in-plane MD modes. Furthermore, a high magnetic field intensities can be observed in the center of the particles (e-f) as a result of the magnetic dipole moment. Finally, the blue shift of the m_y-m_y bonding mode (λ = 480 nm) and red shift of the m_x-m_x bonding mode (λ = 495 nm) with respect to the single particle spectrum (λ = 485 nm) are in

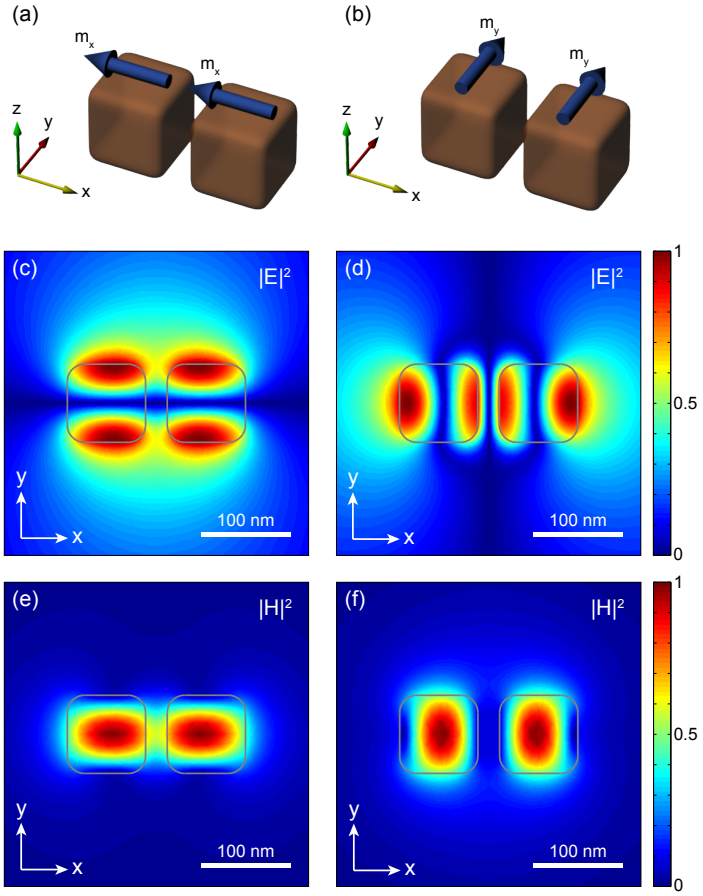

Figure 10.3: Schematic of the m_x-m_x bonding mode (a), and m_y-m_y bonding mode (b). In-plane cross cuts (xy-plane) through middle of dimers showing the electric field intensity (c-d) and magnetic field intensity (e-f) of the m_x-m_x bonding mode (c,e) and m_y-m_y bonding mode (d,f) respectively. The particle surroundings are also shown (gray contours). The calculated eigenfrequencies are $f_{m_x-m_x} = (561 + 19i)$ THz and $f_{m_y-m_y} = (579 + 31i)$ THz.

agreement with theoretical predictions [49] and DF scattering measurements on spherical dimers [51].

10.4 Cathodoluminescence spectroscopy

After the observation of hybridization in the DF scattering spectra, we use cathodoluminescence (CL) imaging spectroscopy to study the resonant modes in more detail. CL spectroscopy uses a focused 30 keV electron beam in a scanning electron microscope as a broadband light source to locally excite the sample [267, 298]. The high spatial resolution of the source allows for deep-subwavelength mapping of the optical modes [271], and has been used to study resonant modes in both metallic [67–69, 279, 299] and dielectric [271, 285] nanophotonic structures. Furthermore, the electron beam is a point source that primarily couples to the vertical component of the electric fields [270], which allows for the excitation of eigenmodes that are difficult to excite with plane waves due to the anti-symmetric character of their mode profiles. Similar to the results obtained for single Si nanocylinders (see Chapter 8), this experimental technique allows for spatial and spectral mapping of the resonant modes inside our Si dimers. Here, we apply this technique to directly image the field profiles of hybridized eigenmodes.

10.4.1 Single particle

Before considering the dimers, we first study the resonant modes of a single Si cube. In the experiment, we scan the electron beam over the sample in 8 nm steps and collect a full CL spectrum at each pixel. Next, the background is subtracted and we sum over the pixels corresponding to the particle to obtain the CL spectrum (see Section 10.6 for experimental details).

Figure 10.4a shows the CL spectrum for a single Si cube. Two clear peaks can be observed at λ = 485 nm and λ = 430 nm, and the shoulder of a third peak around λ = 390 nm. For λ > 500 nm a high but flat background signal is observed, which is caused by imperfect subtraction of the large background signal induced by defect luminescence in the SiO_2 layer. Note that the resonant wavelengths show excellent agreement with the DF scattering spectrum for the single particle (blue line in Fig. 10.2), which indicates the peaks at λ = 485 nm and 430 nm correspond to the in-plane MD and ED mode respectively.

To characterize the spatial mode profile, Fig. 10.4b shows the two-dimensional CL intensity maps for wavelengths corresponding to all three resonant peaks. For λ = 390 nm, the CL intensity is maximum in a bright spot in the center. For λ = 430 nm and 485 nm on the other hand, a clear ring of maximum intensity is observed along the circumference of the particle, although the low intensity in the center of the ring is more pronounced for λ = 430 nm than for 485 nm.

To corroborate that the electron beam couples to the in-plane ED and MD modes, we calculated the eigenmodes for an individual cube and compare them to the CL intensity maps. Since the electron beam primarily couples to the vertical component of the electric fields [270], we now consider $|E_z|^2$ only instead of $|E|^2$. Three different eigenmodes are found for the single particle that can be excited by electron irradiation along the z-axis (see Fig. 10.4d for schematics). Figure 10.4c

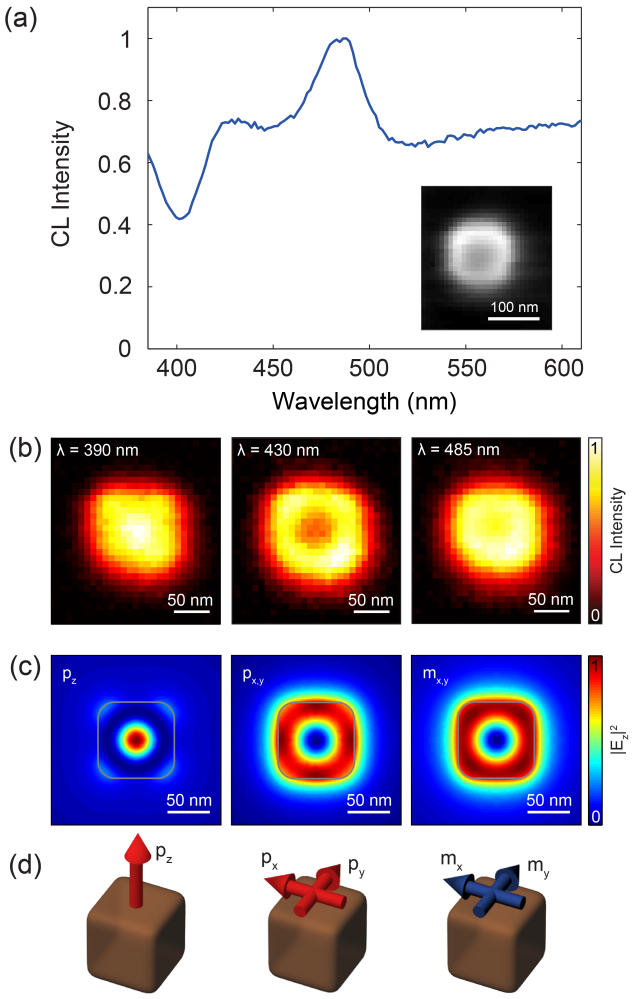

Figure 10.4: (a) Normalized CL spectrum for single square. SEM image of the particle collected simultaneously with the CL spectrum is shown as an inset. (b) Two-dimensional CL intensity maps for resonant peaks in (a) at $\lambda = 390$ nm, $\lambda = 430$ nm, and $\lambda = 485$ nm. (c) $|E_z|^2$ of the vertical electric dipole (p_z, left), in-plane electric dipole (p_x, p_y, center), and in-plane magnetic dipole (m_x, m_y, right). The corresponding eigenfrequencies are: $f_{p_z} = (826+52i)$ THz, $f_{p_{x,y}} = (807+35i)$ THz , and $f_{m_{x,y}} = (589+15i)$ THz. The profiles in (c) have been obtained by averaging over the two in-plane directions to account for degeneracy; the field for $p_{x,y}$ is plotted 25 nm above the center of the particle. (d) Schematic representations of the eigenmodes.

presents cross cuts along the xy-plane showing $|E_z|^2$ for the p_z mode (left), the degenerate $p_{x,y}$ mode (center), and degenerate $m_{x,y}$ mode (right). Here, p_i refers to an electric dipole moment along the i-axis. Note that the degeneracy is taken into account by averaging the modal intensity profiles over both orientations. Furthermore, note that $E_z = 0$ in the plane across the middle of the particle for $p_{x,y}$. For this reason, the crosscut is taken 25 nm above the center of the particle, where E_z is non-zero.

The bright spot in the center for $\lambda = 390$ nm is clearly reproduced by the field profile of the out-of-plane p_z mode, which has a higher eigenfrequency due to the asymmetry of the particle induced by the non-unity aspect ratio. Also the rings of high intensity observed for $\lambda = 430$ nm and $\lambda = 485$ nm (Fig. 10.4b) are well reproduced by the E_z fields of the in-plane $p_{x,y}$ mode and in-plane $m_{x,y}$ modes respectively. Altogether this confirms that the peaks at $\lambda = 430$ nm and 485 nm correspond to the in-plane ED and MD mode respectively, and demonstrates that CL spectroscopy allows for systematic mapping of the modal field profiles inside the particles with deep sub-wavelength resolution.

10.4.2 Dimers

Next, we study coupled dimer structures. Figure 10.5 compares the normalized CL spectrum for a single cube (blue) with that for dimers with different spacings and a rectangle (red). Analogous to the trends in the DF scattering spectra in Fig. 10.2, the CL spectrum for 100 nm spacing strongly resembles that of the single particle, which indicates weak coupling. However, for 25 nm spacing the CL spectrum changes drastically, showing a nearly-flat high intensity for $\lambda > 430$ nm, which indicates efficient excitation of a wide range of (hybridized) modes. Note that the electron beam also couples to anti-symmetric eigenmodes, which were not considered for plane wave excitation in Fig. 10.2. For touching particles ($sp = 0$) the lowest order mode strongly red shifts to $\lambda \sim 530$ nm, and resonance peaks corresponding to higher order modes occur. The resonant peaks observed for $sp = 0$ are attributed to the geometrical modes of a rectangle, which shows a very similar spectrum (red). The spectrum for $sp = 0$ shows a small red shift with respect to that of the rectangle due to the slightly longer effective length of the touching cubes.

We now examine the spatial CL intensity maps of the hybridized modes for $sp = 25$ nm. Due to the local excitation of the electron beam both symmetric and anti-symmetric combinations of the ED and MD modes are excited in the hybridized system, with large spectral overlap. As a result of the large spectral overlap, the two-dimensional CL intensity maps are comprised of multiple (hybridized) eigenmodes. However, two dominant hybridized mode profiles are clearly visible. Figure 10.6a shows the spatial CL intensity maps for $\lambda = 450$ nm and $\lambda = 490$ nm. The strong asymmetry in the intensity profile on the individual dimer particles is a direct indication of hybridization, and well-defined modal field profiles can be observed in Fig. 10.6a. For $\lambda = 450$ nm high CL intensities are located at the outside of the dimer, whereas high intensities are located near the

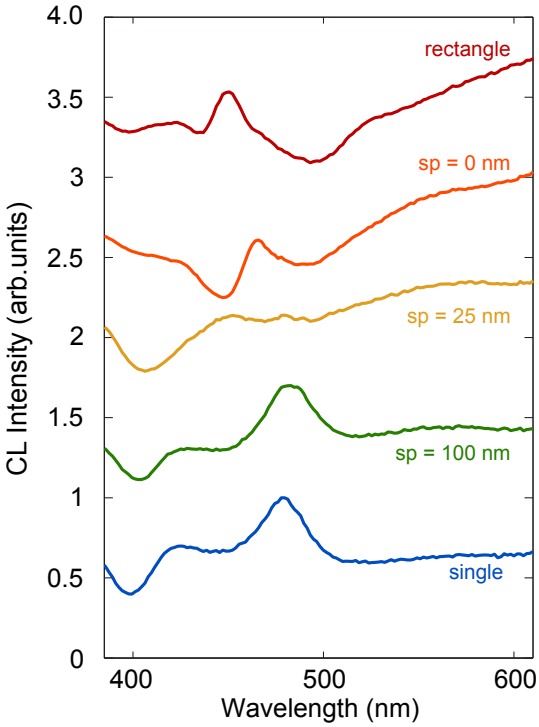

Figure 10.5: CL intensity spectra for single square (blue), dimers with various spacings, and rectangle (red). Note that the spectra are vertically offset for visibility.

center of the dimer for $\lambda = 490$ nm (see Fig. 10.6b for cross cuts). Note that for very small spacings heterogeneous coupling (between ED and MD modes) may also play a role [51].

To further study the hybridization observed in Fig. 10.6a, we reconsider the calculated eigenmodes and compare them with the two-dimensional CL intensity maps. Figure 10.6c shows crosscuts of $|E_z^2|$ for the p_x-p_x bonding mode (left) and the m_y-$m_{y'}$ anti-bonding mode (right), where y' refers to the opposite orientation of y). The corresponding eigenfrequencies are $f_{p_x-p_x} = (728+148i)$ THz and $f_{m_y-m_{y'}} = (582+9i)$ THz, respectively. Schematic representations of the bonding modes are shown in Fig. 10.6d.

We argue that Fig. 10.6a shows modal field maps of the f_{p_x-px} and $f_{m_y-my'}$ hybridized modes respectively for four reason: (i) The calculated field profiles strongly resemble the corresponding measured intensity maps. Note that the lack of high field intensity in the middle of the CL map for $\lambda = 450$ nm is attributed to the finite size of the electron beam and the strong local asymmetry in the field profile. To illustrate this, Fig. 10.6d shows the dipole orientation (left). At the center of

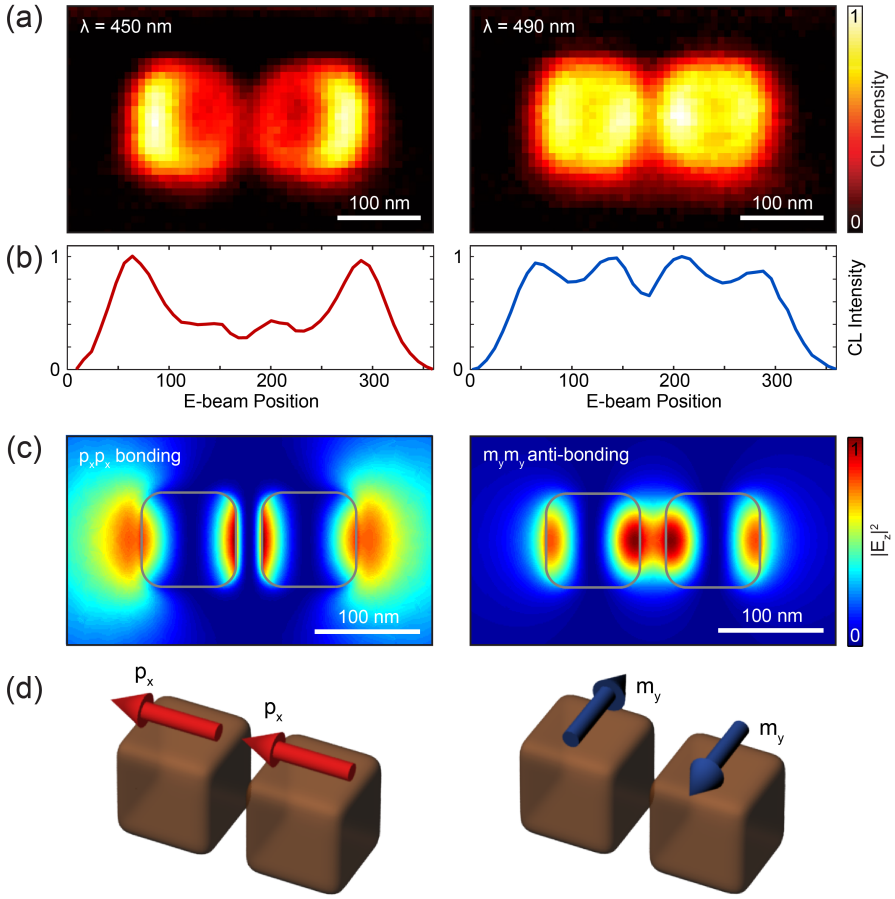

Figure 10.6: (a) Two-dimensional CL intensity maps for $\lambda = 450$ nm (left) and $\lambda = 490$ nm (right) showing hybridized modal field profiles. (b) Cross cuts through (a) showing the high field intensity on the outside (left) and inside (right) of the dimer. (c) Cross cuts displaying $|E_z|^2$ for the p_x-p_x bonding mode (left) and the m_y-m_y anti-bonding mode (right). The corresponding eigenfrequencies are $f_{p_x-px} = (728+148i)$ THz and $f_{m_y-my'} = (582+9i)$ THz. Note that the left cross cut is taken 25 nm above the center of the particle, as $E_z = 0$ in the center for $p_{x,y}$ modes. (d) Schematic representation of the hybridized dipolar modes.

the dimer the E_z fields of the dipoles are oriented anti-parallel, which limits the excitation efficiency by the electron beam. (ii) The p_x-p_x ($\lambda = 450$ nm) bonding mode is strongly red shifted with respect to the p_x mode of the single particle ($\lambda = 430$ nm), which is consistent with earlier work [51]. The resonance wavelength for the m_y-$m_{y'}$ mode ($\lambda = 490$ nm) on the other hand, shows only a weak red shift

compared to the single-particle m_y mode (λ = 485 nm). The relatively large and small spectral shifts are also consistent with those obtained from the calculated eigenfrequencies. (iii) The spatial intensity profile observed for λ = 450 nm (left) dominates the CL intensity maps over a large spectral range (430 < λ < 480 nm), while the spatial intensity profile observed for λ = 490 nm (right) is relatively weak and only observed for a narrow spectral range. This is in agreement with previous work [51], which showed that the p_x-p_x bonding mode dominates the scattering spectrum over a wide spectral range. (iv) The imaginary part of the calculated eigenfrequencies matches this trend: Im$\{f_{p_x-p_x}\}$ = 148 THz, which indicates large radiative losses as a result of the large effective dipole moment, corresponding to a large bandwidth. Im$\left\{f_{m_y-m_{y'}}\right\}$ = 9 THz on the other hand, which indicates weak radiative losses due to the weak coupling to plane waves as a result of the modal asymmetry, corresponding to a narrow line width. Altogether, Fig. 10.6 shows that CL can be used to directly map modal field profiles of both bonding and anti-bonding hybridized eigenmodes.

10.4.3 Rectangular dimers

Finally, to map hybridized eigenmodes with further increased complexity, we focus on a larger dimer structure which exhibits higher-order modes and more complex modal field profiles. The dimer is comprised of two rectangular bars with 100 nm width and height, and 300 nm length and 35 nm spacing (see Fig. 10.7a). These individual resonators have well defined leaky resonances that can be described theoretically as modified Fabry-Pérot modes [31].

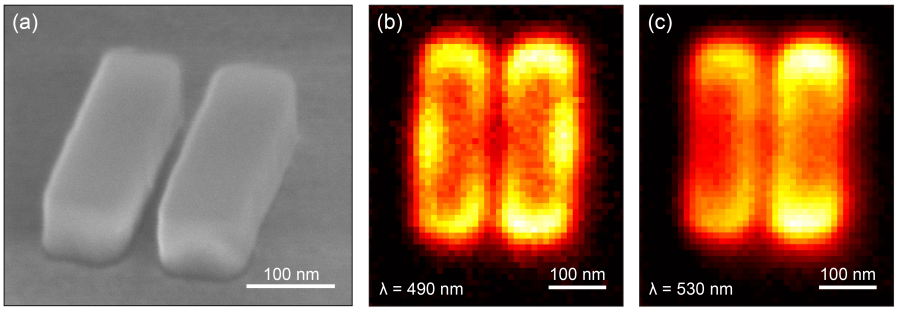

Figure 10.7: (a) SEM image (imaged under 52°) of a dimer comprised of rectangular particles with 300 nm length, 100 nm width and 100 nm height; the particle spacing is 35 nm. (b,c) Two-dimensional CL intensity map for λ = 490 nm (b) and λ = 530 nm (c), showing hybridization of higher-order eigenmodes.

The individual bars exhibit a large collection of geometrical modes as a result of their size, and each mode gives rise to a distinct resonant peak in the CL spectrum (not shown here). Coupling between the large number of modes results into a

rich hybridization scheme. Without going through a detailed analysis analogous to Fig. 10.6, we present two examples of CL intensity maps that unambiguously show field profiles of hybridized higher-order resonant modes. Figure 10.7b displays the measured mode map for λ = 490 nm, which shows high field intensities on the outside of the dimer. The mode map for λ = 530 nm on the other hand (c), shows high field intensities on the inside of the dimer. Furthermore, subtle variations in CL intensity inside each bar can be observed as a result of the higher-order modes. This example demonstrates how CL can be used to directly map complex hybridized field profiles inside single nanostructures, which allows for detailed characterization of resonant modes of coupled structures.

10.5 Conclusions

In conclusion, we have demonstrated direct imaging of hybridized eigenmodes in coupled resonant silicon nanoparticles. Using dark-field spectroscopy, we study the influence of gap size on the scattering spectrum and show strong spectral splitting as a result of mode hybridization. Using finite-element modeling we analyze the eigenmodes of the coupled nanoparticles, and identify the hybridized modes that dominate the scattering spectrum. Catholoduminescence (CL) imaging spectroscopy is used to directly image the modal field profiles of individual and coupled nanoparticles with deep-subwavelength resolution, showing strongly hybridized field profiles. Detailed analysis of the CL results and eigenmode calculations shows that the measured modal field profiles correspond to the hybridized p_x-p_x bonding and m_y-$m_{y'}$ anti-bonding modes. Finally, we study dimers composed of large dielectric bars to explore the ability of CL imaging to map highly-complex hybridized field profiles inside single resonant nanostructures. Our results demonstrate the ability to characterize the complex resonant properties of coupled nanostructures. Based on the detailed fundamental understanding of coupled resonators, nanostructures with accurately engineered field confinement and scattering profiles can be designed, paving the way for more complex applications and devices.

10.6 Methods

Fabrication

12 × 12 mm pieces of silicon-on-insulator (SOI) wafer (100 nm Si layer, 300 nm SiO_2 layer) were first cleaned by 10 min of sonification in acetone, 5 min of sonification in isopropanol (IPA), and blow dried. After a bake-out at 110°C, the samples were cooled with N_2 and spin coated with hydrogen silsesquioxane (HSQ, Fox 15), diluted with methylisobutylketon (MIBK) in a 1:2 ratio (3000 rpm, 45 s). The resist was baked at 180°C for 2 min, after which a small droplet of water containing 50 nm diameter Au colloids was deposited in the corner of the sample, to allow for accurate alignment of the electron microscope.

Electron beam lithography is performed using a Raith e-LINE system. Single squares and dimers were written in the HSQ resist using area exposure (30 kV acceleration voltage, 7.5 μm aperture, 17.8 pA beam current) and a dose of 1150 μAs/cm^2. The resist was developed by submerging in MF-319 (Microposit developer) at 50°C for 70 s, and subsequently rinsed in deionized water to stop the development.

Next, the HSQ pattern was used as an etch mask during the reactive-ion etching (RIE) step. An Oxford PlasmaPro 100 Cobra was used to anisotropically etch away the Si top layer. First, a short (10 s) Cl-based etch (50 sccm Cl_2, 7 mTorr, 30 W forward power, 750 W ICP power) was used to etch away the native oxide formed on the sample. Next, a 40 s etch using HBr (48 sccm) and O_2 (2 sccm) was used to anisotropically etch through the Si layer (7 mTorr, 30 W forward power, 750 W ICP power). The substrate temperature was controlled at 50°C during the etching. Finally, the residual HSQ etch mask was removed by a 2 min dip in hydrofluoric (HF) acid (1% concentration in water), and subsequently rinsed in deionized water and blow dried.

Dark-field spectroscopy

Dark-field scattering spectra of the single particles and dimers were obtained using a WiTec α300SR microscope. The sample was illuminated (unpolarized dark field configuration) using a 100× Zeiss microscope objective (EC Epiplan-Neofluar, HD M27, 0.9 *NA*, 0.28 mm working distance) and a halogen lamp. Scattered light was focused into a 50 μm-core collection fiber and sent to a spectrograph (UHTS 300, WiTec, 600 lines/mm, center wavelength 500 nm), equipped with a back-illuminated CCD camera (1024 × 127 pixels, $T = -60$°C). The experimental spectral range was 430–570 nm.

During the experiment, the sample was scanned through the focus of the objective in a two-dimensional plane using a 3D-piezo stage. Each scan used 15 × 15 pixels over a scan area of 3 × 3 μm (200 nm step size), with a 1 s integration time per pixel. Figure 7.8 shows a typical intensity map obtained from the scattering of a single particle ($\lambda = 472$ nm). Data is averaged over the pixels that have an intensity larger than 85% of the maximum observed intensity (threshold) to increase the signal to noise (e.g. 3 pixels in Fig. 10.8). To correct for the system response, a Lambertian reference was used (Labsphere certified reflectance standard). The dark-field scattering spectra are calculated as $(I_{part} - I_{dark})/(I_{lamb} - I_{dark})$, where I_{part} is the scattering spectrum of the particle, I_{lamb} the lambertian reference spectrum, and I_{dark} the dark spectrum of the CCD.

Note that the particle spacings reported in Fig. 10.2 are obtained from SEM images, using a thresholding routine and the calibrated pixel size.

Cathodoluminescence spectroscopy

A scanning-electron microscope (FEI XL-30 SFEG) was used to irradiate the nanoparticles with a focused electron beam (30 keV, ~20 nA current). The CL radiation is collected by an Al parabolic mirror and redirected out of the SEM.

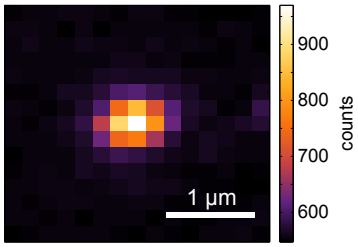

Figure 10.8: Intensity map of a typical dark-field measurement. Map is for a single particle at $\lambda = 472$ nm.

Spectral analysis was performed using a spectrograph (Acton SpectraPro 2300, 150 lines/mm, center wavelength 650 nm) and a liquid-nitrogen cooled back-illuminated CCD camera (Spec 10 100B, Princeton instruments, 1340 × 100 pixels). The CCD chip was hardware-binned to 335 × 1 pixels. During the scans, the electron beam was scanned over the particle using a 50 ms integration time per pixel. The CL data are corrected for system response using a measured transition radiation spectrum from aluminium and comparing that to theory [270, 300]. The background CL signal from the substrate was subtracted from the measured data, which includes the transition radiation of the SiO_2 layer and Si substrate, as well as intrinsic defect luminescence from the SiO_2. To correctly subtract the variable background from the CL signal, we use a triangular interpolation routine, which interpolates the background intensity between the corners of the scan for each wavelength. We used thresholding of SEM data to determine which pixels contribute to the particle CL spectra.

Eigenmode calculations

Finite-element modeling was performed using COMSOL Multiphysics 5.0. The simulation volume was a quadrant of a sphere, with a radius of 480 nm, and was surrounded by a PML layer with 240 nm thickness. The dimers were positioned in the center of the sphere. The simulation volume used a homogeneous relative permittivity of 1, while a non-dispersive relative permittivity of 20 was used for the silicon particles. For the flat sides of the quarter sphere we used perfect electric or magnetic conductor boundary conditions, depending on the orientation and nature (electric or magnetic) of the dipole resonance. In the simulation volume mesh elements were tetrahedral, with vertex lengths between 0.3–10 nm inside and close to the silicon particles and 30 nm near the PML boundary. The PML mesh was swept from the PML boundary, with five layers along the radial direction and a maximum transverse vertex length of 30 nm.

11

Single-step soft-imprinted large-area nanopatterned anti-reflection coating

We demonstrate an effective nanopatterned anti-reflection coating on glass that is based on sol-gel chemistry and large-area substrate-conformal soft-imprint technology. The printed 120 nm tall silica nanocilinders with a diameter of 245 nm in a square array with 325 nm pitch, form an effective-index (n = 1.20) anti-reflection coating that reduces the double-sided reflection from a borosilicate glass slide from 7.35% to 0.57% (averaged over the visible spectral range) with a minimum reflectance < 0.05% at 590 nm. The nano-glass coating is made using a simple process involving only spin-coating and an imprint step, without vacuum technology or annealing required. The refractive index of the nano-glass layers can be tailored over a broad range by controlling the geometry ($1.002 < n < 1.44$ in theory), covering a wide range that is not achievable with natural materials. We demonstrate that the nano-glass coating effectively eliminates glare from smart-phone display windows and significantly improves the efficiency of glass-encapsulated solar cells. These features, that are achieved over an angular range as wide as $\pm 50^\circ$, together with strong hydrophobicity and mechanical durability, make nano-glass coatings a promising technology to improve the functionality of optoelectronic devices based on glass encapsulation.

11.1 Introduction

Light that impinges on the interface between two materials with different refractive indices exhibits reflection. In many applications, such reflection losses are unwanted. For example, reflection losses at the air/glass interface reduce the efficiency of photovoltaic modules [301], and the glare of reflected sunlight off the screen of mobile electronic devices reduces the visibility of the screen. Anti-reflection (AR) coatings, optically thin (dielectric) layers with carefully chosen refractive index and thickness, can minimize these reflection losses through interference effects. An optimized AR coating for material with index n in air has a refractive index $\sqrt{n}$ and an optical thickness $t = \lambda/4\sqrt{n}$, where λ is the free-space wavelength for which the AR effect is optimized.

While such AR interference coatings are commonly used for high-index materials, such as for example silicon solar cells [302], applying such coatings on glass ($n \approx 1.5$) is difficult, as no material is readily available in nature with a refractive index $n = \sqrt{1.5} = 1.22$. Alkali halides such as MgF ($n = 1.38$) and LiF ($n = 1.39$) have refractive index lower than glass [303], but are still far from ideal. Lower refractive indices can be obtained using sub-wavelength structuring of materials. For example, porous materials can have indices lower than that of the constituent bulk materials [304–307]. However, such coatings are often randomly structured, and therefore offer limited control over the index. As a result, such layers often lack large-scale uniformity and do not provide the theoretically achievable minimum reflection.

Directional scattering of resonant nanostructures has also been used to form efficient AR coatings [33, 308] however such coatings require high-refractive index nanostructures and have a bandwidth limited by the resonance line width. Alternatively, tapered sub-wavelength nanostructures can be used to create a "graded index" material, giving rise to a gradual change in refractive index rather than a sudden one [309–314]. Although the graded-index AR coatings are inherently more broadband than interference AR coatings, they often require complex fabrication schemes and are often composed of fragile high-aspect-ratio surface geometries.

AR coatings for glass substrates have been demonstrated using colloidal self-assembly [315] and lithography [314–316], porous silica solgels [304–307], sputtering [317], anodic aluminum oxide formation [318], laser interference-lithography [312] and nanoimprint lithography [309, 310, 313, 314]. A disadvantage of many of the techniques mentioned above is that they often require complex (many-step) fabrication procedures [309–314, 317], provide limited control over pattern spatial homogeneity and reproducibility [305–307, 315, 316, 318] and are not substrate conformal [311]. On the other hand, the more simple fabrication schemes yield relatively poor performance and/or uniformity [305, 315, 316, 318]. The combination of high performance anti-reflection properties, accurate control over nanoscale geometry, and facile fabrication procedure has so far not been realized.

Here, we use substrate-conformal imprint lithography (SCIL) [157] to demon-

strate an interference-based AR coating that: 1) is simple to fabricate using a single-step process; 2) allows for large-area cost-effective fabrication with large-area uniformity; 3) is substrate conformal, thereby allowing printing on rough surfaces; 4) exhibits reflectance equal to the theoretical minimum for AR coatings. Further advantage is that the method is easily optimized for specific applications (i.e. different types of substrate materials); and that the printed AR coating is strongly hydrophobic. This prevents scattering losses due to accumulation of water droplets, and makes the surface self-cleaning. Our SCIL-based AR coating fabrication method requires no external pressure [309–311], no elevated temperatures [306, 310–314] no sacrificial layers [312, 313], no UV-irradiation [309], no etching [307, 311, 312, 314, 315], or other vacuum techniques [312, 317, 318] and exhibits excellent large-range homogeneity and reproducibility [305–307, 309–311, 314–316, 318].

11.2 Fabrication

The AR coating is fabricated out of liquid-silica solgel, which is based on the liquid alkoxide tetra-methyl-ortho-silicate (TMOS), $Si(OCH_3)_4$ [157]. After hydrolysis, this precursor yields methanol and silicon hydroxyl $(CH_3O)_3Si\text{-}OH$, which can subsequently condensate into stable Si-O-Si bonds to form silica. Accurate control over the degree and rate of condensation is essential to prevent porosity and thereby the formation of stress-induced cracks in the solidified nanopatterned coating. Partial substitution of TMOS by the organic alkoxide methyl-tri-methoxy-silane (MTMS), $CH_3\text{-}Si(OCH_3)_3$, provides control over the degree of cross linking. This allows the formation of gels with a higher concentration of silicon precursors, and thereby results in a less porous material and less shrinkage. Furthermore, cured MTMS layers are optically transparent and its methyl group makes the resulting solgel layer hydrophobic.

To start the solgel fabrication [157], 7.1 grams of MTMS is mixed with 7.93 grams of TMOS in a polypropylene jar (250 mL). Next, 3 grams of 1-propanol is added to increase the mixability with water, followed by 6.6 grams of 1M formic acid in water. Next, the temperature of the mixture is controlled by an external water bath and the mixture is left to react at 36°C for 120 min. After this, 10.3 grams of water is added, as well as 92.4 grams of 1-propanol to dilute the hydrolysis mixture. The mixture is left at room temperature for 30 min, and subsequently stored at −25°C. Next, the imprint resist is fabricated from this mixture by adding a dilution mixture consisting out of 7.64 grams of 2-ethoxy-ethyl ether, 20.63 grams of water, and 99.06 grams of 1-propanol. The final imprint resist is stored at least 16 hours at −25°C before use.

The AR coating fabrication process consists of a single imprint procedure in which the substrate is spin coated (800 rpm, 10 s) with a 90 nm thick layer of the silica-based solgel, into which a nanopatterned PDMS stamp is subsequently applied (Fig. 11.1a). Capillary forces pull the stamp into the solgel, creating a

substrate-conformal imprint. After 30 minutes of drying in ambient conditions, the solgel has solidified and the stamp can be reused thousands of times [157]. The resulting silica nanostructures are dielectric and exhibit no optical absorption throughout the entire visible spectral range, as confirmed with spectroscopic ellipsometry (see Supplemental Section 11.9.1). The imprinted silica nanopattern is sub-wavelength and designed such that the effective index of the coating corresponds to the theoretical optimum for an interference AR coating on glass.

The pattern is composed of a square array of silica nanocylinders. The array pitch is 325 nm, such that no diffraction of free-space light occurs in the visible spectral range. Figure 11.1b shows a scanning electron microscope (SEM) image of an array of silica cylinders printed onto a silicon substrate, showing the cylindrical shape of the nanoparticles. A thin flat residual layer of solgel is clearly visible below the particles and is measured to be 30 nm thick. The particles are slightly tapered, with diameters of ~225 and ~260 nm at the top and bottom, respectively. The large-scale uniformity of the printed pattern is clearly visible in Fig. 11.1c. The height of the particles was measured to be 120 nm using atomic force microscopy (inset Fig. 11.1c).

11.3 Reflection experiments

Next, borosilicate microscope slides (24 × 24 × 1 mm, SCHOTT AG, refractive index n = 1.485 as retrieved from reflection measurements) were cleaned (base piranha and O_2 descum plasma) and patterned. Samples were coated at the front only, or at the front and the rear. When patterning the rear side of the glass, the front is protected during processing by coating the pattern with a thick layer of S1813 photo resist (2000 rpm, 32 s). After patterning the rear, the protective layer is easily removed by rinsing in acetone. An integrating sphere optical setup was used to measure the total reflectance of a flat reference substrate, and one- and two-side coated glass substrates (see Supplemental Section 11.9.2 for schematic). A white supercontinuum laser (Fianium SC400-4, unpolarized) was used as a light source, attenuated using the reflection of a glass wedge and a neutral density filter (ND 3.0). The samples were mounted at the back of an integrating sphere (LabSphere) with an 8° angle of incidence to prevent the specular reflection from escaping through the sphere entrance. A 105-μm-core collection fiber (Thorlabs, FG105 UCA, NA = 0.22) directs the light to a spectrograph (Acton SpectraPro 2300i) and a Si CCD camera (Pixis 400). Spectra are measured over two spectral ranges (420–800 nm and 800–1000 nm) using two different gratings (150 lines/mm, blazed for 500 nm and 800 nm). Each spectrum is the result of 100 accumulations of 250 ms integration time. A 15-point moving average (6 nm bandwidth) is used to smoothen out experimental noise. A silver mirror (Thorlabs PF10-03-P01) is used for a reference reflection measurement, taking into account the specified reflection for the mirror (see Supplemental Section 11.9.2). For the patterned substrates, the spectra shown are the average of the spectra measured on the front and rear sides.

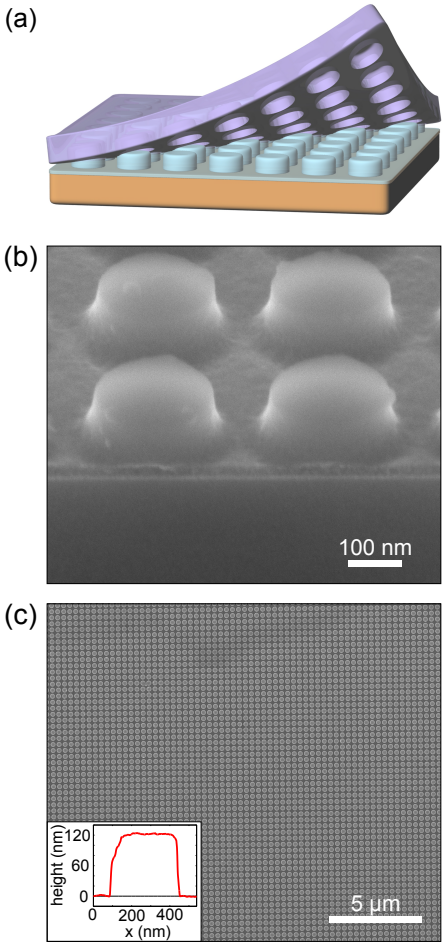

Figure 11.1: (a) Schematic of the one-step nanoimprint lithography fabrication method. The spin-coated solgel is patterned by a PDMS stamp to create an effective-index AR coating. (b) SEM image of the solgel nanocylinder array on a Si substrate, showing the cylindrical shape of the nanoparticles and the 30 nm residual solgel layer (cleaved sample imaged under 52°). (c) SEM image showing the large-scale uniformity. A line trace of an AFM scan is shown as an inset.

The nanostructured AR coating causes a strong broadband reduction in reflection (Fig. 11.2a). For both the one- and two-sided substrate, a clear minimum in reflection can be observed around $\lambda = 590$ nm as a result of the interference-induced anti-reflection effect. The reflection at $\lambda = 590$ nm is reduced from 7.3% to 3.8% by patterning one side of the substrate, and further reduced to $< 0.05\%$ (the measurement error) when both sides are patterned. The low reflection minimum indicates

that the effective index of the AR nanopatterned layer is very close to the optimal value of $n = 1.22$. We calculate the average reflectance (weighted for the AM1.5 solar spectrum intensity) over spectral bands relevant for display applications (e.g. for outside use) and solar panels based on Si solar cells. For display applications (phone screens, tablets, etc.), only the spectral range up to $\lambda = 700$ nm is relevant due to the sensitivity of the human eye [319], whereas for solar applications the full measured spectral range is relevant. The results are shown in Table 11.1, showing an average reflectance of 0.57% in the visible spectral range and 0.97% for the full spectral range.

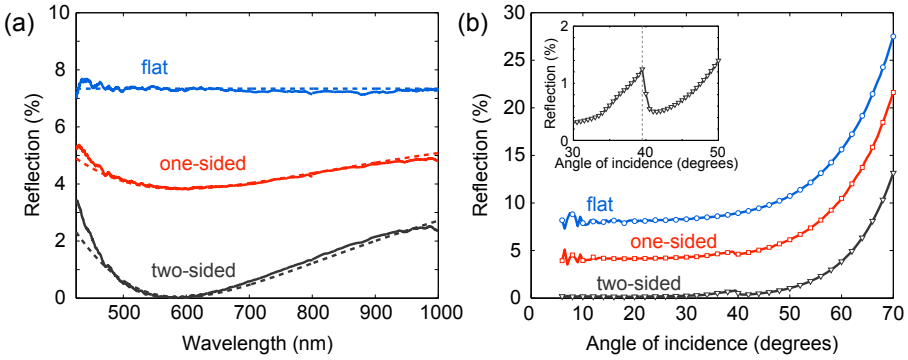

Figure 11.2: (a) Measured total reflection spectra for a flat reference (blue), and one-side patterned (red), and two-side patterned (black) glass substrates. The dashed lines show the calculated reflection. (b) Measured specular reflection as a function of angle of incidence for the same samples ($\lambda = 532$ nm, averaged over s- and p-polarization). A high-resolution plot of the angular response of the two-side patterned substrate around 40 degrees is shown as an inset (s-polarization).

Table 11.1: AM1.5 averaged reflectance for display (425–700 nm) and solar (425–1000 nm) applications for flat, one-side and two-side coated borosilicate glass.

Reflectance (%)	Display applications	Solar applications
Flat	7.35	7.30
One-side coated	4.10	4.24
Two-side coated	0.57	0.97

Finally, haze (random scattering of light) induced by the nanopattern AR coating should be minimized for display applications. The design of our nanopattern coating as an effective index AR coating does not distort the plane-wave nature of light propagating through the nanparticle layer (see Supplemental Section 11.9.3). As a result, the nanopattern AR coating exhibits extremely low haze in the visible spectral range (see Supplemental Section 11.9.4 for photograph).

Note that the wavelength of the 0% reflection dip can be tuned by varying the height of the nanocylinders, to match a specific application. For example, slightly lower nanoparticles will blue-shift the interference dip and further minimize the average reflectance for display applications. Furthermore, the size of the nanoparticle can be tuned to obtain a different effective index that can be optimized for substrates with different index. Assuming a minimum particle/hole diameter of 20 nm as the limiting resolution of SCIL, the effective index can in theory be tuned in the range n_{eff} = 1.001–1.439, providing efficient AR coatings for substrates with index in the range n = 1.002–2.070. Our coating thus allows full tunability according to the application and substrate used.

11.4 Effective medium calculations

To demonstrate that the anti-reflection properties of the nanopatterned surface are the result of the effective index experienced by the light, we performed transfer-matrix calculations using Fresnel equations and an effective index for the nanopattern layer. We neglect the tapered side walls and approximate the shape of the nanoparticles as prefect cylinders with d = 245 nm and h = 120 nm. Using a 325 nm pitch and refractive index for the solidified solgel n_{solgel} = 1.44 (see Supplemental Fig. 11.5), the volume-averaged effective index is calculated to be n_{eff} = 1.20, very close to optimum of 1.22. Note that for sub-wavelength structures with an index close to 1.5, this simple geometrical average is a very good approximation to more advanced effective medium calculations [320], such as the Maxwell-Garnett and Bruggeman theories [321, 322]. The calculations take into account the 30 nm thick residual layer and the angle of incidence of 8°. We calculate the coherent reflection and transmission coefficients of both interfaces separately, and use the fact that the substrate is thick in order to treat the interaction between the front and back interfaces of the glass incoherently. Using an infinite geometric progression we take into account the infinite number of reflections between the top and bottom interface and average over both polarizations.

The results for all three interfaces show very good correspondence with the measurements (Fig. 11.2a). Both the trends and absolute reflections are well reproduced by the calculations, confirming that the AR coating can be described by an effective medium (see Supplemental Fig. 11.7a for simulated field and phase profiles). Note that for both the one- and two-sided substrates, a clear discrepancy between measurement and calculation is observed for $\lambda < 500$ nm. We attribute this to light that is diffracted into the substrate and then coupled out again. Although the 325 nm pitch is small enough to prevent diffraction in free space, diffraction in the substrate can occur when $\lambda \leq 527$ nm (for 8° angle of incidence). Since the diffraction angle lies above the critical angle of a glass-air interface, this light is trapped in guided modes until it couples back out through the reverse process, thereby contributing to reflection and transmittance. Such mode coupling is not captured by the effective medium calculations, hence the discrepancy. Note that

in many applications the glass is in optical contact with another medium on the rear, such that this interface will not give rise to total internal reflection in the glass, eliminating the increase in reflection. Alternatively, decreasing the pitch to 250 nm, which is well possible with the SCIL technique, will eliminate diffraction effects in the visible spectral range altogether (see Supplemental Section 11.9.3 for FDTD simulations).

11.5 Angle-resolved reflection experiments

We measured the angle-dependent specular reflection using a dual rotation stage (Huber) to control the angle of incidence θ between 6–70° in steps of 0.5°. A λ = 532 nm diode laser (WiTec), polarization-maintaining single-mode fiber (WiTec) and outcoupler (Thorlabs CFC-8X-A) were used to illuminate the samples with ~20 mW of polarized light (300:1 s/p polarization ratio). The polarization was controlled with the outcoupler orientation and analyzed with a polarizer. The reflected light was sent through a diffuser (Thorlabs DG10-1500-MD) mounted in front of a calibrated power meter (Thorlabs PM300) in order to illuminate the detector surface uniformly. For each angle of incidence, the mean of 100 power measurements was recorded.

The polarization-averaged angle-resolved reflectance is shown in Fig. 11.2b (see Supplemental Fig. 11.9 for polarization-resolved data). The nanopattern reduces the reflectance for the entire measured angular range. The two-side coated substrate has a reflectance < 1% for angles up to 50°. Comparing the reflection at 50° with that at 10° shows that the nanopattern reduces the angular sensitivity. The absolute increase in reflectance over this angular range is 2.8% for the flat substrate, whereas it is reduced to 2.2% and only 0.9% for the one- and two-sided substrates respectively. Such low angular sensitivity is of major importance for stationary photovoltaic modules, for which reflection off the front glass plate at large angles of incidence reduces the annual yield [301, 323].

The patterned substrates both show a small drop in reflection around 40°. To study this in more detail, a high-resolution plot of the two-side patterned substrate, illuminated by s-polarized light, is shown as an inset (Fig. 11.2b). A strong decrease of 0.7% absolute in reflection is observed when $\theta > 39.5°$, which is caused by diffraction into guided modes in the substrate. For $8 \leq \theta \leq 39.5°$, the −1 diffraction order can couple to guided modes (see Supplemental Fig. 11.10 for dispersion calculations and schematic). Light that couples to guided modes couples back out and contributes to the measured reflection amplitude. The dashed line indicates the angle for which the dispersion curve of the diffracted order crosses the light line and beyond which coupling to guided modes no longer occurs. The data shows excellent agreement with the dispersion calculations. Again, coupling to the guided modes will be reduced for encapsulated substrates.

11.6 Wetting properties

Next, we study the wetting properties of our nanoimprinted coating. Adhesion of water droplets and nucleation of fog on the surface of transparent substrates causes scattering and thereby increases the overall reflectance. The solgel is more hydrophobic than the bare glass due to the presence of methyl groups. Nanostructuring the surface can further enhance the hydrophobicity, as water droplets partially rest on the nanostructure and partially on air inclusions [312, 324]. Besides a reduction in scattering from water droplets, hydrophobic coatings enhance self-cleaning of the surface as dust particles are picked up and removed by water droplets while rolling off the surface [312, 325]. To quantify the hydrophobicity of our nanopatterned AR coating, 2.5 μL droplets of dH_2O were deposited on bare flat substrates (cleaned with acetone and cleanroom wipe), and substrates coated with flat and patterned solgel layers. Optical microscope images (WiTec α 300 SR) were taken from the side to image the water contact angle.

The hydrophobicity of the solgel is clearly visible, as the contact angle (Fig. 11.3b) is much larger than that of a water droplet on the bare flat substrate (Fig. 11.3a). Indeed, the nanopatterned solgel further increases the water contact angle (Fig. 11.3c). Geometrical analysis of the droplets shapes (insets) shows contact angles of 40°, 79° and 97° for the bare flat, flat solgel, and patterned solgel substrates respectively. The contact angle being larger than 90° implies the surface is hydrophobic by definition [325]. Finally, to test the mechanical rigidity of the nanopattern coating we applied, pressed and removed both office tape and vinyl duct tape (3M 3903i) onto the patterned surface. In both cases, the nanopattern was resistant to tape stripping, as no surface modification was observed by SEM imaging (see Supplemental Section 11.9.7 for details).

The very low reflectance (0.57% averaged in visible spectral range) and low angle sensitivity (< 1.0% up to 50°) of the nanopatterned AR coating is comparable to or better than what was obtained with complex graded index moth-eye AR coatings [309–313], while our fabrication method is much simpler. While the high-aspect ratio of the moth-eye structures is beneficial for hydrophobicity [309, 312, 313], the reduced aspect ratio of our nanopattern coating makes it much less fragile.

11.7 Prototype devices

To demonstrate the large-area applicability and ease of fabrication of the AR coating, we printed the nanopattern on the surface of a smart phone screen (Apple iPhone 4) and compare it to a flat non-patterned screen. Prior to the imprint procedure, the screen was cleaned with isopropanol and a cleanroom wipe. Figure 11.4a shows a photograph of the reflection of fluorescent ceiling lighting off bare and nano-imprinted screens. A clear reduction in the reflected intensity can be seen from the reduced intensity of the reflected fluorescent lamp. Such reduced reflectance strongly improves the readability of the smartphone

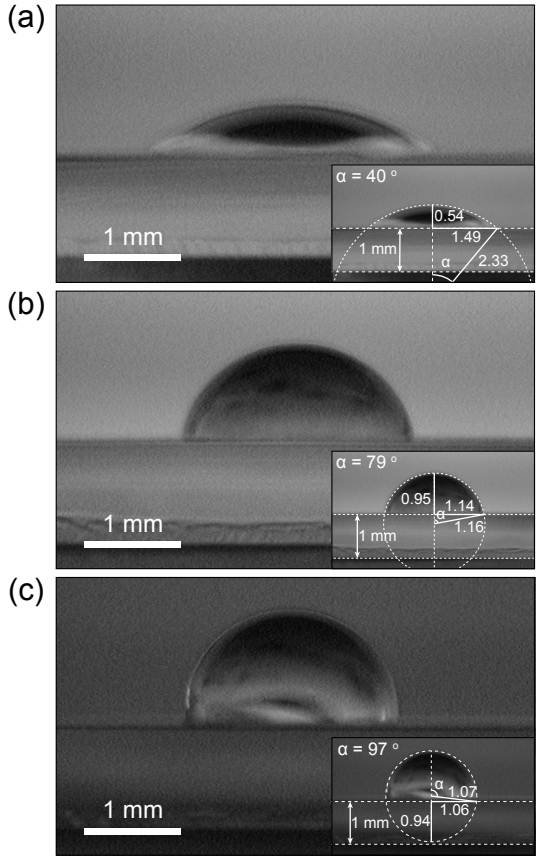

Figure 11.3: Optical microscope image of dH_2O droplets on a flat reference glass substrate (a), flat solgel layer (b), and nano-patterned solgel layer (c), showing the hydrophobic behavior of the nanopatterned AR coating. From bottom to top, the microscope stage, the glass substrate and the droplet are clearly visible. The geometrical analysis and the calculated contact angles are shown as insets.

screen. The improved contrast between light emitted by the screen and glare from surrounding light (e.g. sun) also reduces the screen brightness that is required for good readability, and can reduce the screen's energy consumption.

To demonstrate the applicability to solar applications, we apply a nanoimprinted AR coating to Si photovoltaic cells encapsulated in glass. We use n-type diffused front-junction c-Si solar cells, which are encapsulated by lamination with a 300 μm thick EVA layer, a 3-mm-thick low-iron glass slide at the front and a white backsheet. The cells were 5 × 5 cm^2 in size, and framed in a 6 × 6 cm^2 mini-module. Before patterning the front surface is cleaned with acetone, isopropanol

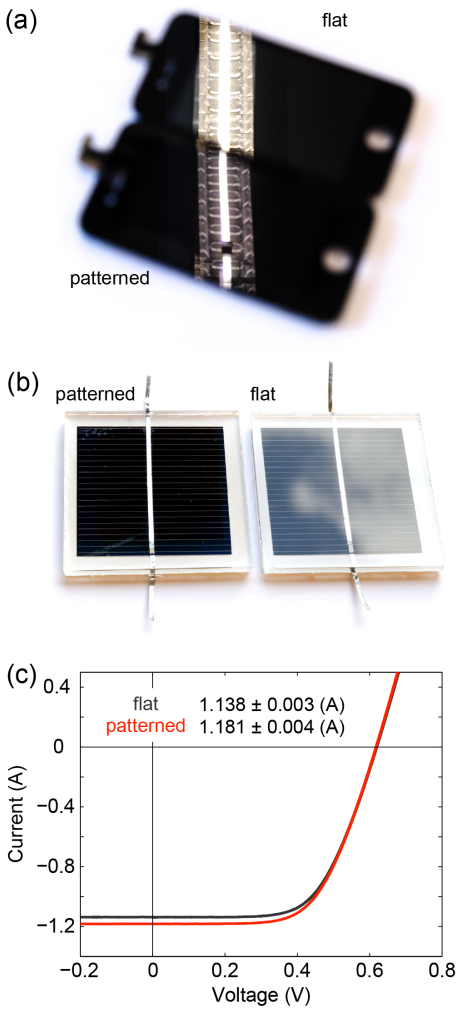

Figure 11.4: (a) Photograph of smartphone screens with (bottom) and without (top) AR coating. The reflection of the fluorescent lighting is clearly reduced. (b) Photograph of glass-encapsulated c-Si solar cells with (left) and without (right) AR coating. The cell area is 5 × 5 cm^2. (c) Current-voltage measurements on the glass-encapsulated solar cells with (red) and without (black) AR coating. The short-circuit current I_{sc} for the two cells is listed: a 3.8% relative increase is observed due to the AR coating.

and cleanroom wipes. Figure 11.4b shows a photograph of the reflection of the clouded outdoor sky off both mini-modules. A clear decrease in reflectance can readily be observed by eye.

To test the influence on cell performance, we measured the current-voltage characteristics of the same cell before and after nanopatterning. A solar simulator (Newport Oriel Sol2A) was used to illuminate the cell with 1.000 ± 0.005 sun intensity. Using a source-measuring unit (Agilent B2902A), the voltage over the cell is scanned from −1.0 to +1.0 V in steps of 2 mV, and the photocurrent is measured. The standard deviation in photocurrent as a result of positioning uncertainties was measured to be < 0.5%, by repeatedly positioning the cell in the solar simulator and measuring the I-V response.

Patterning the photovoltaic modules with the nanopatterned AR coating causes the short-circuit current generated by the cell to increase from 1.138 ± 0.003 to 1.181 ± 0.004 A (Fig. 11.4c). This corresponds to a 3.8% relative increase in current, increasing the peak output power from 441 to 453 mW. Note that the modules have been measured without masking of the white area around the cell. Thus, the measured current has a contribution coming from light diffused by the white back sheet and trapped into the glass. This example clearly demonstrates the potential of our nanopattern AR coating for PV applications. The nanopattern applied to both the smart phone screens and photovoltaic modules was the same as that used in Figs. 11.1-11.3, and not optimized for the smartphone and solar module glass.

11.8 Conclusions

In conclusion, we demonstrate a nano-patterned anti-reflection coating for glass substrates that is fabricated by a simple, single-step silica solgel soft-imprint process. This pattern can be applied to large-areas and can be scaled up to a roll-to-roll process. The imprint-process has very high large-scale uniformity, is substrate conformal, and gives accurate control over effective refractive index and thickness. The pattern made using silica solgel can in theory be optimized for substrates with n = 1.003–2.070 by tuning the nanoparticle diameter. Higher indices may be achieved by modifying the solgel composition. We demonstrate that application of the nanopatterned AR coating to both sides of a glass substrate reduces the average reflectance from 7.35% to 0.59% in the visible spectral range, with a minimum reflectance < 0.05% at λ = 590 nm. Angle-resolved reflection measurements show < 1.0% reflectance for the entire angular range up to 50°. We apply the nanopattern anti-reflection coating to smart-phone screens and glass-encapsulated c-Si solar cells. A strong reduction in reflectance can be observed by eye, improving the display visibility in outdoor applications. Photovoltaic modules showed a 3.8% relative increase in short-circuit current, corresponding to a 2.8% relative increase in power output. Furthermore, the nanopattern anti-reflection coating makes the surface hydrophobic and can be applied to any type of glass.

11.9 Supplementary information

11.9.1 Ellipsometry on silica solgel

Spectroscopic ellipsometry was used to determine the optical constants of the silica-based solgel. A Si wafer was spin coated with a 90 nm thick layer of solgel (800 rpm, 10 s) and left to dry for 30 minutes in ambient conditions. A Cauchy model was used as a model in the ellipsometry analysis. The real part of the refractive index for $400 \leq \lambda \leq 1100$ nm ranged from $n = 1.448$ to $n = 1.432$ (Fig. 11.5). The imaginary part of the index (κ) is found to be smaller than 0.005, by comparing calculated ellipsometry data with the experimental data, taking into account the measurement errors.

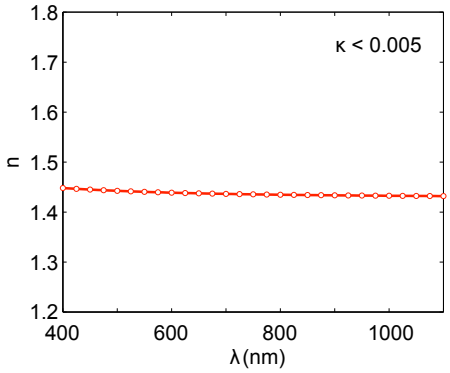

Figure 11.5: Real part of the refractive index obtained from spectroscopic ellipsometry. The imaginary part of the refractive index κ is smaller than 0.005 over the entire spectral range.

11.9.2 Integrating sphere measurement procedure

Figure 11.6 illustrates a top view of the experimental procedure used to measure the total reflection spectra reported in Fig. 11.2a. The incoming light is an attenuated white-light supercontinuum laser (Fianium SC400-4). The light enters the integrating sphere (LabSphere, 4") through the entrance port and travels through the sphere unperturbed. An 8° mount at the exit port is used to mount the samples and reference sample systematically with an 8° angle of incidence, to prevent the specularly reflected light to escape back out of the entrance port. The inside of the sphere is coated with white scattering powder (Spectralon) such that the specularly reflected light is randomized and trapped inside the sphere, until it is collected at the collection port (at the top of the sphere).

To accurately determine the reflection spectrum of a sample, the spectrum measured on the sample (I_{sample}) has to be compared to the spectrum measured

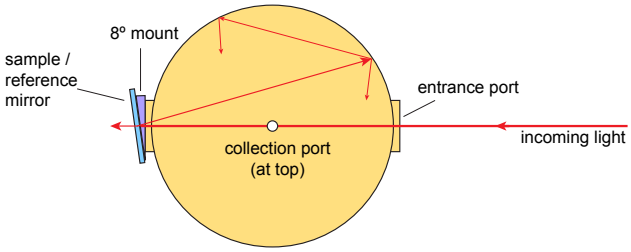

Figure 11.6: Schematic (top view) of integrating sphere setup used to measure the total reflection spectra reported in Fig. 11.2a.

on a reference sample with 100% reflection ($I_{100\%}$), such that the system response of the light source, optics, sphere, collection fiber, spectrograph and CCD camera can be eliminated:

$$R_{sample} = \frac{I_{sample}}{I_{100\%}} \tag{11.1}$$

In our experiments, we used a protected silver mirror (Thorlabs, PF10-03-P01) as reference sample. To take into account the non-perfect reflectance of the mirror in the reference measurement (I_{mirror}), we use the reflectance spectrum specified by the supplier (R_{mirror}) to correct for the non-perfect reflection of the mirror:

$$R_{sample} = \frac{I_{sample}}{I_{100\%}} = \frac{I_{sample}}{I_{mirror}} R_{mirror} \tag{11.2}$$

The mirror spectrum can be obtained from the supplier's website:
http://www.thorlabs.de/images/TabImages/Thorlabs_Protected_Silver_Coating.xlsx

11.9.3 FDTD simulations

To further corroborate that the nanopattern AR coating functions as an effective medium, as well as to demonstrate the coupling to guided substrate modes in the blue spectral range, we performed finite-difference time-domain (FDTD) simulations of light reflecting off the top interface using Lumerical Solutions [137]. A constant refractive index of $n = 1.44$ is used for the solgel nanoparticles ($d = 245$ nm, 325 nm pitch) and the 30 nm residual layer, and the substrate is assumed to be semi-infinite ($n_{sub} = 1.485$). A broad-band plane wave ($\lambda = 400$–1000 nm) is used as a source from the top with normal incidence. Periodic boundary conditions and a 2.5 nm refinement mesh are used. Figure 11.7a shows the real part of the electric field (top) and its phase (bottom) for light with $\lambda = 600$ nm propagating through the nanopatterned layer. Both the field and the phase front clearly demonstrate that the light propagates through the nanoparticle array as an unperturbed plane-wave,

thereby showing that the nanopattern AR coating functions as an effective medium for $\lambda = 600$ nm.

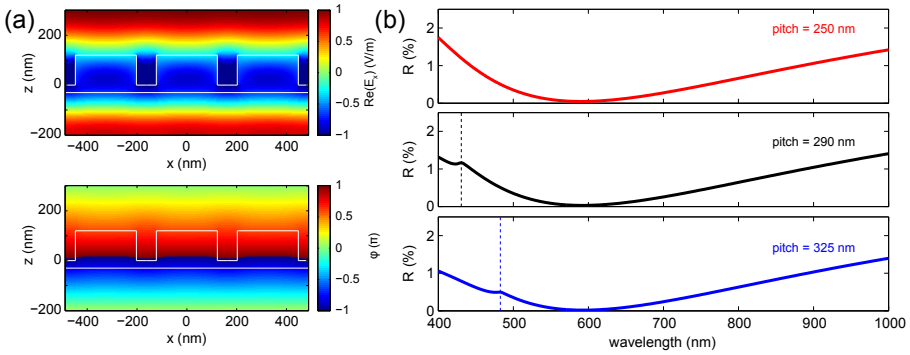

Figure 11.7: (a) Simulated real part of the electric field (top) and its phase (bottom) for $\lambda = 600$ nm showing flat phase fronts after propagation through the nanopattern AR coating. (b) Simulated reflection spectra for top interface with different nanoparticle pitch (constant effective index $n_{eff} = 1.196$).

To demonstrate that diffractive coupling to guided modes occurs in the blue spectral range we compare the simulated reflectance spectra for different nanopartice array pitch while keeping the effective index of the nanoparticle coating constant ($n_{eff} = 1.196$). Figure 11.7b shows the reflection spectra for 250 nm (top, red), 290 nm (black, middle), and 325 nm pitch (blue, bottom) used in the experiments. The nanoparticle height is 120 nm for all pitches, and the particle diameter is 188.5 nm, 218.6 nm and 245 nm respectively. The vertical dashed lines indicate the calculated maximum wavelength for which diffractive coupling occurs under normal incidence. Note that these simulations only consider the top interface, such that the diffracted light is not coupled back out. As a result, diffractive coupling to guided substrate modes is observed as a reduction in reflectance rather than an increase. Figure 11.7b demonstrates that: first, the spectral range where mode coupling occurs shifts with pitch, as expected for diffractive coupling, and second, mode coupling in the visible spectral range can be eliminated by reducing the pitch to 250 nm.

Final proof for the diffraction of light in the blue spectral range can be obtained from the power scattered into the diffracted orders, as calculated using Lumerical's far-field transformation routine [137]. The total field (all E and H components) is simulated 50 nm below the interface. A far-field projection, taking into account the periodicity of the structure, is then used to calculate which fraction of the transmitted light is coupled to the different diffraction orders. For $\lambda \geq 483$ nm, all transmitted light is coupled to the 0^{th} order (normal) transmission. However, for $\lambda < 483$ nm light couples to the ± 1 diffraction orders. For example, at $\lambda = 430$ nm the total calculated transmittance into the substrate is 99.2%, of which 5.6% is coupled

to the ±1 diffraction orders and 93.6% to the 0^{th} diffractive order. The 5.6% of the incoming light can subsequently couple back out and thereby contribute the experimentally measured reflection.

11.9.4 Haze

Haze, or diffuse scattering is an undesired property for optical coatings with potential applications in display applications. Haze reduces the visibility and readability of the underlying display as a result of uncontrolled random scattering. The nanopattern AR coating shown in this work is designed to have limited or even no scattering (see Fig. 11.7a), and should therefore exhibit extremely low haze levels. To demonstrate this, Fig. 11.8 shows a photograph of the AMOLF logo imaged through flat (left), one-side (center) and two-side (right) coated substrates. Applying the coating clearly improves the readability of the text as a result of reduced reflection of outdoor light, while no scattering is visible (i.e. extremely low haze).

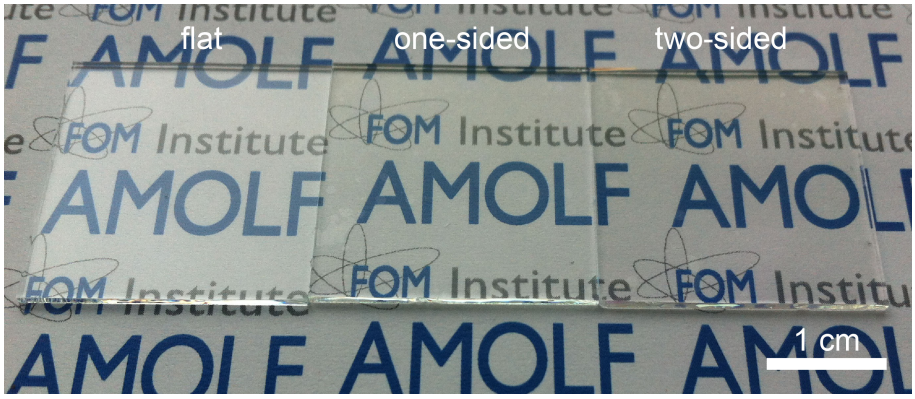

Figure 11.8: Photograph of text imaged through flat (left), one-side (center) and two-side (right) coated substrates.

11.9.5 Polarization-controlled specular reflection measurements

Figure 11.9 shows the measured angle-resolved specular reflectance for s- (open symbols) and p-polarized (closed symbols) light for a flat (blue), one-side coated (red) and double-side coated (black) substrate (λ = 532 nm, 325 nm pitch). A significantly higher reflectance is observed for s-polarized light for all substrates as expected. For both s- and p-polarized light, the AR coating strongly reduces the reflectance over the entire angular range. A small drop in reflection is observed at θ = 39.5° for s-polarized light; it is less pronounced for p-polarized light, indicating that s-polarized light couples more efficiently to the guided modes in the substrate.

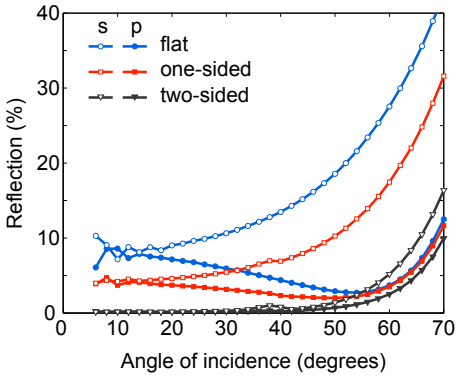

Figure 11.9: Measured specular reflection (λ = 532 nm) for a flat (blue), one side coated (red) and double-side coated substrate (black). Open symbols show the reflection for s-polarized light, closed symbols for p-polarized light.

11.9.6 Dispersion calculations of diffracted orders

Figure 11.10a shows the calculated dispersion curves for the 0^{th} (red) and $\pm 1^{st}$ (blue) grating orders ($G = 2\pi/p$) as a function of angle of incidence, upon scattering from the nanopatterned interface ($\lambda = 532$ nm, $p = 325$ nm). A continuum of guided modes lies between the light line in air and in the substrate (n = 1.485, shaded regions) because the substrate is thick (1 mm). Mode coupling occurs for the -1^{st} diffraction order that crosses the continuum of (backward propagating) modes for $8.5° < \theta < 39.5°$. The coupling mechanism is schematically illustrated in Fig. 11.10b.

11.9.7 Duct tape stripping

To study the mechanical rigidity of the nanopattern AR coating, we applied, pressed and removed both office tape and vinyl duct tape (3M 3903i) onto the patterned surface. Figure 11.11 shows SEM images (FEI Verios, 2 kV, 100 pA) of the sample after tape removal. Clear lines of residual adhesive are visible. However, the underlying nanopattern is undamaged (see insets).

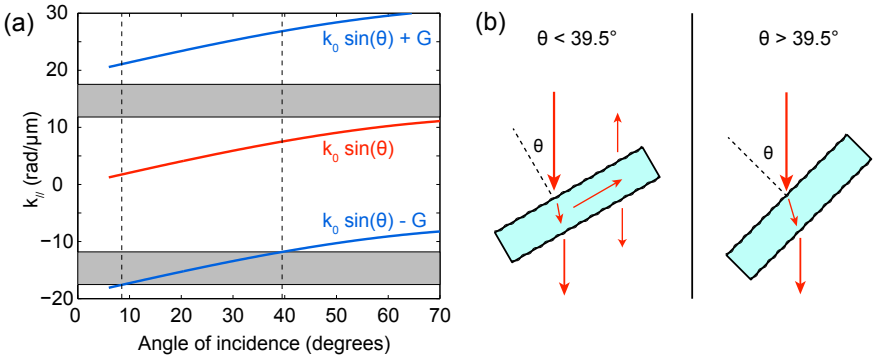

Figure 11.10: (a) Calculated dispersion curves for λ = 532 nm and p = 325 nm, showing coupling to guided modes occurs for $8.5° < \theta < 39.5°$. The continuum of guided modes is indicated by the shaded areas. (b) Schematic indicating the mode coupling mechanism for $\theta < 39.5°$ and lack of mode coupling for $\theta > 39.5°$.

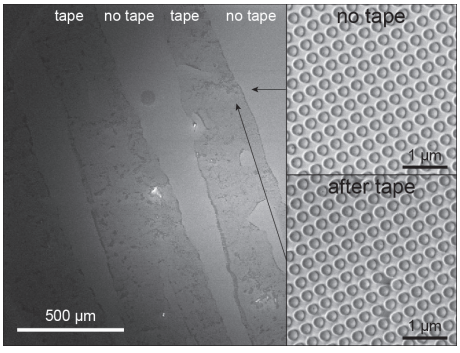

Figure 11.11: SEM image of nanopattern AR coating after duct tape removal. The insets show large-magnification SEM images of both regions exposed (bottom) and unexposed (top) to the tape adhesive.

12

Applications

In this Chapter, we present two applications inspired by the work in this thesis. First, we present silver nanowire networks that act as transparent electrodes on high-efficiency Si heterojunction solar cells. We design an ITO/nanowire network/Si_3N_4 hybrid electrode to replace the standard 80 nm thick ITO transparent conducting layer on top of the cells. We find a drastic improvement in the conductivity, which enables an increasing in the macroscopic finger spacing by a factor 2.5, yielding an increase in efficiency from 14.8% to 16.0%. Second, we present a soft-imprinted dielectric nanopattern that acts as a flat plasmonic back scattering electrode in nanocrystalline-Si solar cells. We grow flat layers of nanocrystalline-Si, use substrate-conformal imprint-lithography to print a silica nanopattern on the back of the cell, and overcoat it with Ag to form a flat scattering electrode. We find a strong enhancement in the photocurrent without a loss in voltage that is typically observed for non-flat scattering layers.

12.1 Introduction

In this thesis, we have studied the fundamental aspects of plasmonic and dielectric nanostructures with potential for applications in photovoltaic energy conversion. In this Chapter, we discuss two possible applications that are inspired by the work in described in this thesis. In Section 12.2 we demonstrate the application of silver

nanowire networks (Chapters 2–4) as a transparent electrode for high-efficiency Si heterojunction solar cells. Next, in Section 12.3 we demonstrate the application of soft-imprinted silica nanopatterns (Chapter 11) to form a flat plasmonic scattering electrode for enhanced light trapping in nanocrystalline Si solar cells.

12.2 Silver NW networks as a transparent electrodes on Si heterojuction solar cells

12.2.1 Introduction

Silicon heterojunction solar cells hold the current power conversion efficiency record for single junction Si cells [326], with an efficiency of 25.6% [327]. The key feature of heterojuction cells that gives rise to such high efficiencies is the high quality passivation by hydrogenated amorphous Si (a-Si:H) that gives extremely low carrier recombination losses. Thin (doped) a-Si:H layers are used to form a junction with the c-Si base absorber, and simultaneously provide highly passivated c-Si surfaces. Due to the short carrier diffusion length in the a-Si, a transparent conducting electrode (TCE) is required for the mm-scale transport of charges towards the electrode fingers. The standard industrial TCE is indium-tin-oxide (ITO). However, ITO is brittle [103, 104], contains the scarce element indium [145], absorbs UV light [80], and is deposited using expensive sputtering processes. These drawbacks motivate the replacement of ITO with alternative TCE designs. Furthermore, heterojunction cells generate large currents, thereby challenging the limited conductivity of the ITO layer. The conductivity of the ITO determines the maximum spacing of the fingers of the macroscopic top electrode, and thereby the shading losses. An increase in the conductivity of the TCE without a concomitant reduction in transparency would allow for a larger finger spacing and thus higher efficiency.

In Chapter 2 we have demonstrated the fabrication of two-dimensional periodic networks of Ag nanowires (NW) as a TCE using electron beam lithography. Next, in Chapter 3 we developed a soft-imprint procedure to fabricate these NW networks over large areas. We found that Ag NW networks can provide strongly reduced sheet resistance at an optical transmittance comparable to ITO. This makes engineered NW networks highly suitable for cells that generate large currents.

Here, we demonstrate the applicability of Ag NW networks as a transparent electrode on large-scale high-efficiency Si heterojunction solar cells. We use 2×2 cm flat cells as a model system to replace the standard 80 nm thick ITO layer with a hybrid ITO/Ag NW/Si_3N_4 layer in which highly conductive Ag NW networks are incorporated. We find a strong improvement in conductivity while maintaining high optical transmittance. The high conductivity of the hybrid electrode allows for a 2.5-fold increase of finger spacing and a four-fold reduction in ITO thickness. We demonstrate that the Ag NW networks strongly improve the fill factor of the devices, which gives rise to an enhancement of the power conversion efficiency

from 14.8% to 16.0%. Furthermore, this work demonstrates the first realization of engineered Ag NW networks on device-scale Si cells.

12.2.2 Heterojunction cell electrode design

Figure 12.1a shows the layer structure of a standard (flat) Si heterojunction cell. The cell is composed of three major parts (offset in the figure): a top transparent conductor with electrode, a passivated c-Si absorber layer with heterojunction, and bottom electrode/reflector. Details on the cell layers are presented in Fig. 12.1a. We use 2 × 2 cm Si heterojunction cells fabricated from high-quality flat float-zone wafers as a model system to study alternative geometries for the combined top TCE and macroscopic electrode (fingers and bus-bars). The spacing of the electrode fingers is maximized to minimize shading losses, but at the same time constrained by the resistivity of the TCE.

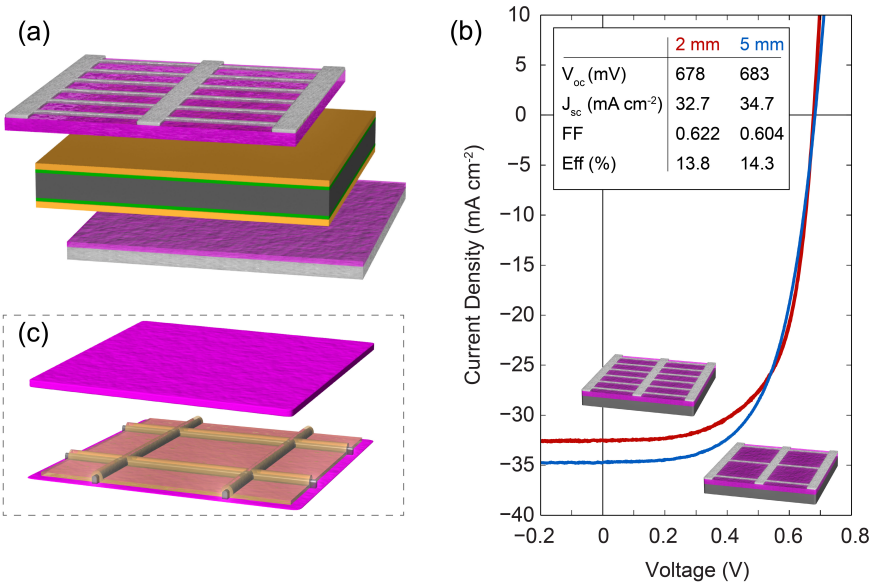

Figure 12.1: (a) Schematic of the standard heterojunction cell. From top to bottom the layers correspond to: macroscopic Ag contact (light gray), 80 nm ITO (purple), 5 nm p-type a-Si:H (orange), 5 nm intrinsic a-Si:H passivation layer (green), 300 μm n-type c-Si (dark gray) absorber, 5 nm intrinsic a-Si:H passivation layer (green), 5 nm n-type a-Si:H (orange), ITO (purple), and thick Ag back reflector/contact (light gray). This work considers alternative geometries for the top TCE and macroscopic grid. (b) Measured JV-curves for flat reference cell with 2 mm (red) and 5 mm (red) spaced fingers. The cell parameters are listed as an inset. Schematics of the macroscopic grids are also shown as an inset. (c) Standard 80 nm thick ITO (top) and ITO/Ag NW/Si_3N_4 hybrid geometry (bottom).

To explore the effect of increased finger spacing, Figure 12.1b shows current-voltage measurements on cells with a standard 80 nm thick ITO layer as a TCE, for electrode finger spacings of 2 mm (red) and 5 mm (blue). A 2 mA/cm^2 improvement in the short-circuit current density (J_{sc}) is observed for the 5-mm-spaced fingers compared to the 2-mm-spaced fingers as a result of reduced shading losses (see inset for cell parameters). Although the efficiency is improved by 0.5% as a result of this increase in J_{sc}, both cells have a relatively low fill factor (FF) as a result of series resistance in the TCE. This series resistance is further increased by the increase in finger spacing, as is apparent from the reduction in FF from 0.622 to 0.604.

Here, we present an ITO/Ag NW/Si_3N_4 hybrid electrode geometry to replace the standard 80 nm ITO layer as a TCE (Fig. 12.1c). The hybrid TCE allows for strongly improved conductivity at similar transmittance, and reduces the use of ITO by a factor 4. The hybrid electrode is composed of three layers. First, a 20 nm thin ITO layer is used to (i) allow for micron-scale charge transport to the nearest NW; (ii) protect the highly sensitive a-Si layers during fabrication of the NW network; (iii) prevent a red shift of the localized surface plasmon resonance of the Ag NWs into the spectral range where the solar spectrum is most intense. Second, a highly conductive Ag NW network with minimized wire width and 1–4 μm wire pitch is used to provide mm-scale charge transport towards the electrode fingers. Third, a 60 nm Si_3N_4 layer which forms an efficient anti-reflection (AR) layers in combination with the 20 nm ITO layer.

12.2.3 Large-scale nanowire network fabrication

Large-scale (2 × 2 cm) networks of Ag nanowires were fabricated onto the 20 nm ITO layer using substrate-conformal imprint-lithography (SCIL, see Chapter 3). In short, the wafers are spin coated with a sacrificial layer of PMMA, followed by a thin layer of liquid-silica solgel. A flexible nano-imprint stamp is applied and the solgel solidifies, leaving behind a patterned wafer. The pattern is transferred into the PMMA using reactive-ion etching, creating a shadow mask for the metal deposition. Next, 120 nm Ag is thermally evaporated onto the shadow mask, and lift-off is performed by dissolving the PMMA layer. The macroscopic top electrode is fabricated by thermal evaporation of 500 nm of Ag through a physical shadow mask. The fingers have 5 mm spacing, are ~190 μm wide, and connected to a bus-bar at the side of the cell. Each imprinted wafer contains four 2 × 2 cm fields, comprised of three different NW pitch (1, 2, and 4 μm) and a flat reference. The flat reference cell originates from the same Si wafer and is subjected to the same processing steps.

SEM images of the soft-imprinted Ag NW networks with different pitches on the thin ITO are shown in Figs. 12.2a-c. The large differences in NW density can be clearly observed. For all pitches, the NWs show smooth surfaces and high-quality interconnecting junctions. The NW width is 80 ± 5 nm as measured using high-resolution SEM imaging, and the height is 120 nm as measured with AFM.

To quantify the conductivity, sheet resistance measurements were performed on the 2 × 2 cm NW networks. To this end, the same fabrication process without the

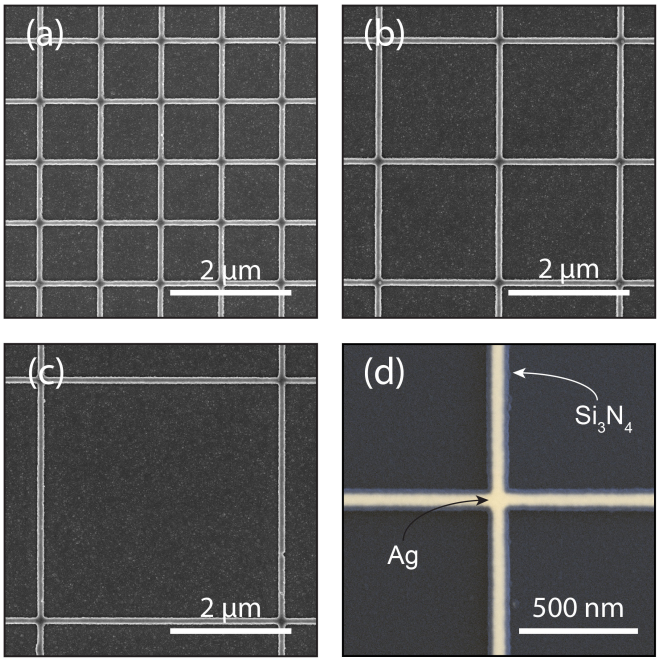

Figure 12.2: SEM images of the printed silver NW networks with a pitch of 1 μm (a), 2 μm (b), and 4 μm (c). The nanowire width is 80 ± 5 nm. The nanowire height is 120 nm, measured with AFM. (d) Combined back-scattering and secondary electron micrographs, showing the Ag NW (yellow) conformally coated with Si_3N_4 (light blue).

macroscopic Ag fingers is performed on bare borosilicate substrates. Four-point probe measurements showed sheet resistances of 4.0 Ω/sq, 7.2 Ω/sq, and 15.0 Ω/sq for the 1, 2, and 4 μm pitched networks respectively. This demonstrates the drastic improvement in conductivity compared to the ITO layers, which showed 150 Ω/sq and 280 Ω/sq for the 80 nm and 20 nm thick layers respectively.

Finally, the NW networks were coated with 60 nm of Si_3N_4 using plasma-enhanced chemical-vapor deposition (PECVD) to complete the hybrid electrode. Figure 12.2d shows a color-coded SEM image clearly showing the conformal coating of the Si_3N_4 (light blue) around the Ag NWs (yellow), obtained from combined back-scattering and secondary-electron micrographs.

12.2.4 Device performance

Next, we study the performance of the devices with thin ITO and 5 mm finger spacing. We first characterize the optical absorption of the cells. Using a white-light

supercontinuum laser, an integrating sphere, spectrograph and CCD, the total reflection spectra (R) of the cells were measured. The total cell absorption (including parasitic losses in the (hybrid) electrode and a-Si layers) were calculated as $Abs = 1 - R$. Note that the reflection spectra were measured in between the macroscopic fingers using a ~2 mm diameter spot.

Figure 12.3a shows the measured absorption spectrum for the 1 μm (green), 2 μm (blue), and 4 μm (red) pitched network cells. The absorption of a flat reference cell (20 nm ITO and 60 nm Si_3N_4) is also shown (gray). The spectral shape of the absorption spectrum of the flat cell clearly shows the effect of the AR-coating; > 0.995 absorption is achieved for the flat cell around $\lambda = 700$ nm. A significant reduction in absorption compared to the flat cell can be observed for the 1 μm pitched cell as a result of optical losses, which comprise both scattering and absorption in the NWs. The absorption significantly improves for increasing pitch. In fact, the maximum absorption for the 4 μm pitched cell is 0.977, only ~0.02 lower than that of the flat cell. These results show that the best hybrid TCE yields an optical transmission close to that of the standard TCE, with more than an order of magnitude better conductivity (see Section 12.2.3).

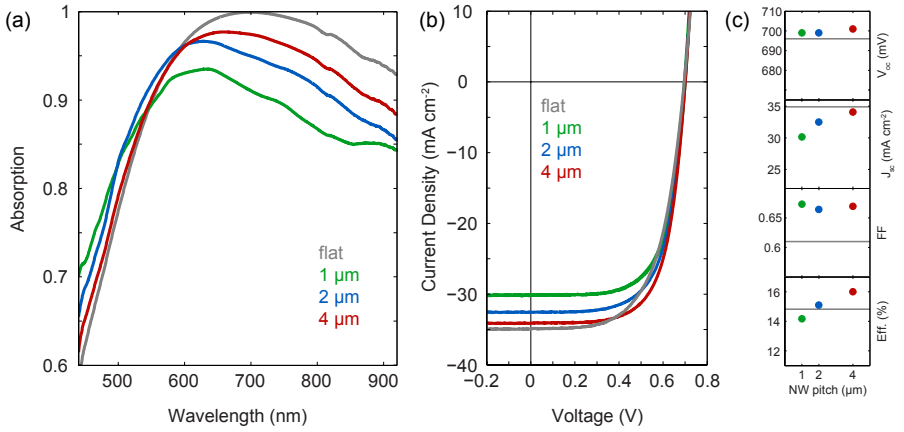

Figure 12.3: (a) Measured total absorption spectra for the flat reference cell (gray), and NW network cells with a pitch of 1 μm (green), 2 μm (blue), and 4 μm (red). (b) J-V curves for the corresponding cells. (c) Summary of cell parameters extracted from (b).

Current-voltage curves of the cells were measured under 1 sun illumination using a calibrated solar simulator. The resulting J-V curves are shown in Fig. 12.3b, and the summary of the cell parameters is presented in Fig. 12.3c. The open-circuit voltage (V_{oc}) is 696–701 mV for all cells, which shows that the application of Ag NW networks in the hybrid electrode does not strongly affect the electrical quality of the solar cell. Furthermore, the trend in short-circuit current density (J_{sc}) clearly

resembles the decrease in optical losses with increasing pitch; the J_{sc} increases from 30.1 mA/cm^2 for 1 μm pitch to 34.1 mA/cm^2 for 4 μm pitch, compared to 34.9 mA/cm^2 for the flat reference cell. This demonstrates that although the NW networks give rise to optical losses, the J_{sc} of the 4 μm pitched cell approaches that of the flat cell.

The main benefit of the hybrid electrode is apparent from the fill factor (FF) of the NW network cells compared to that of the flat cell. Due to the large current generated by the cell, the series (sheet) resistance in the ITO layer strongly reduces the FF to 0.610. The highly conductive NW networks effectively mitigate these resistance losses, and increase FF to 0.665–0.673 (Fig. 12.3c). The FF is similar for all NW network cells, which indicates that the conductivity provided by the 4 μm pitched network is sufficient to eliminate the losses due to series resistance. Smaller pitches only introduce larger optical losses, thereby reducing J_{sc}. Larger pitches on the other hand may further increase J_{sc}, up to the point where the resistivity of the hybrid electrode becomes the limiting factor and reduces FF.

The power conversion efficiency (Fig. 12.3c, lower panel) shows a strong improvement for larger wire pitch. It increases from 14.2% for the 1 μm pitched cell to 15.1% and 16.0% for the 2 μm and the 4 μm pitched cells respectively, exceeding the 14.8% efficiency of the reference cell. This demonstrates how the high conductivity of engineered Ag NW networks can be used to enhance the performance of high-efficiency Si heterojunction solar cells.

12.2.5 Conclusions

We use substrate-conformal imprint lithography to demonstrate the applicability of Ag nanowire networks as a transparent electrode on large-scale highly-efficient Si heterojunction solar cells. We present an ITO/Ag NW/Si_3N_4 hybrid transparent electrode to replace the standard 80 nm thick ITO as a transparent conducting layer. We find drastic improvements in conductivity with minimized reduction in transmittance compared to ITO. As a result, the finger spacing of the macroscopic electrode can be increased be a factor 2.5 and the thickness of the ITO is reduced by a factor 4. We find that the Ag NW networks strongly improve the fill factor of the devices, thereby enhancing the power conversion efficiency from 14.8% to 16.0%. The delicate balance between conductivity and optical losses requires a systematic optimization of the combined transparent conducting electrode and macroscopic electrode design. The flat model system studied here provides key insights into the optimization of NW network designs when applied on practical device geometries that can be implemented in industrial fabrication processes. The next step is to implement NW networks with advanced light trapping schemes such as nanotexturing [328] or coatings of resonant nanoparticles [33, 73], which allows direct comparison with the commercial textured heterojunction Si solar cells. We anticipate that further development of hybrid transparent electrodes will lead to improved front-contacted heterojunction Si solar cells.

12.3 Soft-imprinted flat plasmonic scattering electrode for nc-Si solar cells

12.3.1 Introduction

Thin-film nanocrystalline silicon (nc-Si) solar cells are an attractive alternative to wafer-based Si, offering both flexibility and in principle low production costs. nc-Si solar cells are formed by growing thin Si layers on a substrate using chemical vapor deposition (CVD) methods. Unlike wafer-based Si, these cells are therefore compatible with low-cost flexible substrates [329, 330]. However, the CVD growth process is relatively slow so that the costs of thin-film Si solar cells scale with the active layer thickness. Moreover, the carrier drift length in nc-Si layers is relatively short due to the high density of grain boundaries and crystal defects. As a result, the use of thin (~1 μm) active layers is beneficial for both the fabrication costs and the carrier collection efficiency of the solar cells.

Due to the indirect band gap of nc-Si, the absorption coefficient is relatively low. Therefore, thin-film nc-Si solar cells rely strongly on light trapping schemes to realize sufficient absorptance in the red and near infra-red spectral range. Typically, light trapping inside the active layer is realized by growing the nc-Si layers on top of a (randomly) textured substrate such as naturally textured Al-doped ZnO layers [331], or nanopatterned back reflectors [332]. However, conformal growth of thin-film nc-Si on nanoscale textured substrates results into crack formation and defective filaments in the active nc-Si layer [329, 331, 333, 334]. High recombination rates at these defect sites and shunting pinholes cause low fill factors (FF) and open-circuit voltages (V_{oc}), with correspondingly poor device performance. The record-efficiency nc-Si cell exhibits a V_{oc} that is only 67% of the limiting value calculated using the Shockley-Queisser (SQ) model [335]. For the record cell J_{sc} is only 61% of the SQ limited value, the lowest fraction of all photovoltaic semiconductor materials. To prevent cracks in the absorber layer, nc-Si layers must be fabricated on flat substrates which typically results into diminished light trapping.

Recently, attempts have been made to realize light trapping in flat nc-Si layers by using flattened light-scattering substrates [336, 337]. Although high-quality cells have been realized using this concept, the fabrication procedure requires extensive chemical-mechanical polishing and is limited to cells that are grown in the substrate configuration (starting from back side of the solar cell). In the superstrate configuration on the other hand, the cell is grown on top of a glass front sheet. This configuration has cost advantages compared to the substrate configuration as the glass serves as a highly transparent encapsulant that is stable under UV exposure, and is an excellent moisture barrier.

In Chapter 11, we used substrate-conformal imprint-lithography (SCIL) to fabricate large-area silica nanopatterns as an anti-reflection coating for glass substrates. Here, we use the same SCIL procedure to demonstrate the applicability of soft-imprinted silica nanopatterns as strongly scattering back electrodes for nc-Si solar cells that are grown as a flat layer in the superstrate configuration. First,

high-quality nc-Si films are grown on flat glass, which prevents the formation of cracks in the absorber layer. Next we use SCIL to fabricate on the back of the cell a silica nanopattern comprised of a square array of nanocylinders, which is subsequently overcoated with Ag to form a plasmonic scattering back electrode.

We study the J-V characteristics of the nanopatterned cell, and compare it to a cell grown on top of a randomly textured substrate and a flat reference cell. We find a strong enhancement of the photocurrent for the nanopatterned cell, without the reduction in V_{oc} and FF associated with cracks in the nc-Si layer. Using spectral absorption measurements and external quantum efficiency (EQE) measurements, we identify the role of plasmonic scattering and compare this to the scattering in the randomly textured cells. An enhancement of the electrical properties of the nanopatterned cell is observed compared to the randomly textured cell due to the improved material quality of the nc-Si layer.

12.3.2 Cell design and fabrication

Figure 12.4 shows the layer structure of the flat reference cell (a), a randomly front-textured cell (b), and the flat plasmonic scattering electrode cell (c). Light is incident from the top and an Al-doped ZnO layer is used as a transparent top electrode. Light is absorbed in the nc-Si layer, and a thin layer of indium-tin-oxide (ITO) is used in between the Ag back contact/reflector to prevent recombination at the Ag/nc-Si interface. The flat reference cell (a) exhibits no light trapping. In the front-textured cell (b), the bottom interface of the ZnO layer is randomly textured. This texture propagates through the nc-Si layer and ITO layer, such that three interfaces are textured. Incident light is scattered by all three interfaces, enhancing the effective optical path length inside the cell by coupling to guided modes in the nc-Si layer. The conformal growth of the nc-Si layer on top of the nanotextured ZnO layer induces cracks in the absorber layer (indicated in Fig. 12.4b), which deteriorate the cell performance. In the plasmonic scattering electrode cell (c), the ZnO and nc-Si layers are both flat which allows for the growth of high-quality nc-Si. Light trapping is achieved by introducing a nanopatterned back electrode.

The three cells are fabricated in superstrate configuration. Starting with flat glass, a thick (500 nm) layer of Al doped ZnO (1%) is sputtered as a front transparent electrode. For the random front-textured cell (Fig. 12.4b), the surface of the ZnO layer was textured by a short wet etch in diluted hydrochloric acid. Next, a 25 nm p-doped nc-Si layer was deposited using plasma-enhanced CVD (PECVD), followed by the deposition of a 1 μm thick intrinsic layer using hot-wire CVD (HWCVD) [338]. To complete the p-i-n junction, PECVD was used to grow a 27 nm n-doped nc-Si layer on top of the intrinsic layer. A thin (80 nm) layer of ITO was then sputtered as a diffusion barrier in between the Ag and nc-Si. Finally, a thick (~500 nm) layer of Ag was thermally evaporated through a physical shadow mask to form a back reflector and contact, followed by a thin Al layer to prevent oxidation of the Ag layer. The cell area is 4 × 4 mm, defined by the shadow mask.

For the flat plasmonic scattering electrode cell (Fig. 12.4c), SCIL was used to

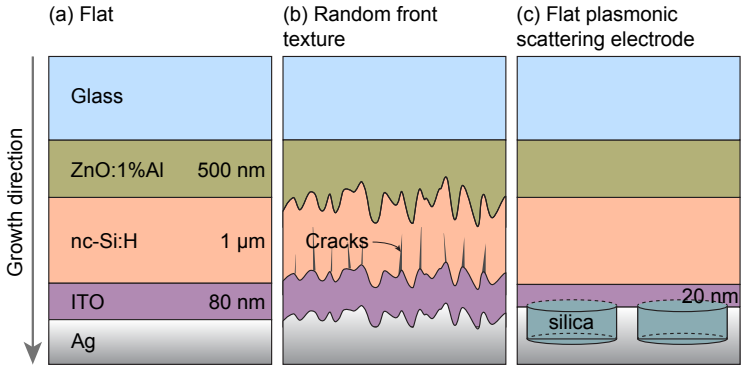

Figure 12.4: Schematic layer structure for a flat thin-film Si solar cell grown in the superstrate configuration (a), cell with randomly textured front (b), and cell with flat plasmonic scattering back reflector (c). The cracks as a result of nc-Si growth on textured substrates are indicated in (b).

pattern the rear of the cell. A thinner layer of ITO (20 nm) was used to allow for strong optical interaction between the nc-Si layer and the nanopattern. The ITO layer was spin coated with a 90 nm thick layer of liquid-silica solgel, into which the nanopatterned imprint stamp was subsequently applied. After 30 min of drying in ambient conditions, the stamp was removed and a patterned silica layer is left behind on the substrate. Figure 12.5a shows a SEM image of the resulting silica nanopattern, which comprises a two-dimensional array of cylinders with 245 nm diameter, 120 nm height, and 325 nm pitch. The pattern is uniform over a large area and shows very few defects. Next, a CHF_3-based reactive-ion etch (RIE) is used to remove the thin residual solgel layer in between the cylinders, to allow for electrical contact between the ITO layer and the Ag back reflector. During the etch process, the height of the cylinders is reduced to ~65 nm, and the side walls are slightly tapered due to slight non-perfect anisotropy of the etch. Finally, the Ag and Al layers are evaporated on top of the silica nanopattern to complete the flat plasmonic scattering electrode.

Figure 12.5b shows a focused-ion beam (FIB) cross section of the scattering electrode (imaged upside down compared to Fig. 12.4c). The solgel nanopattern and Ag overcoating are clearly visible. Furthermore, the top of the Ag/Al layer shows the cylindrical shape of the nanopattern as a result of the directional deposition of the Ag layer. Note that the SCIL stamp used here is identical to that used in Chapter 11, and the pattern is not fully optimized for light trapping in these nc-Si solar cells.

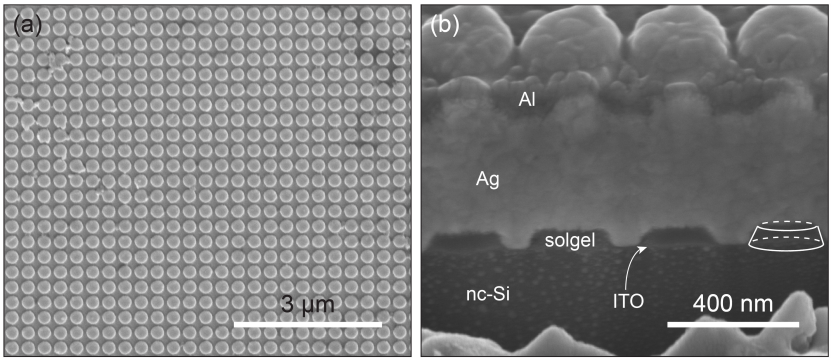

Figure 12.5: (a) SEM image showing a top view of the imprinted solgel cylinders. (b) FIB cross section of the cell showing the flat nc-Si layer and the patterned back contact. The layers are labeled and the outline of the solgel is sketched to illustrate the slightly tapered cylindrical shape.

12.3.3 Cell performance

To characterize the device performance we first measure J-V curves under AM1.5G illumination conditions using a calibrated solar simulator. Figure 12.6a shows the resulting J-V curves for the flat (blue), front-size textured (green) and plasmonic scattering electrode (red) solar cell. A summary of the cell parameters is displayed in Fig. 12.6b. A high V_{oc} (510 mV) and FF (0.59) are observed for the flat reference cell. However, the short-circuit current is low (J_{sc} = 11.6 mA/cm^2) due to the absence of light trapping. The power conversion efficiency of the flat cell is 3.5%. We note that these experiments are done with very low-efficiency cells that serve as a model system. The results presented here can be applied to high-efficiency thin-film cells as well.

Applying a front texture to the cell enhances the J_{sc} to 12.2 mA/cm^2 as a result of enhanced optical absorption. At the same time, the influence of the front texture on the material quality of the absorber layer is apparent from the large deterioration of the electrical properties of the cell: the high defect density and cracks in the nc-Si layer reduce V_{oc} to 450 mV and FF to 0.50, resulting in an efficiency of only 2.7%. The increase in J_{sc} therefore comes at the price of a strong reduction in V_{oc} and FF.

Using a flat scattering layer instead of a random texture prevents the strong reduction in V_{oc} (Fig. 12.6a): the plasmonic scattering electrode cell shows a V_{oc} of 510 mV, equal to that of the flat cell. This directly shows the profitability of growing flat absorber layers. Furthermore a strong increase in photocurrent is observed when using the scattering back electrode; J_{sc} increases from 11.6 mA/cm^2 for a flat cell to 15.3 mA/cm^2 for the flat scattering electrode. As a result, the efficiency increases from 3.5% to 4.1%. Note that the increase in efficiency is tempered by the reduction in FF from 0.59 for a flat cell to 0.53 for the plasmonic scattering elec-

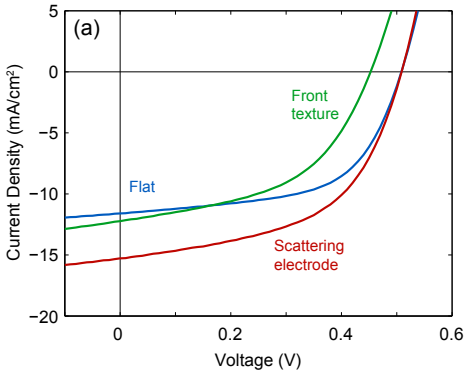

(b)	V_{oc} (mV)	J_{sc} (mA/cm²)	FF	Eff. (%)
Flat	510	11.6	0.59	3.5
Front texture	450	12.2	0.50	2.7
Scattering electrode	510	15.3	0.53	4.1

Figure 12.6: (a) Current density-voltage measurements for the flat (blue), front-side textured (green), and plasmonic scattering back electrode (red). (b) Corresponding cell parameters. The efficiencies in these cells, that serve as a model system, are very low, but the concept demonstrated here can be applied to high-efficiency thin-film cells as well.

trode cell. We attribute this drop in FF to an increase in the surface recombination near the ITO as a result of an overexposure during the RIE step. Despite the lower FF, the large increase in J_{sc} and the higher V_{oc} clearly demonstrate the advantage of the use of a strongly scattering flat back electrode.

Finally, we note that a significant reduction in the shunt resistance is observed for all devices (finite slope for $V < 0$) compared to the flat cell, which we found to be correlated to the use of ITO as the rear diffusion barrier. Optimization of the compatibility of the SCIL fabrication procedure with the use of ZnO, rather than ITO, may further enhance the cell performance.

12.3.4 Spectral response

To gain insight in the origin of the strong enhancement in J_{sc}, we compare the spectral response of the three solar cell geometries. Figure 12.7 shows the measured absorptance (top, calculated as $Abs = 1-R$) and external quantum efficiency (EQE, bottom) of the flat (blue), front-side textured (green) and plasmonic scattering electrode (red) solar cell. Detailed comparison of the absorptance and EQE shows three overall trends; (i) all cells show high (> 0.8) absorptance for $\lambda < 600$ nm. However, the EQE is low in this spectral range due to strong optical absorption in the ZnO layer and the electrically dead p-doped layer. (ii) Fabry-Pérot resonances in the thick (front) ZnO layer occur for $350 < \lambda < 550$ nm. For $\lambda > 550$ nm, incomplete absorption in the nc-Si layer gives rise to additional fringes with a smaller free spectral range due to the larger thickness and refractive index. (iii) The EQE for all cells decreases for $\lambda > 600$ nm due to incomplete absorption and enhanced

parasitic losses.

Furthermore, there are two cell-specific trends; (i) the front-side textured cell shows the highest absorptance over entire spectral range, indicating very effective light trapping inside the cell. In this cell, the interference fringes are damped due to randomization of wave vectors at the textured interfaces of the cell. Despite the high absorptance, the EQE of the front-side textured cell is much lower than that of both flat cells for $\lambda < 600$ nm, which indicates a low charge collection efficiency as a result of the low material quality (low internal quantum efficiency). (ii) The flat (plasmonic) scattering electrode cell shows lower absorptance than the random front-side textured cell, but significantly higher than the flat reference cell. This indicates that light trapping occurs, though less efficient than in the textured cell, which we attribute to the limited number of spatial frequencies in the periodic pattern of the flat scattering electrode [75, 339]. For $\lambda > 600$ nm the flat scattering electrode cell and textured cell have comparable EQE but the EQE averaged over the full spectral range in Fig. 12.7 is significantly higher for the flat plasmonic scattering electrode, which explains the higher J_{sc}.

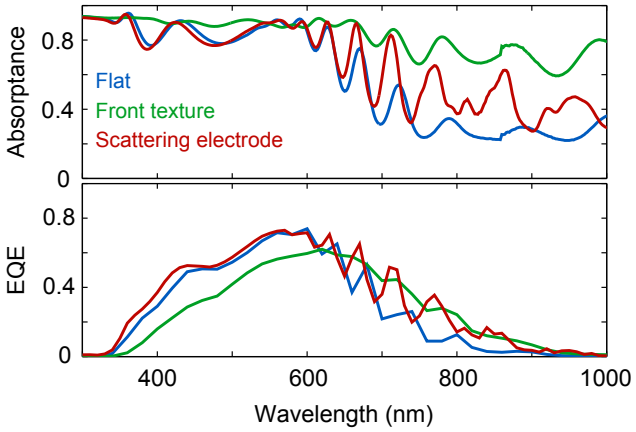

Figure 12.7: Measured absorptance (top, calculated as $1 - R$) and EQE (bottom) of the flat (blue), front-side textured (green), and plasmonic scattering back electrode (red).

Overall, the results in Fig. 12.7 demonstrate that despite the fact that the flat scattering electrode exhibits lower overall optical absorption than the random front-side textured cell, it produces a higher EQE due to the high material quality of the flat nc-Si layer.

Finally, we performed FDTD simulations [137] to study the scattering mechanism that gives rise to the EQE enhancement observed in Fig. 12.7. In the simulations, we assume the silica particle to have a perfect cylindrical shape with a diameter of 245 nm, 65 nm height, and 325 nm pitch (experimental geometry).

Using periodic boundary conditions in the in-plane directions we first simulate the response of an infinite array. Figure 12.8a shows the simulated absorptance in the intrinsic nc-Si layer for a flat (blue) and flat plasmonic scattering electrode cell (red). A broadband enhancement of the absorptance is observed for the scattering electrode, in agreement with the measured EQE in Fig. 12.7. Multiple spectrally sharp peaks are observed in the spectral range where Si is weakly absorbing. To explain these absorptance peaks, Figure 12.8b shows a cross cut of the E_z distribution at one of the peaks (λ = 895 nm, see dot in (a)). A standing wave pattern in the in-plane direction can be observed, which is an indication of coupling to guided modes in the nc-Si layer [340]. The limited number of peaks in Fig. 12.8a is a direct result of the finite number of spatial frequencies in the periodic scattering electrode, which results into coupling to waveguide modes at a limited number of wavelengths [75, 339]. Further optimization of the spectrum of spatial frequencies for these specific cells by using engineered random scattering patterns will result into a larger density of peaks, and more broadband enhancement in the absorptance.

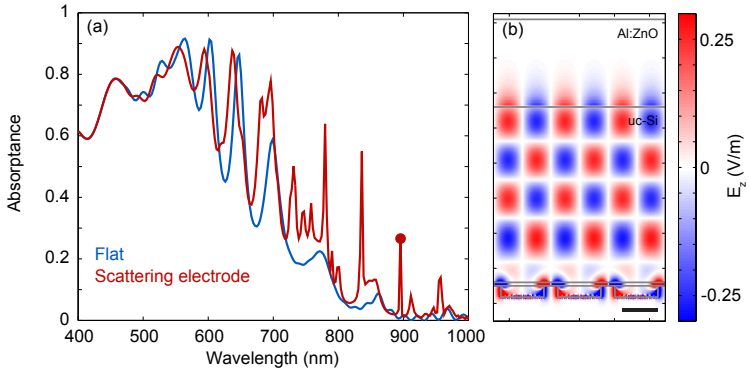

Figure 12.8: (a) Simulated absorption in the intrinsic nc-Si layer for the flat (blue) and plasmonic scattering back electrode cells (red). (b) Cross cut of the E_z distribution throughout the cell (showing three unit cells) for λ = 895 nm (see dot in (a)). Note that the color bar is saturated for visibility. The scale bar is 200 nm.

12.3.5 Conclusions

We present soft-imprinted silica nanopatterns that function as strongly scattering back electrodes in thin-film nc-Si solar cells. Unlike the randomly textured front contacts that are typically used to achieve light trapping, the plasmonic scattering electrode allows for the growth of flat nc-Si layers with high material quality. Compared to the front-side textured cell, we find an enhancement in J_{sc} without the loss in V_{oc} that is observed for the front-side textured cell as a result of carrier

recombination at defects in the nc-Si layer. Using spectral absorption measurements and *EQE* measurements, we find that the front-side textured cell exhibits strong absorption but low external quantum efficiency. The plasmonic scattering electrode cell on the other hand, shows slightly lower optical absorption compared to the textured cell, but a significantly higher *EQE* due to the high material quality of the nc-Si layer. The cell performance can be further enhanced by optimization of the scattering electrode geometry.

References

[1] L. Rayleigh, *XXXIV. On the transmission of light through an atmosphere containing small particles in suspension, and on the origin of the blue of the sky*, Philosophical Magazine Series 5 **47**, 375 (1899).

[2] U. Kreibig and M. Vollmer, *Optical Properties of Metal Clusters*, Springer-Verlag, Berlin, 1995.

[3] K. L. Kelly, E. Coronado, L. L. Zhao, and G. C. Schatz, *The Optical Properties of Metal Nanoparticles: The Influence of Size, Shape, and Dielectric Environment*, The Journal of Physical Chemistry B **107**, 668 (2003).

[4] I. O. Sosa, C. Noguez, and R. G. Barrera, *Optical Properties of Metal Nanoparticles with Arbitrary Shapes*, The Journal of Physical Chemistry B **107**, 6269 (2003).

[5] K.-S. Lee and M. A. El-Sayed, *Gold and Silver Nanoparticles in Sensing and Imaging: Sensitivity of Plasmon Response to Size, Shape, and Metal Composition*, The Journal of Physical Chemistry B **110**, 19220 (2006).

[6] J. A. Scholl, A. L. Koh, and J. A. Dionne, *Quantum plasmon resonances of individual metallic nanoparticles*, Nature **483**, 421 (2012).

[7] I. Zorić, M. Zäch, B. Kasemo, and C. Langhammer, *Gold, Platinum, and Aluminum Nanodisk Plasmons: Material Independence, Subradiance, and Damping Mechanisms*, ACS Nano **5**, 2535 (2011).

[8] J. M. McMahon, G. C. Schatz, and S. K. Gray, *Plasmonics in the ultraviolet with the poor metals Al, Ga, In, Sn, Tl, Pb, and Bi*, Physical Chemistry Chemical Physics **15**, 5415 (2013).

[9] E. Hutter and J. H. Fendler, *Exploitation of Localized Surface Plasmon Resonance*, Advanced Materials **16**, 1685 (2004).

[10] L. Novotny and N. van Hulst, *Antennas for light*, Nature Photonics **5**, 83 (2011).

[11] T. H. Taminiau, F. D. Stefani, and N. F. v. Hulst, *Single emitters coupled to plasmonic nano-antennas: angular emission and collection efficiency*, New Journal of Physics **10**, 105005 (2008).

[12] A. G. Curto, G. Volpe, T. H. Taminiau, M. P. Kreuzer, R. Quidant, and N. F. van Hulst, *Unidirectional Emission of a Quantum Dot Coupled to a Nanoantenna*, Science **329**, 930 (2010).

[13] L. Tang, S. E. Kocabas, S. Latif, A. K. Okyay, D.-S. Ly-Gagnon, K. C. Saraswat, and D. A. B. Miller, *Nanometre-scale germanium photodetector enhanced by a near-infrared dipole antenna*, Nature Photonics **2**, 226 (2008).

[14] M. W. Knight, H. Sobhani, P. Nordlander, and N. J. Halas, *Photodetection with active optical antennas*, Science **332**, 702 (2011).

[15] P. Fan, K. C. Y. Huang, L. Cao, and M. L. Brongersma, *Redesigning Photodetector Electrodes as an Optical Antenna*, Nano Letters **13**, 392 (2013).

[16] M.-K. Kwon, J.-Y. Kim, B.-H. Kim, I.-K. Park, C.-Y. Cho, C. C. Byeon, and S.-J. Park, *Surface-Plasmon-Enhanced Light-Emitting Diodes*, Advanced Materials **20**, 1253 (2008).

[17] G. Lozano, D. J. Louwers, S. R. K. Rodriguez, S. Murai, O. T. A. Jansen, M. A. Verschuuren, and J. Gomez Rivas, *Plasmonics for solid-state lighting: enhanced excitation and directional emission of highly efficient light sources*, Light: Science & Applications **2**, e66 (2013).

[18] J. N. Anker, W. P. Hall, O. Lyandres, N. C. Shah, J. Zhao, and R. P. Van Duyne, *Biosensing with plasmonic nanosensors*, Nature Materials **7**, 442 (2008).

[19] C. Sonnichsen, B. M. Reinhard, J. Liphardt, and A. P. Alivisatos, *A molecular ruler based on plasmon coupling of single gold and silver nanoparticles*, Nature Biotechnology **23**, 741 (2005).

[20] N. Liu, M. Hentschel, T. Weiss, A. P. Alivisatos, and H. Giessen, *Three-Dimensional Plasmon Rulers*, Science **332**, 1407 (2011).

[21] I. Sersic, M. Frimmer, E. Verhagen, and A. F. Koenderink, *Electric and Magnetic Dipole Coupling in Near-Infrared Split-Ring Metamaterial Arrays*, Physical Review Letters **103**, 213902 (2009).

[22] V. M. Shalaev, *Optical negative-index metamaterials*, Nature Photonics **1**, 41 (2007).

[23] N. Yu, P. Genevet, M. A. Kats, F. Aieta, J.-P. Tetienne, F. Capasso, and Z. Gaburro, *Light Propagation with Phase Discontinuities: Generalized Laws of Reflection and Refraction*, Science **334**, 333 (2011).

[24] N. Meinzer, W. L. Barnes, and I. R. Hooper, *Plasmonic meta-atoms and metasurfaces*, Nature Photonics **8**, 889 (2014).

[25] C. Loo, A. Lowery, N. Halas, J. West, and R. Drezek, *Immunotargeted Nanoshells for Integrated Cancer Imaging and Therapy*, Nano Letters **5**, 709 (2005).

[26] C. Ayala-Orozco, C. Urban, M. W. Knight, A. S. Urban, O. Neumann, S. W. Bishnoi, S. Mukherjee, A. M. Goodman, H. Charron, T. Mitchell, M. Shea, R. Roy, S. Nanda, R. Schiff, N. J. Halas, and A. Joshi, *Au Nanomatryoshkas as Efficient Near-Infrared Photothermal Transducers for Cancer Treatment: Benchmarking against Nanoshells*, ACS Nano **8**, 6372 (2014).

[27] M. G. Cerruti, M. Sauthier, D. Leonard, D. Liu, G. Duscher, D. L. Feldheim, and S. Franzen, *Gold and Silica-Coated Gold Nanoparticles as Thermographic Labels for DNA Detection*, Analytical Chemistry **78**, 3282 (2006).

[28] C. F. Bohren and D. R. Huffmann, *Absorption and Scattering of Light by Small Particles*, John Wiley & Sons, New York, 1983.

[29] G. Mie, *Beiträge zur Optik trüber Medien, speziell kolloidaler Metallösungen*, Annalen der Physik **330**, 377 (1908).

[30] Y. H. Fu, A. I. Kuznetsov, A. E. Miroshnichenko, Y. F. Yu, and B. Luk´yanchuk, *Directional visible light scattering by silicon nanoparticles*, Nature Communications **4**, 1527 (2013).

[31] L. Huang, Y. Yu, and L. Cao, *General Modal Properties of Optical Resonances in Subwavelength Nonspherical Dielectric Structures*, Nano Letters **13**, 3559 (2013).

[32] A. E. Miroshnichenko and Y. S. Kivshar, *Fano Resonances in All-Dielectric Oligomers*, Nano Letters **12**, 6459 (2012).

[33] P. Spinelli, M. A. Verschuuren, and A. Polman, *Broadband omnidirectional antireflection coating based on subwavelength surface Mie resonators,* Nature Communications **3**, 692 (2012).

[34] A. E. Krasnok, A. E. Miroshnichenko, P. A. Belov, and Y. S. Kivshar, *All-dielectric optical nanoantennas,* Optics Express **20**, 20599 (2012).

[35] J. A. Schuller, E. S. Barnard, W. Cai, Y. C. Jun, J. S. White, and M. L. Brongersma, *Plasmonics for extreme light concentration and manipulation,* Nature Materials **9**, 368 (2010).

[36] E. D. Palik and G. Ghosh, *Handbook of Optical Constants of Solids,* volume 1, Academic, San Diego, 1998.

[37] A. B. Evlyukhin, C. Reinhardt, A. Seidel, B. S. Luk´yanchuk, and B. N. Chichkov, *Optical response features of Si-nanoparticle arrays,* Physical Review B **82**, 045404 (2010).

[38] A. B. Evlyukhin, C. Reinhardt, and B. N. Chichkov, *Multipole light scattering by nonspherical nanoparticles in the discrete dipole approximation,* Physical Review B **84**, 235429 (2011).

[39] A. B. Evlyukhin, S. M. Novikov, U. Zywietz, R. L. Eriksen, C. Reinhardt, S. I. Bozhevolnyi, and B. N. Chichkov, *Demonstration of Magnetic Dipole Resonances of Dielectric Nanospheres in the Visible Region,* Nano Letters **12**, 3749 (2012).

[40] A. B. Evlyukhin, R. L. Eriksen, W. Cheng, J. Beermann, C. Reinhardt, A. Petrov, S. Prorok, M. Eich, B. N. Chichkov, and S. I. Bozhevolnyi, *Optical spectroscopy of single Si nanocylinders with magnetic and electric resonances,* Scientific Reports **4**, 4126 (2014).

[41] A. I. Kuznetsov, A. E. Miroshnichenko, Y. H. Fu, J. Zhang, and B. Luk´yanchuk, *Magnetic light,* Scientific Reports **2**, 492 (2012).

[42] C. Kittel, *Introduction to Solid State Physics,* Wiley, New York, 8th edition, 2005.

[43] A. García-Etxarri, R. Gómez-Medina, L. S. Froufe-Pérez, C. López, L. Chantada, F. Scheffold, J. Aizpurua, M. Nieto-Vesperinas, and J. J. Sáenz, *Strong magnetic response of submicron Silicon particles in the infrared,* Optics Express **19**, 4815 (2011).

[44] M. K. Schmidt, R. Esteban, J. J. Sáenz, I. Suárez-Lacalle, S. Mackowski, and J. Aizpurua, *Dielectric antennas - a suitable platform for controlling magnetic dipolar emission,* Optics Express **20**, 13636 (2012).

[45] I. Staude, A. E. Miroshnichenko, M. Decker, N. T. Fofang, S. Liu, E. Gonzales, J. Dominguez, T. S. Luk, D. N. Neshev, I. Brener, and Y. Kivshar, *Tailoring Directional Scattering through Magnetic and Electric Resonances in Subwavelength Silicon Nanodisks,* ACS Nano **7**, 7824 (2013).

[46] S. Person, M. Jain, Z. Lapin, J. J. Sáenz, G. Wicks, and L. Novotny, *Demonstration of Zero Optical Backscattering from Single Nanoparticles,* Nano Letters **13**, 1806 (2013).

[47] C. Wang, Z. Y. Jia, K. Zhang, Y. Zhou, R. H. Fan, X. Xiong, and R. W. Peng, *Broadband optical scattering in coupled silicon nanocylinders,* Journal of Applied Physics **115**, (2014).

[48] J. Yan, P. Liu, Z. Lin, H. Wang, H. Chen, C. Wang, and G. Yang, *Directional Fano Resonance in a Silicon Nanosphere Dimer,* ACS Nano **9**, 2968 (2015).

[49] P. Albella, M. A. Poyli, M. K. Schmidt, S. A. Maier, F. Moreno, J. J. Sáenz, and J. Aizpurua, *Low-Loss Electric and Magnetic Field-Enhanced Spectroscopy with Subwavelength Silicon Dimers,* The Journal of Physical Chemistry C **117**, 13573 (2013).

[50] G. Boudarham, R. Abdeddaim, and N. Bonod, *Enhancing the magnetic field intensity with a dielectric gap antenna,* Applied Physics Letters **104**, 021117 (2014).

[51] U. Zywietz, M. K. Schmidt, A. B. Evlyukhin, C. Reinhardt, J. Aizpurua, and B. N. Chichkov, *Electromagnetic Resonances of Silicon Nanoparticle Dimers in the Visible,*

ACS Photonics **2**, 913 (2015).

[52] R. M. Bakker, D. Permyakov, Y. F. Yu, D. Markovich, R. Paniagua-Domínguez, L. Gonzaga, A. Samusev, Y. Kivshar, B. Luk´yanchuk, and A. I. Kuznetsov, *Magnetic and Electric Hotspots with Silicon Nanodimers*, Nano Letters **15**, 2137 (2015).

[53] Q. Zhao, L. Kang, B. Du, H. Zhao, Q. Xie, X. Huang, B. Li, J. Zhou, and L. Li, *Experimental Demonstration of Isotropic Negative Permeability in a Three-Dimensional Dielectric Composite*, Physical Review Letters **101**, 027402 (2008).

[54] Q. Zhao, J. Zhou, F. Zhang, and D. Lippens, *Mie resonance-based dielectric metamaterials*, Materials Today **12**, 60 (2009).

[55] L. Zou, W. Withayachumnankul, C. M. Shah, A. Mitchell, M. Bhaskaran, S. Sriram, and C. Fumeaux, *Dielectric resonator nanoantennas at visible frequencies*, Optics Express **21**, 1344 (2013).

[56] D. Lin, P. Fan, E. Hasman, and M. L. Brongersma, *Dielectric gradient metasurface optical elements*, Science **345**, 298 (2014).

[57] L. Cao, J. S. White, J.-S. Park, J. A. Schuller, B. M. Clemens, and M. L. Brongersma, *Engineering light absorption in semiconductor nanowire devices*, Nature Materials **8**, 643 (2009).

[58] L. Cao, J.-S. Park, P. Fan, B. Clemens, and M. L. Brongersma, *Resonant Germanium Nanoantenna Photodetectors*, Nano Letters **10**, 1229 (2010).

[59] P. Fan, Z. Yu, S. Fan, and M. L. Brongersma, *Optical Fano resonance of an individual semiconductor nanostructure*, Nature Materials **13**, 471 (2014).

[60] S.-K. Kim, R. W. Day, J. F. Cahoon, T. J. Kempa, K.-D. Song, H.-G. Park, and C. M. Lieber, *Tuning Light Absorption in Core/Shell Silicon Nanowire Photovoltaic Devices through Morphological Design*, Nano Letters **12**, 4971 (2012).

[61] R. Yan, J.-H. Park, Y. Choi, C.-J. Heo, S.-M. Yang, L. P. Lee, and P. Yang, *Nanowire-based single-cell endoscopy*, Nature Nanotechnology **7**, 191 (2012).

[62] X. Duan, Y. Huang, R. Agarwal, and C. M. Lieber, *Single-nanowire electrically driven lasers*, Nature **421**, 241 (2003).

[63] M. D. Kelzenberg, D. B. Turner-Evans, B. M. Kayes, M. A. Filler, M. C. Putnam, N. S. Lewis, and H. A. Atwater, *Photovoltaic Measurements in Single-Nanowire Silicon Solar Cells*, Nano Letters **8**, 710 (2008).

[64] P. Krogstrup, H. I. Jorgensen, M. Heiss, O. Demichel, J. V. Holm, M. Aagesen, J. Nygard, and A. Fontcuberta i Morral, *Single-nanowire solar cells beyond the Shockley-Queisser limit*, Nature Photonics **7**, 306 (2013).

[65] S. Z. Oener, S. A. Mann, B. Sciacca, C. Sfiligoj, J. Hoang, and E. C. Garnett, *Au-Cu2O core-shell nanowire photovoltaics*, Applied Physics Letters **106**, 023501 (2015).

[66] A. Jäger-Waldau, *PV Status Report 2014*, Technical report, European Union, DG Joint Research Centre, 2014.

[67] T. Coenen, E. J. R. Vesseur, and A. Polman, *Deep Subwavelength Spatial Characterization of Angular Emission from Single-Crystal Au Plasmonic Ridge Nanoantennas*, ACS Nano **6**, 1742 (2012).

[68] T. Coenen, F. Bernal Arango, A. Femius Koenderink, and A. Polman, *Directional emission from a single plasmonic scatterer*, Nature Communications **5** (2014).

[69] T. Coenen and A. Polman, *Optical Properties of Single Plasmonic Holes Probed with Local Electron Beam Excitation*, ACS Nano **8**, 7350 (2014).

[70] K. R. Catchpole and A. Polman, *Design principles for particle plasmon enhanced solar cells*, Applied Physics Letters **93**, 191113 (2008).

[71] P. Spinelli, M. Hebbink, R. de Waele, L. Black, F. Lenzmann, and A. Polman, *Optical*

Impedance Matching Using Coupled Plasmonic Nanoparticle Arrays, Nano Letters **11**, 1760 (2011).

[72] P. Spinelli, C. van Lare, E. Verhagen, and A. Polman, *Controlling Fano lineshapes in plasmon-mediated light coupling into a substrate,* Optics Express **19**, A303 (2011).

[73] P. Spinelli, B. Macco, M. A. Verschuuren, W. M. M. Kessels, and A. Polman, *Al_2O_3/TiO_2 nano-pattern antireflection coating with ultralow surface recombination,* Applied Physics Letters **102**, 233902 (2013).

[74] V. E. Ferry, M. A. Verschuuren, H. B. T. Li, E. Verhagen, R. J. Walters, R. E. I. Schropp, H. A. Atwater, and A. Polman, *Light trapping in ultrathin plasmonic solar cells,* Optics Express **18**, A237 (2010).

[75] V. E. Ferry, M. A. Verschuuren, M. C. v. Lare, R. E. I. Schropp, H. A. Atwater, and A. Polman, *Optimized Spatial Correlations for Broadband Light Trapping Nanopatterns in High Efficiency Ultrathin Film a-Si:H Solar Cells,* Nano Letters **11**, 4239 (2011).

[76] M. van Lare, F. Lenzmann, and A. Polman, *Dielectric back scattering patterns for light trapping in thin-film Si solar cells,* Optics Express **21**, 20738 (2013).

[77] H. R. Stuart and D. G. Hall, *Absorption enhancement in silicon-on-insulator waveguides using metal island films,* Applied Physics Letters **69**, 2327 (1996).

[78] H. A. Atwater and A. Polman, *Plasmonics for improved photovoltaic devices,* Nature Materials **9**, 205 (2010).

[79] V. E. Ferry, J. N. Munday, and H. A. Atwater, *Design Considerations for Plasmonic Photovoltaics,* Advanced Materials **22**, 4794 (2010).

[80] V. E. Ferry, A. Polman, and H. A. Atwater, *Modeling Light Trapping in Nanostructured Solar Cells,* ACS Nano **5**, 10055 (2011).

[81] M. van Lare, F. Lenzmann, M. A. Verschuuren, and A. Polman, *Mode coupling by plasmonic surface scatterers in thin-film silicon solar cells,* Applied Physics Letters **101**, 221110 (2012).

[82] M. L. Brongersma, Y. Cui, and S. Fan, *Light management for photovoltaics using high-index nanostructures,* Nature Materials **13**, 451 (2014).

[83] E. R. Martins, J. Li, Y. Liu, J. Zhou, and T. F. Krauss, *Engineering gratings for light trapping in photovoltaics: The supercell concept,* Physical Review B **86**, 041404 (2012).

[84] P. Spinelli, V. E. Ferry, J. v. d. Groep, M. v. Lare, M. A. Verschuuren, R. E. I. Schropp, H. A. Atwater, and A. Polman, *Plasmonic light trapping in thin-film Si solar cells,* Journal of Optics **14**, 024002 (2012).

[85] S. A. Mann, R. R. Grote, R. M. Osgood, and J. A. Schuller, *Dielectric particle and void resonators for thin film solar cell textures,* Optics Express **19**, 25729 (2011).

[86] C. Battaglia, C.-M. Hsu, K. Söderström, J. Escarré, F.-J. Haug, M. Charrière, M. Boccard, M. Despeisse, D. T. L. Alexander, M. Cantoni, Y. Cui, and C. Ballif, *Light Trapping in Solar Cells: Can Periodic Beat Random?,* ACS Nano **6**, 2790 (2012).

[87] S. Jeong, M. D. McGehee, and Y. Cui, *All-back-contact ultra-thin silicon nanocone solar cells with 13.7% power conversion efficiency,* Nature Communications **4** (2013).

[88] J. Müller, B. Rech, J. Springer, and M. Vanecek, *TCO and light trapping in silicon thin film solar cells,* Solar Energy **77**, 917 (2004).

[89] J. Grandidier, D. M. Callahan, J. N. Munday, and H. A. Atwater, *Light Absorption Enhancement in Thin-Film Solar Cells Using Whispering Gallery Modes in Dielectric Nanospheres,* Advanced Materials **23**, 1272 (2011).

[90] J. Grandidier, R. A. Weitekamp, M. G. Deceglie, D. M. Callahan, C. Battaglia, C. R. Bukowsky, C. Ballif, R. H. Grubbs, and H. A. Atwater, *Solar cell efficiency enhancement*

via light trapping in printable resonant dielectric nanosphere arrays, physica status solidi (a) **210**, 255 (2013).

[91] Y. Yao, J. Yao, V. K. Narasimhan, Z. Ruan, C. Xie, S. Fan, and Y. Cui, *Broadband light management using low-Q whispering gallery modes in spherical nanoshells*, Nature Communications **3**, 664 (2012).

[92] M. D. Kelzenberg, S. W. Boettcher, J. A. Petykiewicz, D. B. Turner-Evans, M. C. Putnam, E. L. Warren, J. M. Spurgeon, R. M. Briggs, N. S. Lewis, and H. A. Atwater, *Enhanced absorption and carrier collection in Si wire arrays for photovoltaic applications*, Nature Materials **9**, 239 (2010).

[93] M. D. Kelzenberg, D. B. Turner-Evans, M. C. Putnam, S. W. Boettcher, R. M. Briggs, J. Y. Baek, N. S. Lewis, and H. A. Atwater, *High-performance Si microwire photovoltaics*, Energy & Environmental Science **4**, 866 (2011).

[94] E. Garnett and P. Yang, *Light Trapping in Silicon Nanowire Solar Cells*, Nano Letters **10**, 1082 (2010).

[95] L. Cao, P. Fan, A. P. Vasudev, J. S. White, Z. Yu, W. Cai, J. A. Schuller, S. Fan, and M. L. Brongersma, *Semiconductor Nanowire Optical Antenna Solar Absorbers*, Nano Letters **10**, 439 (2010).

[96] S. A. Mann and E. C. Garnett, *Resonant Nanophotonic Spectrum Splitting for Ultrathin Multijunction Solar Cells*, ACS Photonics **2**, 816 (2015).

[97] K. X. Wang, Z. Yu, V. Liu, Y. Cui, and S. Fan, *Absorption Enhancement in Ultrathin Crystalline Silicon Solar Cells with Antireflection and Light-Trapping Nanocone Gratings*, Nano Letters **12**, 1616 (2012).

[98] S. A. Mann and E. C. Garnett, *Extreme Light Absorption in Thin Semiconductor Films Wrapped around Metal Nanowires*, Nano Letters **13**, 3173 (2013).

[99] L. Hu, H. Wu, and Y. Cui, *Metal nanogrids, nanowires, and nanofibers for transparent electrodes*, MRS Bulletin **36**, 760 (2011).

[100] H. Wu, D. Kong, Z. Ruan, P.-C. Hsu, S. Wang, Z. Yu, T. J. Carney, L. Hu, S. Fan, and Y. Cui, *A transparent electrode based on a metal nanotrough network*, Nature Nanotechnology **8**, 421 (2013).

[101] P. Kuang, J.-M. Park, W. Leung, R. C. Mahadevapuram, K. S. Nalwa, T.-G. Kim, S. Chaudhary, K.-M. Ho, and K. Constant, *A New Architecture for Transparent Electrodes: Relieving the Trade-Off Between Electrical Conductivity and Optical Transmittance*, Advanced Materials **23**, 2469 (2011).

[102] P. B. Catrysse and S. Fan, *Nanopatterned Metallic Films for Use As Transparent Conductive Electrodes in Optoelectronic Devices*, Nano Letters **10**, 2944 (2010).

[103] K. Tvingstedt and O. Inganäs, *Electrode Grids for ITO Free Organic Photovoltaic Devices*, Advanced Materials **19**, 2893 (2007).

[104] M.-G. Kang, M.-S. Kim, J. Kim, and L. J. Guo, *Organic Solar Cells Using Nanoimprinted Transparent Metal Electrode*, Advanced Materials **20**, 4408 (2008).

[105] H.-K. Kim, D.-G. Kim, K.-S. Lee, M.-S. Huh, S. H. Jeong, K. I. Kim, and T.-Y. Seong, *Plasma damage-free sputtering of indium tin oxide cathode layers for top-emitting organic light-emitting diodes*, Applied Physics Letters **86**, 183503 (2005).

[106] S. De, T. M. Higgins, P. E. Lyons, E. M. Doherty, P. N. Nirmalraj, W. J. Blau, J. J. Boland, and J. N. Coleman, *Silver Nanowire Networks as Flexible, Transparent, Conducting Films: Extremely High DC to Optical Conductivity Ratios*, ACS Nano **3**, 1767 (2009).

[107] L. Hu, H. S. Kim, J.-Y. Lee, P. Peumans, and Y. Cui, *Scalable Coating and Properties of Transparent, Flexible, Silver Nanowire Electrodes*, ACS Nano **4**, 2955 (2010).

[108] J. H. Yim, S.-y. Joe, C. Pang, K. M. Lee, H. Jeong, J.-Y. Park, Y. H. Ahn, J. C. de Mello,

and S. Lee, *Fully Solution-Processed Semitransparent Organic Solar Cells with a Silver Nanowire Cathode and a Conducting Polymer Anode*, ACS Nano **8**, 2857 (2014).

[109] M. G. Kang and L. J. Guo, *Nanoimprinted Semitransparent Metal Electrodes and Their Application in Organic Light-Emitting Diodes*, Advanced Materials **19**, 1391 (2007).

[110] T. Nakanishi, E. Tsutsumi, K. Masunaga, A. Fujimoto, and K. Asakawa, *Transparent Aluminum Nanomesh Electrode Fabricated by Nanopatterning Using Self-Assembled Nanoparticles*, Applied Physics Express **4**, 025201 (2011).

[111] T. Gao, B. Wang, B. Ding, J.-k. Lee, and P. W. Leu, *Uniform and Ordered Copper Nanomeshes by Microsphere Lithography for Transparent Electrodes*, Nano Letters **14**, 2105 (2014).

[112] P.-C. Hsu, S. Wang, H. Wu, V. K. Narasimhan, D. Kong, H. Ryoung Lee, and Y. Cui, *Performance enhancement of metal nanowire transparent conducting electrodes by mesoscale metal wires*, Nature Communications **4**, 2522 (2013).

[113] G. V. Hartland, *Optical studies of dynamics in noble metal nanostructures*, Chemical Reviews **111**, 3858 (2011).

[114] R. Sundararaman, P. Narang, A. S. Jermyn, W. A. Goddard Iii, and H. A. Atwater, *Theoretical predictions for hot-carrier generation from surface plasmon decay*, Nature Communications **5** (2014).

[115] M. L. Brongersma, N. J. Halas, and P. Nordlander, *Plasmon-induced hot carrier science and technology*, Nature Nanotechnology **10**, 25 (2015).

[116] M. W. Knight, Y. Wang, A. S. Urban, A. Sobhani, B. Y. Zheng, P. Nordlander, and N. J. Halas, *Embedding Plasmonic Nanostructure Diodes Enhances Hot Electron Emission*, Nano Letters **13**, 1687 (2013).

[117] H. Chalabi, D. Schoen, and M. L. Brongersma, *Hot-Electron Photodetection with a Plasmonic Nanostripe Antenna*, Nano Letters **14**, 1374 (2014).

[118] S. Mukherjee, F. Libisch, N. Large, O. Neumann, L. V. Brown, J. Cheng, J. B. Lassiter, E. A. Carter, P. Nordlander, and N. J. Halas, *Hot Electrons Do the Impossible: Plasmon-Induced Dissociation of H_2 on Au*, Nano Letters **13**, 240 (2013).

[119] S. Linic, P. Christopher, and D. B. Ingram, *Plasmonic-metal nanostructures for efficient conversion of solar to chemical energy*, Nature Materials **10**, 911 (2011).

[120] V. Ferry, M. Verschuuren, H. Li, E. Verhagen, R. Walters, R. Schropp, H. Atwater, and A. Polman, *Light trapping in thin film plasmonic solar cells*, in *25th European Photovoltaic Solar Energy Conference and Exhibition*, p. 10–14 (2010).

[121] J. Woerle and H. Rost, *Roll-to-roll production of transparent conductive films using metallic grids*, MRS Bulletin **36**, 789 (2011).

[122] J.-Y. Lee, S. T. Connor, Y. Cui, and P. Peumans, *Solution-Processed Metal Nanowire Mesh Transparent Electrodes*, Nano Letters **8**, 689 (2008).

[123] F. S. F. Morgenstern, D. Kabra, S. Massip, T. J. K. Brenner, P. E. Lyons, J. N. Coleman, and R. H. Friend, *Ag-nanowire films coated with ZnO nanoparticles as a transparent electrode for solar cells*, Applied Physics Letters **99**, 183307 (2011).

[124] S. M. Bergin, Y.-H. Chen, A. R. Rathmell, P. Charbonneau, Z.-Y. Li, and B. J. Wiley, *The effect of nanowire length and diameter on the properties of transparent, conducting nanowire films*, Nanoscale **4**, 1996 (2012).

[125] K. S. Kim, Y. Zhao, H. Jang, S. Y. Lee, J. M. Kim, K. S. Kim, J.-H. Ahn, P. Kim, J.-Y. Choi, and B. H. Hong, *Large-scale pattern growth of graphene films for stretchable transparent electrodes*, Nature **457**, 706 (2009).

[126] F. Bonaccorso, Z. Sun, T. Hasan, and A. C. Ferrari, *Graphene photonics and optoelectronics*, Nature Photonics **4**, 611 (2010).

[127] K. Aydin, V. E. Ferry, R. M. Briggs, and H. A. Atwater, *Broadband polarization-independent resonant light absorption using ultrathin plasmonic super absorbers*, Nature Communications **2**, 517 (2011).

[128] V. J. Logeeswaran, N. P. Kobayashi, M. S. Islam, W. Wu, P. Chaturvedi, N. X. Fang, S. Y. Wang, and R. S. Williams, *Ultrasmooth Silver Thin Films Deposited with a Germanium Nucleation Layer*, Nano Letters **9**, 178 (2009).

[129] W. Chen, M. D. Thoreson, S. Ishii, A. V. Kildishev, and V. M. Shalaev, *Ultra-thin ultra-smooth and low-loss silver films on a germanium wetting layer*, Optics Express **18**, 5124 (2010).

[130] H. Liu, B. Wang, E. S. P. Leong, P. Yang, Y. Zong, G. Si, J. Teng, and S. A. Maier, *Enhanced Surface Plasmon Resonance on a Smooth Silver Film with a Seed Growth Layer*, ACS Nano **4**, 3139 (2010).

[131] T. W. Ebbesen, H. J. Lezec, H. F. Ghaemi, T. Thio, and P. A. Wolff, *Extraordinary optical transmission through sub-wavelength hole arrays*, Nature **391**, 667 (1998).

[132] L. Martín-Moreno, F. J. García-Vidal, H. J. Lezec, K. M. Pellerin, T. Thio, J. B. Pendry, and T. W. Ebbesen, *Theory of Extraordinary Optical Transmission through Subwavelength Hole Arrays*, Physical Review Letters **86**, 1114 (2001).

[133] J. V. Coe, J. M. Heer, S. Teeters-Kennedy, H. Tian, and K. R. Rodriguez, *Extraordinary transmission of metal films with arrays of subwavelength holes*, Annual Review of Physical Chemistry **59**, 179 (2008).

[134] S. H. Lim, W. Mar, P. Matheu, D. Derkacs, and E. T. Yu, *Photocurrent spectroscopy of optical absorption enhancement in silicon photodiodes via scattering from surface plasmon polaritons in gold nanoparticles*, Journal of Applied Physics **101**, 104309 (2007).

[135] B. Luk´yanchuk, N. I. Zheludev, S. A. Maier, N. J. Halas, P. Nordlander, H. Giessen, and C. T. Chong, *The Fano resonance in plasmonic nanostructures and metamaterials*, Nature Materials **9**, 707 (2010).

[136] V. E. Ferry, M. A. Verschuuren, H. B. T. Li, R. E. I. Schropp, H. A. Atwater, and A. Polman, *Improved red-response in thin film a-Si:H solar cells with soft-imprinted plasmonic back reflectors*, Applied Physics Letters **95**, 183503 (2009).

[137] Lumerical Solutions Inc., *www.lumerical.com/tcad-products/fdtd/*.

[138] E. D. Palik, *Handbook of Optical Constants of Solids*, Academic, New York, 1985.

[139] L. Rayleigh, *III. Note on the remarkable case of diffraction spectra described by Prof. Wood*, Philosophical Magazine Series 6 **14**, 60 (1907).

[140] F. J. García de Abajo and A. Howie, *Relativistic Electron Energy Loss and Electron-Induced Photon Emission in Inhomogeneous Dielectrics*, Physical Review Letters **80**, 5180 (1998).

[141] F. J. García de Abajo and A. Howie, *Retarded field calculation of electron energy loss in inhomogeneous dielectrics*, Physical Review B **65**, 115418 (2002).

[142] H. Kim, C. M. Gilmore, A. Piqué, J. S. Horwitz, H. Mattoussi, H. Murata, Z. H. Kafafi, and D. B. Chrisey, *Electrical, optical, and structural properties of indium-tin-oxide thin films for organic light-emitting devices*, Journal of Applied Physics **86**, 6451 (1999).

[143] R. Ji, A. Krüger, M. Hornung, M. Verschuuren, R. v. d. Laar, and J. v. Eekelen, *Full Field Nanoimprint on Mask Aligners Using Substrate Conformal Imprint Lithography Technique*, Acta Physica Polonica A **116**, S187 (2009).

[144] M. Verschuuren and H. V. Sprang, *3D Photonic Structures by Sol-Gel Imprint Lithography*, MRS Online Proceedings Library **1002**, N03 (2007).

[145] A. Kumar and C. Zhou, *The Race To Replace Tin-Doped Indium Oxide: Which Material*

Will Win?, ACS Nano **4**, 11 (2010).

[146] S.-B. Kang, Y.-J. Noh, S.-I. Na, and H.-K. Kim, *Brush-painted flexible organic solar cells using highly transparent and flexible Ag nanowire network electrodes*, Solar Energy Materials and Solar Cells **122**, 152 (2014).

[147] S. Schubert, L. Müller-Meskamp, and K. Leo, *Unusually High Optical Transmission in Ca:Ag Blend Films: High-Performance Top Electrodes for Efficient Organic Solar Cells*, Advanced Functional Materials **24**, 6668 (2014).

[148] R. Chen, S. R. Das, C. Jeong, M. R. Khan, D. B. Janes, and M. A. Alam, *Co-Percolating Graphene-Wrapped Silver Nanowire Network for High Performance, Highly Stable, Transparent Conducting Electrodes*, Advanced Functional Materials **23**, 5150 (2013).

[149] Q. Gan, F. J. Bartoli, and Z. H. Kafafi, *Plasmonic-Enhanced Organic Photovoltaics: Breaking the 10% Efficiency Barrier*, Advanced Materials **25**, 2385 (2013).

[150] J.-L. Wu, F.-C. Chen, Y.-S. Hsiao, F.-C. Chien, P. Chen, C.-H. Kuo, M. H. Huang, and C.-S. Hsu, *Surface Plasmonic Effects of Metallic Nanoparticles on the Performance of Polymer Bulk Heterojunction Solar Cells*, ACS Nano **5**, 959 (2011).

[151] J. K. Mapel, M. Singh, M. A. Baldo, and K. Celebi, *Plasmonic excitation of organic double heterostructure solar cells*, Applied Physics Letters **90**, 121102 (2007).

[152] M. E. Sykes, A. Barito, J. A. Amonoo, P. F. Green, and M. Shtein, *Broadband Plasmonic Photocurrent Enhancement in Planar Organic Photovoltaics Embedded in a Metallic Nanocavity*, Advanced Energy Materials **4**, 1301937 (2014).

[153] K. Tvingstedt, N.-K. Persson, O. Inganäs, A. Rahachou, and I. V. Zozoulenko, *Surface plasmon increase absorption in polymer photovoltaic cells*, Applied Physics Letters **91**, 113514 (2007).

[154] M.-G. Kang, T. Xu, H. J. Park, X. Luo, and L. J. Guo, *Efficiency Enhancement of Organic Solar Cells Using Transparent Plasmonic Ag Nanowire Electrodes*, Advanced Materials **22**, 4378 (2010).

[155] T. H. Reilly, J. van de Lagemaat, R. C. Tenent, A. J. Morfa, and K. L. Rowlen, *Surface-plasmon enhanced transparent electrodes in organic photovoltaics*, Applied Physics Letters **92**, 243304 (2008).

[156] J.-Y. Lee, S. T. Connor, Y. Cui, and P. Peumans, *Semitransparent Organic Photovoltaic Cells with Laminated Top Electrode*, Nano Letters **10**, 1276 (2010).

[157] M. A. Verschuuren, *Substrate Conformal Imprint Lithography for Nanophotonics*, PhD thesis, Utrecht University, Utrecht (2010).

[158] S. Günes, H. Neugebauer, and N. S. Sariciftci, *Conjugated Polymer-Based Organic Solar Cells*, Chemical Reviews **107**, 1324 (2007).

[159] J. van de Groep, P. Spinelli, and A. Polman, *Transparent Conducting Silver Nanowire Networks*, Nano Letters **12**, 3138 (2012).

[160] D. S. Germack, C. K. Chan, R. J. Kline, D. A. Fischer, D. J. Gundlach, M. F. Toney, L. J. Richter, and D. M. DeLongchamp, *Interfacial Segregation in Polymer/Fullerene Blend Films for Photovoltaic Devices*, Macromolecules **43**, 3828 (2010).

[161] J. Lee, K. Vandewal, S. R. Yost, M. E. Bahlke, L. Goris, M. A. Baldo, J. V. Manca, and T. V. Voorhis, *Charge Transfer State Versus Hot Exciton Dissociation in Polymer-Fullerene Blended Solar Cells*, Journal of the American Chemical Society **132**, 11878 (2010).

[162] E. Verhagen, *Subwavelength light confinement with surface plasmon polaritons*, PhD thesis, Utrecht University, Utrecht (2009).

[163] D. Gupta, M. M. Wienk, and R. A. J. Janssen, *Efficient Polymer Solar Cells on Opaque Substrates with a Laminated PEDOT:PSS Top Electrode*, Advanced Energy Materials **3**, 782 (2013).

[164] R. R. Grote, S. J. Brown, J. B. Driscoll, R. M. Osgood, and J. A. Schuller, *Morphology-dependent light trapping in thin-film organic solar cells*, Optics Express **21**, A847 (2013).

[165] I. Massiot, N. Vandamme, N. Bardou, C. Dupuis, A. Lemaître, J.-F. Guillemoles, and S. Collin, *Metal Nanogrid for Broadband Multiresonant Light-Harvesting in Ultrathin GaAs Layers*, ACS Photonics **1**, 878 (2014).

[166] F. Afshinmanesh, A. G. Curto, K. M. Milaninia, N. F. van Hulst, and M. L. Brongersma, *Transparent Metallic Fractal Electrodes for Semiconductor Devices*, Nano Letters **14**, 5068 (2014).

[167] M. M. Wienk, M. Turbiez, J. Gilot, and R. A. J. Janssen, *Narrow-Bandgap Diketo-Pyrrolo-Pyrrole Polymer Solar Cells: The Effect of Processing on the Performance*, Advanced Materials **20**, 2556 (2008).

[168] K. Ghaffarzadeh and R. Das, *Transparent Conductive Films (TCF) 2015-2025: Forecasts, Markets, Technologies*, presented at *IDTechEx* (2015).

[169] D. S. Hecht, L. Hu, and G. Irvin, *Emerging Transparent Electrodes Based on Thin Films of Carbon Nanotubes, Graphene, and Metallic Nanostructures*, Advanced Materials **23**, 1482 (2011).

[170] S. Ye, A. R. Rathmell, Z. Chen, I. E. Stewart, and B. J. Wiley, *Metal Nanowire Networks: The Next Generation of Transparent Conductors*, Advanced Materials **26**, 6670 (2014).

[171] Q. Cao, S. H. Hur, Z. T. Zhu, Y. G. Sun, C. J. Wang, M. A. Meitl, M. Shim, and J. A. Rogers, *Highly Bendable, Transparent Thin-Film Transistors That Use Carbon-Nanotube-Based Conductors and Semiconductors with Elastomeric Dielectrics*, Advanced Materials **18**, 304 (2006).

[172] Z. Wu, Z. Chen, X. Du, J. M. Logan, J. Sippel, M. Nikolou, K. Kamaras, J. R. Reynolds, D. B. Tanner, A. F. Hebard, and A. G. Rinzler, *Transparent, Conductive Carbon Nanotube Films*, Science **305**, 1273 (2004).

[173] L. Hu, D. S. Hecht, and G. Grüner, *Percolation in Transparent and Conducting Carbon Nanotube Networks*, Nano Letters **4**, 2513 (2004).

[174] S.-I. Na, S.-S. Kim, J. Jo, and D.-Y. Kim, *Efficient and Flexible ITO-Free Organic Solar Cells Using Highly Conductive Polymer Anodes*, Advanced Materials **20**, 4061 (2008).

[175] A. A. Argun, A. Cirpan, and J. R. Reynolds, *The First Truly All-Polymer Electrochromic Devices*, Advanced Materials **15**, 1338 (2003).

[176] G. Eda, G. Fanchini, and M. Chhowalla, *Large-area ultrathin films of reduced graphene oxide as a transparent and flexible electronic material*, Nature Nanotechnology **3**, 270 (2008).

[177] J. van de Groep, D. Gupta, M. A. Verschuuren, M. M. Wienk, R. A. J. Janssen, and A. Polman, *Large-area soft-imprinted nanowire networks as light trapping transparent conductors*, Scientific Reports **5**, 11414 (2015).

[178] E. C. Garnett, W. Cai, J. J. Cha, F. Mahmood, S. T. Connor, M. Greyson Christoforo, Y. Cui, M. D. McGehee, and M. L. Brongersma, *Self-limited plasmonic welding of silver nanowire junctions*, Nature Materials **11**, 241 (2012).

[179] B. Han, K. Pei, Y. Huang, X. Zhang, Q. Rong, Q. Lin, Y. Guo, T. Sun, C. Guo, D. Carnahan, M. Giersig, Y. Wang, J. Gao, Z. Ren, and K. Kempa, *Uniform Self-Forming Metallic Network as a High-Performance Transparent Conductive Electrode*, Advanced Materials **26**, 873 (2014).

[180] D.-S. Leem, A. Edwards, M. Faist, J. Nelson, D. D. C. Bradley, and J. C. de Mello, *Efficient Organic Solar Cells with Solution-Processed Silver Nanowire Electrodes*, Advanced Materials **23**, 4371 (2011).

[181] K. Critchley, B. P. Khanal, M. L. Górzny, L. Vigderman, S. D. Evans, E. R. Zubarev, and N. A. Kotov, *Near-Bulk Conductivity of Gold Nanowires as Nanoscale Interconnects and the Role of Atomically Smooth Interface*, Advanced Materials **22**, 2338 (2010).

[182] P.-C. Hsu, D. Kong, S. Wang, H. Wang, A. J. Welch, H. Wu, and Y. Cui, *Electrolessly Deposited Electrospun Metal Nanowire Transparent Electrodes*, Journal of the American Chemical Society **136**, 10593 (2014).

[183] H. Wu, L. Hu, M. W. Rowell, D. Kong, J. J. Cha, J. R. McDonough, J. Zhu, Y. Yang, M. D. McGehee, and Y. Cui, *Electrospun Metal Nanofiber Webs as High-Performance Transparent Electrode*, Nano Letters **10**, 4242 (2010).

[184] B. Shakhashiri, *Chemical Demonstrations: A Handbook for Teachers of Chemistry*, volume 4, The University of Wisconsin Press, 1992.

[185] B. Fultz and J. Howe, *Transmission Electron Microscopy and Diffractometry of Materials*, Springer, 2000.

[186] C. V. Thompson, *Grain Growth in Thin Films*, Annual Review of Materials Science **20**, 245 (1990).

[187] A. F. Mayadas and M. Shatzkes, *Electrical-Resistivity Model for Polycrystalline Films: the Case of Arbitrary Reflection at External Surfaces*, Physical Review B **1**, 1382 (1970).

[188] M. W. Rowell and M. D. McGehee, *Transparent electrode requirements for thin film solar cell modules*, Energy & Environmental Science **4**, 131 (2011).

[189] M. Dressel and G. Gruner, *Electrodynamics of Solids: Optical Properties of Electrons in Matter*, Cambridge University Press, Cambridge, 2002.

[190] A. Polman, *Plasmonics Applied*, Science **322**, 868 (2008).

[191] S. A. Maier, M. L. Brongersma, P. G. Kik, S. Meltzer, A. A. G. Requicha, and H. A. Atwater, *Plasmonics - A Route to Nanoscale Optical Devices*, Advanced Materials **13**, 1501 (2001).

[192] R. Zia and M. L. Brongersma, *Surface plasmon polariton analogue to Young´s double-slit experiment*, Nature Nanotechnology **2**, 426 (2007).

[193] J. A. Dionne, L. A. Sweatlock, M. T. Sheldon, A. P. Alivisatos, and H. A. Atwater, *Silicon-Based Plasmonics for On-Chip Photonics*, IEEE Journal of Selected Topics in Quantum Electronics **16**, 295 (2010).

[194] K. F. Macdonald, Z. L. Sámson, M. I. Stockman, and N. I. Zheludev, *Ultrafast active plasmonics*, Nature Photonics **3**, 55 (2009).

[195] R.-M. Ma, R. F. Oulton, V. J. Sorger, G. Bartal, and X. Zhang, *Room-temperature sub-diffraction-limited plasmon laser by total internal reflection*, Nature Materials **10**, 110 (2011).

[196] M. A. Noginov, G. Zhu, A. M. Belgrave, R. Bakker, V. M. Shalaev, E. E. Narimanov, S. Stout, E. Herz, T. Suteewong, and U. Wiesner, *Demonstration of a spaser-based nanolaser.*, Nature **460**, 1110 (2009).

[197] S. Pillai, K. Catchpole, T. Trupke, and M. Green, *Surface plasmon enhanced silicon solar cells*, Journal of Applied Physics **101**, 093105 (2007).

[198] P. K. Jain, X. Huang, I. H. El-Sayed, and M. A. El-Sayed, *Noble metals on the nanoscale: optical and photothermal properties and some applications in imaging, sensing, biology, and medicine*, Accounts of Chemical Research **41**, 1578 (2008).

[199] B. M. Reinhard, S. Sheikholeslami, A. Mastroianni, A. P. Alivisatos, and J. Liphardt, *Use of plasmon coupling to reveal the dynamics of DNA bending and cleavage by single EcoRV restriction enzymes*, Proceedings of the National Academy of Sciences of the United States of America **104**, 2667 (2007).

[200] R. Marty, G. Baffou, A. Arbouet, C. Girard, and R. Quidant, *Charge distribution induced*

inside complex plasmonic nanoparticles, Optics Express **18**, 3035 (2010).

[201] S. K. Dondapati, M. Ludemann, R. Müller, S. Schwieger, A. Schwemer, B. Händel, D. Kwiatkowski, M. Djiango, E. Runge, and T. A. Klar, *Voltage-Induced Adsorbate Damping of Single Gold Nanorod Plasmons in Aqueous Solution*, Nano Letters **12**, 1247 (2012).

[202] C. Novo, A. M. Funston, A. K. Gooding, and P. Mulvaney, *Electrochemical Charging of Single Gold Nanorods*, Journal of the American Chemical Society **131**, 14664 (2009).

[203] M. Nonnenmacher, M. P. O´Boyle, and H. K. Wickramasinghe, *Kelvin probe force microscopy*, Applied Physics Letters **58**, 2921 (1991).

[204] B. M. Askerov and S. Figarova, *Thermodynamics, Gibbs Method and Statistical Physics of Electron Gases*, Springer, New York, 2010.

[205] N. Ashcroft and N. Mermin, *Solid State Physics*, Harcourt, New York, 1976.

[206] G. Baffou, R. Quidant, and F. García de Abajo, *Nanoscale control of optical heating in complex plasmonic systems*, ACS Nano **4**, 709 (2010).

[207] F. J. Blatt, P. A. Schroeder, and C. F. Foiles, *Thermoelectric Power of Metals*, Plenum Press, New York, 1976.

[208] N. Noginova, A. V. Yakim, J. Soimo, L. Gu, and M. A. Noginov, *Light-to-current and current-to-light coupling in plasmonic systems*, Physical Review B **84**, 035447 (2011).

[209] H. Kurosawa and T. Ishihara, *Surface plasmon drag effect in a dielectrically modulated metallic thin film*, Optics Express **20**, 1561 (2012).

[210] T. Hatano, B. Nishikawa, M. Iwanaga, and T. Ishihara, *Optical rectification effect in 1D metallic photonic crystal slabs with asymmetric unit cell*, Optics Express **16**, 8236 (2008).

[211] W. L. Barnes, W. A. Murray, J. Dintinger, E. Devaux, and T. W. Ebbesen, *Surface Plasmon Polaritons and Their Role in the Enhanced Transmission of Light through Periodic Arrays of Subwavelength Holes in a Metal Film*, Physical Review Letters **92**, 107401 (2004).

[212] J. Parsons, E. Hendry, C. P. Burrows, B. Auguié, J. R. Sambles, and W. L. Barnes, *Localized surface-plasmon resonances in periodic nondiffracting metallic nanoparticle and nanohole arrays*, Physical Review B **79**, 073412 (2009).

[213] A. Rakic, A. Djurisic, J. Elazar, and M. Majewski, *Optical properties of metallic films for vertical-cavity optoelectronic devices*, Applied Optics **37**, 5271 (1998).

[214] S. A. Maier, *Plasmonics: Fundamentals and Applications*, Springer, New York, 2007.

[215] J. M. Luther, P. K. Jain, T. Ewers, and A. P. Alivisatos, *Localized surface plasmon resonances arising from free carriers in doped quantum dots*, Nature Materials **10**, 361 (2011).

[216] G. Garcia, R. Buonsanti, E. L. Runnerstrom, R. J. Mendelsberg, A. Llordes, A. Anders, T. J. Richardson, and D. J. Milliron, *Dynamically modulating the surface plasmon resonance of doped semiconductor nanocrystals*, Nano Letters **11**, 4415 (2011).

[217] J. Gordon and S. Ernst, *Surface-plasmons as a probe of the electrochemcial interface*, Surface Science **101**, 499 (1980).

[218] V. Palermo, M. Palma, and P. Samorì, *Electronic Characterization of Organic Thin Films by Kelvin Probe Force Microscopy*, Advanced Materials **18**, 145 (2006).

[219] J. P. Holman, *Heat Transfer*, McGraw-Hill Education, Europe, 10th edition, 2009.

[220] N. D. Lang and W. Kohn, *Theory of Metal Surfaces: Induced Surface Charge and Image Potential*, Physical Review B **7**, 3541 (1973).

[221] T. Sannomiya, H. Dermutz, C. Hafner, J. Vörös, and A. B. Dahlin, *Electrochemistry on a Localized Surface Plasmon Resonance Sensor*, Langmuir **26**, 7619 (2010).

[222] P. B. Johnson and R. W. Christy, *Optical Constants of the Noble Metals*, Physical Review B **6**, 4370 (1972).

[223] J. Braun, B. Gompf, G. Kobiela, and M. Dressel, *How Holes Can Obscure the View: Suppressed Transmission through an Ultrathin Metal Film by a Subwavelength Hole Array*, Physical Review Letters **103**, 203901 (2009).

[224] A. F. Koenderink and A. Polman, *Complex response and polariton-like dispersion splitting in periodic metal nanoparticle chains*, Physical Review B **74**, 033402 (2006).

[225] R. W. Alexander, G. S. Kovener, and R. J. Bell, *Dispersion Curves for Surface Electromagnetic Waves with Damping*, Physical Review Letters **32**, 154 (1974).

[226] G. S. Kovener, J. Alexander, R. W., and R. J. Bell, *Surface electromagnetic waves with damping. I. Isotropic media*, Physical Review B **14**, 1458 (1976).

[227] A. Manjavacas, J. G. Liu, V. Kulkarni, and P. Nordlander, *Plasmon-Induced Hot Carriers in Metallic Nanoparticles*, ACS Nano **8**, 7630 (2014).

[228] C. Clavero, *Plasmon-induced hot-electron generation at nanoparticle/metal-oxide interfaces for photovoltaic and photocatalytic devices*, Nature Photonics **8**, 95 (2014).

[229] J. Kim, H. Son, D. J. Cho, B. Geng, W. Regan, S. Shi, K. Kim, A. Zettl, Y.-R. Shen, and F. Wang, *Electrical Control of Optical Plasmon Resonance with Graphene*, Nano Letters **12**, 5598 (2012).

[230] M. I. Stockman, *Nanoplasmonics: past, present, and glimpse into future*, Optics Express **19**, 22029 (2011).

[231] K. F. MacDonald and N. I. Zheludev, *Active plasmonics: current status*, Laser & Photonics Reviews **4**, 562 (2010).

[232] A. Agrawal, C. Susut, G. Stafford, U. Bertocci, B. McMorran, H. J. Lezec, and A. A. Talin, *An Integrated Electrochromic Nanoplasmonic Optical Switch*, Nano Letters **11**, 2774 (2011).

[233] S. C. Warren, D. A. Walker, and B. A. Grzybowski, *Plasmoelectronics: Coupling Plasmonic Excitation with Electron Flow*, Langmuir **28**, 9093 (2012).

[234] H. Nakanishi, K. J. M. Bishop, B. Kowalczyk, A. Nitzan, E. A. Weiss, K. V. Tretiakov, M. M. Apodaca, R. Klajn, J. F. Stoddart, and B. A. Grzybowski, *Photoconductance and inverse photoconductance in films of functionalized metal nanoparticles*, Nature **460**, 371 (2009).

[235] X. N. Xie, Y. Xie, X. Gao, C. H. Sow, and A. T. S. Wee, *Metallic Nanoparticle Network for Photocurrent Generation and Photodetection*, Advanced Materials **21**, 3016 (2009).

[236] P. Mulvaney, J. Pérez-Juste, M. Giersig, L. Liz-Marzán, and C. Pecharromán, *Drastic Surface Plasmon Mode Shifts in Gold Nanorods Due to Electron Charging*, Plasmonics **1**, 61 (2006).

[237] A. M. Brown, M. T. Sheldon, and H. A. Atwater, *Electrochemical Tuning of the Dielectric Function of Au Nanoparticles*, ACS Photonics **2**, 459 (2015).

[238] M. T. Sheldon, J. van de Groep, A. M. Brown, A. Polman, and H. A. Atwater, *Plasmoelectric potentials in metal nanostructures*, Science **346**, 828 (2014).

[239] K. Chen, C. Durak, J. R. Heflin, and H. D. Robinson, *Plasmon-Enhanced Second-Harmonic Generation from Ionic Self-Assembled Multilayer Films*, Nano Letters **7**, 254 (2007).

[240] A. Boltasseva and H. A. Atwater, *Low-Loss Plasmonic Metamaterials*, Science **331**, 290 (2011).

[241] E. Feigenbaum, K. Diest, and H. A. Atwater, *Unity-Order Index Change in Transparent Conducting Oxides at Visible Frequencies*, Nano Letters **10**, 2111 (2010).

[242] H. W. Lee, G. Papadakis, S. P. Burgos, K. Chander, A. Kriesch, R. Pala, U. Peschel, and

H. A. Atwater, *Nanoscale Conducting Oxide PlasMOStor*, Nano Letters (2014).

[243] P. T. Landsberg and G. Tonge, *Thermodynamic energy conversion efficiencies*, Journal of Applied Physics **51**, R1 (1980).

[244] W. Shockley and H. J. Queisser, *Detailed Balance Limit of Efficiency of p-n Junction Solar Cells*, Journal of Applied Physics **32**, 510 (1961).

[245] L. A. Sweatlock, *Plasmonics: Numerical Methods and Device Applications*, PhD thesis, California Institute of Technology, Pasadena (2008).

[246] R. F. Service, *Ever-Smaller Lasers Pave the Way for Data Highways Made of Light*, Science **328**, 810 (2010).

[247] Y.-J. Lu, J. Kim, H.-Y. Chen, C. Wu, N. Dabidian, C. E. Sanders, C.-Y. Wang, M.-Y. Lu, B.-H. Li, X. Qiu, W.-H. Chang, L.-J. Chen, G. Shvets, C.-K. Shih, and S. Gwo, *Plasmonic Nanolaser Using Epitaxially Grown Silver Film*, Science **337**, 450 (2012).

[248] K. C. Y. Huang, M.-K. Seo, T. Sarmiento, Y. Huo, J. S. Harris, and M. L. Brongersma, *Electrically driven subwavelength optical nanocircuits*, Nature Photonics **8**, 244 (2014).

[249] P. Fan, C. Colombo, K. C. Y. Huang, P. Krogstrup, J. Nygard, A. Fontcuberta i Morral, and M. L. Brongersma, *An Electrically-Driven GaAs Nanowire Surface Plasmon Source*, Nano Letters **12**, 4943 (2012).

[250] X. Dai, S. Zhang, Z. Wang, G. Adamo, H. Liu, Y. Huang, C. Couteau, and C. Soci, *GaAs/AlGaAs Nanowire Photodetector*, Nano Letters **14**, 2688 (2014).

[251] Z. Wu, K. Parvez, X. Feng, and K. Müllen, *Graphene-based in-plane micro-supercapacitors with high power and energy densities*, Nature Communications **4** (2013).

[252] J. R. Piper and S. Fan, *Total Absorption in a Graphene Monolayer in the Optical Regime by Critical Coupling with a Photonic Crystal Guided Resonance*, ACS Photonics **1**, 347 (2014).

[253] G. Dingemans and W. M. M. Kessels, *Recent progress in the development and understanding of silicon surface passivation by aluminum oxide for photovoltaics*, in *25th European Photovoltaic Solar Energy Conference and Exhibition*, p. 1083–1090 (2010).

[254] J. R. Piper, V. Liu, and S. Fan, *Total absorption by degenerate critical coupling*, Applied Physics Letters **104**, 251110 (2014).

[255] S. Thongrattanasiri, F. H. L. Koppens, and F. J. García de Abajo, *Complete Optical Absorption in Periodically Patterned Graphene*, Physical Review Letters **108**, 047401 (2012).

[256] J. A. Schuller and M. L. Brongersma, *General properties of dielectric optical antennas*, Optics Express **17**, 24084 (2009).

[257] R. Sainidou, J. Renger, T. V. Teperik, M. U. González, R. Quidant, and F. J. García de Abajo, *Extraordinary All-Dielectric Light Enhancement over Large Volumes*, Nano Letters **10**, 4450 (2010).

[258] G. Grzela, D. Hourlier, and J. Gómez Rivas, *Polarization-dependent light extinction in ensembles of polydisperse vertical semiconductor nanowires: A Mie scattering effective medium*, Physical Review B **86**, 045305 (2012).

[259] A. Raman, Z. Yu, and S. Fan, *Dielectric nanostructures for broadband light trapping in organic solar cells*, Optics Express **19**, 19015 (2011).

[260] Y. Yu, V. E. Ferry, A. P. Alivisatos, and L. Cao, *Dielectric Core-Shell Optical Antennas for Strong Solar Absorption Enhancement*, Nano Letters **12**, 3674 (2012).

[261] A. P. Vasudev, J. A. Schuller, and M. L. Brongersma, *Nanophotonic light trapping with patterned transparent conductive oxides*, Optics Express **20**, A385 (2012).

[262] J. Tang, Z. Huo, S. Brittman, H. Gao, and P. Yang, *Solution-processed core-shell nanowires for efficient photovoltaic cells*, Nature Nanotechnology **6**, 568 (2011).

[263] K. L. van der Molen, P. Zijlstra, A. Lagendijk, and A. P. Mosk, *Laser threshold of Mie resonances*, Optics Letters **31**, 1432 (2006).

[264] A. Alù and N. Engheta, *Cloaking a Sensor*, Physical Review Letters **102**, 233901 (2009).

[265] P. Fan, U. K. Chettiar, L. Cao, F. Afshinmanesh, N. Engheta, and M. L. Brongersma, *An invisible metal-semiconductor photodetector*, Nature Photonics **6**, 380 (2012).

[266] T. J. Kippenberg and K. J. Vahala, *Cavity Opto-Mechanics, In Practical Applications of Microresonators in Optics and Photonics*, CRC Press, Boca Raton, FL, 2009.

[267] T. Coenen, E. J. R. Vesseur, and A. Polman, *Angle-resolved cathodoluminescence spectroscopy*, Applied Physics Letters **99**, 143103 (2011).

[268] T. Coenen, E. J. R. Vesseur, A. Polman, and A. F. Koenderink, *Directional Emission from Plasmonic Yagi–Uda Antennas Probed by Angle-Resolved Cathodoluminescence Spectroscopy*, Nano Letters **11**, 3779 (2011).

[269] T. Coenen and A. Polman, *Polarization-sensitive cathodoluminescence Fourier microscopy*, Optics Express **20**, 18679 (2012).

[270] F. J. García de Abajo, *Optical excitations in electron microscopy*, Reviews of Modern Physics **82**, 209 (2010).

[271] R. Sapienza, T. Coenen, J. Renger, M. Kuttge, N. F. van Hulst, and A. Polman, *Deep-subwavelength imaging of the modal dispersion of light*, Nature Materials **11**, 781 (2012).

[272] M. A. S. Kalceff, *Cathodoluminescence microcharacterization of the defect structure of irradiated hydrated and anhydrous fused silicon dioxide*, Physical Review B **57**, 5674 (1998).

[273] J. D. Jackson, *Classical Electrodynamics*, John Wiley & Sons, Hoboken, NJ, 1999.

[274] A. Snyder and J. Love, *Optical Waveguide Theory*, Chapman & Hall, London, 1996.

[275] R. E. Slusher, A. F. J. Levi, U. Mohideen, S. L. McCall, S. J. Pearton, and R. A. Logan, *Threshold characteristics of semiconductor microdisk lasers*, Applied Physics Letters **63**, 1310 (1993).

[276] M. Kuttge, F. J. García de Abajo, and A. Polman, *Ultrasmall Mode Volume Plasmonic Nanodisk Resonators*, Nano Letters **10**, 1537 (2009).

[277] Y. Yu and L. Cao, *Coupled leaky mode theory for light absorption in 2D, 1D, and 0D semiconductor nanostructures*, Optics Express **20**, 13847 (2012).

[278] N. Yamamoto, S. Ohtani, and F. J. García de Abajo, *Gap and Mie Plasmons in Individual Silver Nanospheres near a Silver Surface*, Nano Letters **11**, 91 (2011).

[279] E. J. R. Vesseur and A. Polman, *Plasmonic Whispering Gallery Cavities As Optical Nanoantennas*, Nano Letters **11**, 5524 (2011).

[280] L. Novotny and B. Hecht, *Principles of Nano-Optics*, Cambridge University Press, New York, 2006.

[281] M. Kuttge, E. J. R. Vesseur, A. F. Koenderink, H. J. Lezec, H. A. Atwater, F. J. García de Abajo, and A. Polman, *Local density of states, spectrum, and far-field interference of surface plasmon polaritons probed by cathodoluminescence*, Physical Review B **79**, 113405 (2009).

[282] C. Hoppener and L. Novotny, *Antenna-Based Optical Imaging of Single Ca^{2+} Transmembrane Proteins in Liquids*, Nano Letters **8**, 642 (2008).

[283] N. Yu, R. Blanchard, J. Fan, Q. J. Wang, C. Pflügl, L. Diehl, T. Edamura, M. Yamanishi, H. Kan, and F. Capasso, *Quantum cascade lasers with integrated plasmonic antenna-array collimators*, Optics Express **16**, 19447 (2008).

[284] C. M. Soukoulis and M. Wegener, *Past achievements and future challenges in the development of three-dimensional photonic metamaterials*, Nature Photonics **5**, 523 (2011).

[285] T. Coenen, J. van de Groep, and A. Polman, *Resonant Modes of Single Silicon Nanocavities Excited by Electron Irradiation*, ACS Nano **7**, 1689 (2013).

[286] K. G. Lee, X. W. Chen, H. Eghlidi, P. Kukura, R. Lettow, A. Renn, V. Sandoghdar, and S. Gotzinger, *A planar dielectric antenna for directional single-photon emission and near-unity collection efficiency*, Nature Photonics **5**, 166 (2011).

[287] W. Lukosz and R. E. Kunz, *Light emission by magnetic and electric dipoles close to a plane interface. I. Total radiated power*, Journal of the Optical Society of America **67**, 1607 (1977).

[288] M. Kerker, D. S. Wang, and C. L. Giles, *Electromagnetic scattering by magnetic spheres*, Journal of the Optical Society of America **73**, 765 (1983).

[289] J. C. Johnson, H.-J. Choi, K. P. Knutsen, R. D. Schaller, P. Yang, and R. J. Saykally, *Single gallium nitride nanowire lasers*, Nat Mater **1**, 106 (2002).

[290] J. C. Ginn, I. Brener, D. W. Peters, J. R. Wendt, J. O. Stevens, P. F. Hines, L. I. Basilio, L. K. Warne, J. F. Ihlefeld, P. G. Clem, and M. B. Sinclair, *Realizing Optical Magnetism from Dielectric Metamaterials*, Physical Review Letters **108**, 097402 (2012).

[291] P. Moitra, Y. Yang, Z. Anderson, I. I. Kravchenko, D. P. Briggs, and J. Valentine, *Realization of an all-dielectric zero-index optical metamaterial*, Nature Photonics **7**, 791 (2013).

[292] S. Liu, M. B. Sinclair, T. S. Mahony, Y. C. Jun, S. Campione, J. Ginn, D. A. Bender, J. R. Wendt, J. F. Ihlefeld, P. G. Clem, J. B. Wright, and I. Brener, *Optical magnetic mirrors without metals*, Optica **1**, 250 (2014).

[293] E. Prodan, C. Radloff, N. J. Halas, and P. Nordlander, *A Hybridization Model for the Plasmon Response of Complex Nanostructures*, Science **302**, 419 (2003).

[294] P. Nordlander, C. Oubre, E. Prodan, K. Li, and M. I. Stockman, *Plasmon Hybridization in Nanoparticle Dimers*, Nano Letters **4**, 899 (2004).

[295] J. van de Groep and A. Polman, *Designing dielectric resonators on substrates: Combining magnetic and electric resonances*, Optics Express **21**, 26285 (2013).

[296] COMSOL Multiphysics 5.0, *www.comsol.com*.

[297] K. H. Drexhage, *Influence of a dielectric interface on fluorescence decay time*, Journal of Luminescence **1–2**, 693 (1970).

[298] T. Coenen, B. J. Brenny, E. J. Vesseur, and A. Polman, *Cathodoluminescence microscopy: Optical imaging and spectroscopy with deep-subwavelength resolution*, MRS Bulletin **40**, 359 (2015).

[299] E. J. R. Vesseur, T. Coenen, H. Caglayan, N. Engheta, and A. Polman, *Experimental Verification of $n = 0$ Structures for Visible Light*, Physical Review Letters **110**, 013902 (2013).

[300] B. J. M. Brenny, T. Coenen, and A. Polman, *Quantifying coherent and incoherent cathodoluminescence in semiconductors and metals*, Journal of Applied Physics **115**, 244307 (2014).

[301] C. Ballif, J. Dicker, D. Borchert, and T. Hofmann, *Solar glass with industrial porous SiO_2 antireflection coating: measurements of photovoltaic module properties improvement and modelling of yearly energy yield gain*, Solar Energy Materials and Solar Cells **82**, 331 (2004).

[302] M. Cid, N. Stem, C. Brunetti, A. F. Beloto, and C. A. S. Ramos, *Improvements in anti-reflection coatings for high-efficiency silicon solar cells*, Surface and Coatings

Technology **106**, 117 (1998).

[303] H. H. Li, *Refractive index of alkaline earth halides and its wavelength and temperature derivatives*, Journal of Physical and Chemical Reference Data **9**, 161 (1980).

[304] D. Chen, *Anti-reflection (AR) coatings made by sol-gel processes: A review*, Solar Energy Materials and Solar Cells **68**, 313 (2001).

[305] D. R. Uhlmann, T. Suratwala, K. Davidson, J. M. Boulton, and G. Teowee, *Sol-gel derived coatings on glass*, Journal of Non-Crystalline Solids **218**, 113 (1997).

[306] G. Aben, T. Kockelkorel, Y. Li, K. Matloka, M. Plaum, R. de Rijk, H. Schoot, and N. Voicu, *Light transmittance enhancement over lifetime performance of anti-reflective PV module cover glass*, Online poster, *www.dsm.com/corporate/markets-products/markets/energy/khepricoat.html* (2015).

[307] B. E. Yoldas and D. P. Partlow, *Wide spectrum antireflective coating for fused silica and other glasses*, Applied Optics **23**, 1418 (1984).

[308] K. X. Wang, Z. Yu, S. Sandhu, V. Liu, and S. Fan, *Condition for perfect antireflection by optical resonance at material interface*, Optica **1**, 388 (2014).

[309] K.-S. Han, J.-H. Shin, and H. Lee, *Enhanced transmittance of glass plates for solar cells using nano-imprint lithography*, Solar Energy Materials and Solar Cells **94**, 583 (2010).

[310] S.-H. Hong, B.-J. Bae, K.-S. Han, E.-J. Hong, H. Lee, and K.-W. Choi, *Imprinted moth-eye antireflection patterns on glass substrate*, Electronic Materials Letters **5**, 39 (2009).

[311] H. Deniz, T. Khudiyev, F. Buyukserin, and M. Bayindir, *Room temperature large-area nanoimprinting for broadband biomimetic antireflection surfaces*, Applied Physics Letters **99**, 183107 (2011).

[312] K.-C. Park, H. J. Choi, C.-H. Chang, R. E. Cohen, G. H. McKinley, and G. Barbastathis, *Nanotextured Silica Surfaces with Robust Superhydrophobicity and Omnidirectional Broadband Supertransmissivity*, ACS Nano **6**, 3789 (2012).

[313] H. K. Raut, S. S. Dinachali, Y. C. Loke, R. Ganesan, K. K. Ansah-Antwi, A. Góra, E. H. Khoo, V. A. Ganesh, M. S. M. Saifullah, and S. Ramakrishna, *Multiscale Ommatidial Arrays with Broadband and Omnidirectional Antireflection and Antifogging Properties by Sacrificial Layer Mediated Nanoimprinting*, ACS Nano **9**, 1305 (2015).

[314] W.-L. Min, B. Jiang, and P. Jiang, *Bioinspired Self-Cleaning Antireflection Coatings*, Advanced Materials **20**, 3914 (2008).

[315] K. Askar, B. M. Phillips, Y. Fang, B. Choi, N. Gozubenli, P. Jiang, and B. Jiang, *Self-assembled self-cleaning broadband anti-reflection coatings*, Colloids and Surfaces A: Physicochemical and Engineering Aspects **439**, 84 (2013).

[316] H. Hattori, *Anti-Reflection Surface with Particle Coating Deposited by Electrostatic Attraction*, Advanced Materials **13**, 51 (2001).

[317] J. Szczyrbowski, G. Bräuer, G. Teschner, and A. Zmelty, *Antireflective coatings on large scale substrates produced by reactive twin-magnetron sputtering*, Journal of Non-Crystalline Solids **218**, 25 (1997).

[318] S. Jeasung, *Study of nanostructured glass surfaces for photovoltaic applications*, PhD thesis, National University of Singapore, Singapore (2013).

[319] L. T. Sharpe, A. Stockman, W. Jagla, and H. Jägle, *A luminous efficiency function, $V*(\lambda)$, for daylight adaptation*, Journal of Vision **5**, 948 (2005).

[320] D. G. Stavenga, S. Foletti, G. Palasantzas, and K. Arikawa, *Light on the moth-eye corneal nipple array of butterflies*, Proceedings of the Royal Society B: Biological Sciences **273**, 661 (2006).

[321] J. C. Maxwell Garnett, *Colours in Metal Glasses and in Metallic Films*, Philosophical Transactions of the Royal Society of London. Series A **203**, 385 (1904).

[322] D. A. G. Bruggeman, *Berechnung verschiedener physikalischer Konstanten von heterogenen Substanzen. I. Dielektrizitätskonstanten und Leitfähigkeiten der Mischkörper aus isotropen Substanzen*, Annalen der Physik **416**, 636 (1935).

[323] J. H. Fatehi and K. J. Sauer, *Modeling the incidence angle dependence of photovoltaic modules in PVsyst*, in *IEEE 40th Photovoltaic Specialist Conference (PVSC)*, p. 1335–1338 (2014).

[324] A. B. D. Cassie and S. Baxter, *Wettability of porous surfaces*, Transactions of the Faraday Society **40**, 546 (1944).

[325] P. Forbes, *Self-cleaning materials*, Scientific American **299**, 88 (2008).

[326] M. A. Green, K. Emery, Y. Hishikawa, W. Warta, and E. D. Dunlop, *Solar cell efficiency tables (Version 45)*, Progress in Photovoltaics: Research and Applications **23**, 1 (2015).

[327] Panasonic press release, *Panasonic HIT Solar Cell Achieves World's Highest Energy Conversion Efficiency of 25.6% at Research Level*, April 10, 2014.

[328] A. Mavrokefalos, S. E. Han, S. Yerci, M. S. Branham, and G. Chen, *Efficient Light Trapping in Inverted Nanopyramid Thin Crystalline Silicon Membranes for Solar Cell Applications*, Nano Letters **12**, 2792 (2012).

[329] R. E. I. Schropp, J. K. Rath, and H. Li, *Growth mechanism of nanocrystalline silicon at the phase transition and its application in thin film solar cells*, Journal of Crystal Growth **311**, 760 (2009).

[330] Y. Baojie, Y. Guozhen, J. Yang, and S. Guha, *High efficiency amorphous and nanocrystalline silicon thin film solar cells on flexible substrates*, in *Active-Matrix Flatpanel Displays and Devices (AM-FPD), 19th International Workshop on*, p. 67–70 (2012).

[331] H. Tan, E. Psomadaki, O. Isabella, M. Fischer, P. Babal, R. Vasudevan, M. Zeman, and A. H. M. Smets, *Micro-textures for efficient light trapping and improved electrical performance in thin-film nanocrystalline silicon solar cells*, Applied Physics Letters **103**, 173905 (2013).

[332] J. Bhattacharya, N. Chakravarty, S. Pattnaik, W. Dennis Slafer, R. Biswas, and V. L. Dalal, *A photonic-plasmonic structure for enhancing light absorption in thin film solar cells*, Applied Physics Letters **99**, 131114 (2011).

[333] T. Matsui, M. Tsukiji, H. Saika, T. Toyama, and H. Okamoto, *Influence of substrate texture on microstructure and photovoltaic performances of thin film polycrystalline silicon solar cells*, Journal of Non-Crystalline Solids **299–302, Part 2**, 1152 (2002).

[334] M. Python, D. Dominé, T. Söderström, F. Meillaud, and C. Ballif, *Microcrystalline silicon solar cells: effect of substrate temperature on cracks and their role in post-oxidation*, Progress in Photovoltaics: Research and Applications **18**, 491 (2010).

[335] A. Polman, E. C. Garnett, B. Ehrler, M. W. Knight, and W. C. Sinke, *Photovoltaic materials - record efficiencies and future challenges*, Unpublished (2015).

[336] H. Sai, Y. Kanamori, and M. Kondo, *Flattened light-scattering substrate in thin film silicon solar cells for improved infrared response*, Applied Physics Letters **98**, 113502 (2011).

[337] K. Söderström, G. Bugnon, F. J. Haug, S. Nicolay, and C. Ballif, *Experimental study of flat light-scattering substrates in thin-film silicon solar cells*, Solar Energy Materials and Solar Cells **101**, 193 (2012).

[338] R. E. I. Schropp, *Advances in solar cells made with hot wire chemical vapor deposition (HWCVD): superior films and devices at low equipment cost*, Thin Solid Films **403–404**, 17 (2002).

[339] M. C. van Lare and A. Polman, *Optimized Scattering Power Spectral Density of*

Photovoltaic Light-Trapping Patterns, ACS Photonics **2**, 822 (2015).

[340] P. Spinelli and A. Polman, *Light Trapping in Thin Crystalline Si Solar Cells Using Surface Mie Scatterers,* IEEE Journal of Photovoltaics **4**, 554 (2014).

Summary

Efficient photovoltaic energy conversion requires accurate control over the flow and absorption of light in semiconductor materials to optimize the conversion from optical power to electrical power. For thin semiconductor films in particular, light trapping inside the active layer is essential to achieve sufficient optical absorption. Such light management requires control over the light-matter interaction at the nanoscale. Nanostructures with a size comparable to the wavelength of light show strong interaction with light as a result of optical resonances. These resonances can be designed to give rise to strong localized absorption or directional scattering, which provides control over the flow of light.

In this thesis, we explore how resonant nanophotonic structures can be used to control optical processes in photovoltaic energy conversion. We study the fundamental aspects of resonant light scattering by metallic and dielectric nanostructures, and apply these insights to design novel photovoltaic architectures with improved light management. First, we study how resonant networks of silver nanowires are transparent for light and conductive for electrical charge, and how fundamental understanding of the plasmon scattering mechanisms can be used to optimize the transmission of light through these networks. Next, we demonstrate how metal nanostructures can directly induce photo-voltages as a result of their resonant behavior, and how this effect can be used to realize all-metal optoelectric power conversion. Then, we investigate the resonant properties of dielectric nanoparticles, and how interference between the resonant modes gives rise to directional scattering. Finally, we describe two photovoltaic applications inspired by the work in this thesis.

In Chapter 2 we present a transparent conducting electrode design composed of a periodic two-dimensional network of silver nanowires. Using electron-beam lithography (EBL), we fabricate Ag nanowire networks on glass with wire diameters of 45–110 nm, and a pitch of 500, 700, and 1000 nm. The structures show anomalous optical transmission over a broad spectral range in the visible, with an average transmission of 91% for the best transmitting network, and a sheet resistance of only 6.5 Ω/sq for the best conducting network. The most dilute networks

outperform the industry-standard material indium-tin-oxide (ITO) as a transparent conductor. By comparing measurements and simulations we show that the transmission is governed by the interplay of localized plasmon resonances, grating diffraction, and surface plasmon polaritons.

In Chapter 3 we use substrate-conformal imprint-lithography (SCIL) to demonstrate the large-area application of the nanowire networks described in Chapter 2. We systematically study the influence of wire width (55–130 nm) and pitch (300–1000 nm) on the network transmittance and sheet resistance, and demonstrate improved performance compared to ITO. We use P3HT-PCBM polymer solar cells as a model system to show the applicability of large-area networks as a transparent electrode in functional devices. Angle-resolved external quantum efficiency (EQE) measurements are used to show light trapping by coupling to guided modes in the absorber layer. These results demonstrate how engineered 2D networks can unify the functions of transparent conductor and light trapping structure in one geometry.

In Chapter 4 we show how the relatively expensive and time-consuming vacuum-based metal deposition step that was used in Chapters 2 and 3 can be replaced with a solution-based process. Using SCIL we fabricate a template onto a glass substrate, comprised of a square array of trenches in a PMMA film (50–130 nm trench width, 300–1000 nm pitch). Next, the reduction of a $AgNO_3$ by glucose in aqueous solution is used to locally infill the trenches with silver, resulting into solution-grown engineered Ag nanowire networks on glass. We use rapid thermal annealing to smoothen the surface of the wires. We find an almost three-fold decrease in the resistivity of the networks compared to evaporated silver networks (3.5 Ω/sq vs 10.7 Ω/sq) at a spectrally averaged transmission of 76%. Using detailed characterization and a conductivity model, we demonstrate that the better performance is due to the larger grain size obtained in the solution-grown nanowire grid compared to the evaporated grid, which results in a strong reduction of electron scattering by grain boundaries.

In Chapter 5 we demonstrate a novel photoelectric effect based on the frequency-dependent optical absorption of resonant plasmonic nanostructures: that we term the *plasmoelectric* effect. We experimentally demonstrate this effect on 60-nm-diameter Au colloids on ITO, and on sub-wavelength arrays of 100-nm-diameter holes with pitch in the range of 150-300 nm in a 20 nm thick gold film. When illuminated with narrow-band radiation at wavelengths below (above) resonance, Kelvin probe force microscopy on the hole arrays shows a 100 mV negative (positive) surface potential on the array. This induced electrochemical potential (i.e. the plasmoelectric potential) is a thermodynamically spontaneous response driven by an increase in entropy, related to increased optical absorption by electrostatic charging.

In Chapter 6 we present in detail the thermodynamic theory underlying the plasmoelectric effect that was introduced in Chapter 5. We analyze a model system consisting of a single 20-nm-diameter silver particle in vacuum that is electrically connected to ground. Using minimization of the thermodynamic free energy

we find that the plasmoelectric effect is driven by an increase in entropy due to a minute temperature increase due to increased optical absorption as a result of a change in charge density. We find that surface potentials as large as 473 mV are induced under 100 W/m^2 monochromatic illumination, as a result of a 11 mK increase in the steady-state temperature of the nanoparticle. Next, we discuss the applicability of this analysis for realistic experimental geometries, and show that the plasmoelectric effect is generic for optical structures in which the resonance wavelength is linked to the charge density.

Chapter 7 describes the first steps towards the experimental demonstration of circuit-based plasmoelectric power conversion. We design a plasmonic hole array in a 20-nm-thick Au film that shows near-unity absorption as a result of resonant coupling to a damped SPP mode, and use full-wave simulations to study the resonant modes in the structure. Using EBL and focused-ion beam milling we fabricate plasmoelectric micro-capacitor devices that consist of a Au–Al_2O_3–Ag multilayer structure, with the plasmonic hole array integrated into the top plate. We experimentally study the absorption spectra and spatial absorption profiles of the devices, and find up to 89% absorption in the hole array at resonance (λ = 798 nm). Finally, towards the first demonstration of plasmoelectric power conversion, we design an AC optoelectronic experiment to measure the charging/discharging current of the micro-capacitor as a result of the plasmoelectric effect.

Chapters 2–7 focused on resonant metallic nanostructures. Next, we investigate (resonant) dielectric/semiconductor nanoparticles that also play an important role in light scattering for photovoltaics. In Chapter 8, we study the resonant properties of single silicon nanocylinders. Using angle-resolved cathodoluminescence imaging spectroscopy (ARCIS) we locally excite and detect the geometrical resonances inside single nanocylinders with diameters in the range of 60–350 nm. We measure the resonance spectra of all particles, and find that the cylinders support multiple resonances in the 400–700 nm spectral range that red shift with size. Using the high spatial resolution of ARCIS, we measure the modal field profiles inside the cylinders and observe good correspondence with numerical simulations and a 2D analytical model. Finally, we characterize the angle-resolved radiation distributions and use these to distinguish between electric and magnetic dipolar modes in the nanoparticles.

In Chapter 9 we use numerical simulations to systematically study the influence of particle geometry and dielectric environment on the resonant modes inside single dielectric resonators in the visible and near infra-red spectral range. By varying the height of the nanoparticle we show the key role of retardation in the excitation of the magnetic dipole mode (MD). Furthermore, we explore how the size, shape, and refractive index of the nanoparticle, as well as the substrate refractive index influence the resonance wavelength, spectral width, and spectral overlap of the electric dipole (ED) and MD mode. We study how dipoles and plane waves can couple to the resonant modes, and show that accurate design of a multilayer structure can be used to selectively excite the ED and MD mode. Finally, we demonstrate that the radiation profiles of the resonant modes resemble that of a point dipole,

and that spectral overlap of the ED and MD modes can be used to achieve strongly directional scattering.

Chapter 10 investigates how coupling between resonant dielectric nanoparticles that are placed in close proximity gives rise to hybridization of the resonant modes. Using EBL we pattern the top layer of a silicon-on-insulator (SOI) wafer into single and coupled pairs (dimers) of silicon cubes with 90 nm width and 100 nm height. The particle spacing is varied in the range of 0–100 nm. Using a dark-field scattering spectroscope, we study the influence of particle spacing on the scattering spectrum, and observe spectral broadening of the resonant peaks as a result of hybridization for 25 nm spacing. Using finite-element modeling we calculate the eigenmodes of the individual particles and dimers, and identify the hybridized modes as the longitudinal and parallel bonding of two magnetic dipole modes. Next, we use ARCIS to directly map the modal field profiles of the hybridized modes inside the particles. Finally, we resolve highly complex hybridized mode profiles in dimers composed of large silicon bars.

In Chapter 11 we demonstrate an effective nanopatterned anti-reflection coating on glass, composed of a 2D array of non-resonant silica nanocylinders. The coating is fabricated from solgel using a single SCIL step, without the need of vacuum technology or annealing. The cylinders are 120 nm tall, have a diameter of 245 nm, are spaced 325 nm apart, and form a layer with an effective index anti-reflection coating with $n = 1.20$. We demonstrate that the coating reduces the average double-side reflection from a borosilicate slide from 7.35% to 0.57%, with a minimum reflectance $< 0.05\%$ at $\lambda = 590$ nm. We show that the coating is well described by effective medium theory, and that it effectively eliminates the glare from smart-phone display screens as well as glass encapsulated solar cells. The coating is hydrophobic and its refractive index can be tailored over a wide range by engineering the geometry.

Chapter 12 describes two applications inspired by the work in this thesis. First, we present silver nanowire networks that act as transparent electrodes on high-efficiency Si heterojunction solar cells. We design an ITO/nanowire network/Si_3N_4 hybrid electrode to replace the standard 80 nm thick ITO transparent conducting layer on top of the cells. We find a drastic improvement in the conductivity, which enables an increasing in the macroscopic finger spacing by a factor 2.5, yielding an increase in efficiency from 14.8% to 16.0%. Second, we present a soft-imprinted dielectric nanopattern that acts as a flat plasmonic back scattering electrode in nanocrystalline Si solar cells. We grow flat layers of nanocrystalline Si, use substrate-conformal imprint-lithography to print a silica nanopattern on the back of the cell, and overcoat it with Ag to form a flat scattering electrode. We find a strong enhancement in the photocurrent without a loss in voltage that is typically observed for non-flat scattering layers.

Overall, this thesis provides fundamental insights in light scattering and absorption by resonant metallic and dielectric nanostructures that can be used in the design and development of improved photovoltaic devices and other optoelectronic applications.

Samenvatting

Efficiënte fotovoltaïsche energieconversie vereist precieze controle over de voortplanting en absorptie van licht in halfgeleidermaterialen om de conversie van licht naar elektrisch vermogen te optimaliseren. Vooral voor dunne-laag halfgeleidermateriaal is het opsluiten van licht in de actieve laag essentieel om het licht adequaat te kunnen absorberen. Dergelijke manipulatie van licht vergt controle over de interactie tussen licht en materie op de nanoschaal. Nanostructuren die in grootte vergelijkbaar zijn met de golflengte van licht ondergaan door middel van optische resonanties sterke interactie met licht. Deze resonanties kunnen worden gebruikt om licht lokaal te absorberen of directioneel te verstrooien, hetgeen de mogelijkheid biedt de voortplanting en het invangen van licht te controleren.

In dit proefschrift onderzoeken we hoe resonante nanofotonische structuren kunnen worden gebruikt om de optische processen te controleren die belangrijk zijn voor fotovoltaïsche energieconversie. We bestuderen de fundamentele aspecten van resonante verstrooiing van licht door metalen en diëlektrische nanostructuren. Vervolgens passen we de verkregen inzichten toe om nieuwe zonnecelarchitecturen te realiseren, waarbinnen licht beter omgezet kan worden. We bestuderen hoe netwerken bestaande uit zilveren nanodraden tegelijkertijd licht kunnen doorlaten en stroom kunnen geleiden. Tevens bestuderen we hoe fundamenteel begrip van de plasmonische verstrooiingsprocessen kan worden ingezet om de transparantie van deze netwerken te optimaliseren. We demonstreren hoe metallische nanostructuren direct elektrische potentialen kunnen induceren ten gevolge van resonante interacties met licht. Vervolgens laten we zien hoe met dit fenomeen optische energie door middel van volledig metalen structuren naar elektrische energie kan worden geconverteerd. We bestuderen de resonante eigenschappen van diëlektrische nanodeeltjes en we onderzoeken hoe interferentie van licht dat verstrooid is door verschillende modes, resulteert in directionaliteit. Tot slot presenteren we twee fotovoltaïsche toepassingen die zijn geïnspireerd door het werk dat in dit proefschrift staat beschreven.

In hoofdstuk 2 presenteren we een ontwerp voor een transparante en geleidende elektrode, bestaande uit een tweedimensionaal regelmatig netwerk van zilveren nanodraden. Met behulp van electron beam lithography (EBL) fabriceren we

netwerken van zilveren nanodraden op glas met draaddiameters van 45–110 nm en afstanden tussen de draden van 500, 700, en 1000 nm. De netwerken tonen abnormaal hoge transmissie over een breed bereik van het zichtbare spectrum. Het meest transparante netwerk heeft een gemiddelde transmissie van 91% en het meest geleidende netwerk een weerstand van slechts 6.5 Ω per vierkant. Het minst dichte netwerk presteert beter als transparante geleider dan indium-tin-oxide (ITO), het standaardmateriaal dat veel wordt gebruikt in de industrie. Door de meetresultaten te vergelijken met simulaties laten we zien dat de transmissie door de netwerken wordt bepaald door een samenspel van gelokaliseerde plasmonenresonanties, diffractie en oppervlakteplasmonpolaritonen (OPP).

In hoofdstuk 3 maken we gebruik van substrate-conformal imprint-lithography (SCIL) om de nanodraadnetwerken die zijn beschreven in hoofdstuk 2 toe te passen op grote oppervlakken. We bestuderen de invloed van draadbreedte (55–130 nm) en draadafstand (300–1000 nm) op de transmissie en weerstand van de netwerken. We laten zien dat de netwerken beter fungeren als transparante geleider dan ITO. We gebruiken P3HT-PCBM polymeer zonnecellen als een modelsysteem om aan te tonen dat de nanodraadnetwerken op grote schaal als transparante elektrode in werkende apparaten kunnen worden toegepast. Met behulp van hoekopgeloste externe kwantumefficiëntiemetingen laten we zien dat licht in de actieve laag van de zonnecellen wordt opgesloten door middel van het koppelen naar lichtgeleidende modes. Deze resultaten demonstreren hoe tweedimensionale netwerken van nanodraden tegelijkertijd kunnen functioneren als transparante geleider en als geometrie die licht opsluit.

In hoofdstuk 4 laten we zien hoe de relatief dure en tijdsintensieve vacuümmetaaldepositiemethode die is gebruikt in de hoofdstukken 2 en 3 kan worden vervangen door een proces dat is gebaseerd op een chemische vloeistofreactie. We fabriceren een sjabloon op glas met behulp van SCIL, dat bestaat uit een vierkant rooster van kanaaltjes in een laag PMMA (50–130 nm breed, 300–1000 nm afstand tussen de kanaaltjes). Vervolgens gebruiken we de reductie van $AgNO_3$ door glucose in oplossing om de kanaaltjes lokaal te vullen met zilver, zodat een gecontroleerd netwerk van zilveren nanodraden ontstaat op glas, dat gegroeid is uit de oplossing. We vinden dat de weerstand van de nanodraadnetwerken bijna drie maal zo laag is dan die van netwerken bestaande uit opgedampte zilveren netwerken; namelijk 3.5 in plaats van 10.7 Ω per vierkant, bij een spectraal gemiddelde transmissie van 76%. Door de netwerken in detail te karakteriseren en gebruik te maken van een model voor de geleiding in dunne metaallagen tonen we aan dat de verbetering een gevolg is van het feit dat de uit oplossing gegroeide netwerken uit grotere metaalkorrels bestaan dan de opgedampte netwerken. Dit leidt tot een sterke vermindering van elektronverstrooiing aan de grenzen van de korrels.

In hoofdstuk 5 demonstreren we een nieuw foto-elektrisch effect dat gebruik maakt van de frequentieafhankelijke absorptie van licht door resonante plasmonische nanostructuren, we geven het de naam plasmoelektrische effect. We demonstreren dit effect door middel van experimenten op goudcolloïden met een grootte van 60 nm, geplaatst op een ITO substraat en op een patroon van gaten in

een 20 nm dikke goudlaag met een gatdiameter van 100 nm en gatafstand van 150–300 nm. Wanneer deze structuren belicht worden met spectraal nauwe straling met golflengtes kleiner (groter) dan de resonantiegolflengte, laten Kelvin-probe force-microscopy (KPFM) metingen 100 mV negatieve (positieve) oppervlaktepotentialen zien. Deze geïnduceerde elektrochemische potentiaal (de plasmoelektrische potentiaal) is een thermodynamische reactie, gedreven door een toename in de entropie van het systeem, gerelateerd aan een toename in de absorptie van licht as gevolg elektrostatische oplading.

In hoofdstuk 6 presenteren we de aan het in hoofdstuk 5 geïntroduceerde plasmoelektrische effect onderliggende thermodynamische theorie. We analyseren een modelsysteem bestaande uit een enkel zilveren deeltje met een grootte van 20 nm in vacuüm dat elektrisch geaard is. Gebruikmakend van de minimalisatie van de thermodynamische vrije energie, vinden we dat het plasmoelektrische effect gedreven wordt door een toename in de entropie van het systeem, als gevolg van een zeer kleine toename in temperatuur. Deze toename in temperatuur wordt veroorzaakt door een toename in de absorptie van licht, ten gevolge van een verandering in de ladingsdichtheid. We vinden dat een oppervlaktespanning van 473 mV wordt geïnduceerd onder 100 W/m^2 monochromatische belichting ten gevolge van een toename van 11 mK in de temperatuur van het nanodeeltje. Vervolgens bespreken we de toepasbaarheid van deze analyse op realistische experimentele geometrieën en tonen we aan dat het plasmoelektrische effect generiek is voor structuren die een resonante interactie met licht vertonen en waarbij de resonantiegolflengte afhangt van de ladingsdichtheid.

Hoofdstuk 7 beschrijft de eerste stappen in de richting van de experimentele demonstratie van plasmoelektrische energie-omzetting in een elektrisch circuit. We ontwerpen een patroon van gaten in een 20 nm dikke goudlaag dat bijna volledige absorptie vertoont ten gevolge van resonante koppeling naar gedempte OPP. Vervolgens gebruiken we optische simulaties om de resonante modes in de structuur te bestuderen. Gebruik makend van EBL en focused ion-beam milling, fabriceren we plasmoelektrische microcondensatoren die bestaan uit een Au–Al_2O_3–Ag multilaagstructuur met het plasmonische gatenpatroon geïntegreerd in de bovenste plaat. We meten de absorptiespectra en ruimtelijke absorptieprofielen van deze microschakelingen en observeren dat op resonantie (λ = 798 nm) 89% van het licht geabsorbeerd wordt in het gatenpatroon. Tot slot ontwerpen we - met oog op de eerste experimentele demonstratie van plasmoelektrische energie-omzetting - een AC foto-elektrisch experiment, waarbij de ladings- en ontladingsstroom van de microcondensatoren ten gevolge van het plasmoelektrische effect worden gemeten.

Hoofdstukken 2 tot en met 7 bespreken resonante metalen nanostructuren. Hierna verleggen we onze aandacht en bestuderen we resonante diëlektrische en halfgeleidende nanodeeltjes die ook een belangrijke rol spelen in toepassingen van lichtverstrooiing in fotovoltaïca. In hoofdstuk 8 bestuderen we de resonante eigenschappen van enkele silicium nanocylinders. Gebruikmakend van angle-resolved cathodoluminescence imaging spectroscopy (ARCIS) exciteren we de geometrische resonanties in nanocylinders met een diameter van 60–350 nm

lokaal en detecteren de resonantiespectra van de deeltjes. We vinden meerdere resonanties in het spectrale bereik van 400–700 nm en vinden dat deze resonanties roodverschuiven voor grotere diameters. Gebruikmakend van het hoge plaatsopgelost vermogen van ARCIS meten we de optische modeprofielen in de deeltjes en vinden goede overeenkomst met numerieke simulaties en een tweedimensionaal analytisch model. Tot slot karakteriseren we de hoekopgeloste stralingsprofielen en gebruiken deze om onderscheid te maken tussen de elektrische en magnetische dipoolresonanties in de nanodeeltjes.

In hoofdstuk 9 gebruiken we numerieke simulaties om de invloed van de geometrie en diëlektrische omgeving op de resonante modes in enkele diëlektrische deeltjes te bestuderen. Door de hoogte van het deeltje te variëren tonen we de essentiële rol van retardatie aan voor de excitatie van de magnetische dipoolresonantie (MD). Verder onderzoeken we hoe grootte, vorm en brekingsindex van zowel het nanodeeltje als van het substraat, de golflengte, de spectrale breedte en de spectrale overlap van de MD en elektrische dipoolresonantie (ED) beïnvloeden. We bestuderen hoe dipolen en vlakke golven aan de resonanties kunnen koppelen en laten zien dat het precies ontwerpen van een multilaagsubstraat kan worden gebruikt om selectief te koppelen aan de MD en ED modes. Tot slot laten we zien dat de stralingsprofielen van de resonanties vergelijkbaar zijn met die van een puntdipool alsmede dat de spectrale overlap tussen de ED en MD modes kan worden gebruikt om sterke directionaliteit in het verstrooiingsproces te realiseren.

Hoofdstuk 10 bestudeert hoe koppeling tussen resonanties in diëlektrische deeltjes die in elkaars nabijheid staan resulteert in hybridisatie. Met behulp van EBL patroneren we de bovenste laag van een silicon-on-insulator (SOI) wafer tot enkele kubussen en gekoppelde paren van kubussen (dimeren) van silicium met een breedte van 90 nm en hoogte van 100 nm. De afstand tussen de deeltjes wordt gevarieerd van 0–100 nm. We bestuderen de invloed van deeltjesafstand op het verstrooiingsspectrum met behulp van dark-field (DF) verstrooiingsspectroscopie en observeren spectrale verbreding van de resonantiepieken als gevolg van hybridisatie voor een deeltjesafstand van 25 nm. We berekenen de eigenmodes van de individuele en gekoppelde deeltjes met eindige-element numerieke modellen en identificeren de gehybridiseerde eigenmodes als de longitudinaal en parallel gekoppelde magnetische dipoolresonanties. Vervolgens gebruiken we ARCIS om de modeprofielen van de gehybridiseerde modes direct te meten. Tot slot meten we de modeprofielen van meer complexe gehybridiseerde modes in gekoppelde lange silicium balken.

In hoofdstuk 11 demonstreren we een anti-reflectie coating voor glas, bestaande uit een tweedimensionaal nanopatroon van niet-resonante silica nanocylinders. De coating wordt gefabriceerd uit silica solgel door middel van SCIL en de fabricage vereist geen vacuümtechnologie of verhitting. De cylinders zijn 120 nm hoog, hebben een diameter van 245 nm, staan 325 nm van elkaar af en vormen gezamenlijk een efficiënte anti-reflectie coating met een effectieve brekingsindex van $n = 1.20$. We tonen aan dat de coating de gemiddelde tweezijdige reflectie van een borosilicaatglas substraat vermindert van 7.35% naar 0.57% met

een minimum reflectie < 0.05% bij λ = 590 nm. We laten zien dat de coating goed wordt beschreven door een effectief-medium model en dat de coating zowel de schittering van smart-phone schermen als de reflectie van zonnecellen die ingekapseld zijn in glas op een effectieve wijze elimineert. De coating is waterafstotend en de brekingsindex kan door middel van de geometrie over een groot bereik worden gevarieerd.

Tot slot beschrijft hoofdstuk 12 twee toepassingen van het werk dat in dit proefschrift is gepresenteerd. Ten eerste presenteren we zilveren nanodraadnetwerken die fungeren als transparante en geleidende elektrodes in efficiënte silicium heterojunctie zonnecellen. We ontwerpen een ITO/nanodraad netwerk/Si_3N_4 hybride elektrode om de standaard 80 nm dikke ITO laag als transparante geleidende bovenste laag in deze cellen te vervangen. We observeren een drastische toename in de geleiding van de laag, wat het mogelijk maakt om de afstand tussen de vingers van de macroscopische elektrode met een factor 2.5 is vergroten. Dit resulteert in een toename van de efficiëntie van 14.8% naar 16.0%. Ten tweede presenteren we geprinte patronen van diëlektrische nanodeeltjes die fungeren als vlakke plasmonische verstrooiende achtercontacten in nanokrystallijn Si (nc-Si) zonncellen. We groeien vlakke nc-Si lagen, gebruiken SCIL om een silica nanopatroon te printen op de achterzijde van de cel, en coaten het met zilver om een verstrooiend achtercontact te maken. We vinden een sterke toename in de fotostroom zonder een afname in voltage die normaliter wordt gevonden voor niet-vlakke verstrooiende lagen.

Samenvattend geeft dit proefschrift fundamenteel inzicht in de verstrooiingsprocessen en absorptieprocessen van licht door resonante metalen en diëlektrische nanostructuren. Deze inzichten kunnen worden gebruikt voor het ontwerp en de ontwikkeling van verbeterde zonnecellen en andere foto-elektrische toepassingen.

List of publications

This thesis is based on the following publications:

- *Transparent conducting silver nanowire networks*, J. van de Groep, P. Spinelli, and A. Polman, Nano Lett. **12**, 3138–3144 (2012). **(Chapter 2)**
- *Large-area soft-imprinted nanowire networks as light trapping transparent conductors*, J. van de Groep, D. Gupta, M. A. Verschuuren, M. M. Wienk, R. A. J. Janssen, and A. Polman, Sci. Rep. **5**, 11414 (2015). **(Chapter 3)**
- *Solution-grown silver nanowire ordered arrays as transparent electrodes*, B. Sciacca, J. van de Groep, A. Polman, and E. C. Garnett, Submitted to Adv. Mater. (2015). **(Chapter 4)**
- *Plasmoelectric potentials in metal nanostructures*, M. Sheldon, J. van de Groep, A. M. Brown, A. Polman, and H. A. Atwater, Science **346**, 828–831 (2014). **(Chapter 5)**
- *Theory of the plasmoelectric effect*, J. van de Groep, M. Sheldon, H. A. Atwater, and A. Polman, Submitted to Sci. Rep. (2015). **(Chapter 6)**
- *Integrated circuits for AC plasmoelectric power conversion*, J. van de Groep, S. A. Mann, M. Sheldon, E. C. Garnett and A. Polman, in preparation. **(Chapter 7)**
- *Resonant Mie modes of single silicon nanocavities excited by electron irradiation*, T. Coenen*, J. van de Groep*, and A. Polman, ACS Nano **7**, 1689-1698 (2013). (*equal author contribution) **(Chapter 8)**
- *Designing dielectric resonators on substrates: Combining magnetic and electric resonances*, J. van de Groep and A. Polman, Opt. Express **21**, 26285–26302 (2013). **(Chapter 9)**
- *Direct imaging of hybridized eigenmodes in coupled silicon nanoparticles*, J. van de Groep, T. Coenen, S. A. Mann, and A. Polman, in preparation **(Chapter 10)**

- *Single-step soft-imprinted large-area nanopatterned antireflection coating*, J. van de Groep, P. Spinelli, and A. Polman, Nano Lett. **15**, 4223–4228 (2015). **(Chapter 11)**

- *Transparent Ag nanowire hybrid-electrodes for silicon heterojunction solar cells*, M. W. Knight, J. van de Groep, P. C. P. Bronsveld, W. C. Sinke, and A. Polman, in preparation. **(Chapter 12.2)**

- *Plasmonic scattering back reflector for light trapping in flat nano-crystalline silicon solar cells of high material quality*, L. van Dijk, J. van de Groep, L. W. Veldhuizen, M. Di Vece, A. Polman, and R. E. I. Schropp, in preparation. **(Chapter 12.3)**

Patent application:

- *Nanoglass: nanopatterned anti-reflection coating for glass*, P. Spinelli, J. van de Groep, and A. Polman, European Patent Application 13005573.4-1562 (2014).

Other publications by the author:

- *Rate of runaway evaporative cooling*, J. van de Groep, P. van der Straten, and J. M. Vogels, Phys. Rev. A **84**, 033628 (2011).

- *Microphotonic parabolic light directors fabricated by two-photon lithography*, J. H. Atwater, P. Spinelli, E. Kosten, J. Parsons, C. van Lare, J. van de Groep, J. Garcia De Abajo, A. Polman, and H. A. Atwater, Appl. Phys. Lett. **99**, 151113 (2011).

- *Plasmonic light trapping in thin-film Si solar cells*, P. Spinelli, V.E. Ferry, J. van de Groep, C. van Lare, M. A. Verschuuren, R. E. I. Schropp, H. A. Atwater, and A. Polman, J. Opt.**14**, 024002 (2012).

- *Optics of milled external light trap for thin film c-Si solar cells*, L. van Dijk, J. van de Groep, A. Polman, M. Di Vece, and R. E. I. Schropp, in preparation.

- *Metal-insulator-semiconductor nanowire network solar cells*, S. Z. Oener, J. van de Groep, B. Macco, P. C. P. Bronsveld, A. Weeber, W. M. M. Kessels, A. Polman, and E. C. Garnett, in preparation.

Acknowledgements

Pas bij het schrijven van het dankwoord werd mij duidelijk hoeveel mensen hebben bijgedragen aan dit proefschrift. Daarvoor wil ik graag mijn dank uitspreken.

Allereerst wil ik graag mijn promotor Albert Polman bedanken voor deze kans. De afgelopen jaren waren een fantastische ervaring en een uitdaging. Doordat je altijd de juiste vragen weet te stellen en kansen ziet in nieuwe onderzoeksrichtingen, heb ik enorm veel van je geleerd. Verder zorgt jouw oneindige optimisme voor een goede drijfveer. Je doet je werk als groepsleider met veel toewijding, maar ook met oog voor de persoonlijke aspecten in het leven van je groepsleden. Ik heb hier veel steun aan gehad gedurende de afgelopen jaren.

During my years in the group, I have enjoyed working with a large group of postdocs, PhD students and master students that contributed to the great atmosphere in the group. I learned a lot from the many discussions during group meetings and enjoyed our coffee breaks and conference trips. James Parsons, Robb Walters, Bonna Newman, Mark Knight, Rutger Thijssen, Ernst-Jan Vesseur, Claire van Lare, Pierpaolo Spinelli, Toon Coenen, Ruben Maas, Benjamin Brenny, Marie-Anne van de Haar, Lourens van Dijk, Hinke Schokker, Hugo Doeleman, Bas Zegers, and Julia Attevelt, thank you for a great time. Rutger, jouw alwetendheid in het lab was onmisbaar in mijn eerste jaren. Ruben, we kennen elkaar al vanuit onze studie in Utrecht en jij hebt mij zelfs nog werkcollege gegeven! Ik kijk met veel plezier terug naar de vele jaren van samenwerking. Ik waardeer jouw kritische kijk op dingen, dit heeft mij vele malen geholpen wanneer ik vast zat met mijn onderzoek.

Over the past years, 2.48 may have been the most busy and noisy office within AMOLF, but probably also one of the most enjoyable and productive offices. Toon, Piero, Marie-Anne, Lourens and Mark, you are fully responsible for the many productive discussions on challenging scientific problems as well as the chats on daily life. Thank you for all the fun.

The Center for Nanophotonics binnen AMOLF creëert een unieke en uiterst leerzame omgeving waarbinnen op een directe wijze feedback wordt gegeven. Het wekelijkse colloquium heb ik altijd gezien als een kans om te leren van een groep uiterst gemotiveerde, betrokken en intelligente collegae. De kritische houding van alle leden tijdens de lezingen en postersessies was altijd een goede check of je echt

begrijpt waar je over praat. Hartelijk dank aan iedereen die hier aan bij heeft gedragen.

AMOLF strongly encourages collaborations between groups within the center for nanophotonics. Albert, your effort to utilize your professional network for your students has also resulted into multiple fruitful collaborations outside AMOLF. As a result, many people have contributed to the chapters in this thesis. Pierpaolo Spinelli, Toon Coenen, Sander Mann, Beniamino Sciacca, Sebastian Oener, Lourens van Dijk, Erik Garnett, Dhritiman Gupta, Martijn Wienk, René Janssen, Marc Verschuuren, Ana Brown, and Harry Atwater, thank you for the enjoyable collaborations. A special thanks to Matt Sheldon; our long standing intensive collaboration has been a true journey. I have learned a lot from working with you, and your enthusiasm for science has been a great source of inspiration to me.

Als promovendus heb je het bij AMOLF gemakkelijk: er is fantastische ondersteuning voor al je technische problemen. Ik heb dan ook gretig gebruik gemaakt van de services van onze groepstechnicus Dion en de afdelingen elektronica, software, ICT, de tekenkamer en de werkplaats. Verder hebben Hans Zeijlemaker, Andries Lof en vooral Dimitry Lamers een onmisbare rol gespeeld in de ondersteuning en het onderhoud van het nanocenter, waarvoor ik jullie wil bedanken.

Besides work, AMOLF - and team Garnett in particular - has been a great supply of competitors for the Wednesday squash competitions that we started over the last year. Thank you Sebastian, Beniamino, Eric, Annemarie, and Haralds, I enjoyed the distraction from work.

Buiten AMOLF ben ik dankbaar voor de steun en enthousiasme van mijn ouders, broer en zusje, verdere familie en vrienden. Jullie interesse tijdens talloze gezellige avonden was onmisbaar. Wendy, jouw oneindige liefde, geduld en steun hebben voor mij hét verschil gemaakt. Ik heb enorm veel zin in ons avontuur in de VS de komende jaren!

About the author

Jorik van de Groep was born in Putten, The Netherlands, on December 16, 1986. After receiving his high school diploma from Christelijk College Nassau Veluwe in Harderwijk in 2005, he studied both science and innovation management and physics at Utrecht University. He graduated cum laude in 2011, with a thesis on plasmon mediated coupling to guided modes, supervised by prof. dr. Albert Polman at the FOM Institute AMOLF in Amsterdam. He continued his work at AMOLF as a PhD student in the same group. The results of this work are presented in this thesis. In his free time, Jorik enjoys playing squash, traveling, and reading.

The work described in this thesis was performed at the FOM-Institute AMOLF, Science Park 104, 1098 XG Amsterdam, The Netherlands.